

Diss. ETH No. 17471

Site effects in the Rhône valley analysed by ambient noise, weak motion records and numerical simulations

A dissertation submitted to

ETH ZURICH

for the degree of

Doctor of Sciences

presented by

DANIEL ROTEN

Dipl. Natw. ETH

born February 25, 1976

citizen of Ried-Brig (VS)

accepted on the recommendation of

Prof. Dr. Domenico Giardini, examiner

Dr. Donat Fäh, co-examiner

Prof. Dr. Pierre-Yves Bard, co-examiner

2007

Summary

In this thesis earthquake site effects in the Rhône valley, Switzerland, are studied with observational and theoretical methods. In the first part shear-wave velocities of the Rhône sediments are estimated by array measurements of ambient noise. We recorded linear arrays with the receivers arranged on a profile running perpendicular to the valley axis and a reference station on bedrock. Site-to-reference spectral ratios computed from the recorded noise show that standing waves evoked by 2-D resonance dominate the noise wavefield at low frequencies (< 1 Hz). By rotating the ambient noise to the direction perpendicular and parallel to the valley axis we are able to identify the fundamental mode 2-D resonance frequencies SH_{00} and SV_0 . Additionally, circular arrays were recorded to derive apparent velocities of Rayleigh waves with the high-resolution frequency-wavenumber method. However, the 2-D resonance of the basin limits the depth that can be resolved from apparent velocities, because the inversion relies on the supposition that the noise is mainly composed of horizontally propagating surface waves. An alternate inversion scheme is proposed which takes the strong 2-D geometry of the basin into account. The combined inversion seeks for velocity models that explain both dispersion curves and the identified different mode 2-D resonance frequencies. The method is successfully tested on a synthetic dataset and applied to three different sites in the Rhône valley. Further array measurements are performed at numerous sites in the vicinity of Sion.

Results of the ambient noise array measurements reveal a shallow low-velocity layer up to 30 meters deep at most sites, with shear-wave velocities between 150 and 250 ms^{-1} . Below this layer velocities range between 320 and 500 ms^{-1} in the deltaic and lacustrine sediments, and between 600 to 700 ms^{-1} in the coarser material that composes alluvial fans. The glaciolacustrine deposits in the deeper part of the sedimentary fill are characterised by a shear-wave velocity between 700 and 1000 ms^{-1} . The obtained shear-wave velocities are combined with other geophysical and geological information, and a detailed local 3-D velocity model of the Sion area is developed.

For the second part of this work we operated a temporary network of 12 seismic stations in the city of Sion. Site-to-reference spectral ratios are computed from the recorded weak ground motion of 15 local earthquakes to quantify the amplification and to identify the resonance frequencies. At most stations, site-to-reference spectral ratios show a significant amplification of up to 12 at about 0.5 Hz, which is interpreted as two-dimensional resonance of the basin. Addi-

tionally, an average amplification level of at least 5 is observed for the whole frequency band between 1 and 10 Hz.

We apply the high-resolution frequency-wavenumber and the MUSIC (multiple signal characterisation) method to the recorded signals. The wavefield at higher frequencies (1.0 – 2.5 Hz) is dominated by edge-diffracted surface waves, which are detected by their direction of origin and apparent slowness. This leads us to the conclusion that these edge-generated surface waves are mainly contributing to the observed amplification at higher frequencies.

During the third part numerical simulations of wave propagation in the Sion basin are performed with the 3-D finite difference method for frequencies up to 4 Hz. We simulate four of the observed earthquakes to verify the newly developed velocity model. Average site-to-reference spectral ratios computed from the synthetic ground motion are able to reproduce the main characteristics of the observed amplification. Simulated peak ground velocities show that high amplification occurs in spots where edge-generated surface waves create positive interference. We also simulate the 1946 M_L 6.1 earthquake of Sierre and compute peak ground velocities obtained for the old town of Sion. Results suggest that site effects did not contribute substantially to earthquake damage during the 1946 event, which is in agreement with a reconstruction of the damage field.

In the last part the importance of nonlinear soil behaviour during strong ground motion is estimated. A few soil samples were extracted from an excavation pit in Visp and analysed with cyclic triaxial tests to determine the dilatancy parameters. We generate a set of synthetic seismograms and convolve them with the transfer function of the basin to obtain input signals with a realistic frequency content. The response of a shallow sandlayer is simulated with a fully nonlinear 1-D finite difference method. We find that reduced amplification can be expected at rock accelerations above 0.5 ms^{-2} , and that deamplification occurs at ground motion levels of approximately 2 ms^{-2} . Nevertheless, the spectral accelerations simulated for the valley centre are still exceeding the design spectra at about 0.5 Hz for magnitudes above 6.0. At higher frequencies the design spectra are generally in agreement with the strongest simulated accelerations. Our nonlinear simulations suggest that strong nonlinear effects such as liquefaction are likely to occur on the soft unconsolidated Rhône deposits during strong motion, which confirms observations of liquefaction reported after the 1855 M_L 6.4 earthquake of Visp.

The results of this work demonstrate the complexity of wave propagation effects that cause amplification of seismic waves in irregularly shaped structures like the Rhône basin. We conclude that the combination of different approaches, including ambient noise methods, 3-D simulations with a detailed velocity model, earthquake observations and simulations of nonlinear soil response provides an extensive but promising way to characterise the site response in complex sedimentary valleys.

Zusammenfassung

In der vorliegenden Arbeit werden Standorteffekte bei Erdbeben im Rhôneetal anhand empirischer und theoretischer Methoden untersucht. Im ersten Teil werden die Scherwellengeschwindigkeiten der Rhôneablagerungen durch Arraymessungen der seismischen Bodenunruhe bestimmt. Wir führten geradlinige Arraymessungen durch, bei denen die Stationen auf einem senkrecht zur Talachse verlaufenden Profil angeordnet und eine Referenzstation auf Fels stationiert wurden. Die Spektralverhältnisse zwischen den Standorten auf dem Lockermaterial und der Referenzstation zeigen, dass die natürliche Bodenunruhe im tieffrequenten Bereich (< 1 Hz) von stehenden Wellen dominiert wird, die durch 2-D Resonanz hervorgerufen werden. Wir bestimmen die Fundamentalfrequenzen der 2-D Resonanzmodi SH_{00} and SV_0 , indem wir die natürliche Bodenunruhe in die Richtung parallel, beziehungsweise senkrecht zur Talachse rotieren. Zusätzlich wurden kreisförmige Arrays gemessen, um die scheinbaren Geschwindigkeiten von Rayleighwellen mit der hochauflösenden Frequenz-Wellenzahl Methode zu bestimmen. Die 2-D Resonanz des Sedimentbeckens beschränkt aber die maximale Tiefe, die sich durch die scheinbaren Geschwindigkeiten auflösen lässt; denn die Inversion beruht auf der Annahme, dass die Bodenunruhe vor allem aus Oberflächenwellen besteht, die sich horizontal ausbreiten. Daher wurde ein modifiziertes Inversionsschema entwickelt, welches die ausgeprägte 2-D Struktur des Sedimentbeckens berücksichtigt. Die kombinierte Inversion sucht nach Geschwindigkeitsmodellen, welche sowohl die Dispersionskurve, wie auch die beobachteten 2-D Resonanzfrequenzen der unterschiedlichen Moden erklären. Die Methode wird zunächst erfolgreich auf einem synthetischen Datensatz getestet und dann auf drei reale Standorte im Rhôneetal angewendet.

Die Auswertung der Arraymessungen zeigt, dass bei den meisten Standorten eine oberflächennahe Schicht von bis zu 30 Metern Tiefe vorhanden ist, die sehr geringe S-Wellengeschwindigkeiten zwischen 150 und 250 ms^{-1} aufweist. In den feinkörnigen See- und Deltaablagerungen unterhalb dieser Schicht liegen die Geschwindigkeit der S-Wellen zwischen 320 und 500 ms^{-1} , in den grobkörnigen Ablagerungen der Schuttkegel schwanken sie zwischen 600 und 700 ms^{-1} . Die glazialen Ablagerungen im unteren Bereich der Sedimentfüllung weisen ein S-Wellengeschwindigkeit zwischen 700 und 1000 ms^{-1} auf. Die gemessenen S-Wellengeschwindigkeiten werden mit anderen verfügbaren geologischen und geophysikalischen Informationen kombiniert, und ein detailliertes 3-D Geschwindigkeitsmodell der Gegend um Sion wird entwickelt.

Für den zweiten Teil dieser Arbeit wurde ein temporäres Stationsnetz von 12 Seismometern innerhalb der Stadt Sion betrieben. Aus der Bodenbewegung von ca. 15 lokalen Erdbeben werden die Spektralverhältnisse zur Referenzstation berechnet, um die Verstärkung durch die Lockersedimente zu messen und die Resonanzfrequenzen zu bestimmen. Bei den meisten Standorten wird eine bis zu 12-fache Verstärkung bei ungefähr 0.5 Hz beobachtet, welche durch die 2-D Resonanz der Talfüllung verursacht wird. Zusätzlich wird im gesamten Frequenzbereich zwischen 1 und 10 Hz mindestens eine 5-fache Verstärkung gemessen.

Die gemessenen Signale werden mit der hochauflösenden Frequenz-Wellenzahl und der MUSIC (Multiple Signal Characterisation) Methode analysiert. Bei höheren Frequenzen (1.0 – 2.5 Hz) überwiegen an den Talrändern generierte Oberflächenwellen, welche sich durch ihre Geschwindigkeit und Richtung bestimmen lassen. Es liegt daher nahe, dass diese Oberflächenwellen wesentlich zur beobachteten Verstärkung bei höheren Frequenzen beitragen.

Im dritten Teil dieser Arbeit werden 3-D finite Differenzen-Simulationen der Wellenausbreitung im Sedimentbecken von Sion durchgeführt. Wir simulieren zunächst vier beobachtete Beben, um das neu entwickelte Geschwindigkeitsmodell zu überprüfen. Die aus den synthetischen Seismogrammen berechneten durchschnittliche Spektralverhältnisse stimmen mit den Beobachtungen im wesentlichen überein. Die simulierten maximalen Bodengeschwindigkeiten zeigen, dass die höchsten Verstärkungen dort auftreten, wo sich die an den Talrändern generierten Oberflächenwellen überlagern. Zusätzlich wurde eine Simulation des Erdbebens von 1946 bei Sierre (M_L 6.1) durchgeführt und die maximalen Bodengeschwindigkeiten in der Altstadt von Sion berechnet. Die Resultate legen nahe, dass Standorteffekte bei diesem Ereignis nicht massgeblich zum Schaden beigetragen haben, was von einer Rekonstruktion des Schadensbildes bestätigt wird.

Im letzten Kapitel wird der Einfluss des nichtlinearen Bodenverhaltens bei starker Bodenbewegung abgeschätzt. Dazu wurden mehrere Bodenproben aus einer Baugrube in Visp entnommen und mit triaxialen zyklischen Versuchen analysiert, um die Dilatanzparameter zu bestimmen. Wir generieren eine Reihe von synthetischen Seismogrammen und konvolvieren sie mit der Übertragungsfunktion des Sedimentbeckens, um Eingangssignale mit einem repräsentativem Frequenzgehalt zu erhalten. Anschliessend wird das Verhalten der oberflächennahen Sandschicht mit einem vollkommen nichtlinearen 1-D FD Programm simuliert. Wir schliessen aus den Ergebnissen, dass reduzierte Amplifikation bei Beschleunigungen ab 0.5 ms^{-2} auf Fels zu erwarten ist, und dass Deamplifikation bei Beschleunigungen über 2 ms^{-2} eintritt. Bei Magnituden ab 6.0 liegen die spektralen Beschleunigungen in der Talmitte im tieffrequenten Bereich (0.5 Hz) aber dennoch über den Bemessungs-Antwortspektren. Bei höheren Frequenzen stimmen die Bemessungsspektren aber in den meisten Fällen mit den simulierten spektralen Beschleunigungen überein. Die nichtlinearen Simulationen legen nahe, dass ausgeprägt nichtlineare Effekte wie Bodenverflüssigung bei starken Beschleunigungen im Rhône-tal gut möglich sind. Dieses Resultat ist im Einklang mit historischen Beobachtungen von Bodenverflüssigung, welche nach dem

Beben von 1855 in Visp gemacht wurden.

Diese Arbeit zeigt, wie vielseitig die Wellenausbreitungseffekte sind, welche in unregelmässig geformten Strukturen wie im Rhônetal zur Verstärkung der seismischen Bodenbewegung führen. Daraus schliessen wir, dass die Kombination unterschiedlicher Methoden wie Arraymessungen, Modellierungen mit genauen Geschwindigkeitsmodellen, Erdbebenbeobachtungen und Simulationen des nichtlinearen Bodenverhaltens einen zwar aufwändigen, aber erfolgversprechenden Ansatz darstellt, um Standorteffekte in Sedimenttälern zu untersuchen.

Contents

Summary	iii
Zusammenfassung	v
1 Introduction	1
1.1 Site effect evaluation techniques	2
1.1.1 Observational methods	3
1.1.2 Numerical methods	4
1.2 Nonlinear soil behaviour	4
1.3 Previous research on site effects in the Rhône valley	5
1.4 Methods applied in the SHAKE-VAL project	7
1.4.1 Array measurements of ambient noise	8
1.4.2 Temporary dense array in Sion	9
1.4.3 Three-dimensional ground motion prediction	9
1.4.4 Nonlinear behaviour of the soils	10
2 Two-dimensional resonances in Alpine valleys identified from ambient vibration wavefields	11
Summary	11
2.1 Introduction	12
2.2 Geophysical setting	13
2.3 Theory	15
2.3.1 1-D and 2-D resonance	15
2.3.2 Properties of 2-D resonance modes	16
2.3.3 Origin of noise	20
2.4 Method	21
2.4.1 Field experiments	21
2.4.2 Reference station method	24
2.4.3 Analysis of phase behaviour	24
2.4.4 f - k analysis	25
2.4.5 3-D Numerical simulations	26
2.5 Properties of synthetic ambient vibrations	26
2.5.1 Spectral ratios	26
2.5.2 Phase behaviour	30
2.5.3 f - k analysis	31

2.6	Evidence of 2-D resonance in observations	33
2.6.1	Reference spectra	33
2.6.2	Phase behaviour	38
2.6.3	Particle motion	41
2.6.4	f - k analysis	41
2.7	Discussion	44
2.7.1	Properties of 2-D resonance modes	44
2.7.2	f - k analysis	45
2.7.3	Resonance frequencies	45
2.7.4	Horizontal-to-vertical spectral ratios	46
2.8	Conclusions	47
	Acknowledgments	47
3	A combined inversion of Rayleigh wave dispersion and 2-D resonance frequencies	49
	Summary	49
3.1	Introduction	50
3.2	Synthetic noise data	52
3.3	Observed noise data	53
3.3.1	Observations on linear arrays	53
3.3.2	Observations on circular arrays	53
3.4	Noise data processing	54
3.4.1	Identification of 2-D resonance	54
3.4.2	f - k analysis	56
3.4.3	Combined Inversion of Rayleigh wave dispersion curves and 2-D resonance frequencies	57
3.4.4	Inversion with the Neighbourhood algorithm	59
3.5	Results from synthetic ambient noise	60
3.5.1	f - k analysis	61
3.5.2	Inversion of dispersion curve	62
3.5.3	Combined inversion	63
3.6	Results of recorded ambient vibrations	64
3.6.1	2-D resonance behaviour	64
3.6.2	f - k analysis	64
3.6.3	Inversion of dispersion curves and 2-D resonance frequencies	67
3.6.4	Discussion	72
3.7	Conclusion	74
	Acknowledgments	74
4	Site effects in the Rhône valley analysed from weak motion records and numerical simulations	75
	Summary	75
4.1	Introduction	76
4.2	Geophysical setting	77
4.3	Method	81

4.3.1	Weak motion records	81
4.3.2	3-D finite difference simulations	84
4.3.3	Analysis of signal-to-noise ratio	87
4.3.4	Estimation of Fourier amplification	87
4.3.5	Frequency-wavenumber analysis	87
4.4	Observed and simulated Fourier amplifications	89
4.4.1	Vallorcine series	89
4.4.2	Derborance series	91
4.4.3	Northern Switzerland events	91
4.4.4	Site characterisation	91
4.5	Deep valley response	93
4.6	Frequency-wavenumber analysis	98
4.6.1	Vallorcine main event	99
4.6.2	Northern Switzerland event N2	100
4.7	Peak ground velocities	104
4.8	Summary and Conclusions	108
	Acknowledgments	110
5	Estimation of nonlinear site response in a deep Alpine valley	111
5.1	Introduction	111
5.2	Geophysical setting	113
5.3	Method	114
5.3.1	Combined 2-D linear and 1-D nonlinear simulations	115
5.3.2	The Strain Space Multishear Mechanism Model	117
5.3.3	Dilatant behaviour soils	118
5.3.4	Laboratory tests on soil samples	119
5.3.5	Identification of dilatancy parameters	119
5.3.6	1-D nonlinear simulations	122
5.4	Simulation results	122
5.4.1	Example of linear soil response	122
5.4.2	Example of cyclic mobility	124
5.4.3	Example of reduced amplification	125
5.4.4	Example of liquefaction	125
5.4.5	Spectral amplification	125
5.4.6	Absolute spectral accelerations	127
5.4.7	Influence of deep basin on nonlinear soil behaviour	129
5.4.8	Evaluation of liquefaction potential	130
5.5	Discussion	132
5.5.1	Historical reports of liquefaction	132
5.5.2	Influence of deep valley resonance	132
5.5.3	Limitations	133
5.6	Summary and Conclusions	134

6 Discussion and Conclusions	137
6.1 Two-dimensional resonance of the basin	137
6.2 Edge-generated surface waves	138
6.3 Methods for site effect evaluation	140
6.4 Outlook	140
A Additional array measurements	143
A.1 Strong-motion station VMAR	143
A.2 Strong-motion station SVIP	144
A.3 Linear array Saillon	145
B Ratio of response spectra	147
C Simulated normalised response spectra	153
C.1 Vallorcine main shock V1	154
C.2 Northern Switzerland event N2	155
C.3 Derborance main shock D3	156
C.4 Northern Italy event I2	157
Acknowledgements	159
Curriculum Vitae	161
Bibliography	164

List of Figures

1.1	Map of Rhône valley with available geophysical information	6
2.1	Cross section of Rhône valley at Vétroz site.	14
2.2	1-D dispersion analysis of velocity model	16
2.3	Naming convention for directions used in this text.	17
2.4	Amplification, phase and particle motion of the three fundamental modes	18
2.5	Critical shape ratio	19
2.6	Sediment-bedrock interface at the Vétroz site	20
2.7	Array configurations used for noise measurements near Vétroz.	22
2.8	Comparison between disturbed (grey) and undisturbed (black) signals	23
2.9	Beam pattern of array used for f - k analysis of 2002 experiment	25
2.10	Source and receiver distribution used for numerical simulation of microtremor	27
2.11	Amplitude spectra calculated from synthetic noise	28
2.12	Contour plot of synthetic spectral ratios	29
2.13	Spectral ratios for four profiles	30
2.14	Bandpass filtered synthetic ambient noise records	30
2.15	Beam pattern of array configuration for f - k analysis of synthetic microtremors.	31
2.16	f - k -spectra computed from synthetic ambient noise	32
2.17	Average power spectra and average spectral ratios calculated from recorded ambient noise	33
2.18	Average site-to-reference spectral ratios for ambient noise recorded during the 2002 experiment	34
2.19	Average spectral ratios as a function of distance (2002 experiment)	35
2.20	Average site-to-reference spectral ratios for ambient noise recorded during the 2003 experiment	36
2.21	Average spectral ratios as a function of distance (2003 experiment)	37
2.22	Average spectral ratios for both configurations of the 2003 experiment (vertical and perpendicular)	38
2.23	Average spectral ratios for both configurations of the 2003 experiment (axial)	39
2.24	Bandpass filtered time series of ambient noise (axial)	39

2.25	Bandpass filtered time series of ambient noise (vertical and perpendicular)	40
2.26	Cross-correlation maxima (2002 experiment)	41
2.27	Cross-correlation maxima (2003 experiment, first configuration) . .	42
2.28	Cross-correlation maxima (2003 experiment, second configuration)	43
2.29	Particle motion plot of recorded noise	43
2.30	f - k -spectra obtained from observed noise	44
2.31	Horizontal-to-vertical spectral ratios	48
3.1	Linear and circular arrays measured in the Rhône valley	51
3.2	Sediment-bedrock interfaces	52
3.3	Array response beampatterns	55
3.4	Critical equivalent shape ratio for the SH case	56
3.5	f - k example	61
3.6	Synthetic dispersion curve	62
3.7	Simple inversion of synthetic dispersion curve	63
3.8	Combined inversion of synthetic dispersion curve	65
3.9	Spectral ratios for Martigny	66
3.10	Recorded dispersion curves	67
3.11	Results of combined inversion for Martigny	68
3.12	Results of combined inversion for Saillon	70
3.13	Results of combined inversion for Vétroz	71
3.14	Comparison of simple and combined inversion for Martigny	72
3.15	Acceptable velocity models for Martigny, Saillon and Vétroz	73
4.1	Map of the Rhône valley	78
4.2	Inversion results for Sion	79
4.3	Velocity model for Sion area	81
4.4	Accelerograms of Vallorcine main shock	84
4.5	Simulation of Vallorcine main shock	86
4.6	Array response beampatterns	88
4.7	Array resolution limits	89
4.8	Observed and simulated Fourier spectral ratios for Vallorcine series	90
4.9	Observed and simulated Fourier spectral ratios for Derborance series	92
4.10	Observed and simulated Fourier spectral ratios for Northern Switzer- land events	93
4.11	Comparison between observed and simulated average Fourier spectral ratios	94
4.12	Critical shape ratio for Sion (SH case)	95
4.13	Spectral ratios for simulated event N3	96
4.14	Spectral ratios for recorded event N3	97
4.15	f - k results for simulated event V1	99
4.16	f - k results for recorded event V1	100
4.17	f - k results for simulated event N2	101
4.18	Simulation of Northern Switzerland event	102

4.19	f - k results for recorded event N2	103
4.20	Simulated peak ground velocities for event V1 and D3	105
4.21	Simulated peak ground velocities for event N2 and I3	106
4.22	Simulated peak ground velocities for 1946 Sierre earthquake	108
5.1	Map of the Rhône valley	113
5.2	Inversion results from array measurement near Visp	114
5.3	Profile for DBEM simulation and obtained transfer function	115
5.4	Liquefaction resistance curve	120
5.5	Results of undrained cyclic triaxial test number 8	121
5.6	Results of combined 2-D linear and 1-D nonlinear simulations for a M 4.5 event at 40 km hypocentral distance	123
5.7	Results of combined 2-D linear and 1-D nonlinear simulations for a M 5.0 event at 40 km hypocentral distance	124
5.8	Results of combined 2-D linear and 1-D nonlinear simulations for a M 5.5 event at 20 km hypocentral distance	126
5.9	Results of combined 2-D linear and 1-D nonlinear simulations for a M 6.5 event at 20 km hypocentral distance	127
5.10	Ratio between spectral acceleration at valley centre and rock as a function of spectral acceleration on rock	128
5.11	Ratio between spectral acceleration at basin edge and rock as a function of spectral acceleration on rock	129
5.12	Absolute response spectra compared with SIA261 design spectrum	130
5.13	Liquefaction occurrence as a function of hypocentral distance and magnitude	131
5.14	Comparison between simulated ground motion near the basin edge and at the basin centre	133
5.15	Maximum strain as a function of PGA on rock	135
6.1	H/V spectral ratios for Sion compared observed and simulated amplification	139
A.1	Results of array measurements near strong-motion station VMAR .	143
A.2	Results of array measurements near strong-motion station SVIP . .	144
A.3	Spectral ratios for Saillon	145
B.1	Observed and simulated average ratio of response spectra	148
B.2	Observed and simulated response spectral ratios for Vallorcine series	149
B.3	Observed and simulated response spectral ratios for Derborance series	150
B.4	Observed and simulated response spectral ratios for northern Switzer- land events	151
C.1	Normalised acceleration response spectra for simulation of event V1	154
C.2	Normalised acceleration response spectra for simulation of event N2	155
C.3	Normalised acceleration response spectra for simulation of event D3	156

C.4 Normalised acceleration response spectra for simulation of event I2 157

List of Tables

2.1	Geophysical model of the sediment fill.	15
2.2	Resonance frequencies	20
3.1	Geophysical model of the sediment fill	52
3.2	Parameterisations of sediment-bedrock interfaces	58
3.3	Parameter limits for 5-layer velocity model	60
3.4	2-D resonance frequencies	60
3.5	Shear-wave velocities obtained from combined inversion	74
4.1	Geophysical parameters of the different materials in the velocity model	82
4.2	Positions of permanent and temporary stations	82
4.3	Events recorded on the temporary network	83
4.4	Observed fundamental mode 2-D resonance frequencies	98
4.5	Simulated fundamental mode 2-D resonance frequencies	98
5.1	Geophysical parameters of the individual layers	116
5.2	Key soil parameters determined from laboratory testing	119
5.3	Dilatancy parameters identified from the six laboratory tests	121
5.4	Material properties for the nonlinear 1-D simulations	122

Chapter 1

Introduction

Earthquakes pose a serious natural hazard in many parts of the world. Loss of life and structure damage caused by recent large earthquakes (Kashmir 2005, Sumatra-Andaman 2004, Bam 2003) have demonstrated that there is a global need to mitigate the risks associated with earthquake effects.

The intensity of shaking caused by an earthquake at a nearby site depends on the combined contributions from the seismic source, the velocity structure between the source and the site, and the local geology at the site. It has long been understood that soft sedimentary deposits can significantly amplify the intensity of shaking and, therefore, greatly increase building damage and loss of life. Dramatic examples include the 1985 M_s 8.1 Michoacán, Mexico, earthquake (e.g. Anderson *et al.*, 1986) with more than 20,000 fatalities in Mexico City, or the 1995 M 7.3 Great Hanshin earthquake that claimed 6,400 lives in Kobe, Japan (e.g. Kawase, 1996).

There is evidence that local site effects did also contribute significantly to building damage during more recent earthquakes, which occurred in areas with sparse seismic instrumentation. A correlation between increased damage and high frequency amplification was reported for the city of Bam, Iran (Jafari *et al.*, 2005), where the death toll exceeded 40,000 after the M_w 6.5 earthquake of December 2003. Amplification by the deep basin below the city of Adapazarı, Turkey, is believed to have caused the collapse of many five-to-six storey buildings after the 1999 M 7.4 İzmit earthquake (Bakır *et al.*, 2002).

In Switzerland earthquakes represent the most important natural hazard (Bundesamt für Bevölkerungsschutz, 2003). The recent seismic hazard map of Switzerland (Giardini *et al.*, 2004) assigns the highest acceleration levels to the central Valais region based on historical and instrumental earthquake catalogues. The strongest earthquake to hit Switzerland in the 20th century occurred 1946 near Sierre, Valais; it reached a magnitude of 6.1 and caused four fatalities and numerous injuries. 1855 the region of Visp was struck by a M_w 6.4 earthquake, which damaged countless buildings in the upper Valais (Fritsche *et al.*, 2006).

Since the last large earthquake of 1946 agglomerations have expanded extensively in the Valais, making the region more vulnerable. It has been estimated that in 1994 a repeat of the 1855 earthquake would have caused about 250 casualties

and CHF 5 billion worth of damage (Mayer-Rosa, 1993). Today, many residential and industrial areas are located on the soft unconsolidated Rhône sediments, and concern has been raised about the influence of site effects during future M 6 events.

There is a large uncertainty of the ground motion expected from earthquakes comparable to the 1855 and 1946 ruptures, because no event of similar magnitude has been recorded since the first deployment of strong motion accelerometers in the Valais. The greatest uncertainty concerns the extent to which the soft Rhône deposits will amplify the seismic waves. The SHAKE-VAL project aims to reduce these uncertainties by investigating earthquake site effects in complex three-dimensional Alpine valleys with the Rhône basin as a test site.

1.1 Site effect evaluation techniques

On their way from the earthquake source to the observation site, seismic waves undergo multiple reflections, refraction and phase transformations as a consequence of inhomogeneities in the Earth's crust. Since the most abrupt material discontinuities occur near the surface, the level of ground motion and building damage varies strongly, sometimes only within a few meters.

Amplification of ground motion over soft soil is caused by the impedance contrast between sediment and underlying bedrock. The amplitude of incoming seismic waves is increased as they are slowed down in the sediment, and outgoing waves are partly reflected back towards the surface. In the case of one-dimensional (i.e. horizontally layered) structures, this trapping affects only body waves, which are reflected back and forth between the surface and the layer interface.

If lateral heterogeneities are present, as in the case of 2-D or 3-D structures, this trapping will also affect surface waves. Sediment filled valleys are a common example of 2-D or 3-D structures. At lateral discontinuities like as basin edges additional surface waves are generated through wave conversion. These surface waves are sometimes focused by the valley geometry, causing high amplifications in spots of positive interference. Observational evidence for basin-edge generated surface waves and basin focusing effects has been found in many studies (e.g. Frankel *et al.*, 2001; Joyner, 2000). Additionally, 2-D and 3-D structures can be excited in their eigenmodes.

The extreme engineering importance of these soft soil effects has resulted in the development of many methods to determine the amplification, and these tools have been applied in microzonation studies. Site effects are then understood as frequency-dependent amplification relative to a known or virtual reference site.

1.1.1 Observational methods

Many methods to quantify site effects are based on observations of earthquake records or ambient noise.

Site-to-reference spectral ratios. The most direct approach consists in recording earthquakes simultaneously on the soft soil and a reference site on outcropping rock. By dividing the Fourier spectrum of the soft soil site by the spectrum of the reference station, the spectral ratio is obtained, which allows to determine the frequency and amount of amplification (Borcherdt, 1970).

However, this method is expensive in areas of low seismicity, because long recording periods and a large number of instruments are required to gather sufficient earthquake data. Sometimes no suitable reference station is available in the vicinity. Since site effects are especially of interest in populated areas, high noise levels represent another difficulty.

The lack of earthquake data has led to the development of methods that rely only on ambient noise to estimate the amplification (e.g. Kagami *et al.*, 1982; Field and Klaus, 1995). If the noise between the sediment and the reference site is sufficiently correlated this method allows to identify the frequency of amplification. This method is very efficient, but the main problem is that the noise sources are not known and the noise correlation is often poor.

H/V spectral ratios. A very famous method that does not rely on a reference site consists in computing the spectral ratio between horizontal and vertical components of noise records (e.g. Nakamura, 1989). This approach allows to identify the fundamental frequency of amplification with minimal effort given a sufficient velocity contrast between sediment and soil. Numerical studies suggest that the peaks in H/V spectral ratios reflects the ellipticity of fundamental mode Rayleigh waves in the case of a large velocity contrast (Bonney-Claudet *et al.*, 2006). The amount of amplification can not reliably be quantified with this method. However, if the depth to the interface is known, the fundamental frequency identified from the H/V method can be used to estimate shear-wave velocities of the sediment. Fäh *et al.* (2001) developed a method to directly estimate the shear-velocity structure from the ellipticity of H/V curves.

Seismic arrays. Arrays of seismic stations have been used for decades in seismology. While the first installations focused mainly on detection of nuclear tests, arrays were subsequently employed by seismologists to explore the Earth's structure. Today small-scale arrays serve as a powerful tool in site effect studies, and they are increasingly applied to both ambient noise and earthquake signals.

Frequency-wavenumber (Capon, 1969) or spatial autocorrelation (Aki, 1957) methods allow to identify the apparent velocity and direction of origin of wave-trains passing through the array. When applied to earthquake signals, apparent velocities help to distinguish body waves from surface waves, and edge-

generated surface waves can be identified by their direction of origin (e.g. Hartzell *et al.*, 2003; Frankel *et al.*, 2001).

Array records of ambient noise are mostly used to derive dispersion curves of Rayleigh waves (e.g. Kind *et al.*, 2005; Wathelet *et al.*, 2004), which are inverted for the shear-velocity structure of the site. The shear-wave velocities derived from such observations help to establish velocity models, which are then used to quantify the amplification with numerical simulations.

1.1.2 Numerical methods

Numerical simulations of earthquake scenarios help to circumvent the lack of seismic data and to improve the understanding of observed earthquake signals. Various numerical schemes are available to solve the wave equations, and the level of sophistication ranges from simple 1-D plane wave propagation to complicated 3-D simulations including dynamic descriptions of the earthquake rupture process. These simulations are able to identify areas of increased ground motion, which depend on specific details of the earthquake, such as orientation of the causative fault and details of the rupture model. However, the reliability of such simulations depends on the accuracy of the available velocity model. Relevant geophysical parameters are the body wave velocities, densities and the quality factors. In the case of complicated sediment-filled basins, the geometry of the bedrock is also an important factor.

Because the amplification is caused by the trapping of shear- and surface waves in the sediment, the shear-wave velocity represents the most important parameter in the geophysical model. Unfortunately, the shear-wave velocity is also often the least known parameter, because it is difficult to measure. Microtremor array recordings are a cost-efficient way to estimate S-wave velocities, and the method has been applied in microzonation studies all over the world.

3-D numerical simulations are computationally very expensive, because millions of grid points are necessary to describe a large volume. The maximum frequency that can be propagated depends on the spatial step in the numerical grid. Even the fastest supercomputers available today are not able to perform large-scale simulations for the whole frequency range of engineering interest (0 - 10 Hz).

1.2 Nonlinear soil behaviour

Amplification caused by weak ground motion can readily be described in terms of Hooke's law, which states that the relation between stress and strain is linear. Laboratory studies of soil samples, however, have shown for long that Hooke's law breaks down at large ground motion levels. Nonlinear soil response is characterised by a reduced effective shear modulus and increased damping, leading to reduced amplification factors or even deamplification, especially at high frequencies.

In the engineering practise nonlinear soil behaviour is routinely taken into account using equivalent linear models (e.g. the program SHAKE developed by Schnabel *et al.*, 1972). It is well accepted that this physical model is limited to a certain strain level above which the soil behaviour becomes very complex.

Seismologists, on the other hand, have generally been more sceptical about nonlinearity, mainly because linear models were able to explain most observations. But in the last decades more observational evidence of nonlinear soil behaviour was gathered (e.g. Beresnev and Wen, 1996; Field *et al.*, 1997), and improved methodologies to simulate wave propagation in nonlinear materials were developed (e.g. Iai *et al.*, 1990b; Hartzell *et al.*, 2004). Many observations of reduced amplification have been made at strong ground motion levels, among others after the 1989 Loma Prieta earthquake or the 1994 Northridge earthquake.

Additionally, recent observations suggest that nonlinear soil behaviour may significantly alter surficial acceleration time series before reduced amplification becomes appreciable. This suggest that isolating nonlinearity by comparing weak and strong motion may not represent the correct approach, and that nonlinear soil behaviour may be more common than previously thought. Bonilla *et al.* (2005) showed that dilatant soils may partially recover their shear strength during cyclic loading, resulting in spiky waveforms that represent significant accelerations. Such spiky waveforms were observed on vertical arrays after the 1987 Superstition Hills earthquake (Holzer *et al.*, 1989) and the 1993 Kushiro-Oki earthquake (Iai *et al.*, 1995), and they can be reproduced with truly nonlinear 1-D simulations (Bonilla *et al.*, 2005).

Unfortunately such fully nonlinear calculations require a lot of parameters that are not readily available. A number of laboratory tests must be performed on soil samples from the analysed site, and a trial-and-error procedure involving multiple iterations must be followed for determination of dilatancy parameters. But comparisons of simulated and observed amplifications for the 2001 Nisqually earthquake have shown that fully nonlinear models are superior to equivalent linear methods (Hartzell *et al.*, 2004) at soft soil sites. In regions where no strong motion records are available, fully nonlinear simulations represent a valuable tool to estimate the importance of nonlinear soil behaviour.

1.3 Previous research on site effects in the Rhône valley

The Rhône valley is a strongly overdeepened glacial valley filled with unconsolidated glacial, lacustrine and deltaic sediments. Pfiffner *et al.* (1997) investigated the sedimentary fill with a number of high-resolution reflection seismic profiles (Fig. 1.1). Their results revealed a U-shaped basin filled with quaternary deposits up to 1000 meters thick. These findings were confirmed by gravimetric surveys (Rosselli, 2001) performed along a series of 2-D profiles between Aigle and Brig (Fig. 1.1).

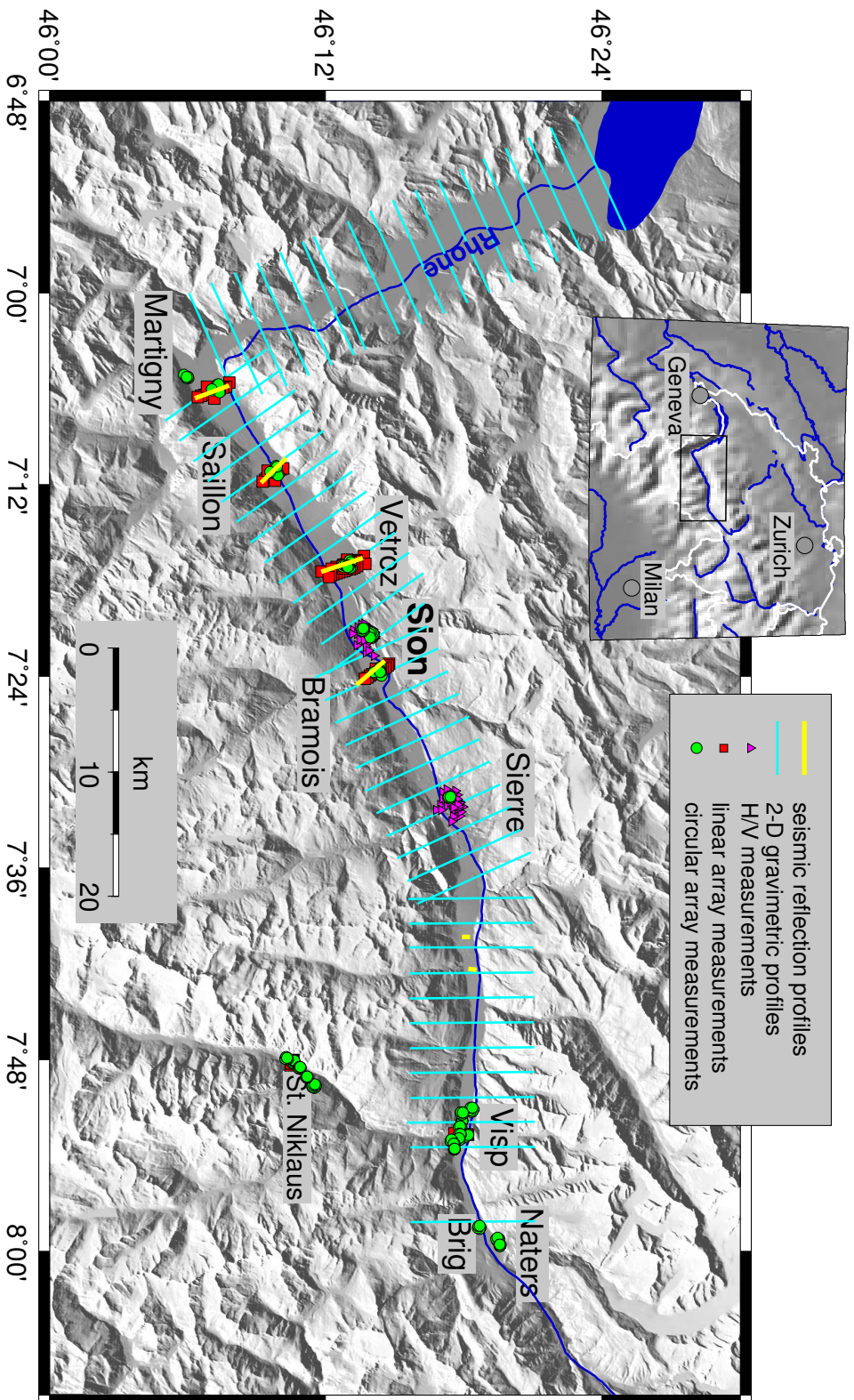


Figure 1.1: Map of Rhône valley with topography (grey shades). Lines show the gravimetric (Rosselli, 2001) and reflection seismic (Piffner *et al.*, 1997; Besson *et al.*, 1993) profiles that were used for this study. Symbols denote the station positions occupied during ambient noise measurements. See legend for details.

Only a few studies on earthquake site effects in the Rhône valley have been published. Frischknecht and Wagner (2004) analysed the seismic response of the basin near Sion using numerical simulations, H/V measurements and weak motion records. The 2-D simulations yielded the largest amplification between 0.5 and 0.8 Hz due to the 2-D resonance of the basin, with amplification factors of up to 12 at the basin centre. Near the basin edges they found the largest amplification at higher frequencies of about 5 Hz. H/V measurements done in the Sion area seemed to confirm this pattern; however, the deep 2-D basin response could not unambiguously be identified from the ambient noise recorded by Frischknecht *et al.* (2005), because the eigenperiod of the employed seismometer was higher than the fundamental frequency of the basin.

Steimen *et al.* (2003) measured ambient noise simultaneously on a reference site and on the sedimentary fill west of Sion. They identified dominant peaks at about 0.30 Hz in site-to-reference spectral ratios, which were attributed to the two-dimensional resonance of the basin.

Frischknecht (2000) operated a small temporary array consisting of six strong motion stations in Sion. Unfortunately they recorded only one significant M_L 3.1 earthquake, and the analysis was aggravated by the limited dynamic range and frequency response of the deployed 12-bit accelerometers.

Clearly, more observations of ambient noise and earthquakes are needed to confirm the results obtained from the numerical simulations of Frischknecht and Wagner (2004).

Recently a number of research projects focused on re-evaluation of historical earthquakes in order to upgrade the earthquake catalogue of Switzerland. Gisler *et al.* (2004) assigned a maximum intensity of VIII to the 1755 M_L 6.1 earthquake of Brig; Fritsche *et al.* (2006) reconstructed the damage field of the 1855 M_L 6.4 earthquake of Visp studying also site effects and building vulnerability.

1.4 Methods applied in the SHAKE-VAL project

In the framework of the SNF projects SHAKE-VAL I and SHAKE-VAL II, we are studying site effects in the Rhône valley with empirical and theoretical methods. The project is composed of four main parts:

- (i) Array measurements of ambient noise
- (ii) Temporary dense array in Sion
- (iii) Three-dimensional ground motion prediction
- (iv) Nonlinear behaviour of the soils

In the first part, array recordings of ambient noise are performed in order to develop a detailed geophysical model of the sedimentary fill. The second part focuses on the analysis of recorded weak ground motion to quantify the amplification and to analyse wave propagation effects. During the third part we will

simulate wave propagation effects in the Sion basin using the velocity model developed in part (i). Finally the importance of nonlinear soil behaviour will be estimated during the last part of the SHAKE-VAL project.

1.4.1 Array measurements of ambient noise

Array recordings of ambient noise are used to study the fundamental frequency of the basin and to derive shear-wave velocities in the sedimentary fill. We used linear and circular array configurations to analyse the noise wavefield at different locations in the Rhône valley (Fig. 1.1). The first measurements were performed near the sites where results from seismic reflection are available. Additional measurements focused on the city of Sion to constrain the velocity model. To analyse the variability of shear-wave velocities in the Valais further arrays were recorded in the upper Valais and in the vicinity of strong motion stations.

For the linear arrays the receivers are arranged along a profile running perpendicular to the valley axis, with one receiver placed on outcropping bedrock. The first two linear arrays were recorded near Vétroz in 2002 to verify results of a previous study (Steimen *et al.*, 2003). Observations made from these first linear arrays confirmed that the low-frequency amplification observed in spectral ratios is caused by the fundamental mode 2-D resonance frequency. By rotating the ambient noise to directions parallel and perpendicular to the valley axis it was possible to isolate the SH_{00} and SV_0 fundamental modes of 2-D resonance and to identify their frequency.

Chapter 2 of this thesis deals with identification of 2-D resonance from the linear arrays recorded near Vétroz. It describes the procedure used to define the different mode 2-D resonance frequencies and how characteristic properties of 2-D resonance can be identified in the recorded ambient vibration wavefield. The chapter is identical to a publication that appeared in *Geophys. J. Int.* (Roten *et al.*, 2006).

To derive shear-wave velocities of the sedimentary fill, we recorded circular arrays at various locations (Fig. 1.1). Concentric array configurations of increasing aperture were used to sample different frequency bands. The fundamental frequency of the basin marks the lower frequency limit that can be processed with frequency-wavenumber techniques. Dispersion curves can therefore only reveal information about the structure down to a certain depth. In order to obtain an estimate of the shear-wave velocities in the lower part of the sedimentary fill, we are introducing a method that uses the different mode 2-D resonance frequencies as an additional constraint in the inversion of dispersion curves. The method is described in chapter 3, which composes the text of another publication (Roten and Fäh, 2007). Such combined inversions of dispersion curves and 2-D resonance frequencies are applied for sites near Vétroz, Saillon and Martigny; the results are given in chapter 3.

We recorded a number of additional arrays that were processed using dispersion curves only. In the first part of chapter 4 shear-wave velocities obtained at a

few sites near Sion are discussed (Fig. 4.2). Results from an additional array measurement near Visp are given in Figure 5.2. Appendix A contains previously unpublished results of further ambient noise array measurements performed during this study.

1.4.2 Temporary dense array in Sion

We operated two temporary arrays of weak motion seismometers in the city of Sion and recorded about 15 local and regional events with a reasonable signal-to-noise ratio. Details of the temporary network are described in chapter 4. We will compute site-to-reference spectral ratios from these signals to identify the fundamental frequency of the basin and to quantify the level of amplification. From spectral ratios we will analyse the two-dimensional response of the Sion basin and compare our observations with the amplification pattern predicted by Frischknecht and Wagner (2004). Two $f-k$ algorithms will be applied to recorded waveforms to estimate the apparent slowness and direction of origin of surface waves propagating through the array. This method allows us to identify edge-generated surface waves, which are contributing significantly to the observed amplification at higher frequencies.

1.4.3 Three-dimensional ground motion prediction

A detailed 3-D velocity model of the Sion area is developed to model strong ground motion. We gathered all available geophysical and geological information to constrain the bedrock geometry, densities and P-wave velocities; the shear-wave velocities are provided by the ambient noise measurements.

We are modelling four of the strongest events from different azimuths and compare the simulated frequency-dependent amplifications with our observations. Wave propagation in the Sion basin is simulated with a parallel, 3-D finite difference code developed by Olsen (1994). We compute peak ground velocities on the surface of the whole computational area to identify spots of significant amplifications, and compare the results with recorded peak ground velocities.

Additionally we will simulate the 1946 M_w 6.1 earthquake of Sierre and compute the peak ground acceleration in the Sion region. The simulated amplification will be correlated with a reconstruction of the reported damage distribution (S. Fritsche pers. comm.) of the 1946 earthquake.

Details of the numerical simulations and a comparison between synthetic and observed amplification are described in chapter 4. The text has been considered for publication in *Geophysical Journal International* and will be resubmitted after a minor revision.

1.4.4 Nonlinear behaviour of the soils

The last part of the SHAKE-VAL project aims to estimate the importance of nonlinear soil behaviour at strong levels of ground motion in the Rhône valley. To determine the key soil parameters a few samples were taken from an excavation pit in Visp and analysed at ETH's geotechnical laboratory. Six triaxial cyclic tests were performed to define the liquefaction resistance and the dilatancy parameters of the soil.

We are using the fully nonlinear 1-D finite difference program *NOAH* developed by Bonilla *et al.* (2005). To simulate both the influence of the deep 2-D basin structure and the shallow nonlinear layer we are convolving our input signals first with the transfer function of the deep basin before propagating them through the 1-D nonlinear layer. Because the seismic source represents the greatest uncertainty in earthquake scenarios for the Valais region, we will employ an empirical method and create a large number of synthetic input seismograms for various magnitudes and distances.

From these simulations we are estimating the ground motion level above which nonlinear soil behaviour is appreciable. We analyse how reduced amplification or even deamplification by the nonlinear material affects the absolute spectral acceleration, and how the applicable design spectra compare with the simulated spectral accelerations. Finally we are analysing the liquefaction occurrence as a function of hypocentral distance and magnitude and compare the results with the observations reported after the 1855 earthquake.

Results of the nonlinear analysis are given in Chapter 5.

Chapter 2

Two-dimensional resonances in Alpine valleys identified from ambient vibration wavefields

D. Roten, D. Fäh, C. Cornou¹ and D. Giardini
Institute of Geophysics, ETH Hönggerberg, 8093 Zürich, Switzerland
E-mail: daniel.roten@sed.ethz.ch

Geophys. J. Int. (2006) **165**, 889–905 doi:10.1111/j.1365-246X.2006.02935.x
Accepted 2006 January 23. Received 2005 December 5; in original form 2005 January 31

Summary

Although numerical simulations have for long shown the importance of 2-D resonances in site effect estimations of sediment-filled valleys, this phenomenon is usually not taken into account by current hazard assessment techniques. We present an approach to identify the resonance behaviour of a typical Alpine valley by analysis of ambient noise recorded simultaneously on a dense array. The applicability of the method is evaluated further using synthetic ambient noise acquired with current 3-D numerical simulation techniques. Resonance frequencies of the fundamental mode SV and the fundamental and first higher mode of SH are identified from measured data with the reference station method, verifying results of previous studies. Patterns of spectral amplitude and phase behaviour obtained from observed and synthetic noise correlate well with properties expected for 2-D resonance. Application of a frequency-wavenumber technique shows that the noise wavefield is dominated by standing waves at low frequencies (0.25 to 0.50 Hz). The different 2-D resonance modes are creating prominent peaks in horizontal-to-vertical spectral ratios, which can not be interpreted in terms of 1-D resonance. We conclude

¹ now at: LGIT, Maison des Geosciences, BP53, 38041 Grenoble Cedex9 - France

that ambient noise records measured simultaneously on a linear array perpendicular to the valley axis may be used for identification of resonance modes in sediment-filled valleys.

Key words: Seismic noise, Sedimentary basin, Spectral analysis, Seismic array, Synthetic waveforms, Rhône valley

2.1 Introduction

It is well established that site-effects caused by unconsolidated deposits must be included in hazard assessments, and instrumental and numerical techniques are now widely used to estimate amplifications caused by 1-D site effects. However, numerical simulations have for long demonstrated the importance of considering 2-D or 3-D geometries, since effects related to such structures can cause amplifications significantly higher than the corresponding 1-D values (e.g. Bard and Bouchon, 1985).

Sediment-filled Alpine valleys are common examples of such 2-D-sites. Depending on the valley geometry, two different effects can be distinguished:

1. In rather shallow valleys, the wavefield is dominated by laterally propagating surface waves generated at the valley edges. This effect is often observed in both synthetic (e.g. Bard and Bouchon, 1980b) and measured data (e.g. Field, 1996; Chávez-García *et al.*, 2003). Lateral variations of the interface between bedrock and sediments can give rise to local 1-D resonances (Fäh *et al.*, 1993).
2. In deeper valleys, the interference of these surface waves with vertically propagating waves gives rise to the evolution of a 2-D resonance pattern. Although this phenomenon evolved in many numerical simulations (e.g. Bard and Bouchon, 1985; Frischknecht and Wagner, 2004), observations on real data are rare (e.g. Kagami *et al.*, 1982; Tucker and King, 1984; King and Tucker, 1984).

Most attempts to identify and quantify these effects involved measurements of earthquake motion on different sites on the sediment fill and on the outcropping rock, using array-based (e.g. Cornou *et al.*, 2003) or reference station dependent (e.g. Chávez-García *et al.*, 2003) methods. In regions with low seismicity, site effect estimations with these procedures would require long and thereby expensive measurement campaigns. Methods based on quick and cheaper microtremor measurements for identification and quantification of such 2-D-effects would, therefore, be desirable.

Numerical microtremor simulations performed by Steimen *et al.* (2003) showed that 2-D resonance in a sediment filled valley can be excited by laterally-incident microtremor waves. Steimen *et al.* (2003) applied a site-to-reference technique to

synthetic microtremor records obtained with a realistic model of the Rhône valley near Vétroz (Switzerland), demonstrating the capability of the method to identify the resonance frequencies of the site. The method was also applied to observed microtremor recordings measured simultaneously at the reference site and at one location on the sediment fill for different points across the valley. But this approach did not allow a comparison of amplification and phase characteristics of records acquired at different positions, since the wavefield was not measured simultaneously at all points. The peaks in spectral ratios obtained from observed microtremors could, therefore, not unambiguously be identified as 2-D resonance modes.

In order to verify the results obtained from the numerical simulations of Steimen *et al.* (2003), we present results of two new measurement campaigns involving simultaneous recording of the noise wavefield on 13 sites on the sediment fill and on the outcropping rock at the Vétroz site.

To take advantage of recent developments in the field of ambient noise research, we repeated the numerical simulation of Steimen *et al.* (2003) for the same geophysical model, but a 3-D computational region and a different noise source definition, using a code developed within the European SESAME (site effects assessment using ambient excitations) project (Moczo and Kristek, 2002).

We will apply the site-to-reference technique to these synthetic and recorded data to seek for characteristic patterns of 2-D resonance in the microtremor wavefield. Additionally, we will introduce a method to analyse the phase behaviour of microtremor records at the resonance frequencies. We will put special emphasis on the problem of distinguishing between laterally propagating surface waves and 2-D-resonance, since this issue gave rise to some discussion in recent publications (Paolucci and Faccioli, 2003; Chávez-García and Stephenson, 2003).

Using results of this synthetic and recorded microtremor analysis, we will try to evaluate the suitability of microtremor records for 2-D site effect assessment.

2.2 Geophysical setting

The Rhône valley is a deeply eroded basin filled with glacial and post-glacial Quaternary sediments. In the framework of a national research project, the sedimentary fill and shape of the valley was investigated using high-resolution reflection seismic lines, with one profile running perpendicular to the valley axis at the Vétroz site (Pfiffner *et al.*, 1997). Based on results of this cross-section, Steimen *et al.* (2003) created a realistic geophysical model of the Vétroz site, only simplified by the introduction of horizontal layers (Fig. 2.1). Interface depths and P-wave velocities (Table 2.1) are provided directly by seismic reflection data (Pfiffner *et al.*, 1997). Shear wave velocities at the uppermost layer are derived from a shallow shear-wave refraction experiment done near Vétroz (Frischknecht, 2000); Steimen *et al.* (2003) estimated shear-wave velocities for lower layers. The quality factors Q_p and Q_s are estimated as well, and densities are available through gravimetric studies (summarised in Frischknecht, 2000). To obtain a mean value \bar{v} for

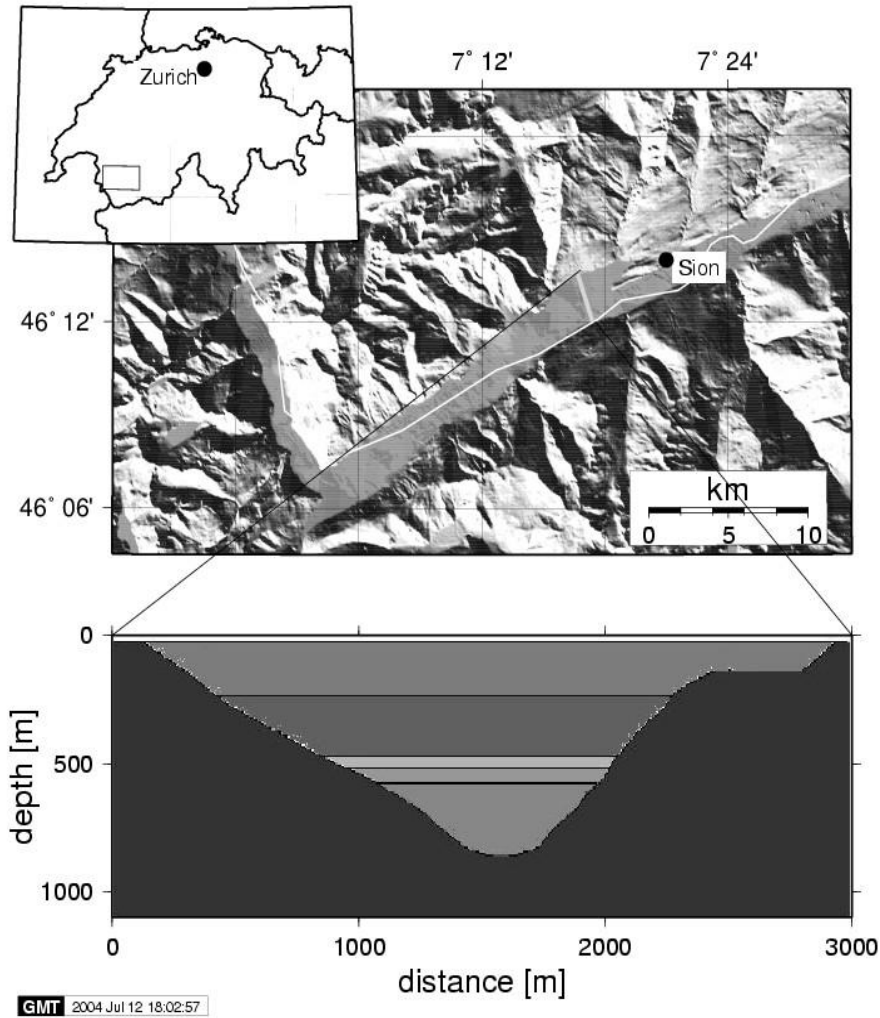


Figure 2.1: Cross section of Rhône valley at Vétroz site. See Table 2.1 for details of sediment fill. (modified from Steimen *et al.*, 2003). Reproduced by permission of swisstopo (BA057507).

the velocities of the whole sediment fill, we use the travelttime-based average:

$$\frac{1}{\bar{v}} = \frac{1}{H} \sum_{i=1}^n \frac{h_i}{v_i} \quad \text{with} \quad H = \sum_{i=1}^n h_i \quad (2.1)$$

where h_i is the the thickness of layer i . For the velocities in Table 2.1, this yields $\bar{v}_p=1929 \text{ ms}^{-1}$ and $\bar{v}_s=651 \text{ ms}^{-1}$.

depth	v_p	v_s	Q_p	Q_s	ρ	geologic interpretation
0	1700	456	50	25	1900	deltaic sediments
210	1930	650	50	25	1900	glaciolacustrine deposits
470	1970	790	50	25	2000	meltout and reworked till
529	2300	920	50	25	2000	lodgment and till
584	2050	820	50	25	2000	subglacial deposit
890	5000	2890	200	100	2500	hard rock

Table 2.1: Geophysical model of the sediment fill. Depths are in m, v_p and v_s in ms^{-1} and ρ in kgm^{-3} .

2.3 Theory

2.3.1 1-D and 2-D resonance

1-D resonance is caused by the trapping of body waves in soft horizontally layered sediments overlying solid bedrock. The 1-D resonance frequency f_h depends on the layer thickness h and the shear-wave velocity v_s of the sedimentary layer:

$$f_h = \frac{v_s}{4h} \quad (2.2)$$

If local 1-D resonance develops in shallow basins, the resonance frequency will depend on the position in the valley and reflect the local sediment thickness.

In the case of 2-D resonance, however, the resonance frequency is the same across the whole valley (Bard and Bouchon, 1985; King and Tucker, 1984; Tucker and King, 1984; Kagami *et al.*, 1982). The frequencies of 2-D resonance modes are higher than the 1-D resonance frequency f_h at the valley centre. As Bard and Bouchon (1985) demonstrated, the frequency of mode SH_{00} is slightly above f_h for shallow valleys and increases with increasing valley depth. The frequencies observed in the case of 2-D resonance can, therefore, not be explained with 1-D analysis of the sediment fill.

Since the shear-wave velocity of the sediments are well known for our site, we will reveal the importance of 2-D resonance effects by comparison of identified peak frequencies with theoretical 1-D values. With the traveltime-based shear-wave velocity average calculated above, an approximate 1-D resonance frequency of 0.18 Hz can be derived for the valley centre from equation 2.2.

For large velocity contrasts the ellipticity of the fundamental mode Rayleigh wave has infinite values close the the fundamental frequency of resonance (e.g. Asten, 2004). This is shown from 1-D analysis of Rayleigh wave dispersion and ellipticity (Fig. 2.2) using the stratigraphy from Table 2.1. The 1-D resonance frequency is reflected by the peak in the fundamental mode ellipticity curve at 0.21 Hz, which is not too different from the value obtained with the traveltime-based shear-wave velocity average.

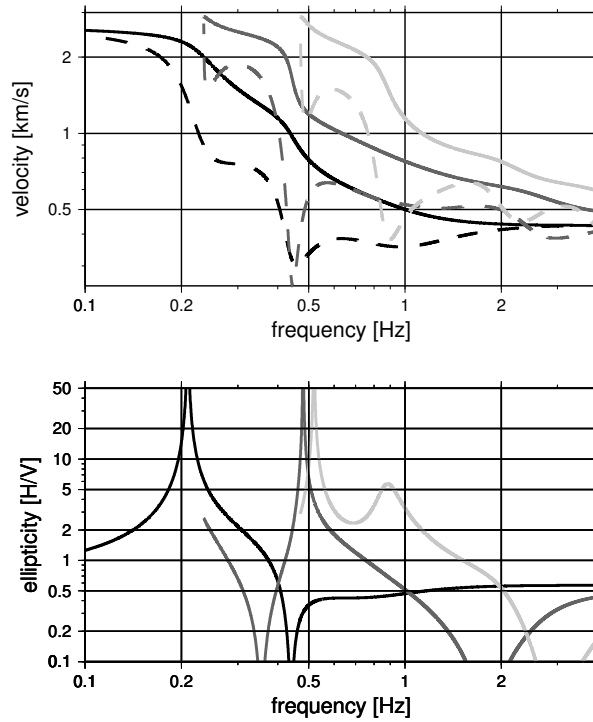


Figure 2.2: 1-D dispersion analysis of velocity model given in Table 2.1 *Top*: Phase (solid) and group velocities (dashed) for fundamental (black), first (darkgrey) and second (lightgrey) higher mode Rayleigh waves. *Bottom*: Particle-motion horizontal/vertical ratios for the same modes, same model. (These values were computed using software from Hermann, 2002).

2.3.2 Properties of 2-D resonance modes

Three fundamental modes

Using the technique from Aki and Larner (1970) to simulate the seismic behaviour of a sine shaped valley on incident SH, SV and P-waves, Bard and Bouchon (1985) showed the existence of three fundamental modes (Fig. 2.4). We will follow the nomenclature of Field (1996) in this paper and use the terms perpendicular and axial for horizontal motion perpendicular and parallel, respectively, to the valley axis (Fig.2.3). Only the axial component is excited in the SH-mode, while the SV- and P-mode excite both the perpendicular and vertical component. In the fundamental mode SH_{00} , the phase is the same across the valley, and the amplification reaches its maximum in the valley centre. At the first higher mode SH_{01} the amplification exhibits a central node and two peaks. The SV_0 fundamental mode is characterised by a maximum amplification in the centre for the perpendicular component and a central node and two maxima for the vertical component. In this mode, the phase is the same across the valley for the perpendicular component, while the phase of the vertical motion changes at the valley centre. The P_0

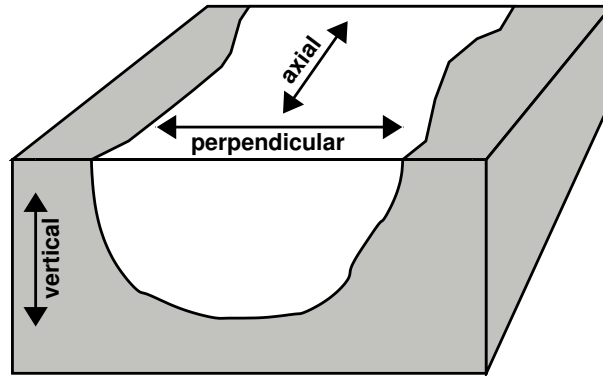


Figure 2.3: Naming convention for directions used in this text.

fundamental mode behaves just vice-versa (Fig. 2.4).

Shape ratio

Since two-dimensional resonance patterns involve both vertical and horizontal interferences, they can only appear in relatively deep valleys. To identify valleys whose seismic behaviour is characterised by two-dimensional resonance, Bard and Bouchon (1985) introduced the concept of the *critical shape ratio*. For sine-shaped valleys, the shape ratio is defined as the ratio of the maximum sediment thickness h to the valley half-width l . For arbitrarily shaped valleys, this parameter is replaced by the 'equivalent' shape ratio $h/2w$, where $2w$ is defined as the total width over which the sediment thickness is greater than half its maximum value. The critical shape ratio depends on the velocity contrast between bedrock and sediment fill (Fig. 2.5). If the shape ratio of a valley is above the critical value, its seismic behaviour at low frequencies will be characterised by two-dimensional resonance. The critical shape ratio depends also on the wave type; its value is higher for P-waves than for SH- and SV-waves (Fig. 2.4).

Using 1350 m for $2w$ and 890 m for h (Pfiffner *et al.*, 1997), we can assign a shape ratio of about 0.65 to the Rhône valley at the Vétroz site. The velocity contrast between bedrock and sediment fill ranges from 3.5 (subglacial deposits) to 6.4 (deltaic sediments). In Figure 2.5, the shape ratio of the Vétroz site for both velocity contrasts is indicated in the diagram, showing that this site is clearly located in the domain of 2-D resonance for the SH-case.

Paolucci's Method

Based on Rayleigh's principle, Paolucci (1999) developed a method which allows a quick calculation of the resonance frequencies of valleys filled with stratified sediments. Equating the total kinetic energy T_{\max} of the system Ω with the total strain energy V_{\max} , the following expression can be derived, which denotes an

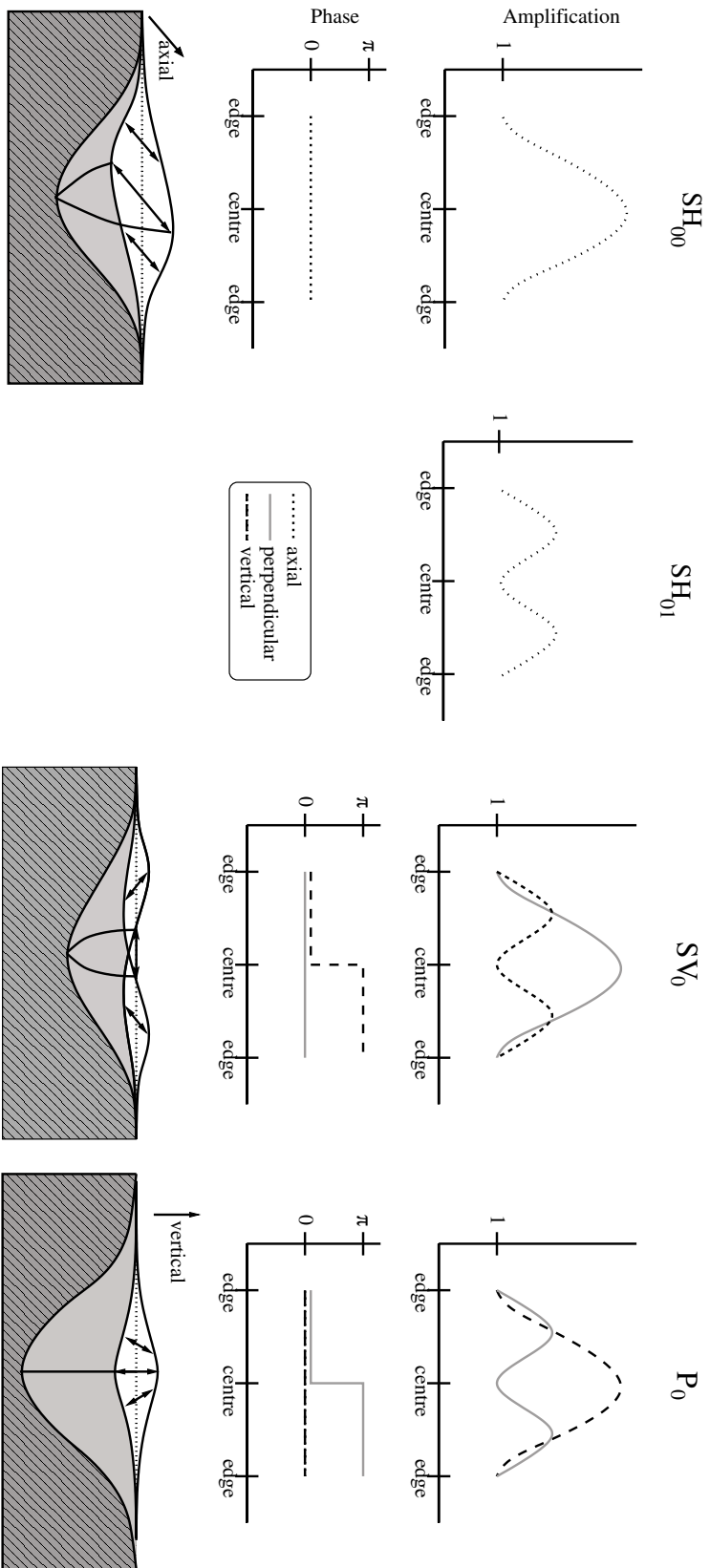


Figure 2.4: Amplification, phase and particle motion of the three fundamental modes of a sine shaped valley for the corresponding critical shape ratio (modified from Bard and Bouchon, 1985; Steimen *et al.*, 2003) and amplification for the first higher mode SH_{01} .

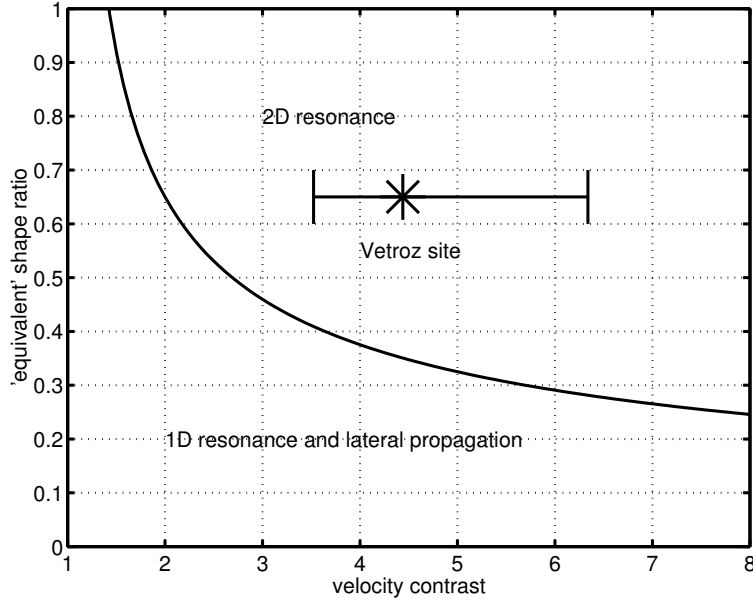


Figure 2.5: Critical shape ratio as a function of the velocity contrast for the SH case. The velocity contrasts obtained from the shear-wave velocities in Table 2.1 are indicated at the shape ratio of 0.65. The asterisk denotes the velocity contrast obtained with the traveltime-based shear-wave velocity average from equation 2.1. (modified from Bard and Bouchon, 1985)

upper bound for the true fundamental frequency ω_0 :

$$\omega_0^2 \leq \min_{\hat{\psi}_k} \frac{\int_{\Omega} \hat{\sigma}_{jl}(\vec{x}) \hat{\epsilon}_{jl}(\vec{x}) d\Omega}{\int_{\Omega} \rho(\vec{x}) \hat{\psi}_k^2(\vec{x}) d\Omega} \quad (2.3)$$

where $\hat{\epsilon}_{jl}$ is the strain tensor, $\hat{\sigma}_{jl}$ the stress tensor, ρ the density and \vec{x} the position in 3-D space. $\hat{\psi}_k$ stands for a set of admissible approximations of the true shape function ψ (refer to Paolucci, 1999, for a detailed description).

Paolucci's program includes four functions to describe the sediment-bedrock interface. The function most appropriate for the Vétroz site denotes the shape of an asymmetric valley:

$$f(x_1, x_3) = \left(1 + \frac{x_1}{a}\right) \left(1 - \frac{x_1}{a}\right)^{\frac{1-\zeta}{1+\zeta}} - (1 + \zeta)(1 - \zeta)^{\frac{1-\zeta}{1+\zeta}} \cdot \frac{x_3}{h} \quad (2.4)$$

where a is the valley half-width, h the maximum depth and ζ a coefficient describing the grade of asymmetry. Figure 2.6 shows the true sediment-bedrock interface of the Rhône valley at the Vétroz site and the function described by equation 2.4 with $a=1120$ m, $h=770$ m and $\zeta=0.20$.

Using the geophysical model given in Table 2.1 and four different shape functions, Schmid (2000) calculated the SV resonance frequencies of the Rhône valley near Vétroz and found values very similar to those reported by Steimen *et al.* (2003).

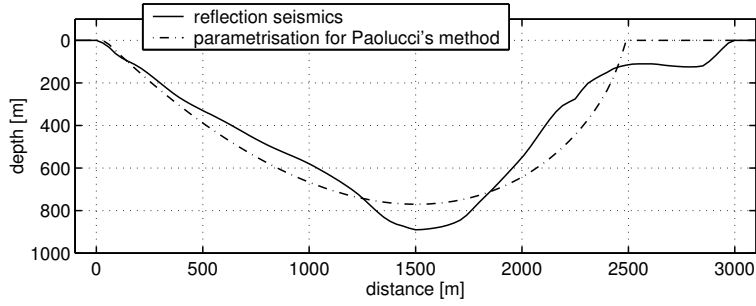


Figure 2.6: Sediment-bedrock interface of the Rhône valley at the Vétroz site derived from reflection seismics and described by equation 2.4 with $a=1120$ m, $h=770$ m and $\zeta=0.20$ (modified from Schmid, 2000).

	SV_0	SH_{00}	SH_{01}	SH_{02}
Paolucci's method	0.34	0.31	0.39	0.47
Steimen modelled	0.34 ± 0.01	0.29 ± 0.02	0.38 ± 0.01	0.47 ± 0.01
Steimen observed	0.35 ± 0.03	0.32 ± 0.03		
3-D simulation	0.35 ± 0.03	0.30 ± 0.03	0.39 ± 0.04	
2002 experiment	0.35 ± 0.03	0.31 ± 0.03	0.43 ± 0.04	
2003 experiment	0.39 ± 0.03	0.35 ± 0.04	0.43 ± 0.04	

Table 2.2: Resonance frequencies [Hz] calculated with the method of Paolucci (1999) compared to values observed and measured by Steimen *et al.* (2003) and in this study.

Table 2.2 lists the fundamental mode SV and the fundamental and higher modes SH frequencies calculated with Paolucci's method using the sediment-bedrock interface from Figure 2.6. The frequencies reported by Steimen *et al.* (2003) are also given in the Table. The values obtained with Paolucci's approach are equal to or slightly higher than those from the numerical simulation of Steimen *et al.* (2003), which demonstrates the capability of the method to provide an upper bound for the 2-D resonance frequencies.

As expected, the 2-D resonance frequencies are substantially higher than the theoretical 1-D resonance frequency calculated above.

2.3.3 Origin of noise

Studies on the nature of noise (Bonneyoy-Claudet *et al.*, 2004) agree that different sources contribute to the noise wavefield at different frequency bands (Gutenberg, 1958; Asten, 1978; Asten and Henstridge, 1984). In general, low-frequency noise (< 0.5 Hz) can be assigned to coastal waves, large-scale meteorological perturbations and cyclones over the oceans (noise in this frequency band was referred to as *microtremor* energy by Steimen *et al.*, 2003). Noise around 1 Hz can be

traced to local meteorological conditions, and noise above 1 Hz to human activities (Bonnetfoy-Claudet *et al.*, 2004).

According to this scheme, the resonance of the structure at Vétroz should mainly be excited by far sources, since the resonance frequencies are well below 0.5 Hz. Indeed Steimen *et al.* (2003) simulated the microtremor wavefield by a source zone far away from the valley. However, the boundary between oceanic, large scale meteorological and human, small scale meteorological noise is not an universal limit, but can be shifted to lower frequencies in deep soft basins (Seo, 1997).

It can, therefore, not be excluded that sources capable of exciting 2-D resonance exist within the valley. Thus we used a different source definition for our numerical simulations and placed all sources within the valley on the sediment surface, simulating man-made noise typical of densely populated urban areas.

2.4 Method

The experiments with real and simulated data were designed for a simultaneous examination of phase behaviour, amplitude and particle motion at different positions across the valley.

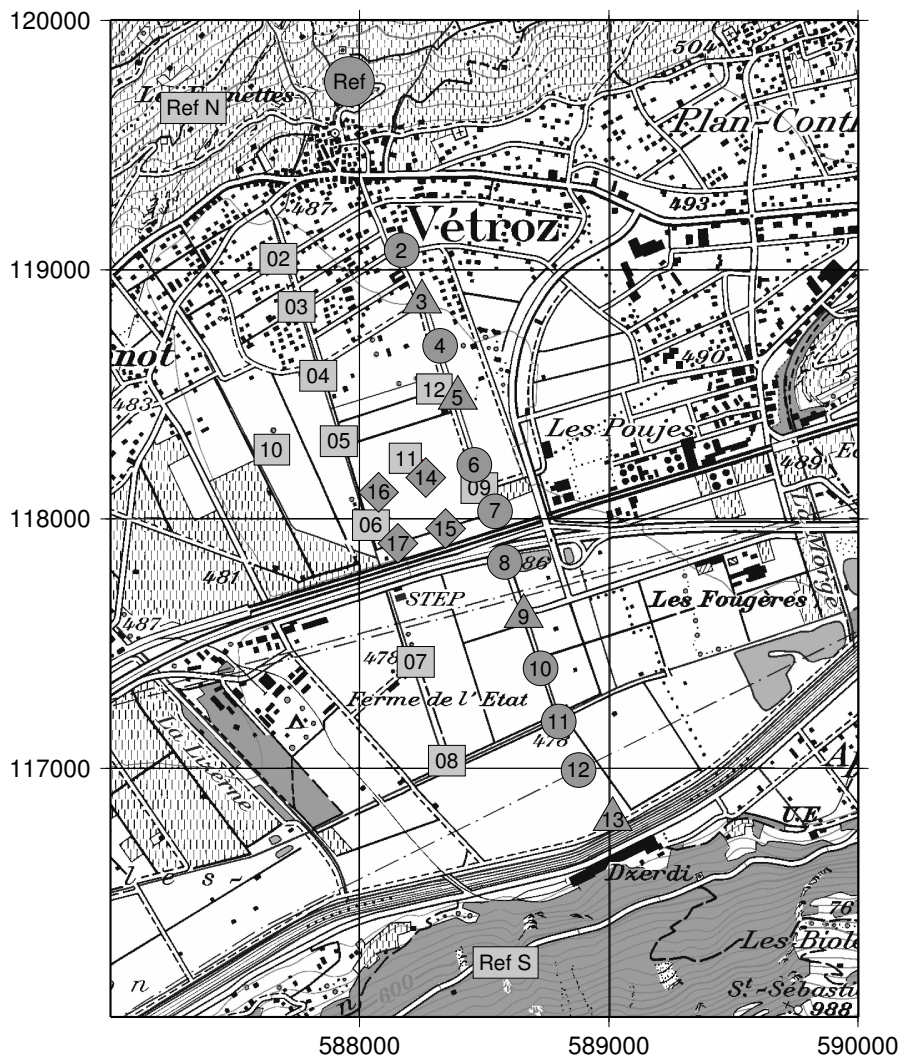
2.4.1 Field experiments

The noise wavefield at the Vétroz site was recorded during two measurement campaigns carried out in May 2002 and November 2003.

May 2002 experiment

The first campaign aimed to validate the results of Steimen *et al.* (2003) by simultaneous measurement of the noise wavefield at all points across the profile and at two reference stations. The positions of the stations during the 2002 experiment are denoted by rectangles in Figure 2.7. Seven stations were deployed on a profile perpendicular to the axis of the valley, with shorter inter-station distances on the northern part. Four stations were set up outside the profile around the middle of the valley to form a small array; these stations are necessary to distinguish between laterally propagating surface waves and global resonance. The remaining two stations were used as reference stations on the North and on the South side of the profile on well-defined bedrock sites.

The noise wavefield was measured by 13 three-component sensors with a natural period of 5 seconds and recorded using DCF77 long-wave radio time signals for synchronisation. The 2002 experiment resulted in about 90 minutes of high-quality data with very few sources of local noise in the frequency range of interest (below about 1 Hz), with the exception of the reference station in the South which was located close to a busy road.



GMT 2004 May 19 12:27:35

Figure 2.7: Configurations used for noise measurements near Vétroz. Station positions of the 2002 experiment are indicated by lightgrey rectangles, those of the 2003 experiment by darkgrey circles, triangles and diamonds. Ticks denote the Swiss coordinate system in meters. Reproduced by permission of swisstopo (BA057507).

The evaluation of the microtremor wavefield recorded during this first experiment yielded promising results, but also raised a couple of new questions, which led us to prepare a second experiment.

November 2003 experiment

The second campaign was designed to investigate the resonance properties with a higher spatial resolution across the profile. Therefore all thirteen stations were first put on a line running parallel to the profile of the first experiment (Circles and triangles in Figure 2.7). The noise wavefield was measured for about 100 minutes with this configuration. In order to distinguish between propagation and resonance, we removed four stations (triangles) from the profile axis and placed them away from the profile in the valley centre (diamonds in Figure 2.7). With this setup, the noise wavefield was recorded during 120 more minutes.

Due to an improperly connected sensor cable, no data was recorded by station 5 for the first part of the experiment. Records acquired by station 6 contain a lot of disturbances of unknown origin, which induce low-frequency spikes in the noise traces. Figure 2.8 (top) compares a low-pass filtered trace from station 6 to an undisturbed trace from station 7 and shows how such a spike influences the amplitude spectrum of the signal. These spikes at station 6 are the main reason for the introduction of the anti-trigger in the spectral ratio method (see below).

Apart from stations 5 and 6, the data collected during the second measurement campaign is of satisfactory quality.

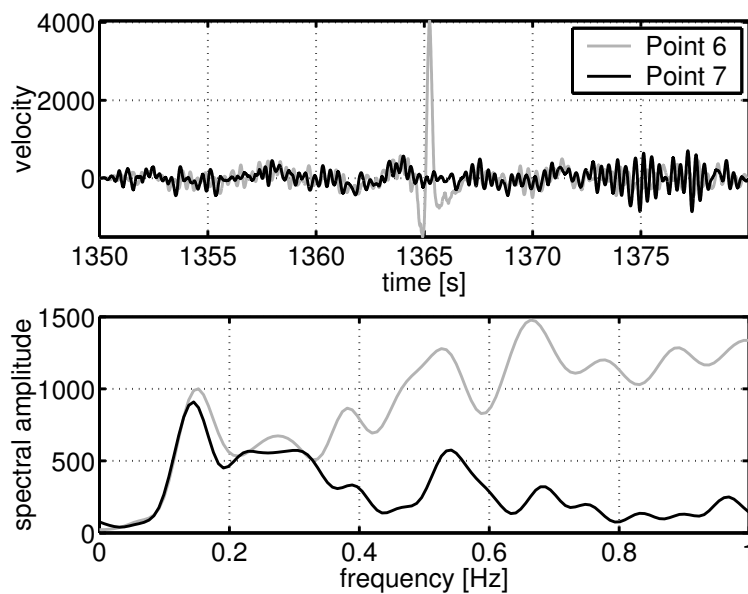


Figure 2.8: Comparison between disturbed (grey) and undisturbed (black) signals. Time series (top) were low-pass filtered below 1 Hz.

2.4.2 Reference station method

The reference station approach is based on the assumption that the signal at the reference site represents the signal at the sediment-bedrock interface, which implies that source and path effects at both sites must be equal. The ratio of the Fourier spectra amplitude is used to estimate the transfer function between soil and rock site (e.g. Borchardt, 1970; Lermo and Chávez-García, 1994). When applied on earthquake data, the reference station method uses only the intense S-wave part of the seismograms. Applications on microtremors exploit the whole record regardless of the shape of the signals.

We used a code similar to the one applied by Steimen *et al.* (2003) for the calculation of reference spectra. Time series are split into 50% overlapping windows of 80 seconds length and tapered with a trapezoidal window. For each time window, the ratio of the smoothed Fourier amplitudes is computed. Then the weighted average of all windows is calculated.

We introduced data weighting to remove effects related to low-frequency disturbances similar to the example in Figure 2.8. The weighting for each window is determined by a simple suppression trigger applied to each time series after low-pass filtering with a cut-off of 1 Hz. If the amplitude of any component at any station exceeds a certain threshold value in a time window, the weighting of this window is set to zero for all stations.

2.4.3 Analysis of phase behaviour

The phase behaviour of motion at the fundamental mode resonance frequencies is a remarkable property of 2-D resonance (Fig. 2.4). The simultaneous measurement of the noise wavefield at all points allows us to analyse this effect. We expect the noise wavefield to exhibit a clear pattern of in-phase and anti-phase behaviour at the fundamental mode SV and SH resonance. Time series of the axial and perpendicular component bandpass filtered around the SH and SV fundamental mode resonance frequency should be in phase at all points on the profile. For vertical traces bandpass filtered around the SV_0 frequency, the phase is expected to change around the valley centre.

The phase behaviour of short sections can easily be revealed by plotting traces next to each other. In order to analyse longer ($> 1h$) time series, we will use a more systematic approach to reveal the dominant phase properties:

The phase of the motion at each point is compared to the motion at a reference point in the middle of the valley. Signals are band-pass filtered around the resonance frequency identified with spectral ratios. The cross-correlation of each filtered signal against the signal at the reference position is calculated, with a maximum lag of two seconds. The lag where the cross-correlation reaches its maximum reveals the dominant phase behaviour: if both signals are exactly in phase, the maximum is reached at a lag of zero; if they are in anti-phase, the maximum should occur at half the period of the signals.

2.4.4 f - k analysis

Peaks in the transfer function of an alluvial valley may result from both 1-D resonance and horizontally propagating surface waves as well as from 2-D resonance (Bard and Bouchon, 1980b). The in- and anti-phase pattern expected for the fundamental SV mode of 2-D resonance may also be explained with propagating Rayleigh waves generated symmetrically at the valley edges (Gaffet *et al.*, 1998; Chávez-García and Stephenson, 2003).

To distinguish between horizontally propagating surface waves and standing waves caused by 2-D resonance, we will calculate f - k spectra from the array formed by seven stations deployed during the 2002 experiment (stations 04, 05, 06, 09, 10, 11 and 12 in Fig. 2.7). To avoid difficulties associated with the anti-phase behaviour of the vertical component in the SV_0 -case, all stations used for the f - k analysis are located on the north side of the valley. The array beam pattern for this configuration is given in Figure 2.9. The first aliasing peak was identified at $k_{\text{aliasing}} = 0.022$ rad/m; the maximum wavenumber that can be analysed with this configuration is, therefore, $k_{\text{aliasing}}/2 = 0.011$ rad/m (e.g. Schisselé *et al.*, 2004), indicated by the solid circle in Figure 2.9. Due to the elongated shape of the array, the resolution is better in East-West than North-South direction.

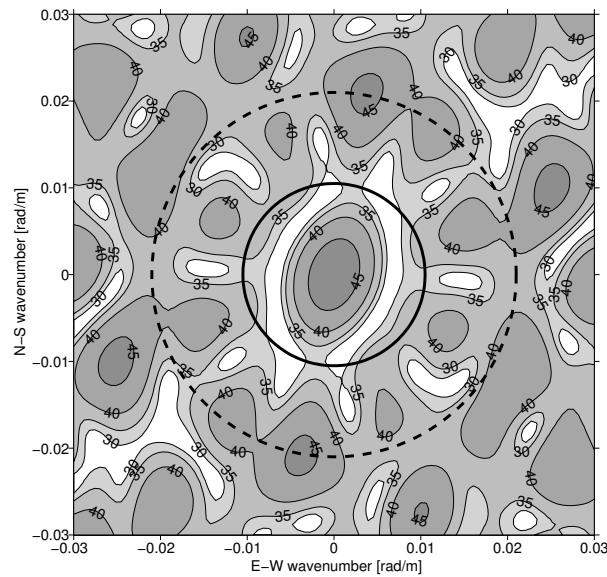


Figure 2.9: Beam pattern of array used for f - k analysis of 2002 experiment. Contour intervals are indicating the array response in dB. The first aliasing peaks are located on the dashed circle and the wavenumber domain that can be analysed with this configuration is within the solid circle.

F - k spectra are calculated with the high-resolution frequency-wavenumber method (Capon, 1969; Kind *et al.*, 2005) by the *continuous array processing* (CAP) program (Ohrnberger *et al.*, 2004). This code is part of a larger software pack-

age created in the framework of the SESAME project (available at <http://www.-geopsy.org>).

2.4.5 3-D Numerical simulations

The numerical ambient noise simulation was performed with the program package *NOISE* developed within the SESAME project. (Moczo *et al.*, 2002; Moczo and Kristek, 2002). This package provides the programs *ransource* and *FDSIM*.

Ransource creates a set of randomly distributed sources and generates a random direction of acting single body force, time function and maximum amplitude for each source. The time function is either a delta-like signal or a pseudo-monochromatic function of random duration and frequency. We placed all sources on the surface of the sediment cover in the valley (Fig. 2.10).

The wave propagation of this source is simulated with *FDSIM*. This code uses an explicit heterogeneous finite-difference scheme which is 4th-order accurate in space and 2nd-order accurate in time. The computation region is represented by a viscoelastic half-space with 3-D surface heterogeneities and a planar surface (Moczo *et al.*, 2001; Kristek *et al.*, 2002).

The FD-grid is staggered and consists of a finer grid on top and a coarser grid below.

We used $721 \times 109 \times 40$ cells for the fine and $241 \times 37 \times 11$ cells for the coarse grid with a spacing of 30 and 90 meters, respectively. The velocity model varies only along two dimensions and corresponds to the profile given in Figure 2.1 and Table 2.1. The simulation was performed in the frequency range between 0.25 and 2.35 Hz.

A number of receivers are distributed regularly along the valley surface; another set of receivers is placed to form four parallel lines running perpendicular to the profile axis, with one station on bedrock. The remaining receivers are arranged in three dense arrays on the surface (Fig. 2.10).

The numerical simulation was running for six weeks on an IBM MPP at the Swiss National Supercomputing centre and resulted in about 90 seconds of synthetic ambient noise.

2.5 Properties of the synthetic ambient vibration wave-field

We will first identify the 2-D resonance frequencies in our synthetic ambient noise.

2.5.1 Spectral ratios

All sources are located on the sediment surface in our simulation. The reference station method will, therefore, not remove source and path effects. Due to the

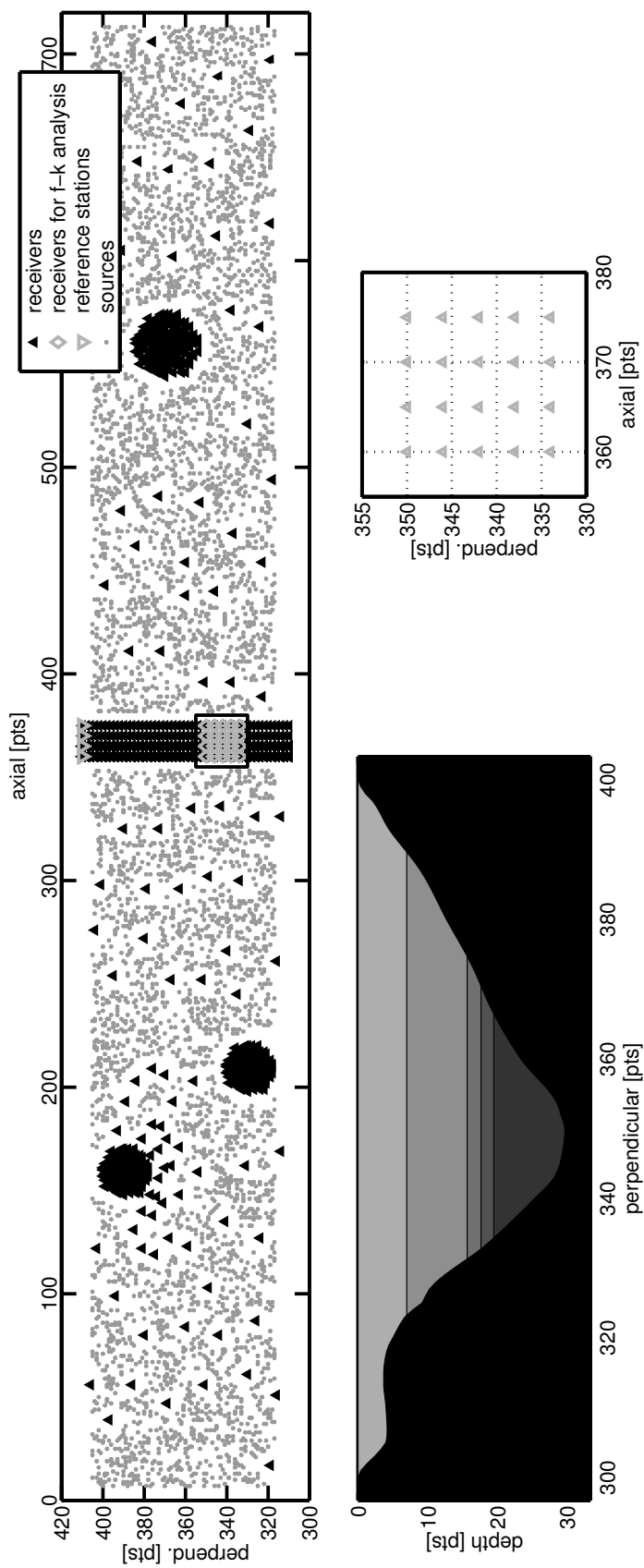


Figure 2.10: *Top*: Source and receiver distribution used for numerical simulation of microtremor. Distances are in grid points, the grid spacing is 30 meters. *Bottom left*: Cross section of velocity model. *Bottom right*: Enlarged section showing the array used for f - k analysis.

large impedance contrast between sediment and bedrock, only a small fraction of energy reaches receivers outside the valley, and spectra at these stations are almost flat compared to stations in the valley (Fig. 2.11). This is quite different

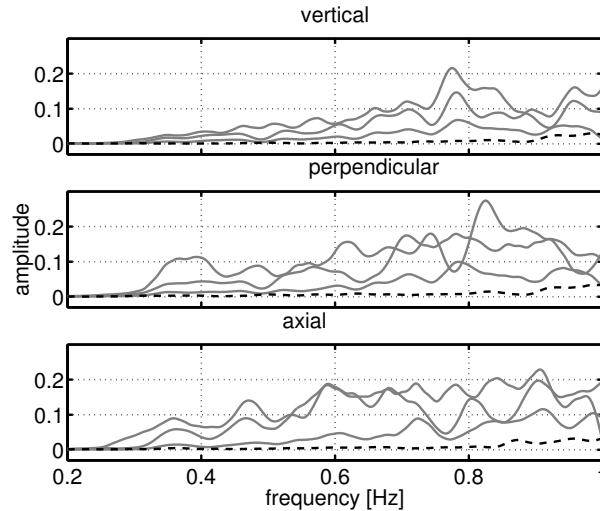


Figure 2.11: Amplitude spectra calculated from synthetic noise of receivers located on bedrock (black, dashed) and on the sediment (grey, solid)

from the situation observed in reality (Fig. 2.17 left). We must keep in mind that spectral ratios applied to our synthetic data will show effects of sources as well as the response of the valley.

Figure 2.12 gives spectral ratios of the signals from the receivers located on the line at axial grid position 360 calculated with the reference station at perpendicular grid position 410 (Fig. 2.10). The spectra are quite heterogeneous, with a lot of peaks at different frequencies. The fundamental mode SV_0 was identified at 0.35 Hz, with two peaks visible on the vertical (top) and one broad peak on the perpendicular component (centre). This is very close to the value of SV_0 reported by Steimen *et al.* (2003) from 2-D simulations. On the axial component (bottom), the fundamental SH_{00} and first higher mode SH_{01} of SH resonance can be identified easily at 0.30 and 0.39 Hz, respectively.

Figure 2.13 (very right) shows a cross section of the perpendicular and vertical spectral ratios at 0.35 Hz for all four profiles. The pattern is similar to the SV_0 fundamental mode predicted by theory (Fig. 2.4), with one central peak on the perpendicular and two peaks on the vertical component (Fig. 2.4). A certain variability in spectral ratio amplitudes can be observed for the four different profiles. Cross sections of the axial component at the fundamental and first higher mode are displayed in Figure 2.13 (left and centre). At the fundamental mode SH_{00} frequency of 0.30 Hz, all cross-sections exhibit a well-defined single peak, but different amplitudes. The first higher mode SH_{01} (0.39 Hz) is characterised by a central node and two maxima at axial grid positions 360. At this frequency, the four sections are quite different in shape and amplitude.

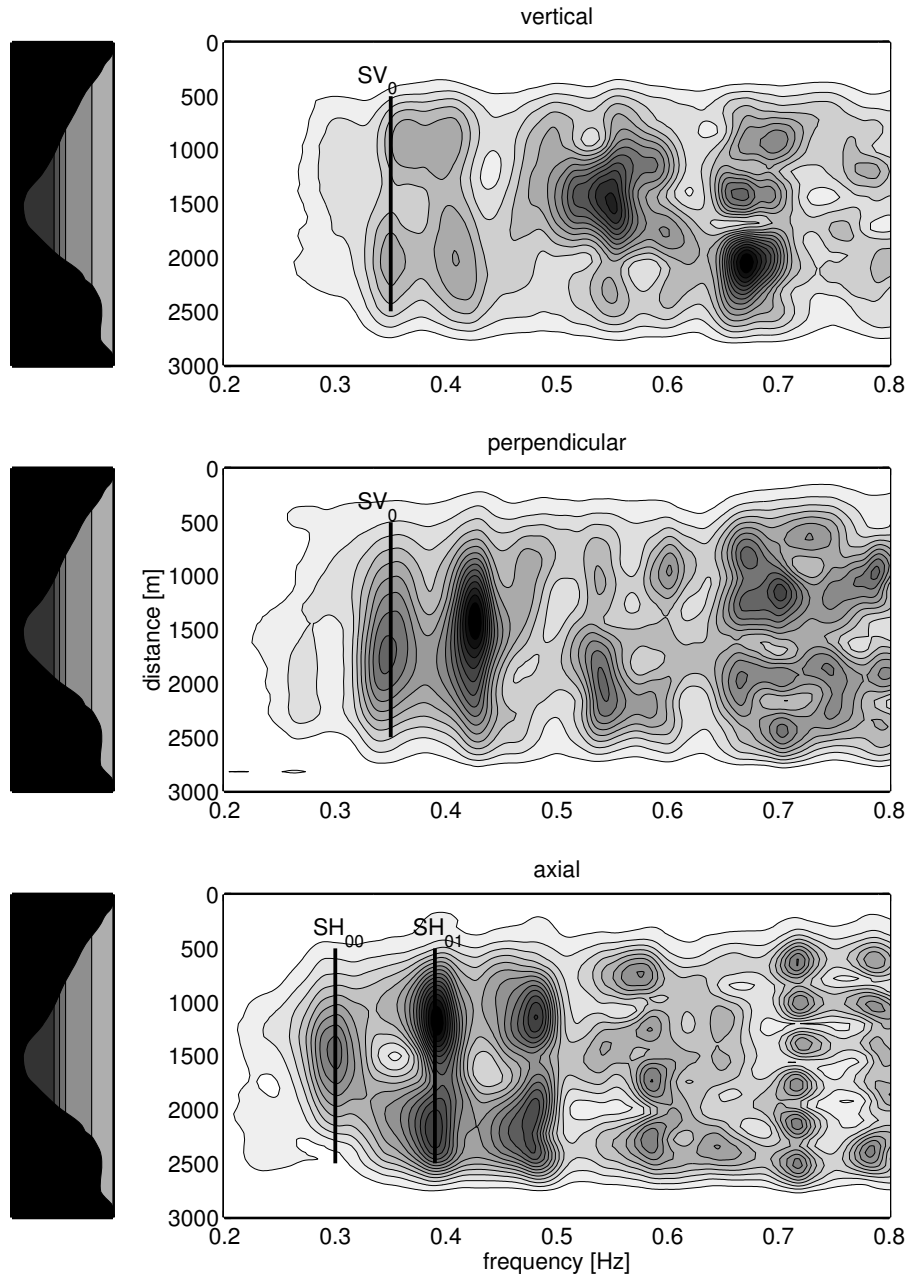


Figure 2.12: Spectral ratios of points located on profile at axial grid position 360 as a function of distance along the profile and frequency

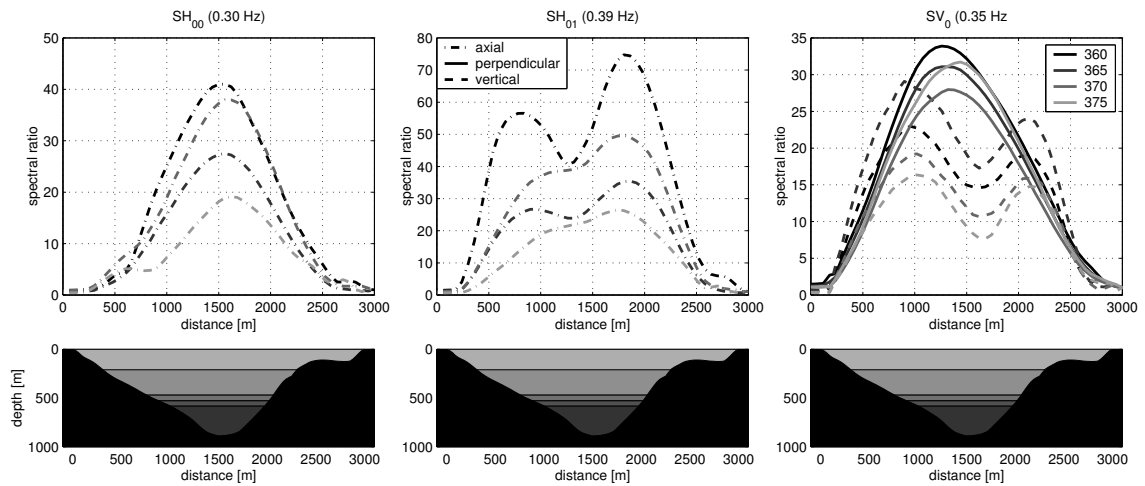


Figure 2.13: Cross sections of perpendicular (solid), vertical (dashed), and axial (dash-dotted) spectral ratios at different resonance frequencies for all four profiles.

2.5.2 Phase behaviour

If the peaks at 0.35 and 0.30 Hz identified from spectral ratios are caused by fundamental 2-D resonance modes, the synthetic ambient vibration wavefield at these frequencies should also exhibit the phase behaviour predicted by theory as summarised in Figure 2.4.

Figure 2.14 shows a section of synthetic ambient noise records bandpass filtered at the corresponding SV_0 and SH_{00} fundamental mode frequencies. On

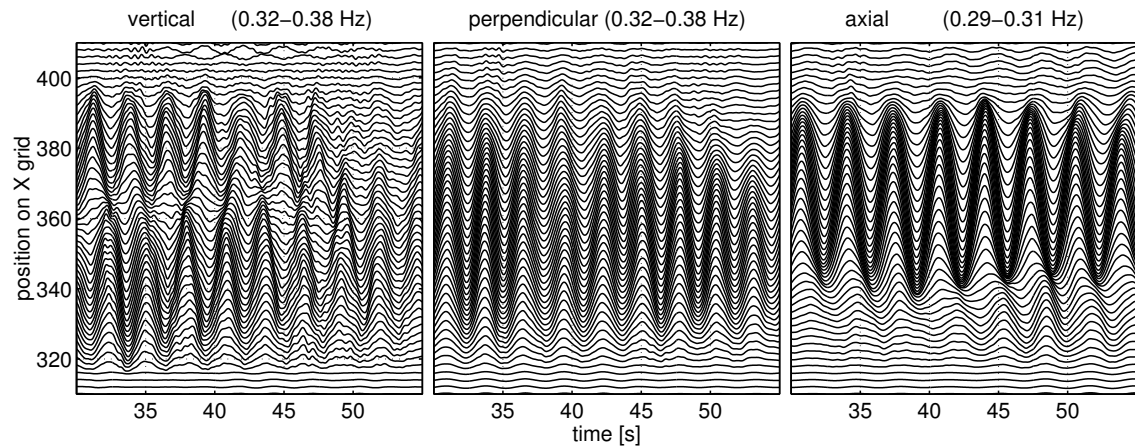


Figure 2.14: Bandpass filtered synthetic ambient noise records for all points on profile at axial grid position 370. The bandpass was applied at the SV_0 (vertical, perpendicular) and SH_{00} (axial) fundamental mode frequency.

the perpendicular component, motion is in phase on all points across the profile.

On the vertical component, a phase reversal occurs at the valley centre, and receivers on the one side of the valley are moving in anti-phase with receivers on the other side. The axial components are also in phase on all stations across the valley. These observations are, therefore, consistent with the behaviour predicted by theory (Fig. 2.4).

2.5.3 f - k analysis

We calculated f - k spectra from synthetic noise, using 20 stations from the four profiles on the lower half of the valley as an array (Fig. 2.10). The array geometry is grid-shaped, with station-intervals in the perpendicular and axial directions of 120 and 150 meters respectively; the array aperture is 480 meters in the perpendicular and 450 meters in axial direction. The array beam pattern for this configuration is given in Figure 2.15.

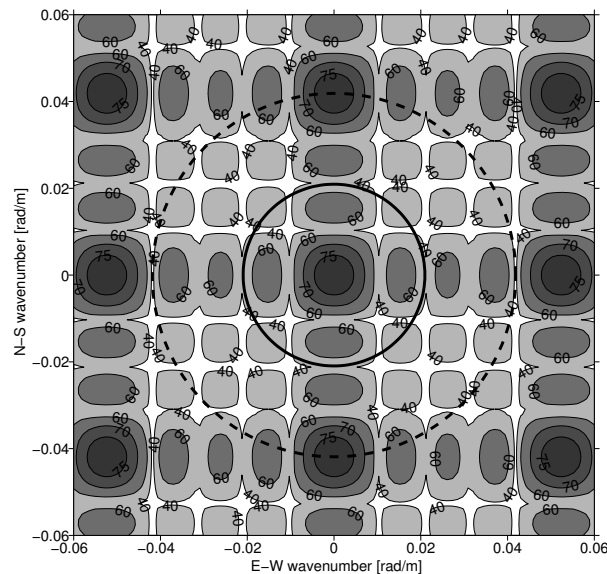


Figure 2.15: Beam pattern of array configuration for f - k analysis of synthetic microtremors. Contour intervals are indicating the array response in dB. The dashed circle indicates the wavenumber where the first aliasing peaks occur and the solid circle shows the Nyquist wavenumber.

Figure 2.16 (top) shows spectra as a function of slowness and azimuth for the vertical and perpendicular component at 0.35 (SV_0) and the axial component at 0.30 Hz (SH_0). The peaks at 0.35 and 0.30 Hz are located very close to the origin, at slownesses of less than 0.25 skm^{-1} . This means that the disturbance reaches all receivers at nearly the same time, which may be explained with a wavefront propagating almost vertically at a slight angle. This is the case for standing waves expected in the case of 2-D resonance.

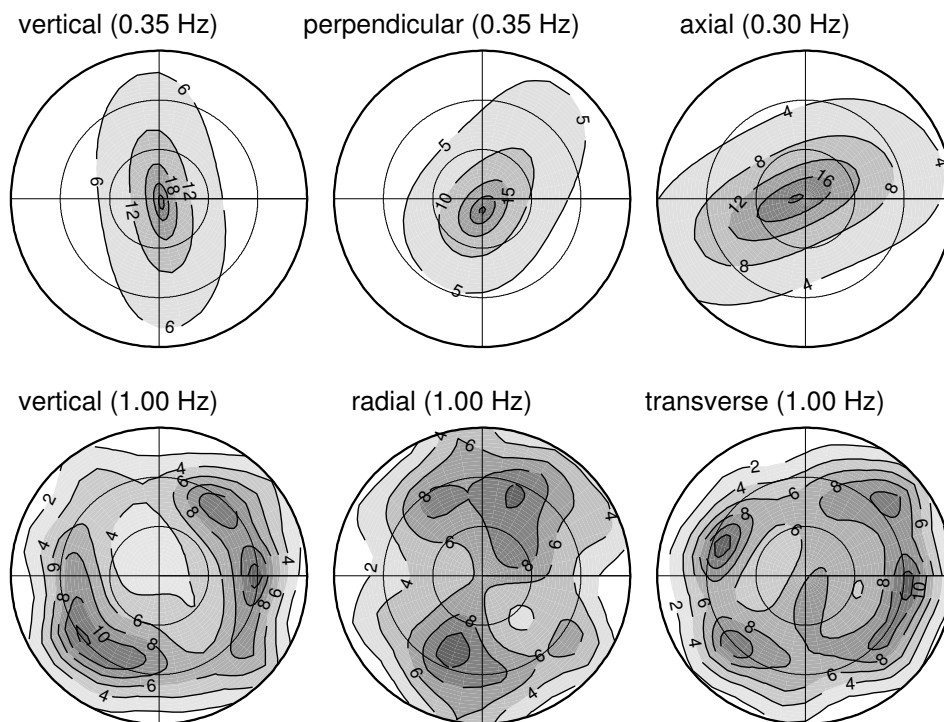


Figure 2.16: f - k spectra as a function of slowness and azimuth for SV_0 and SH_{00} (top) and at 1.00 Hz, where propagation dominates (bottom). Azimuthal directions are like in Figure 2.10, with up/down pointing along the perpendicular and left/right along the axial valley axis. Slowness starts at zero (middle) and reaches 3 skm^{-1} at the outermost ring; concentric grid-lines denote slowness intervals of 1 skm^{-1} . Contour intervals are given in dB. The aliasing slowness is outside the plotted range and not shown.

But horizontally propagating waves do occur at higher frequencies: at 1.00 Hz (Fig. 2.16 bottom), multiple peaks appear at higher slownesses on the vertical axis. This beam pattern develops if Rayleigh waves propagate through the array from different directions. The phase velocity of about 500 ms^{-1} (2 skm^{-1}) corresponds to the 1-D phase velocity at 1 Hz (Fig.2.2) calculated from the sediment fill of the velocity model (Table 2.1).

2.6 Evidence of 2-D resonance in observed ambient vibrations

Using the spectral ratio method, we will now determine the frequencies of possible resonance modes in recorded ambient vibrations. Then we will analyse the wavefield properties at the identified frequencies.

2.6.1 Reference spectra

2002 experiment

Figure 2.17 shows average spectra and average spectral ratios calculated from noise recorded during the 2002 experiment. Spectra of reference stations (black)

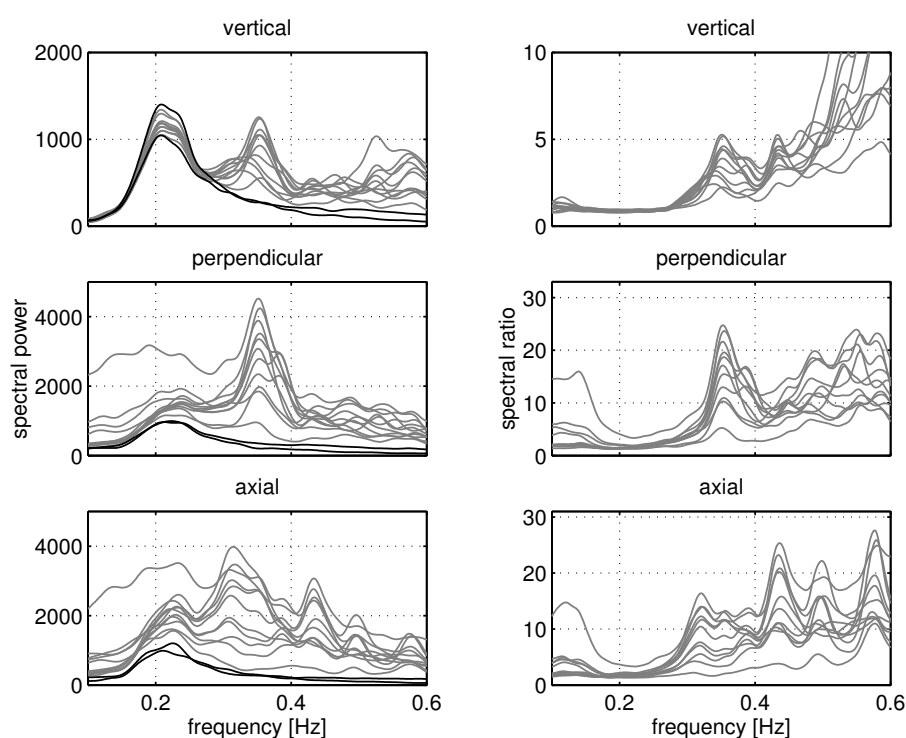


Figure 2.17: Average power spectra (*left*) and average spectral ratios (from the reference station in the North, *right*) calculated from ambient noise recorded during the 2002 Vétroz experiment. Power spectra of reference receivers located on bedrock are plotted black.

are quite characteristic for sites located inland, with a peak at 0.20 Hz related to oceanic microtremor. Application of the spectral ratio method removes this peak from stations located in the valley.

Spectral ratios of the vertical and perpendicular component show a very clear peak at around 0.35 Hz; a secondary peak can be identified at 0.38 Hz. On the

axial component, the first peak is located at 0.31 Hz; further peaks can be seen at around 0.43 and 0.50 Hz.

Figure 2.18 shows spectral ratios at 0.35 Hz as a function of distance along the profile for the vertical and perpendicular component. The pattern of spectral

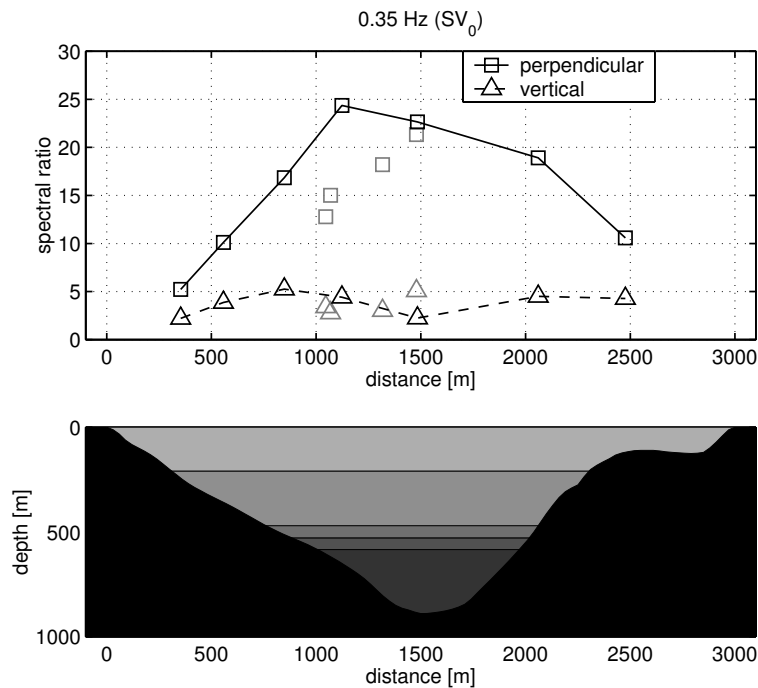


Figure 2.18: Average site-to-reference spectral ratios for ambient noise recorded in the 2002 experiment for vertical and perpendicular component as a function of distance along the profile (from North to South). Points located on the profile axis (Nr. 02-08 in Figure 2.7) are connected with lines and plotted black, points located away from the axis are plotted grey. The reference station is "Ref N" shown in Figure 2.7.

amplitude for points located on the profile axis (points connected with lines in Fig. 2.4) is very close to that expected for the SV_0 mode, with a maximum in the valley centre for the perpendicular component and two maxima and one central node for the vertical component.

Similarly, average spectral ratios of the axial component at the resonance frequency of the fundamental SH_{00} mode (Fig. 2.19 top) compare well with the expected pattern (Fig. 2.4) for points located on the profile axis.

Average spectral ratios at 0.43 Hz (Fig. 2.19 bottom) for points on the profile are indicating a central node and two peaks, which corresponds to the amplification expected for the first higher mode SH_{01} .

However, spectral ratios at stations deployed away from the profile (isolated, grey points in Figures 2.18 and 2.19) are quite different from stations placed on the profile. This variability along the valley axis was also observed in spectral

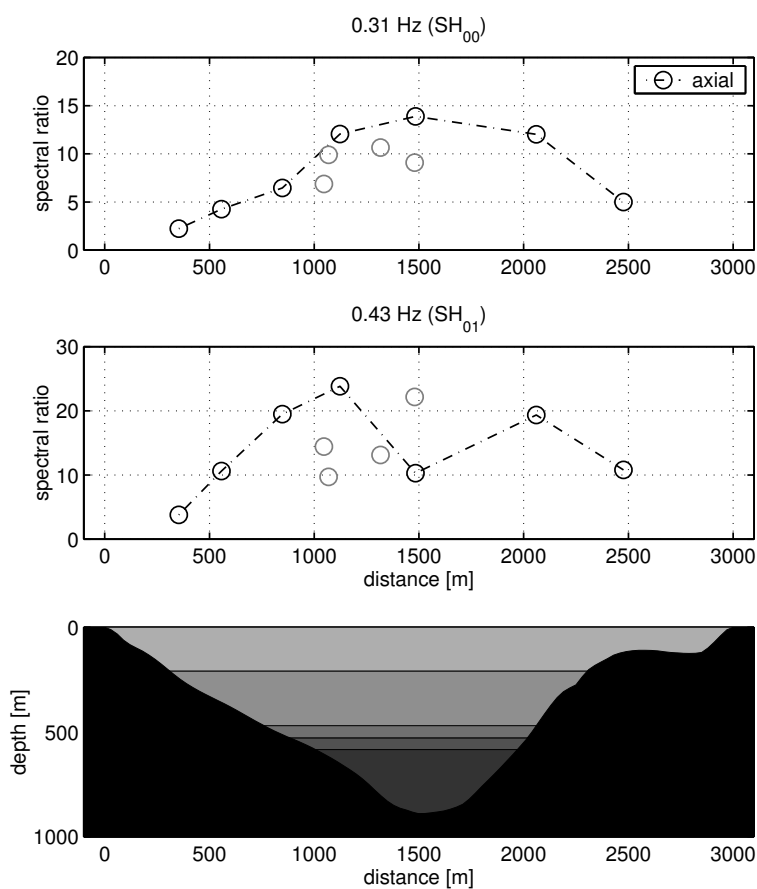


Figure 2.19: Average spectral ratios of 2002 experiment for axial component as a function of distance along the profile at 0.31 (top) and 0.43 (bottom) Hz. Points located on the profile are connected with lines.

ratios calculated from the four profiles in the numerical simulation (Fig. 2.13).

2003 experiment

Figure 2.20 shows average power spectra and spectral ratios obtained from the first configuration of the 2003 experiment. The regular, dense station coverage along the profile used for the first configuration of the 2003 experiment (circles and triangles in Figure 2.7) allows us to display spectral ratios as a function of distance along the profile in a contour diagram (Fig. 2.21).

The peaks of the fundamental mode SV_0 resonance are hardly visible in the vertical component, but very obvious for the perpendicular component, where the maximum amplitude is reached at around 0.39 Hz; this is slightly higher than the frequency of 0.35 identified in the 2002 experiment. On the axial component, modes SH_{00} and SH_{01} can easily be identified at 0.35 and 0.43 Hz, respectively; the frequency of the fundamental mode is again quite higher than the value derived from the first experiment. However, the peaks associated with the fundamental

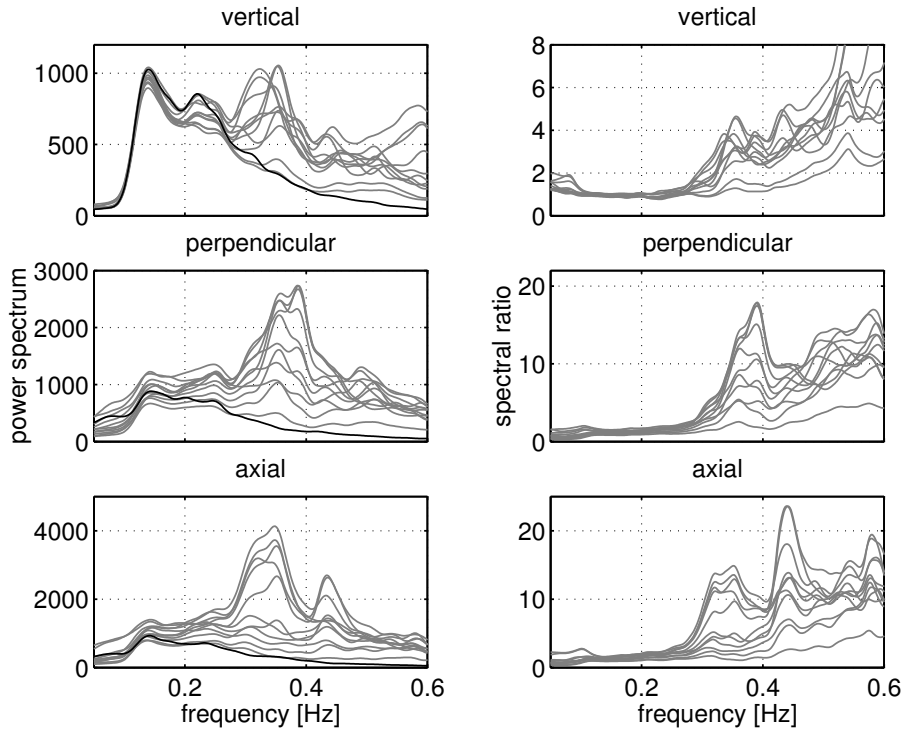


Figure 2.20: Average power spectra (*left*) and average site-to reference spectral ratios (*right*) calculated from ambient noise recorded during the 2003 Vétroz experiment (first configuration). Power spectra of reference receivers located on bedrock are plotted black. The reference station is "Ref" shown in Figure 2.7.

modes are quite broad. From Figure 2.20, it cannot be excluded that the fundamental mode SV_0 and SH_{00} frequencies are still located at 0.35 and 0.31 Hz respectively for this profile. The four peaks at 0.58 Hz (Fig. 2.21) might be associated with the fourth higher mode of SH resonance, consistent with the observation in Figure 2.17; the third higher mode cannot clearly be identified.

A cross-section of Figure 2.21 at 0.38 Hz (Fig. 2.22) shows an amplitude pattern similar to the one observed at 0.35 Hz in the 2002 experiment, with high amplification and one central peak for the perpendicular and two peaks with low amplifications for the vertical component. Both configurations yield similar amplification patterns. For the second configuration, differences in amplitude between points located on and away from the profile axis can again be observed. (Fig. 2.22).

Cross-sections at the SH_{00} frequency of 0.35 Hz (Fig. 2.23 top) are reproducing the pattern observed at 0.31 Hz in the 2002 experiment (Fig. 2.19 top). The second configuration yields higher spectral ratios than the first one. The amplitude pattern at the SH_{01} frequency (Fig. 2.23 bottom) slightly resembles the pattern observed for the 2002 experiment (Fig. 2.19 bottom) with two peaks and one node (the low amplitude of the first peak might be explained with the missing station).

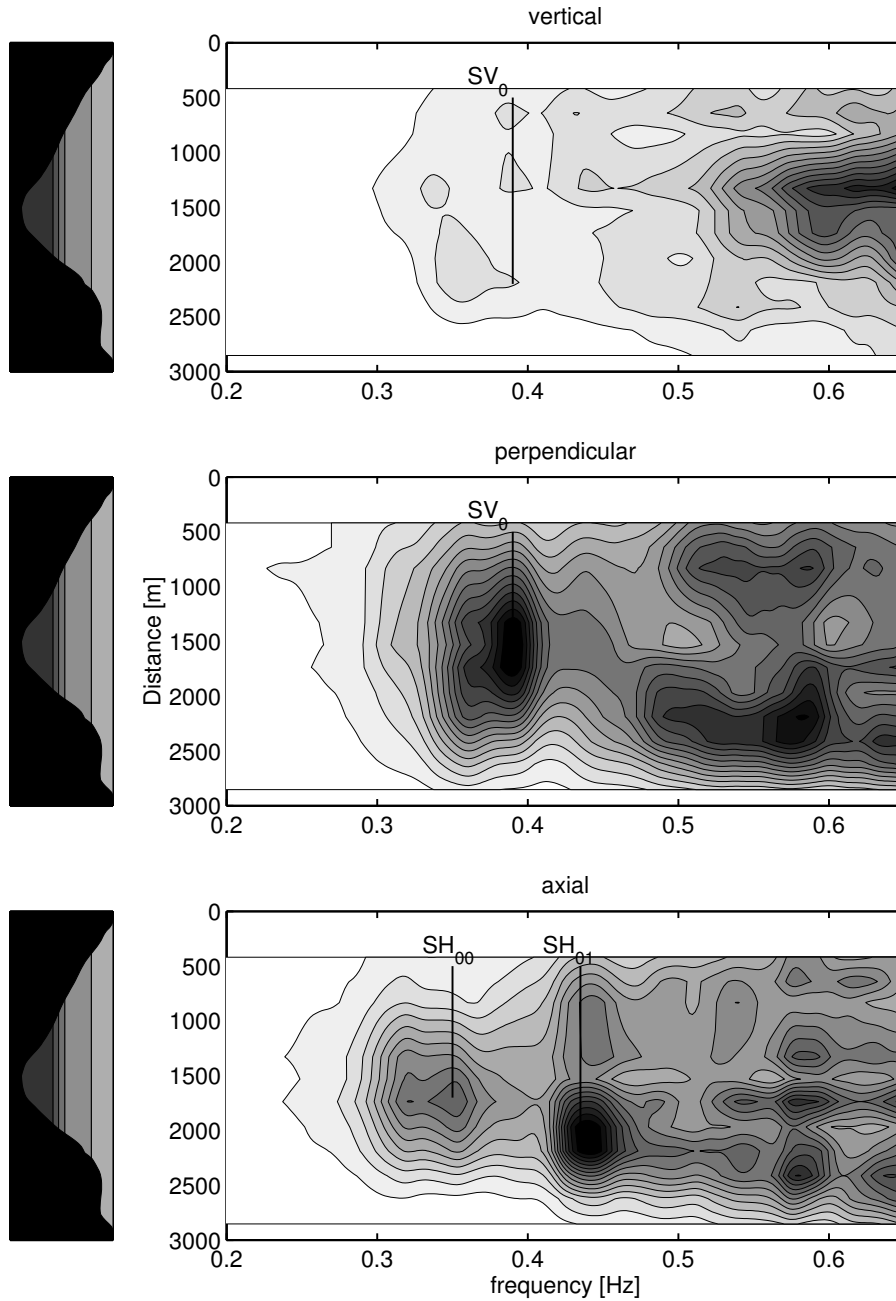


Figure 2.21: Average spectral ratios as a function of distance along the profile for ambient noise recorded at all stations used in the first configuration of the 2003 experiment.

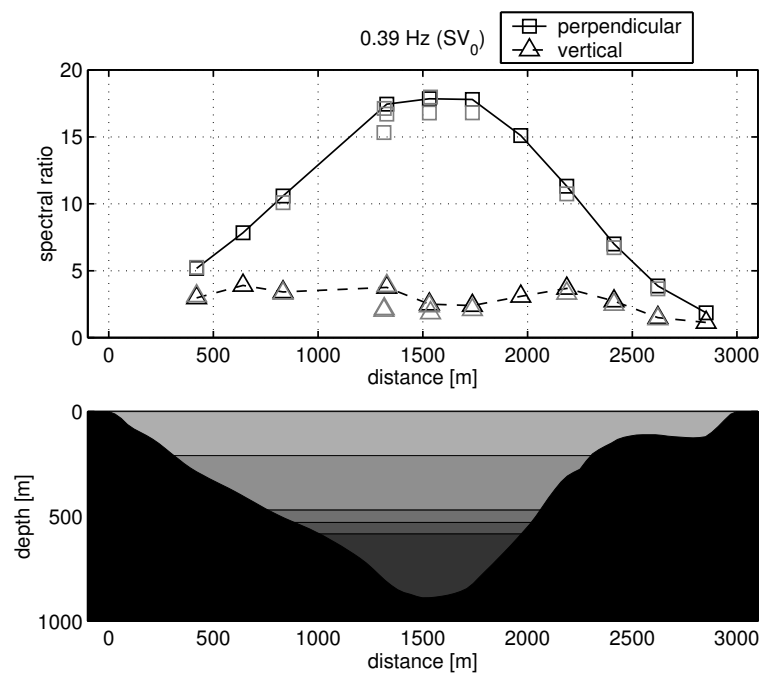


Figure 2.22: Average spectral ratios of 2003 experiment (1st and 2nd configuration) for vertical and perpendicular component as a function of distance along the profile at frequency 0.39 Hz, interpreted as mode SV_0 . Values for the 1st configuration are connected with lines and plotted black.

For both frequencies, the second configuration reveals the variability of spectral ratios along the valley axis.

Table 2.2 compares resonance frequencies identified in the 2002 and 2003 experiments and in the 3-D numerical simulation with values reported by Steimen *et al.* (2003) and calculated with the method of Paolucci (1999).

2.6.2 Phase behaviour

In the fundamental mode of SH resonance, the axial motion is in phase on all points across the valley (Fig. 2.4). If the peak at 0.35 Hz in the spectral ratio is caused by the fundamental SH_{00} mode, this behaviour should also be visible on recorded bandpass filtered traces in this frequency range. Figure 2.24 (top) shows axial components filtered between 0.28 and 0.34 Hz for all stations, demonstrating that both stations along the profile and stations outside the profile axis are in phase as expected. The time window from Figure 2.24 also displays the increase in amplitude towards the valley centre.

Figure 2.25 shows a similar plot for perpendicular and vertical traces bandpass filtered around the SV_0 frequency. While the perpendicular motion is in phase at all points, the phase of the vertical component changes in the valley centre, leading to an anti-phase motion at point 7 and 8 on the South side. This

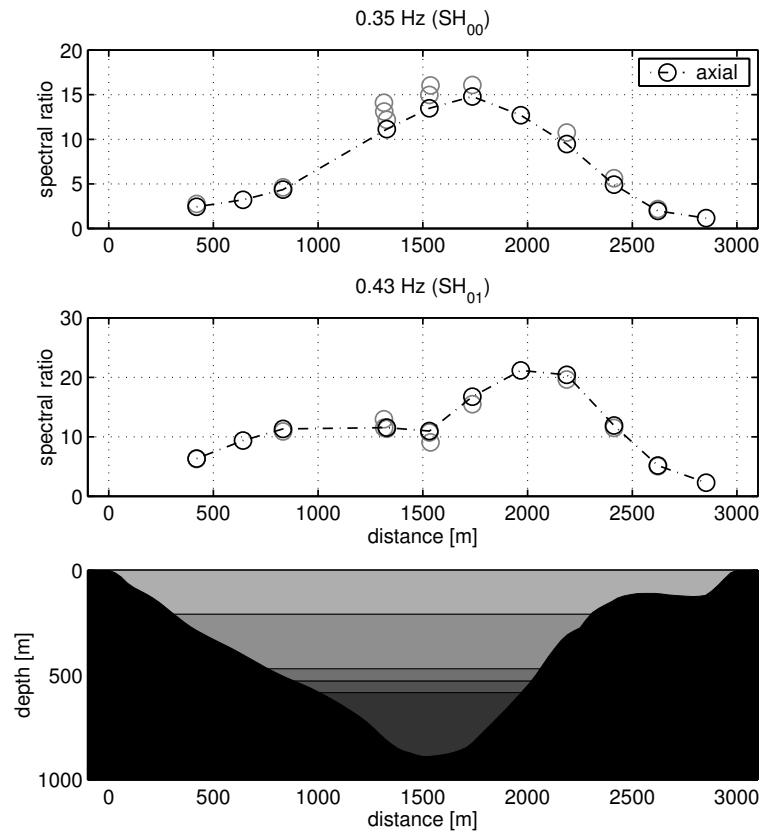


Figure 2.23: Average spectral ratios of 2003 experiment (1st and 2nd configuration) for the axial component as a function of distance along the profile at frequencies 0.35 (top) and 0.43 (bottom) Hz, interpreted as modes SH_{00} and SH_{01} respectively. Values for the 1st configuration are connected with lines and plotted black.

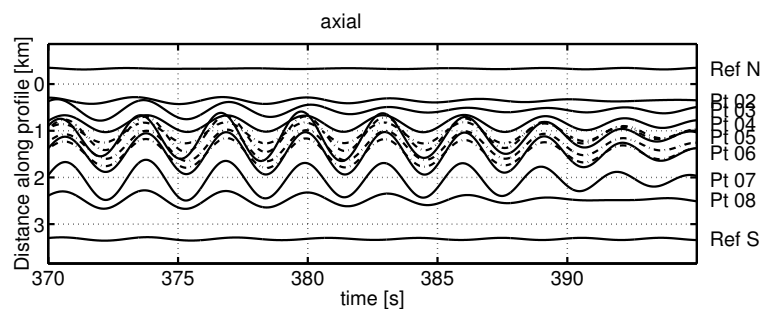


Figure 2.24: Time window of ambient noise recorded on the axial components during the 2002 experiment bandpass filtered around SH_{00} between 0.28 and 0.34 Hz. Seismograms of points outside the profile are printed with dashed lines.

observation is consistent with the pattern predicted for SV_0 by theory (Fig. 2.4) and observed in synthetic ambient vibrations (Fig. 2.14).

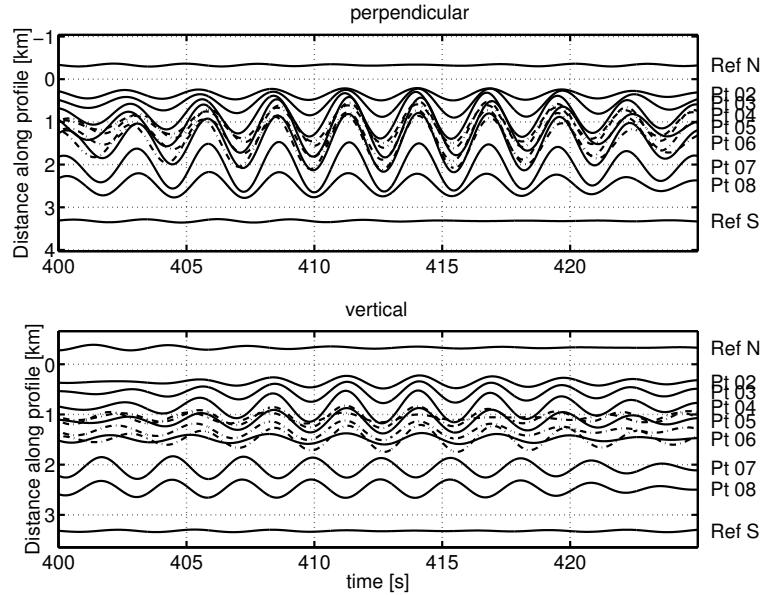


Figure 2.25: Time window of perpendicular (top) and vertical (bottom) components bandpass filtered around SV_0 between 0.32 and 0.38 Hz. Seismograms of points outside the profile are printed with dashed lines. (2002 experiment)

We will now apply the cross-correlation method described above to analyse the dominant phase behaviour of the whole record length. Figure 2.26 shows cross-correlation maxima as a function of distance along the profile axis for the perpendicular, vertical (top) and axial (bottom) component. Signals were bandpass filtered around the fundamental mode SV_0 (0.32 to 0.38 Hz) and SH_{00} (0.28 to 0.34 Hz) frequency. On the axial axis (bottom), the maximum of the cross-correlation is reached for very small lags at all points within the valley, including those located away from the profile axis. This shows that the in-phase motion observed in Figure 2.24 is the dominant behaviour of ambient noise in this frequency range.

Similarly, cross-correlation maxima on the perpendicular component are obtained for very low lags. On the vertical component, however, the maximum cross-correlation is only around zero for points on the Northern valley side. At point 7 and 8, the maximum is reached for a lag of -1.32 seconds; this corresponds to half the period of a 0.38 Hz oscillation. This confirms the pattern predicted by theory for SV_0 and observed in Figure 2.25, that of in-phase motion on the perpendicular axis and a phase change in the valley centre on the vertical axis.

Application of the above method to ambient noise recorded during the 2003 Vétroz experiment produces very similar results (Fig. 2.27 and 2.28). For points on the South side, the maximum is reached for lags between 1.28 and 1.50 Hz on the vertical component, which yields a frequency of 0.33 to 0.39 Hz if the signals

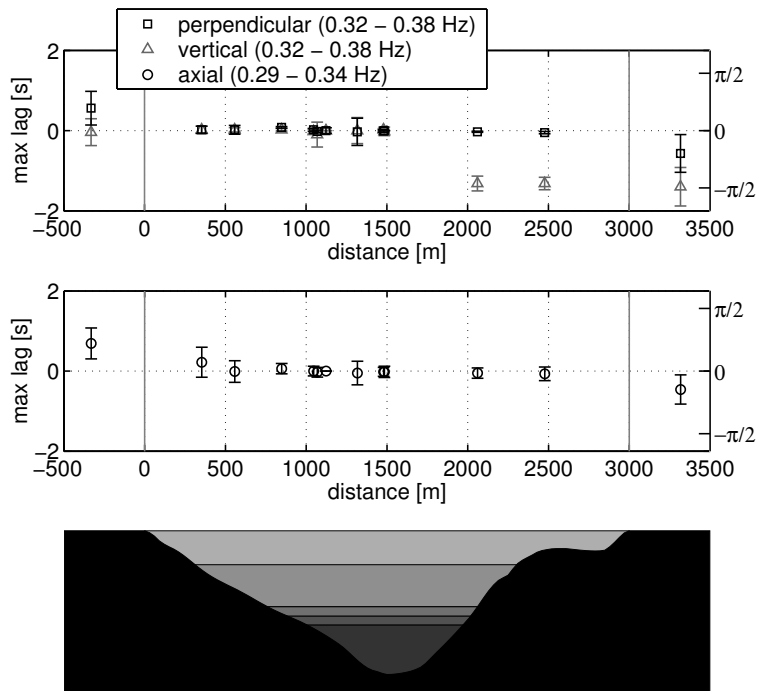


Figure 2.26: Cross-correlation maxima of perpendicular and vertical (top) and axial (bottom) component as a function of distance along the profile (2002 experiment). Error bars are estimated with the value of the cross-correlation maximum. Signals were bandpass filtered around SV_0 (0.32 to 0.38 Hz, top) and SH_{00} (0.29 to 0.34 Hz, bottom). Ticks on the right vertical scale show the phase calculated from the mean value of the frequency band.

are in anti-phase. The outlier at point 8 (vertical) might be explained with the vicinity to the node; the value of the maximum correlation at this point is very low.

2.6.3 Particle motion

The motion at the fundamental mode SV resonance is best visualised by a particle motion plot, which is obtained by plotting the perpendicular against the vertical component at each station (Fig. 2.29). The motion is almost horizontal near the valley centre, where it reaches the highest amplitude. Towards the valley edges, the vertical component is increasing, resulting in an inclined movement.(Fig. 2.4).

2.6.4 f - k analysis

Figure 2.30 displays results of the f - k analysis obtained from the array of the 2002 experiment. The slowness is displayed in a polar plot as a function of az-

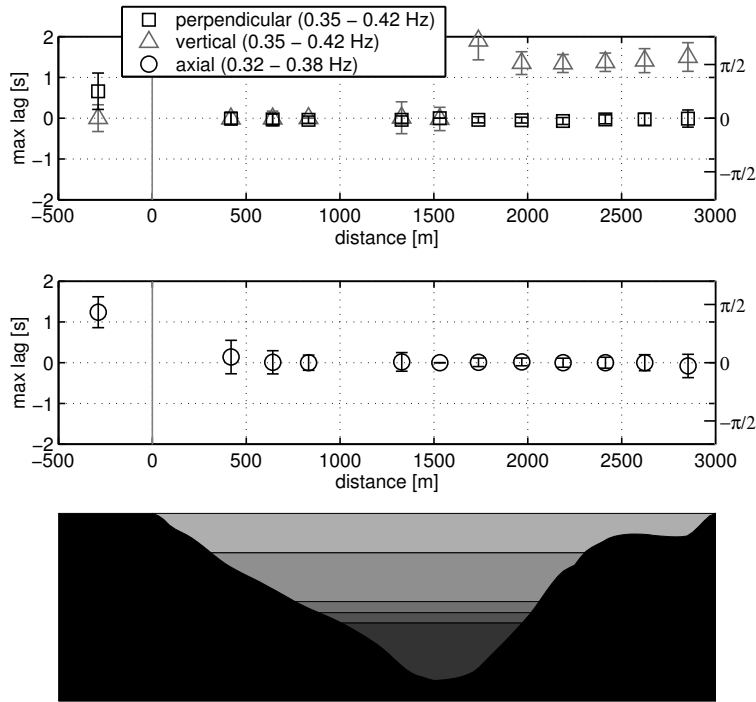


Figure 2.27: Cross-correlation maxima of perpendicular and vertical (top) and axial (bottom) component as a function of distance along the profile (2003 experiment, first configuration). Error bars are estimated with the value of the cross-correlation maximum. Signals were bandpass filtered around SH_0 (0.35 to 0.42 Hz, top) and SH_{00} (0.32 to 0.38 Hz, bottom).

imuth for the fundamental mode frequencies identified in the 2002 (top row) and 2003 (middle row) experiment at the corresponding components; the lowest row shows f - k spectra for a higher frequency of 0.70 Hz.

The peak in the f - k spectrum is located in the origin of the plot at a slowness of zero at the fundamental mode frequencies of the perpendicular, vertical (SV_0) and axial (SH_{00}) component. This implies that the disturbance reaches all receivers at almost the same time. This corresponds to the expected pattern in the case of 2-D resonance, where motion is in phase on all points at the same side of the valley. These patterns can, therefore, not be created by horizontally propagating surface waves, but by standing waves as expected in the case of 2-D resonance.

At 0.70 Hz, however, peaks appear well outside the origin at around 1.5 skm^{-1} in the NNE and SSW of the slowness-azimuth spectrum (vertical axis). This slowness corresponds to a velocity of around 670 ms^{-1} , which is comparable to the value of around 600 ms^{-1} obtained from 1-D dispersion analysis of the sediment fill in our velocity model (Figure 2.2).

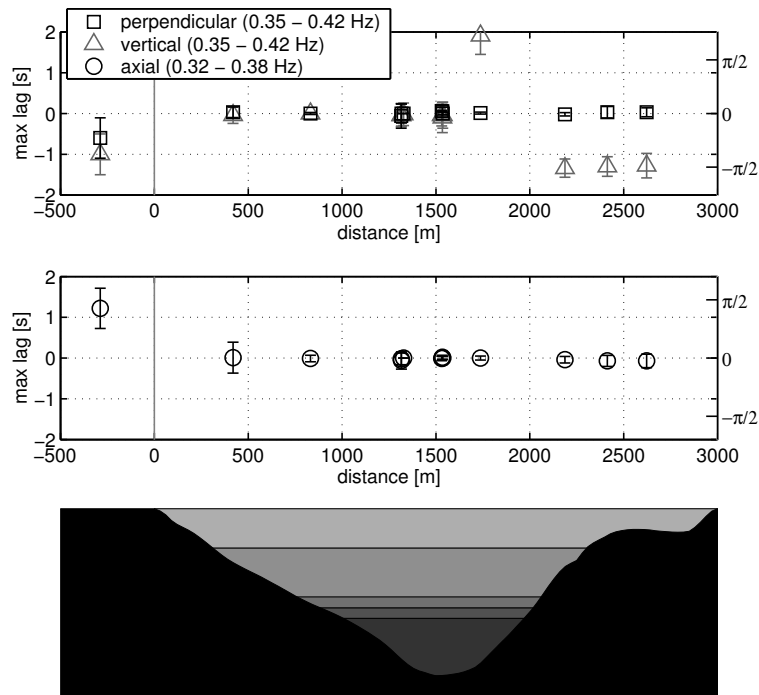


Figure 2.28: As for figure 2.27, but for the second configuration of the 2003 experiment.

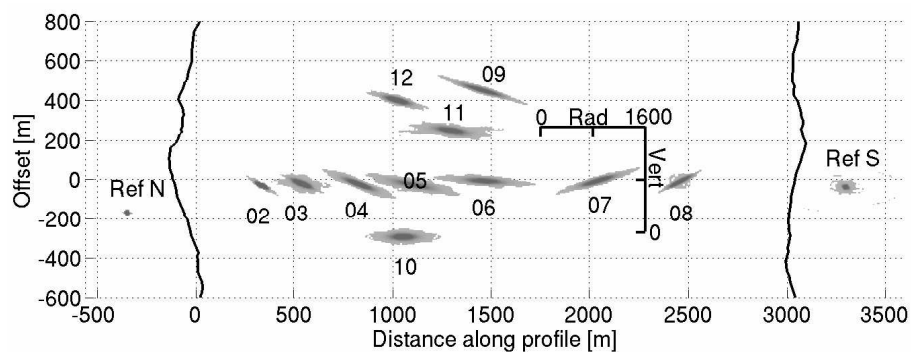


Figure 2.29: Particle motion plot of perpendicular vs. vertical component obtained from traces bandpass filtered between 0.32 and 0.38 Hz with noise recorded during the 2002 experiment. Areas passed multiple times are shaded dark.

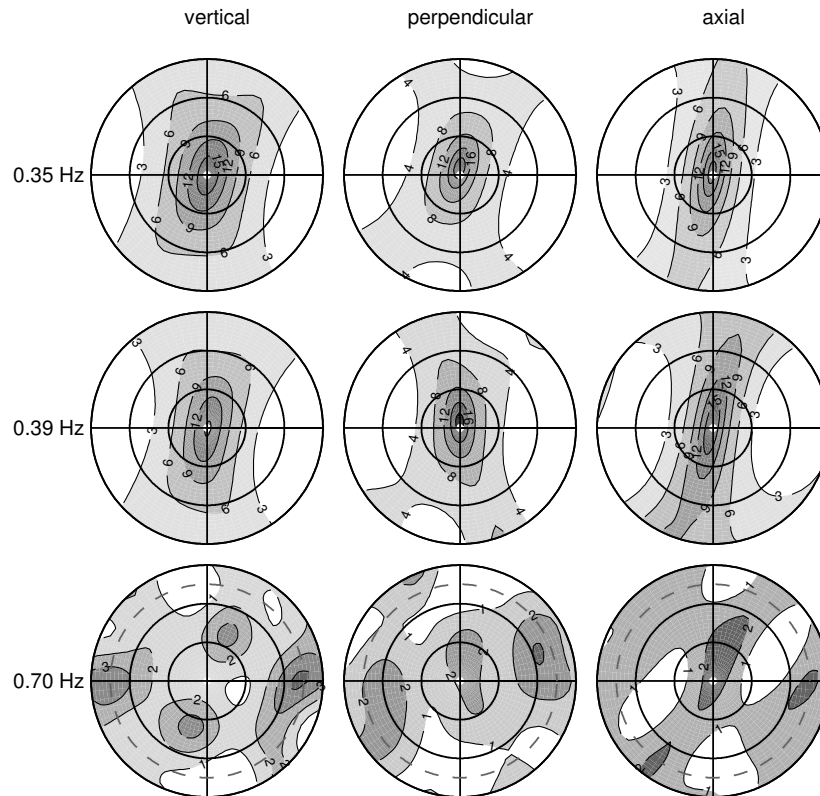


Figure 2.30: f - k spectra as a function of slowness and azimuth for different frequencies and components. Azimuth is 0 on top (North). Slowness starts at zero (middle) and reaches 3 skm^{-1} at the outermost ring; concentric grid-lines denote slowness intervals of 1 skm^{-1} . Contour intervals are given in dB. The grey dashed line at 0.70 shows the Nyquist slowness.

2.7 Discussion

2.7.1 Properties of 2-D resonance modes

The patterns of spectral amplitude observed in recorded and synthetic data compare well with patterns predicted by theory, supporting the interpretation of these wavefield properties as a consequence of 2-D resonance. While nodes in the amplification pattern are usually not very distinct, both in recorded and synthetic data (e.g. Fig.2.18, 2.23, 2.13), this may be explained in terms of interference with 1-D-amplification or effects of nearby sources, which prevent the spectral amplitude at the nodes from becoming very small. A discrepancy between theory and observation is the variability of the spectral amplitude with the position at equal

distances from the valley border (e.g. Fig. 2.18 and 2.19). One possible cause may be the statistical effect of the ambient vibration sources, because some variability was also observed in the synthetic ambient noise field (Fig. 2.13). Alternatively, these observations might be explained by the imperfectly two-dimensional structure of the valley.

Observed phase characteristics are also in agreement with theory. Since stations located on the profile as well stations laterally shifted away from profiles are moving in phase (Fig. 2.26 and Fig. 2.28), these phase characteristics can hardly be caused by laterally propagating surface waves.

2.7.2 f - k analysis

Results of the f - k analysis show that motion is not always exactly in phase at the resonance frequencies, because slownesses are slightly larger than zero (up to 0.25 skm^{-1}); this is especially true for the fundamental modes in the simulation (Fig. 2.16). However, the evidence appears to exclude the possibility that these beam patterns are caused by horizontally propagating surface waves.

A surface wave travelling at a phase velocity of 4000 ms^{-1} does not seem realistic compared with the 1-D dispersion analysis obtained from our velocity model (Fig. 2.2), unless we completely underestimated the shear-wave velocity of the bedrock.

In our numerical simulation, surface waves of this velocity can be ruled out, since the maximum Rayleigh wave velocity cannot exceed the shear-wave velocity of the bedrock (2890 ms^{-1}).

The low slownesses observed in beam patterns at the resonance frequencies can, therefore, only be explained in terms of standing waves evoked by 2-D resonance.

The P-wave fundamental mode (P_0 in Fig. 2.4) was not identified in recorded or simulated data. This might be interpreted as a consequence of the physical and geometrical properties of the valley, since the P-mode requires a higher shape ratio (i.e. a deeper valley or lower velocities) than the SH- or SV-mode to develop.

2.7.3 Resonance frequencies

Resonance frequencies obtained from different methods (Table 2.2) compare well with each other in general. Significant discrepancies exist between the fundamental mode frequencies identified from the 2003 experiment and the frequencies derived with other methods and from the 2002 experiment. Given the width of the peaks in spectral-ratio-frequency plots (Fig. 2.17 and 2.21), these discrepancies are just within the estimated uncertainty. However, the profile of the 2003 experiment is located around 500m away from the profile used for the 2002 experiment and the seismic reflection profile, which provided most of the geophysical information used for estimation of SV_0 and SH_{00} with numerical simulations and

Paolucci's method. It can, therefore, not be excluded that these differences in SV_0 and SH_{00} are caused by lateral variations in the valley geometry.

The frequency of SH_{01} observed in recorded noise is substantially higher than the value obtained from the simulation (Table 2.2). This difference might be caused by discrepancies between real shear-wave velocities and values used in the geophysical model (Table 2.1) or by the existence of non-planar layers in the sediment fill.

The uncertainties in the resonance frequencies identified in simulated data are higher than those reported by Steimen *et al.* (2003) (Table 2.2). This is probably a consequence of exciting the structure with ambient noise originating in the valley instead of laterally incident microtremor energy. Figure 2.12 contains a couple of spikes that could not be assigned to a resonance mode (e.g. at 0.40 Hz) and which may be caused by sources located close to the profile. Amplitude spectra at our reference stations (Fig. 2.17 and Fig. 2.20) show that a considerable amount of low-frequency microtremor energy is present outside the valley; this implies that incident waves must contribute significantly to the excitation of 2-D resonance. However, results of our 3-D simulation show that 2-D resonances can be excited by ambient noise characteristic for urban areas, which is relevant for the applicability of the method.

2.7.4 Horizontal-to-vertical spectral ratios

The amplification pattern at the fundamental mode SV frequency exhibits a maximum on the perpendicular component and a node on the vertical component around the valley centre (Fig. 2.4, 2.18 and 2.22). This suggests that a peak in horizontal-to-vertical spectral ratios will appear around the SV_0 frequency. Figure 2.31 (top) shows a contour plot of horizontal-to-vertical spectra calculated from noise recorded during the 2003 experiment. The most conspicuous peaks appear at 0.38 and 0.43 Hz. These frequencies are markedly higher than the expected 1-D resonance frequency of around 0.20 Hz for the sediment fill, and it would be difficult to assign these peaks to SH_{00} , SV_0 and SH_{01} without our prior knowledge of the noise wavefield.

In order to distinguish between SH and SV resonance, we suggest to calculate the perpendicular/vertical and axial/vertical ratio (Fig. 2.31 middle and bottom) in the case of deep sediment-filled valleys. SV_0 can easily be identified at 0.38 Hz in the perpendicular-to-vertical contour diagram. SH_{00} is also visible on the axial-to-vertical plot at 0.35 Hz. At the estimated frequency of 0.41 Hz for SH_{01} , only one of the two expected peaks is visible.

These results show that peaks in the horizontal-to-vertical ratio cannot be interpreted in terms of fundamental mode of 1-D resonance in deep sediment-filled valleys; horizontal-to-vertical peaks may be related to fundamental or even higher modes of SV or SH 2-D resonance, depending on the excited mode and on the position in the basin.

The 1-D Rayleigh wave ellipticity in Figure 2.2 shows that the fundamental

mode horizontal-to-vertical peak would appear at around 0.21 Hz for a horizontally layered structure with the stratigraphy of our model (Table 2.1). This value is much lower than the peak frequencies obtained from the numerical and experimental methods described in this text, which demonstrates the insufficiency of 1-D analysis to describe the response of this site.

Estimation of either v_s or h from the resonance frequency f_h using the 1-D relation in equation 2.2 or 1-D Rayleigh wave ellipticity would not yield useful results in this case.

2.8 Conclusions

In summary, our observations imply that the noise wavefield at the Vétroz site is dominated by 2-D resonance at lower frequencies (0.25 to 0.50 Hz); horizontally propagating surface waves do occur at higher frequencies. We conclude that ambient noise records measured simultaneously on a dense profile may be used to investigate the resonance behaviour of sediment-filled valleys. Simultaneous measurements allow the identification of resonance modes by their phase properties and their horizontal velocity derived from f - k analysis. Horizontal-to-vertical spectral ratios may yield fundamental or higher modes of 2-D resonance, but the identification of the mode is difficult if both horizontal components are used.

Acknowledgments

We thank the authors of the programs developed within the SESAME project that were used during this study, including Peter Moczo and Josef Kristek for their FD code (NOISE), and Matthias Ohrnberger (cap), Fortunat Kind (capon routine) and Marc Wathelet (geopsy) for their software employed to calculate f - k spectra. The numerical code used for the calculation of 2-D resonance frequencies was kindly provided by Roberto Paolucci. The computations are enabled thanks to an account and help service at computing facilities of CSCS (Swiss National Supercomputing Centre), Manno. Experiment design and data analysis was supported by Sibylle Steimen. Stefan Fritsche, Philipp Kästli-Krushelnytskyj and Marc Lambert helped to perform the field work. We would like to thank Michael Asten and an anonymous reviewer for many valuable comments that helped to improve the manuscript.

This research is part of the European Commission SESAME project (EVG1-CT-2000-00026) funded by the Swiss Federal Office for Education and Science (BBW Nr. 00.0085-2) and the project SHAKE-VAL, funded by the Swiss National Science Foundation (No. 200021-101920).

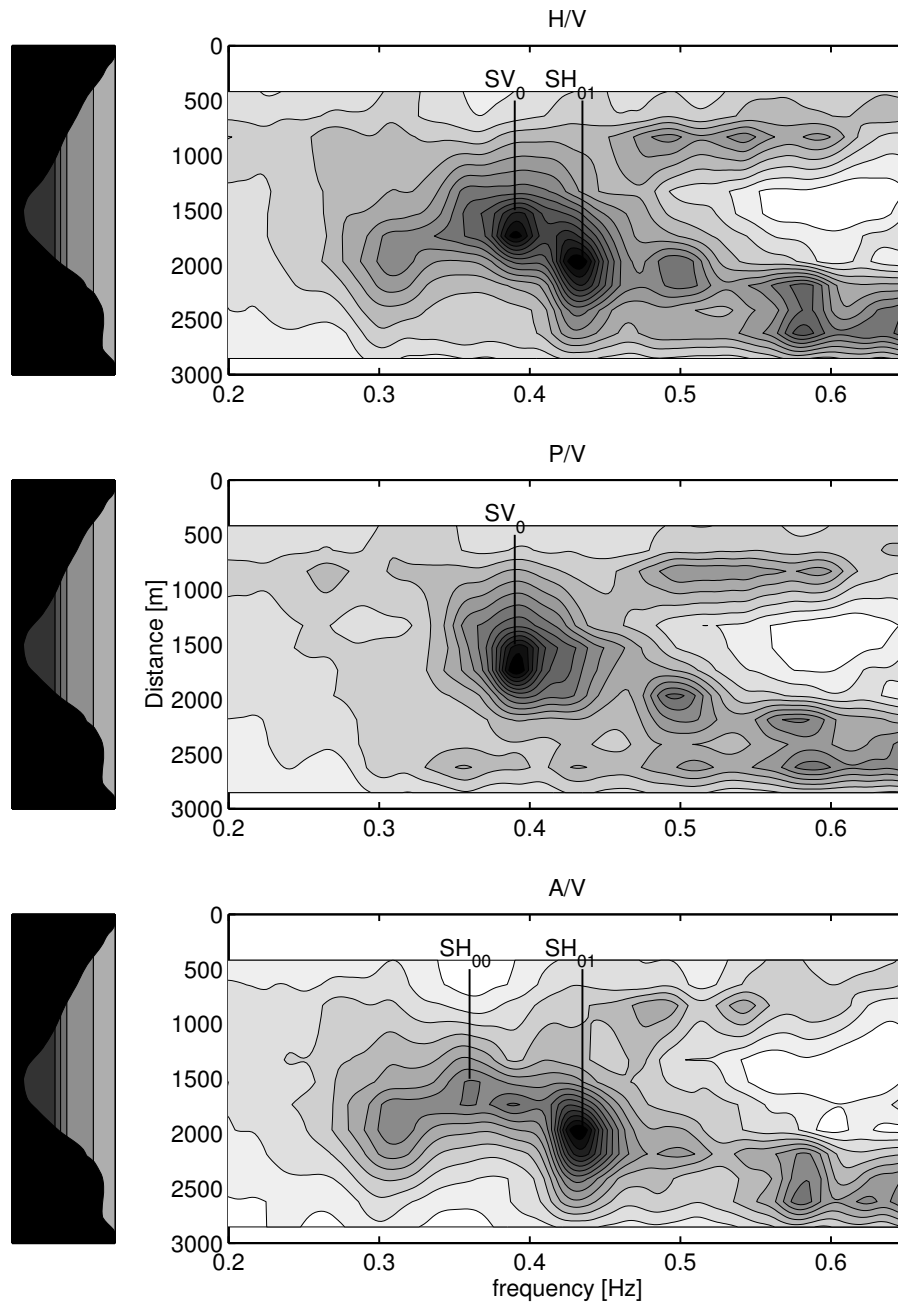


Figure 2.31: Horizontal-to-vertical spectral ratios as a function of distance along the profile and frequency. Top: horizontal/vertical, centre: perpendicular/vertical, bottom: axial/vertical. (2003 experiment, 1st configuration).

Chapter 3

A combined inversion of Rayleigh wave dispersion and 2-D resonance frequencies

D. Roten and D. Fäh

Institute of Geophysics, ETH Hönggerberg, 8093 Zürich, Switzerland.

E-mail: daniel.roten@sed.ethz.ch

Geophys. J. Int. (2007) **168**, 1261–1275 doi:10.1111/j.1365-246X.2006.03260.x

Accepted 2006 October 8. Received 2006 October 6; in original form 2006 March 2

Summary

Shear-wave velocities of the sediment fill of a deep Alpine valley are estimated from ambient noise recorded on linear and circular arrays. We propose a combined inversion of 2-D resonance frequencies identified from site-to-reference spectral ratios and Rayleigh wave dispersion curves obtained from frequency-wavenumber analysis. The method is tested on synthetic noise data and on noise recorded at three sites in the Rhône valley in Southern Switzerland. Previous studies have shown that 2-D resonance dominates the ambient vibration wavefield at low frequencies at the investigated sites. Inversion techniques which assume that the noise wavefield consists mainly of horizontally propagating surface waves will therefore fail to resolve shear-wave velocities at depths below around 500 meters. We show that standard techniques lead to an overestimation of shear-wave velocities at depth when applied to synthetic and observed ambient noise. The combined inversion is able to resolve the shear-wave velocities in the initial velocity model when applied to synthetic noise records. Application of the method to observed ambient noise improves resolution at depth and yields realistic shear-wave velocities for the lower part of the sediment fill.

Key words: Seismic noise, sedimentary basin, seismic array, spectral analysis, shear-wave velocities, Rhône valley

3.1 Introduction

The impact of local ground motion amplification on earthquake damage was demonstrated during many recent damaging earthquakes. In some cases, observed ground motion amplification and increased damage was explained with 1-D analysis of the soil column, e.g. for the 1989 Loma Prieta earthquake (e.g. Hough *et al.*, 1990). Other observations highlighted the importance of 2-D effects, which may cause higher amplification. A well known example is the basin-edge effect responsible for the damage belts reported after the 1995 Kobe earthquake (Kawase, 1996).

Many cities are located along river valleys on soft unconsolidated sediments, a very common example of a 2-D structure. Numerical simulations have shown for long that 2-D effects may contribute significantly to the seismic response of such sediment-filled valleys. Edge-generated surface waves are the dominant effect in rather shallow valleys, while a 2-D resonance pattern develops in deeper basins (Bard and Bouchon, 1980a,b, 1985).

In the framework of the SHAKE-VAL project, we are studying earthquake site effects in the Rhône valley (Fig. 3.1), a deep sedimentary basin in Southern Switzerland. In a previous numerical study performed for the city of Sion, Frischknecht and Wagner (2004) found that 2-D resonance will cause an amplification significantly higher than the expected 1-D value. However, a quantification of ground motion amplification with such simulations is only possible if a realistic geophysical model of the subsurface structure is available.

Because the amplification is caused by the trapping of S- and surface waves in the sediment, the shear-wave velocity is the most important parameter of the geophysical model. Due to growing concern about sediment-induced site effects, methods to estimate shear-wave velocities from microtremor array recordings are becoming increasingly popular in seismic hazard assessment. (e.g. Bard *et al.*, 2005; Wathelet *et al.*, 2005; Kind *et al.*, 2005; Asten *et al.*, 2005). These methods rely on the assumption that the observed noise wavefield consists mainly of horizontally propagating surface waves, which allows measurement of Rayleigh wave phase velocities using either frequency-wavenumber (e.g. Capon, 1969) or spatial auto correlation (SPAC) techniques (Aki, 1957). Under the assumption that the structure underneath the array can be approximated by flat horizontal layers, the Rayleigh wave phase velocity is inverted for the shear-wave velocity. This 1-D assumption imposes problems when the method is applied to more complicated 2-D and 3-D sites, like deep sediment-filled valleys. But methods to estimate shear-wave velocities at such sites would be especially desirable, because the even higher amplification caused by such 2-D or 3-D structures was demonstrated in many numerical experiments.

The valley geometry at the investigated sites (Fig. 3.2) is well known from

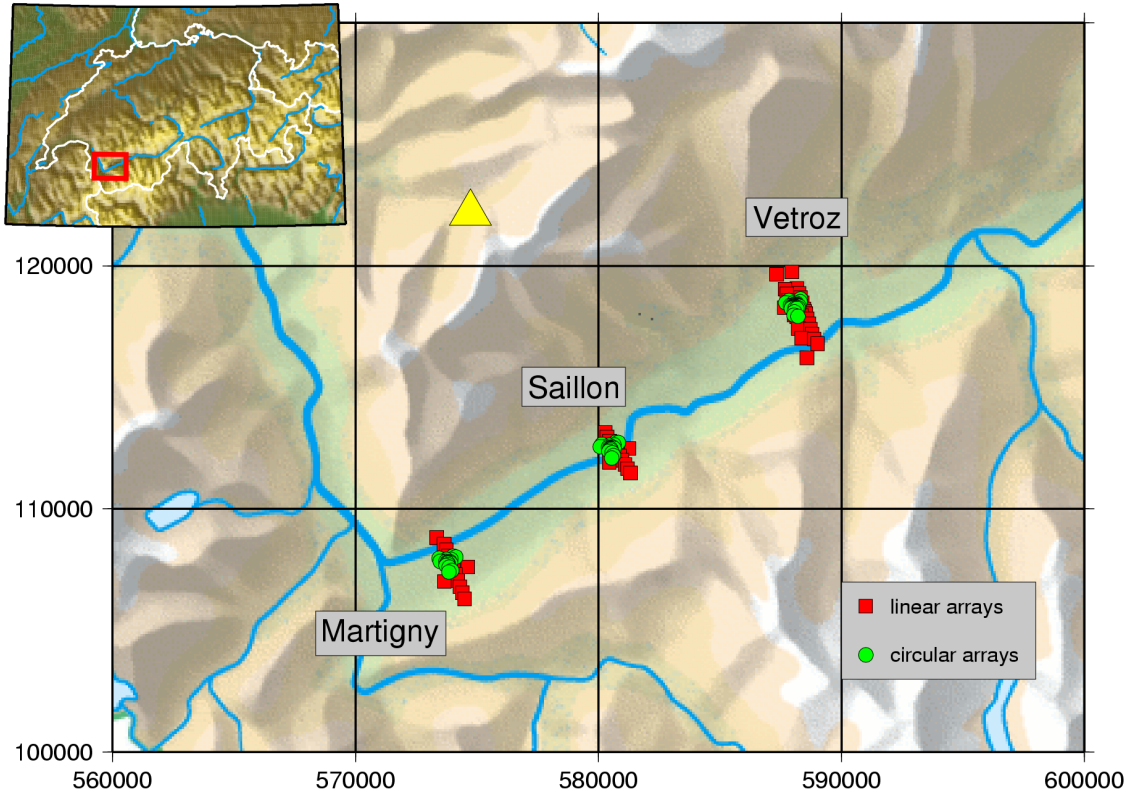


Figure 3.1: Linear (red) and circular (green) arrays measured in the Rhône valley. The yellow triangle indicates the position of the permanent station GRYON. © 2005 Swisstopo.

high-resolution reflection seismic profiles performed during a previous research project (Pfiffner *et al.*, 1997) and from gravimetric studies (Rosselli, 2001). The steep slope of the sediment-bedrock interface implies that the 1-D approximation may at best be valid for the upper layers of the sediment fill. Furthermore, the noise wavefield is dominated by standing waves at low frequencies as a consequence of 2-D resonance (Steimen *et al.*, 2003; Roten *et al.*, 2006). This violates a basic supposition of the microtremor array method, which requires that the noise wavefield be dominated by horizontally propagating surface waves.

In this paper we propose a combined inversion of dispersion curves and 2-D resonance frequencies. The dispersion curves are obtained with circular arrays which sample the upper part of the embanked sediment-filled valleys. To bypass problems caused by the non 1-D structure of the sites and the standing waves at low frequencies, we introduce an approach that combines information about the 2-D resonance behaviour of the sites with observed Rayleigh wave dispersion curves. Our combined inversion aims to find models that explain all observation, and to yield realistic estimations for shear-wave velocities that will serve as input parameters for 3-D numerical earthquake simulations. The method is first tested

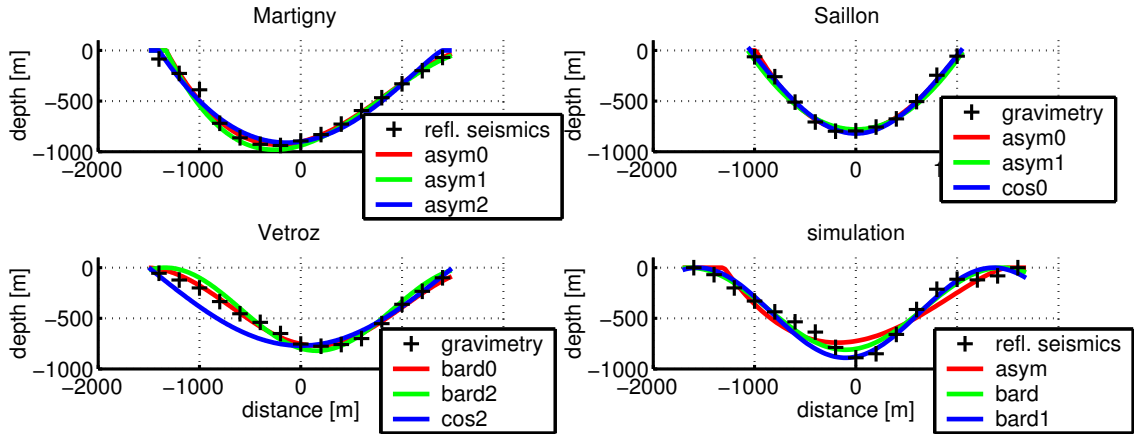


Figure 3.2: Sediment-bedrock interfaces (*pluses*) reported from reflection seismics (Pfiffner *et al.*, 1997) or gravimetry (Rosselli, 2001) and different parameterisations (*solid*) used for calculation of 2-D resonance frequencies (Tab. 3.2)

depth	v_p	v_s	Q_p	Q_s	ρ	geologic interpretation
0	1700	456	50	25	1900	deltaic sediments
210	1930	650	50	25	1900	glaciolacustrine deposits
470	1970	790	50	25	2000	meltout and reworked till
529	2300	920	50	25	2000	lodgment and till
584	2050	820	50	25	2000	subglacial deposit
890	5000	2890	200	100	2500	hard rock

Table 3.1: Geophysical model of the sediment fill used for the numerical simulation. Depths are in m, v_p and v_s in ms^{-1} and ρ in kgm^{-3} (from Steimen *et al.*, 2003)

on a synthetic noise dataset computed for the Vétroz site and then applied to real noise recorded at three similar sites.

3.2 Synthetic noise data

The ambient noise simulations were performed in the framework of the European SESAME project using a 3-D finite difference method (Kristek and Moczo, 2003; Moczo and Kristek, 2002). A detailed description of the noise simulation can be found in Roten *et al.* (2006). The geophysical model for the simulation was created by Steimen *et al.* (2003) and corresponds to the sediment bedrock interface in Figure 3.2 (right bottom) with the sediment fill given in Table 3.1.

Under the assumption that the recorded ambient noise is mostly generated by superficial processes, ambient noise is simulated using a large number of sources on the sediment surface in the valley (Fig. 10 in Roten *et al.*, 2006). We will process

synthetic noise from of a dense circular array with an aperture of 900 meters in the valley centre.

3.3 Observed noise data

We performed a series of microtremor array measurements at three sites in the Rhône valley (Fig. 3.1). At each site ambient noise was recorded with two specific array configurations:

1. For the first configuration, the sensors were aligned in a profile running perpendicular to the valley axis. These linear arrays are used to analyse the resonance behaviour of the valley, as we did for a site near Vétroz in a previous study (Roten *et al.*, 2006). The resonance behaviour and the frequencies of the 2-D resonance modes play an important role in the analysis of circular arrays.
2. The second type of arrays required a circular receiver layout. This setup is needed to measure the apparent velocity of Rayleigh waves propagating through the array from various directions. In order to sample a range of frequencies, concentric circular arrays with increasing aperture were recorded at most sites.

We deployed three-component sensors with an eigenfrequency of 5 seconds for all noise measurements. GPS signals were used for time synchronisation.

3.3.1 Observations on linear arrays

For the linear arrays recorded in Martigny, Saillon and Vétroz, we used very similar array geometries. We installed ten receivers on a profile running perpendicular to the valley axis, with a regular spacing of 200 to 300 meters, depending on the valley width (Fig. 3.1). Two more receivers were placed away from the profile axis near the valley centre. A reference station was deployed on the North side of the valley on bedrock. For the Martigny linear array, the reference site was poorly selected and very noisy. Therefore, the permanent station GRYON from the Swiss Digital Network will be used as a reference (triangle in Fig. 3.1). The noise wavefield was measured simultaneously on all thirteen receivers during at least an hour.

3.3.2 Observations on circular arrays

At all three sites, large circular arrays with apertures of about 800 meters were recorded. For these arrays, the receivers were arranged around a central station on four concentric circles with radii of about 130, 200, 350 and 400 meters, according to a scheme proposed by Kind *et al.* (2005). The array response beampatterns and aliasing limits are given in Figure 3.3.

At Martigny, the large array was reshaped to an array of smaller aperture by moving the stations from the two outermost rings to two inner concentric rings with radii of about 30 and 100 meters.

At the Vétroz site, the shear-wave velocities at higher frequencies were investigated during an additional measurement campaign to sample the structure of the uppermost layers. Three concentric rings of 5 stations with radii of 16, 40 and 90 meters were recorded subsequently, following a recommendation of Bard *et al.* (2005). (Because the array response patterns of the three rings are very similar, only the beampattern of the smallest ring is given in Figure 3.3).

3.4 Noise data processing

The first step in our noise analysis consists in identification of the 2-D resonance frequencies of the site using linear arrays. Then we extract apparent phase velocities for a range of frequencies from noise recorded on the circular arrays. Results from both linear and circular arrays are then used to invert shear-wave velocities of the sediment fill.

3.4.1 Identification of 2-D resonance

The resonance behaviour of a sediment-filled valley depends on the geometry of the sediment-bedrock interface and the shear-wave velocities of the sediment fill. The seismic response of shallow valleys is dominated by the basin-edge effect and by local 1-D resonance. In deep valleys, these edge-generated surface waves interfere with waves propagating vertically, and a 2-D resonance pattern develops. Bard and Bouchon (1985) introduced the *equivalent shape ratio* to distinguish between shallow and deep valleys. It is defined as the maximum valley depth divided by the width over which the sediment-thickness is at least half the maximum depth. The critical shape ratio decreases with increasing velocity contrast between bedrock and sediment fill. If the equivalent shape ratio of a valley is higher than the critical value, the development of 2-D resonance must be expected.

In Figure 3.4, the shape ratios of the analysed sites are plotted for ranges of realistic velocity contrasts with the critical shape ratio for the SH case. All sites are clearly located in the domain of 2-D resonance.

This 2-D resonance involves three fundamental modes, the SH, SV and P mode. Each of these modes has its own resonance frequency and shows a characteristic pattern of amplification and phase behaviour (Fig. 2.4). The SH fundamental mode involves only the component running parallel to the valley axis. The amplification reaches a maximum in the valley centre. At the SH fundamental mode frequency, motion is in phase everywhere in the valley. The SV mode involves the vertical component and the direction perpendicular to the valley axis. The amplification shows a central peak on the perpendicular component

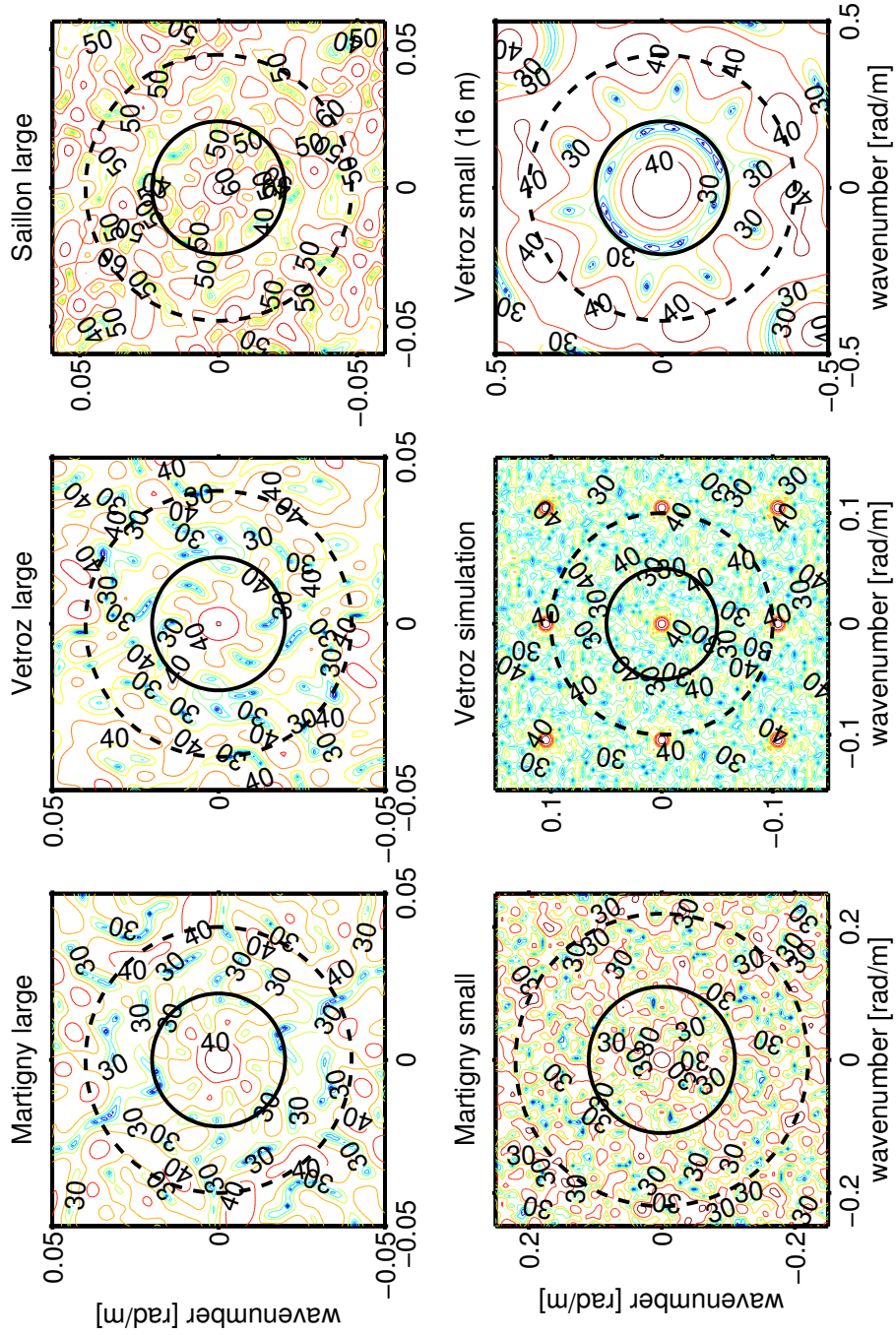


Figure 3.3: Array response beam patterns for the different small and large aperture circular arrays. Contour lines denote the array response in dB. The wavenumbers of the first aliasing peaks are indicated by the dashed circles, and the wavenumber domains that can be analysed with the individual arrays is within the solid circles.

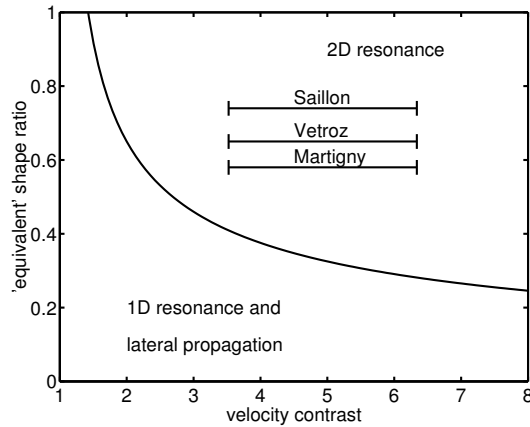


Figure 3.4: Critical equivalent shape ratio for the SH case as a function of velocity contrast and shape ratios of the investigated sites for a range of estimated velocity contrasts (modified from Bard and Bouchon, 1985)

and a central node on the vertical axis. Motion is in phase in the perpendicular direction, while a phase reversal occurs on the vertical component.

As we reported from a previous study (Roten *et al.*, 2006; Steimen *et al.*, 2003), these specific patterns of amplification and phase behaviour were observed in the ambient vibration wavefield recorded at the Vétroz test site. We will now apply the same method to the linear arrays recorded at Martigny and Saillon.

To identify the 2-D resonance frequencies, we calculate site-to-reference spectral ratios, using the code described in Roten *et al.* (2006). Fourier amplitudes are computed from tapered, 50% overlapping time windows of 80 seconds length. Then spectral ratios are calculated from the smoothed Fourier amplitudes for each time window. Average spectral ratios are determined from the individual windows using a weighting scheme.

To eliminate effects of nearby low-frequency disturbances, a simple suppression trigger is applied to each time window after low-pass filtering with a cut-off of 1 Hz. It sets the weight of a time window to zero if the amplitude of any channel at any sensor exceeds a certain threshold value.

3.4.2 f - k analysis

Noise data recorded on the vertical component on the circular arrays are processed with the high-resolution frequency-wavenumber analysis (Capon, 1969) using the algorithm of Kind *et al.* (2005), which is implemented in the continuous array processing software CAP (Ohrnberger *et al.*, 2004). The f - k spectra yield angle and apparent slowness of Rayleigh waves propagating through the array from various directions for a set of frequencies. From the f - k spectra, the dispersion curve was extracted for frequencies well above the 2-D resonance frequencies.

3.4.3 Combined Inversion of Rayleigh wave dispersion curves and 2-D resonance frequencies

Dispersion curves derived from the f - k analysis are inverted for a velocity model with a software developed by Wathelet (2005). The forward problem of calculating the dispersion curves for Love and Rayleigh waves is solved with the method of Dunkin (1965).

The identified resonance frequencies of the different 2-D resonance modes are a function of the valley shape and the shear-wave velocities in the sediment fill. Since the valley shape of the investigated sites is well known from other studies (Besson *et al.*, 1993; Pfiffner *et al.*, 1997; Rosselli, 2001), we will try to use the observed values of the 2-D resonance frequencies to resolve shear-wave velocities in the deeper part of the sediment cover which are not resolved by the array measurements.

We introduce a combined inversion for geophysical models that do not only explain the observed Rayleigh wave dispersion curves, but also the observed 2-D resonance frequencies. The forward problem of calculating the frequencies of the 2-D resonance modes can be solved with a code developed by Paolucci (1999). This program allows to compute the 2-D resonance frequencies of valleys filled with horizontally layered sediments in a fraction of a second. The method is based on Rayleigh's principle, which states that the motion of an undamped elastic system at one of its resonance frequencies can be approximated by a system with a single degree of freedom.

In a 3-D bounded medium, the displacement $s_k(\vec{x})$ a harmonic vibration with frequency $\omega_0 = 2\pi f_0$ can be described as:

$$s_k(\vec{x}, t) = \psi_k(\vec{x})e^{i\omega_0 t} \quad (3.1)$$

where $\psi_k(\vec{x})$ defines the mode-shape along the direction k (Paolucci, 1999). Integrating the kinetic energy over the domain Ω with density ρ and evaluating the maximum gives

$$T_{max} = -\omega_0^2 \int_{\Omega} \frac{1}{2} \rho(\vec{x}) \psi_k^2(\vec{x}) d\Omega \quad (3.2)$$

The strain energy V of the system is given by

$$V(t) = \int_{\Omega} \frac{1}{2} \sigma_{jl}(\vec{x}) \epsilon_{jl}(\vec{x}) d\Omega \quad (3.3)$$

where ϵ_{jl} is the strain tensor and σ_{jl} the stress tensor.

Energy conservation requires that total elastic energy V_{max} equal the total kinetic energy in the system T_{max} . Equating expression 3.2 with equation 3.3 yields

$$\omega_0^2 \leq \min_{\hat{\psi}_k} \frac{\int_{\Omega} \hat{\sigma}_{jl}(\vec{x}) \hat{\epsilon}_{jl}(\vec{x}) d\Omega}{\int_{\Omega} \rho(\vec{x}) \hat{\psi}_k^2(\vec{x}) d\Omega} \quad (3.4)$$

In the above expression, the exact mode shape $\psi_k(\vec{x})$ has been replaced by a set of admissible approximations $\hat{\psi}_k(\vec{x})$. Because of this approximation, the relation provides only an upper bound for the true resonance frequency ω_0 (Paolucci, 1999).

site	model name	valley type	a	h	ζ
Martigny	asym0	asymmetric	1480	930	-0.25
	asym1	asymmetric	1530	980	-0.30
	asym2	asymmetric	1400	910	-0.10
Saillon	asym0	asymmetric	1020	800	-0.05
	asym1	asymmetric	1065	750	0.00
	cos0	cosine	1040	820	
Vétroz	bard0	sine	1700	770	
	bard2	sine	1500	820	
	cos2	cosine	1500	770	
Simulation	asym	asymmetric	1120	770	0.20
	bard0	sine	1540	810	
	bard1	sine	1460	890	

Table 3.2: Different parameterisations of sediment-bedrock interface for the analysed sites (Fig. 3.2)

When applied to 2-D alluvial valleys, the interface between valley and bedrock must be parameterized to define the domain Ω and the approximations of the mode shape $\hat{\psi}$. The code by Paolucci (1999) provides four relations, which define sine-shaped, cosine-shaped, elliptic and asymmetric valleys. For cosine-shaped valleys, the sediment-bedrock interface is described by

$$f(x_1, x_3) = \cos\left(\frac{\pi x_1}{2a}\right) - \frac{x_3}{h} \quad (3.5)$$

where a is the valley width and h the maximum depth. Sine shaped valleys correspond to the definition used by Bard and Bouchon (1985):

$$f(x_1, x_3) = \cos\left(\frac{\pi x_1}{2a}\right) + \frac{x_3}{h} + \frac{1}{2} \quad (3.6)$$

Asymmetric valleys can be approximated with

$$f(x_1, x_3) = \left(1 + \frac{x_1}{a}\right) \left(1 - \frac{x_1}{a}\right)^{\frac{1-\zeta}{1+\zeta}} - (1 + \zeta)(1 - \zeta)^{\frac{1-\zeta}{1+\zeta}} \cdot \frac{x_3}{h} \quad (3.7)$$

where the parameter ζ controls the asymmetry of the interface. To account for uncertainties caused by the parameterisation of the sediment-bedrock interface we used different values for each site (Table 3.2 and Fig. 3.2).

Application of Paolucci's method to the Vétroz site has shown that the 2-D resonance frequencies calculated from equation 3.4 are not more than 0.01 Hz above the values obtained from synthetic ambient noise (Roten *et al.*, 2006).

We implemented the method as an additional constraint in the inversion program of Wathelet (2005). For each velocity model created during the inversion process, the velocity profile is combined with the parameterisation of the

sediment-bedrock interface (Fig. 3.2 and Tab. 3.2), and the corresponding 2-D resonance frequency is computed. Using the L2-norm, the misfit M_{2-D} between the observed and synthetic 2-D resonance frequency is calculated. The total misfit M of each model is obtained by combining the misfit between the observed and synthetic dispersion curve M_{DC} and the 2-D misfit M_{2-D} :

$$M = (1 - w) \cdot M_{DC} + w \cdot M_{2-D} \quad (3.8)$$

The weighting factor w needs to be adjusted depending on the number of data points to achieve a good fit of both dispersion curves and 2-D resonance frequencies.

3.4.4 Inversion with the Neighbourhood algorithm

For the inversion of shear-wave velocities the parameter space is searched with the neighbourhood algorithm introduced by Sambridge (1999a,b). This inversion method has successfully been tested on synthetic and recorded dispersion curves (Wathelet *et al.*, 2004).

The neighbourhood algorithm is based on the partition of the solution space into *Voronoi* cells. The global misfit function is approximated by assigning the misfit in the center of each cell to the whole cell. During each iteration, the sampling of the solution space is refined in regions of low misfit. The algorithm consists of the following stages (Sambridge, 1999a):

1. An initial set of n_s random models is created
2. the misfit of the recent models is calculated. A subset of n_r models with the lowest misfit is selected.
3. For each selected model n_r , n_s/n_r new models are generated by a random walk within the cell.
4. the algorithm is repeated from step (ii) with the new n_s models for N iterations.

Therefore the algorithm only needs two tuning parameters: the sample size for each iteration n_s and the number of cells to resample n_r . A high number for n_s and n_r results in explorative sampling of the whole solution space, but requires a larger number of iterations to provide a sufficient number of acceptable models. If low values for n_s and n_r are used the algorithm samples promising regions in a more exploitative way, at the increased risk of getting trapped in local minima.

For the inversion problem described in this text we sought for acceptable velocity models of 5 to 6 layers (Tab. 3.3). We inverted for the shear-wave velocity in each layer and allowed for variations of the layer depth. To reduce the non-uniqueness of the inversion problem we did not allow for shear-wave velocities decreasing with depth (Wathelet, 2005). Because the P-wave velocity does not influence the 2-D resonance frequency when calculated with the method of Paolucci

layer	depth	v_p	v_s	ρ
1	10 – 300	1700	17 – 1202	1900
2	300 – 500	1930	19 – 1364	1900
3	500 – 550	1970	19 – 1393	2000
4	550 – 600	2200	22 – 1555	2000
5	770 – 890	2200	22 – 1555	2000
6		5000	2890	2500

Table 3.3: Parameter limits for 5-layer velocity model used in inversion of synthetic dispersion data. Units are like in Table 3.1

site	SV ₀	SH ₀₀	SH ₀₁	SH ₀₂
Martigny	0.325	0.29	0.38	0.43
Saillon	0.37	0.32	0.43	
Vétroz	0.35	0.31	0.43	
simulation	0.34	0.30	0.39	

Table 3.4: 2-D resonance frequencies [Hz] of the different modes identified at the analysed sites

(1999), V_p of each layer was constrained to the values reported from reflection seismic (Pfiffner *et al.*, 1997), apart from the shallow uppermost layer for which no value is available from the literature. In order to keep the number of dimensions in the inversion problem low we did not invert for densities but constrained them to the estimations derived from gravimetry (summarised in Frischknecht, 2000).

With this configuration the number of dimensions ranges between 10 and 13. Following the recommendation of using at least twice the number of dimensions for the sample size we used $n_r = n_s = 50$ to ensure good sampling of the solution space. The number of iterations was set to $N = 1000$, therefore an ensemble of 50,000 velocity models was created during each inversion.

3.5 Results from synthetic ambient noise

We will start with analysis of the synthetic ambient noise, because results of this simulation may help to understand recorded dispersion curves better.

Site-to-reference spectral ratios calculated from our synthetic noise records are given in Roten *et al.* (2006). The frequencies of SV₀, SH₀₀ and SH₀₁ were identified at 0.35, 0.30 and 0.39 Hz, respectively (Tab. 3.4).

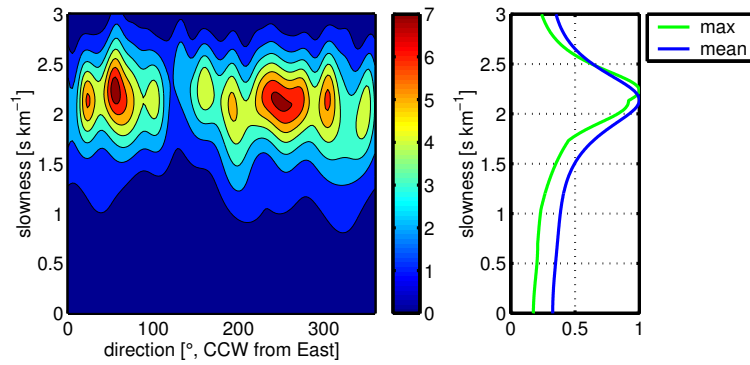


Figure 3.5: *Left*: f - k map obtained from vertical synthetic noise records at 1.26 Hz. The colorbar indicates the array output in dB. *Right*: normalized maximum and mean over all direction as a function of slowness.

3.5.1 f - k analysis

Figure 3.5 shows an example of f - k spectra obtained from the vertical component of synthetic noise traces. Peaks in the f - k map show incident angle and apparent slowness of Rayleigh waves propagating through the array from different directions. From these f - k spectra, the dominant apparent slowness for each frequency was selected manually. Figure 3.5 (right) shows the maximum and mean over all directions as a function of slowness. For most frequencies, we selected the peak in the mean over all directions as apparent slowness. This approach averages the apparent slowness of waves arriving from different directions, and it results in a slightly smoother dispersion curve than if the absolute maximum in the f - k spectrum is selected. No estimation of uncertainty is available because of the short duration of the synthetic noise time series.

Figure 3.6 compares the dispersion curve derived from f - k analysis (circles) with the theoretical 1-D dispersion curve (pluses) for the soil column at the maximum depth (Tab. 3.1). For values above 1.2 Hz, the two curves are very similar. With decreasing frequency, the apparent slowness obtained from the f - k analysis is getting significantly lower than the theoretical value. Triangles in Figure 3.6 show the theoretical 1-D dispersion curve for a soil column closer to the valley edge, for a bedrock depth of 550 meters. This 1-D dispersion curve shows a reasonable match with the apparent slowness between around 0.6 and 0.7 Hz, but it does not explain the bias in the apparent slowness between 0.8 and 1 Hz. In Figure 3.6, the lower resolution boundary of the array is also indicated using a maximum wavelength λ_{\max} of twice the largest sensor spacing (e.g. Ohori *et al.*, 2002; Satoh *et al.*, 2001). The array layout applied on the synthetic noise should therefore be large enough to resolve the structure down to at least 0.5 Hz. This implies that the lower apparent slowness obtained from the f - k analysis compared to the 1-D dispersion at the valley centre may reflect the influence of lateral bedrock on surface wave propagation.

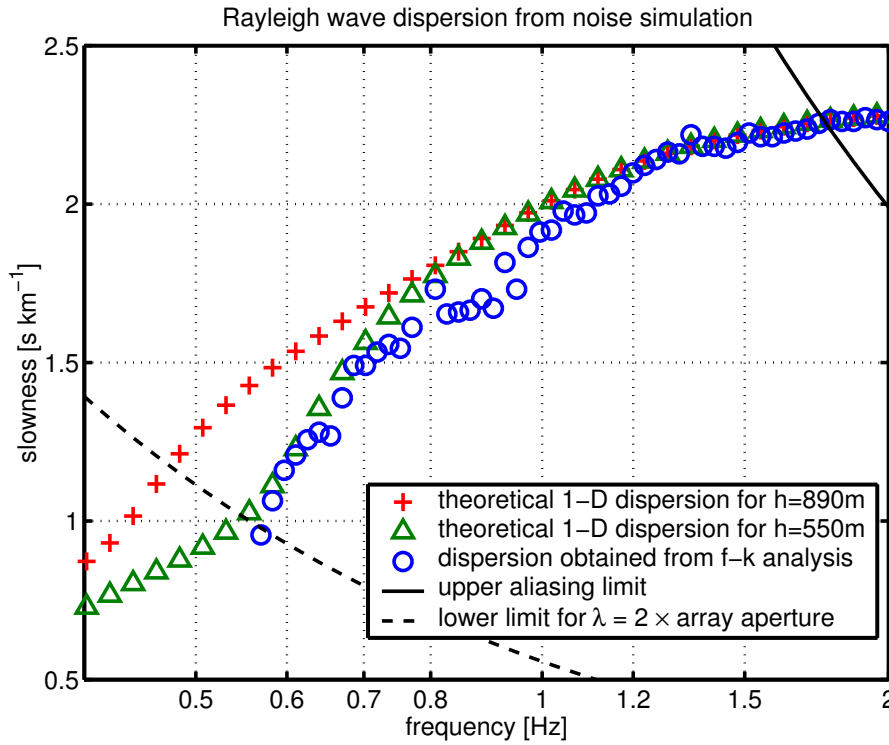


Figure 3.6: Dispersion curve derived from f - k analysis applied to synthetic ambient noise (circles) compared to theoretical 1-D dispersion curve for the soil column at the maximum depth (pluses) and below the array centre (triangles). The solid line shows the upper resolution limit for the array geometry caused by aliasing. The dashed line shows the lower resolution limit for a maximum wavelength corresponding to twice the array aperture.

3.5.2 Inversion of dispersion curve

Assuming that we have some a priori information of the site, we inverted the dispersion curve obtained from the synthetic noise traces in the frequency range between 0.55 and 2 Hz. The inversion algorithm sought for 5-layer velocity models explaining the dispersion curve within the limits given in Table 3.3.

Figure 3.7 shows V_s of the resulting velocity models. The shear-wave velocity of the first two layers and the depth of the second layer are well resolved. Shear-wave velocities of the sediment fill below around 500 m are systematically overestimated by all models with acceptable misfit. This reflects the fact that the synthetic apparent velocities below 1 Hz are significantly lower than Rayleigh phase velocities expected from 1-D analysis of the sediment fill (Fig. 3.6).

Nevertheless, the ambient noise array method works still surprisingly well considering the strong non 1-D structure of the input model. The resolution depth of about 500 meters corresponds to the classical rule of thumb $h \approx \lambda/3$, where λ is the maximum wavelength of 1500 meters obtained from a slowness of about

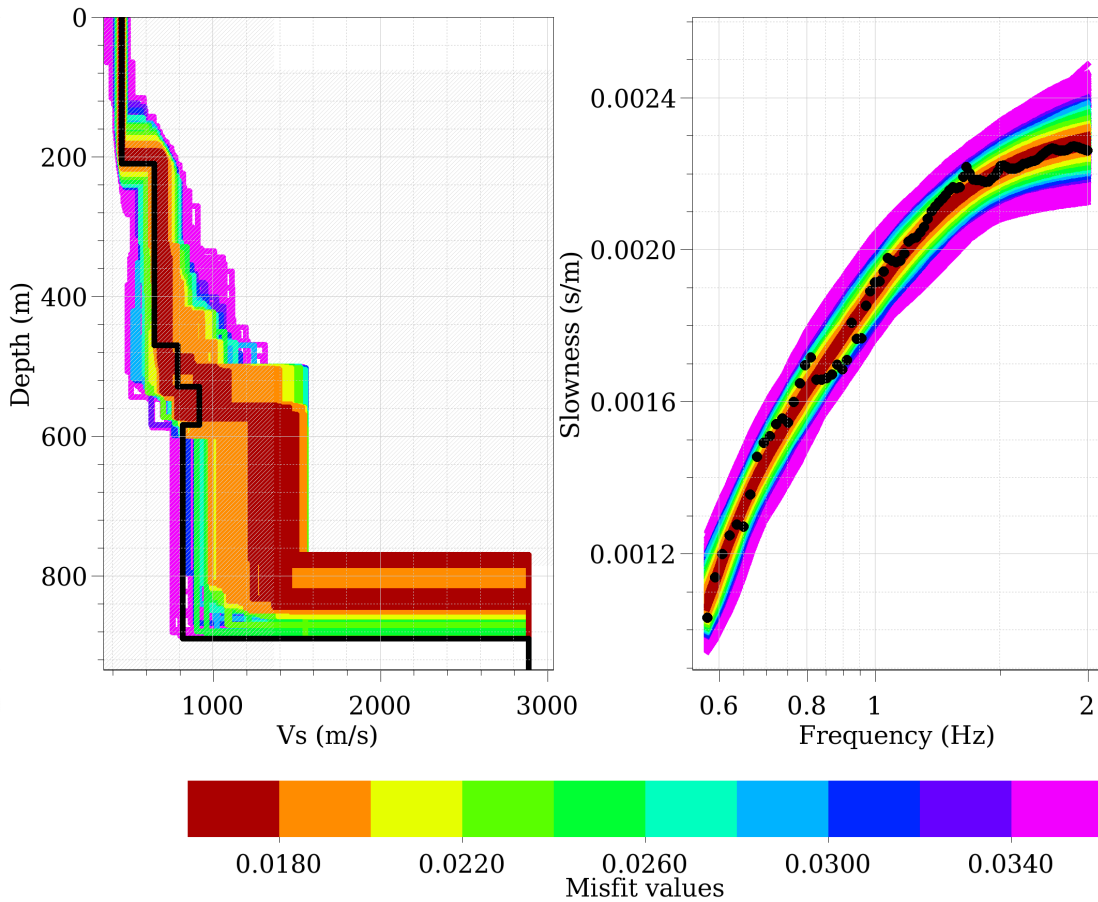


Figure 3.7: Results of inversion of synthetic dispersion data. *Left*: obtained S-wave velocities. Models with an acceptable misfit level of less than 0.02 are plotted darkred and orange. The true velocity model used for the simulation is indicated by the black solid line. *Right*: dispersion data (black dots) and modelled dispersion curves (solid colored lines).

0.0012 s m^{-1} and a frequency of 0.55 Hz. Using only the dispersion curve above 1 Hz would therefore not improve the results but limit the resolution depth to less than 200 meters.

3.5.3 Combined inversion

We will now show results of the combined inversion applied to the synthetic ambient noise dispersion curve. 2-D resonance frequencies for all models were calculated with the three valley parameterisations from Figure 3.2 (right bottom and Table 3.2). For the combined inversion, the depth of the sediment-bedrock interface is fixed to the value of h in the parameterisation in all velocity models.

Because of the discrepancy between theoretical and observed phase velocity

below 1.0 Hz (Fig. 3.6), we only used the dispersion curve between 1.0 and 2.0 Hz for the combined inversion. Figure 3.8 shows the solution for the asymmetrical valley parameterisation. We tried to define an acceptable misfit level such that models with acceptable misfit have computed 2-D resonance frequencies within 0.01 Hz of the observed values (Fig. 3.8 top).

In comparison with the simple inversion of dispersion curves only, the combined inversion greatly improves resolution at depth and provides a useful estimation of shear-wave velocities for the lower sedimentary layers.

For the valley parameterisation shown in Figure 3.8, the bedrock depth was fixed to 770 m, rather than the 890 meters used for the synthetic noise. The other valley parameterisations (Tab. 3.2) allow resolution of shear-wave velocities to greater depth.

3.6 Results of recorded ambient vibrations

Since the combined inversion yields encouraging results when applied to the synthetic ambient noise, we will apply the same method to our recorded noise data.

3.6.1 2-D resonance behaviour

First we analyse the resonance behaviour of the sites by calculating site-to-reference spectral ratios from noise recorded with the linear arrays. Figure 3.9 shows spectral ratios for the Martigny site as a function of frequency and distance along the profile axis in a contour plot. The fundamental mode SV_0 can clearly be identified at 0.32 Hz by a central peak on the component perpendicular to the valley axis and by two peaks and a central node on the vertical component. On the axial component, the fundamental and first higher modes of SH resonance are visible at 0.29 and 0.38 Hz. We assigned the three peaks at 0.43 Hz to the second higher mode of SH. Table 3.4 summarises the resonance frequencies observed at the individual sites. Spectral ratios for the linear profile recorded near Saillon look very similar, but the resonance frequencies are slightly higher here. The resonance frequencies identified at the Vétroz site are also summarised in Table 3.4. Refer to Roten *et al.* (2006) for spectral ratios of the Vétroz linear arrays.

3.6.2 f - k analysis

The frequency-wavenumber analysis was applied to the vertical component of all circular arrays recorded at the three sites. For each frequency, the average and standard deviation of the apparent slowness was obtained by computing f - k spectra for a set of overlapping time windows with frequency-dependent window length. The obtained standard deviation is taken into account for misfit calculation between observed and synthetic dispersion curves.

Figure 3.10 shows the dispersion curves obtained at the three sites. Dispersion curves for Martigny and Vétroz were combined from results of the different aper-

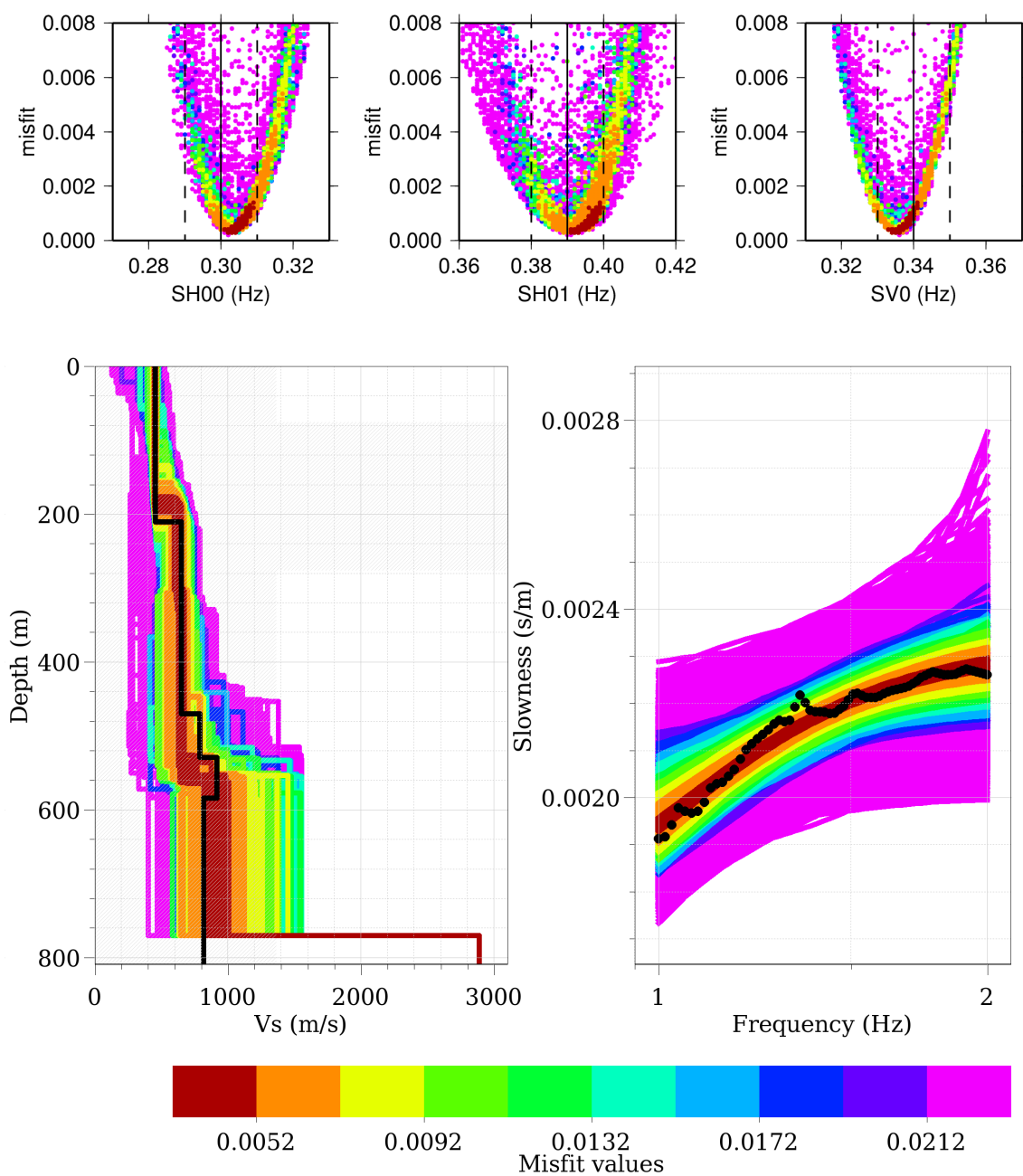


Figure 3.8: Results of combined inversion of the synthetic dispersion curve and 2-D resonance frequencies with the asymmetrical valley parameterisation (Table 3.2). *Top*: 2-D resonance frequencies of the different models as a function of 2-D misfit; the color shade gives the total misfit. *Bottom*: V_s of models and dispersion curves, as for Figure 3.7.

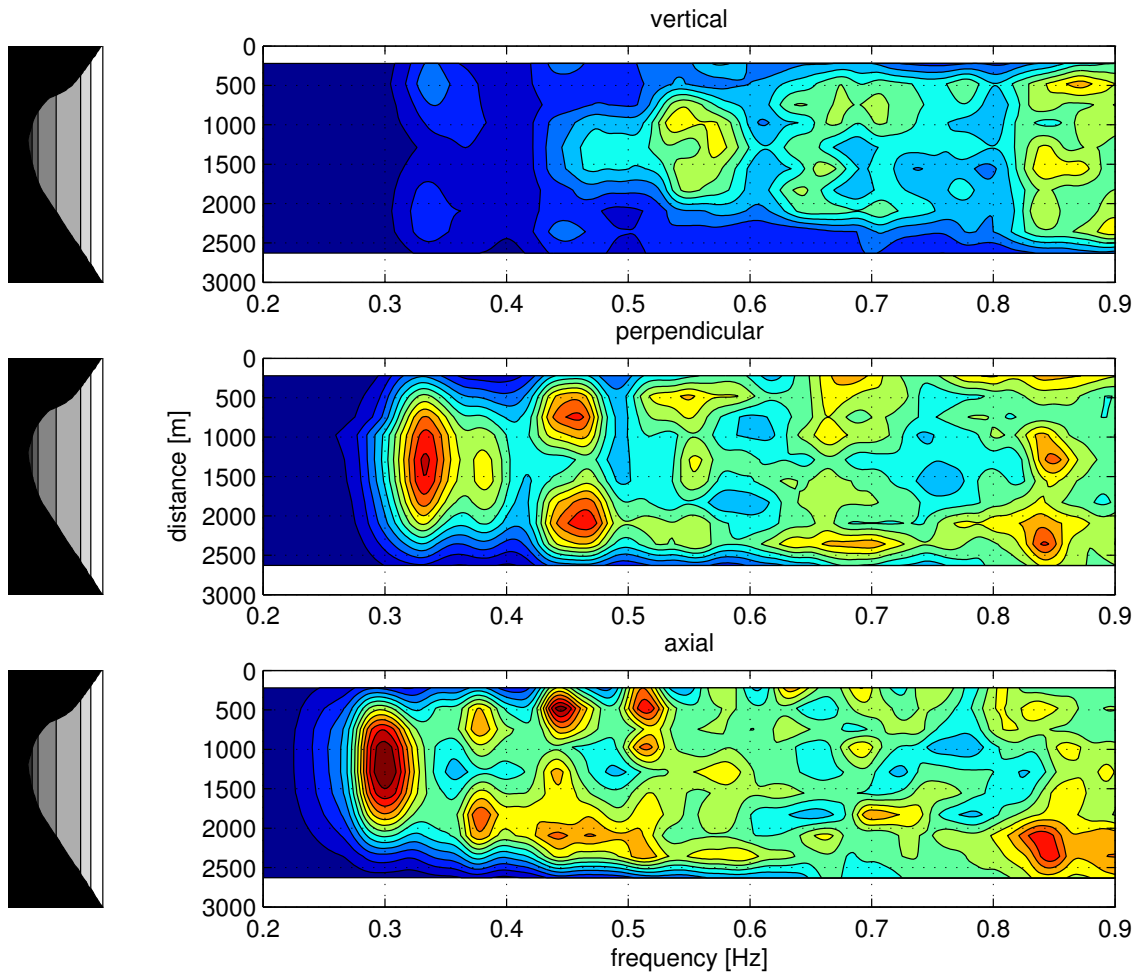


Figure 3.9: Spectral ratios for Martigny as a function of frequency and distance along the profile axis for vertical (*top*), perpendicular (*centre*) and axial (*bottom*) component.

ture arrays, while the curve for Saillon was obtained only from the large array recorded there. The similarity in the apparent slowness suggests that shear-wave velocities of the Rhône sediments are comparable at the three sites. Especially the curves for Saillon and Martigny are almost identical between 0.7 and 3 Hz; the apparent slowness for Vétroz is clearly lower in this frequency range. At Martigny and Vétroz, the apparent slowness increases quickly for frequencies above 4 and 6 Hz. This may indicate the presence of a shallow low-velocity layer, which was also encountered in nearby boreholes.

It's interesting to note that the temporal stability is much better for Saillon and Martigny (and the dispersion curve below 1.5 Hz for Vétroz), where four concentric rings were recorded simultaneously. The apparent slowness for Vétroz, which was determined from concentric circular arrays recorded subsequently, shows systematically larger standard deviations.

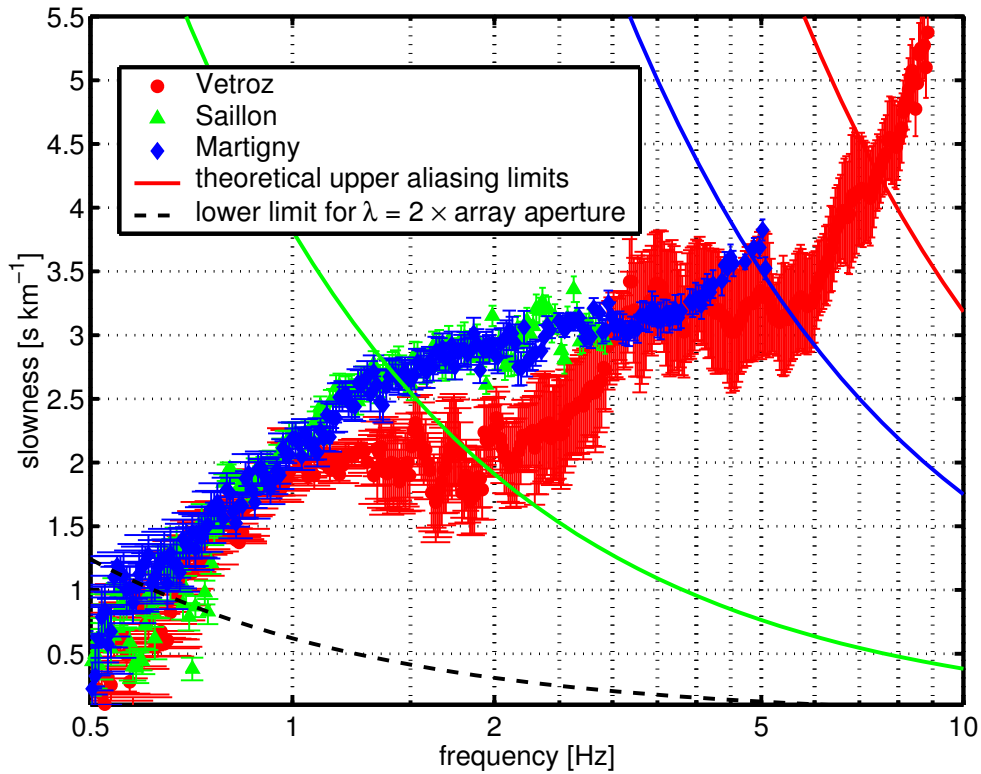


Figure 3.10: Dispersion curves and standard deviations obtained from large and small aperture arrays. The lower resolution limit corresponds to an array aperture of 800 meters. The upper limit was computed from the beampattern of the smallest array at each site.

3.6.3 Inversion of dispersion curves and 2-D resonance frequencies

The parameter limits used for the inversion of observed noise results were similar to the values in Table 3.3. For Martigny and Vétroz, an additional shallow layer of up to 20 meters depth with unknown P- and S-wave velocity was added. We only inverted for velocities of the top 5 to 6 layers, which represent the sedimentary fill of the valley.

Martigny array

Three different valley parameterisations with the asymmetric relation were used (Table 3.2 and Figure 3.2 top Right). Results of the parameterisation using $a=1480$, $h=930$ and $\zeta=-0.25$ are given in Figure 3.11. The solutions with acceptable misfit are explaining the observed dispersion curve very well. All models exhibit a shallow low-velocity layer of 10 meters thickness, with a shear-wave velocity of only around 100 ms^{-1} . The next considerable velocity contrast appears at around

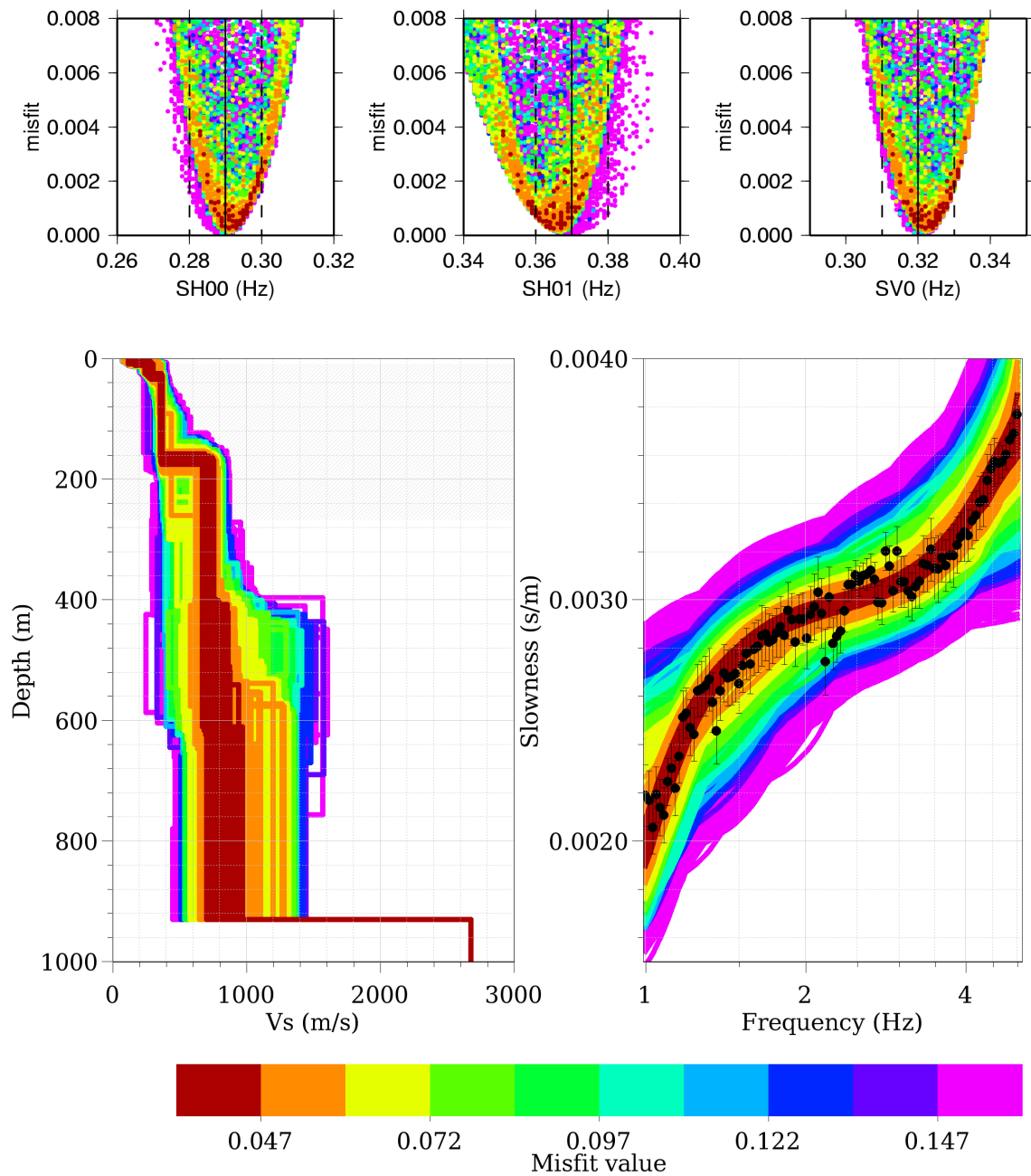


Figure 3.11: Results of the combined inversion for Martigny obtained with the parameterisation 'asym0' (Tab. 3.2). *Top*: 2-D resonance frequencies obtained from the different velocity models as a function of misfit. *Bottom* V_s of models and dispersion curves.

180 meters depth, where the shear-wave velocity rises from around 400 to 700 ms^{-1} . These values are very similar to the geophysical model created by Steimen *et al.* (2003) for Vétroz (Tab. 3.1).

All three parameterisations yield shear-wave velocities between 600 and 800 ms^{-1} for the intermediate part of the sedimentary fill. Shear-wave velocities of the lowermost layers are sensitive to the chosen valley parameterisation and vary between 700 and 1100 ms^{-1} .

The 2-D resonance frequencies of the velocity models with acceptable misfit in Figure 3.11 are well within the uncertainty of the observed values for the three analysed modes SH_{00} , SH_{01} and SV_0 .

Saillon array

Since no small array was recorded at Saillon, we will not be able to resolve the shallow low-velocity structure at this site. We will only invert for a 5-layer model similar to Table 3.3. Because the linear and circular arrays in Saillon were recorded around 500 meters away from the seismic reflection profile, we extracted the sediment-bedrock interface from a 3-D map of the bedrock depth created on the basis of a gravimetric survey (Rosselli, 2001).

Figure 3.12 shows results of the combined inversion using the cosine-shaped valley parameterisation (Tab. 3.2). The resulting shear-velocities are quite similar to the Martigny site, with a strong velocity contrast appearing at about 180 meters depth. Both 2-D resonance frequencies and phase velocities are reproduced well by the velocity models with acceptable misfit.

Vétroz array

Figure 3.13 shows results of the combined inversion for Vétroz obtained for a cosine-shaped valley and $a=1500$, $h=770$ ('cos2' in Fig. 3.2 and Tab. 3.2). Similar to Martigny, a low-velocity layer of about 10 meters thickness can be resolved. A further small velocity contrast appears at around 70 meters, where velocities increase from 350 to around 450 ms^{-1} . Shear-velocities between 70 and 200 meters are therefore slightly higher than at Saillon and Martigny, which reflects the lower apparent slowness between 1 and 3 Hz observed in the dispersion curve (Fig. 3.10). The velocity contrast at about 180 meters is less distinct than at Saillon and Martigny, and V_s is slightly lower for depths between 200 and 500 meters.

Shear-wave velocities in Figure 3.13 are compared with results from shallow S-wave seismics performed near Vétroz and velocities extrapolated from standard penetration tests (SPT) in the Sion area (Frischknecht, 2000). All methods show similar results, though results from seismics and SPT measurements show a more gradual velocity increase for the uppermost layer. These data are only available for depths of less than 200 meters; for the deeper part of the sedimentary fill there are no other studies available that we could compare with our results.

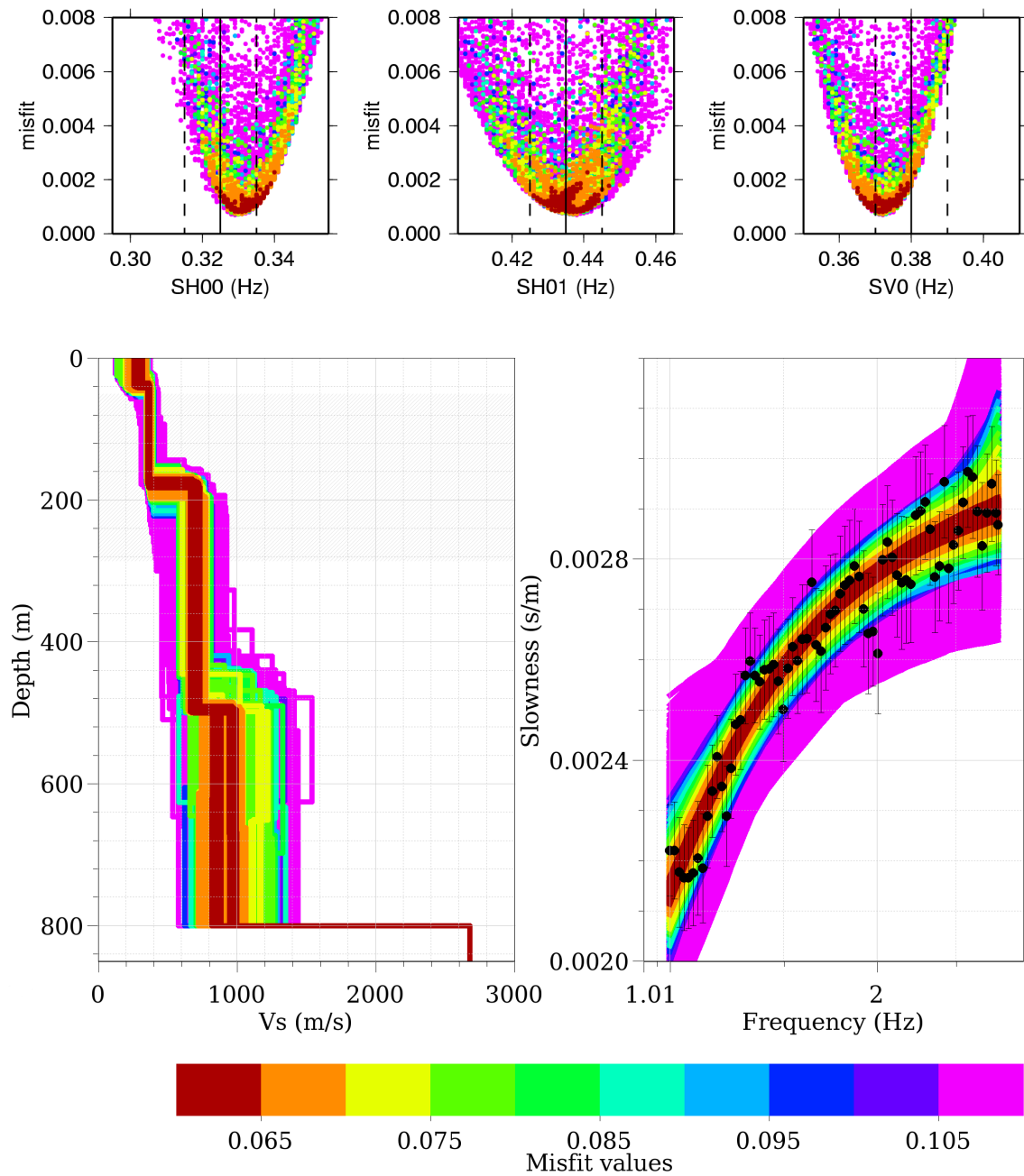


Figure 3.12: Results of the combined inversion for Saillon obtained with the cosine shaped parameterisation. *Top:* 2-D resonance frequencies of the different velocity models as a function of misfit. *Bottom* V_s of models and dispersion curves, as for Figure 3.11

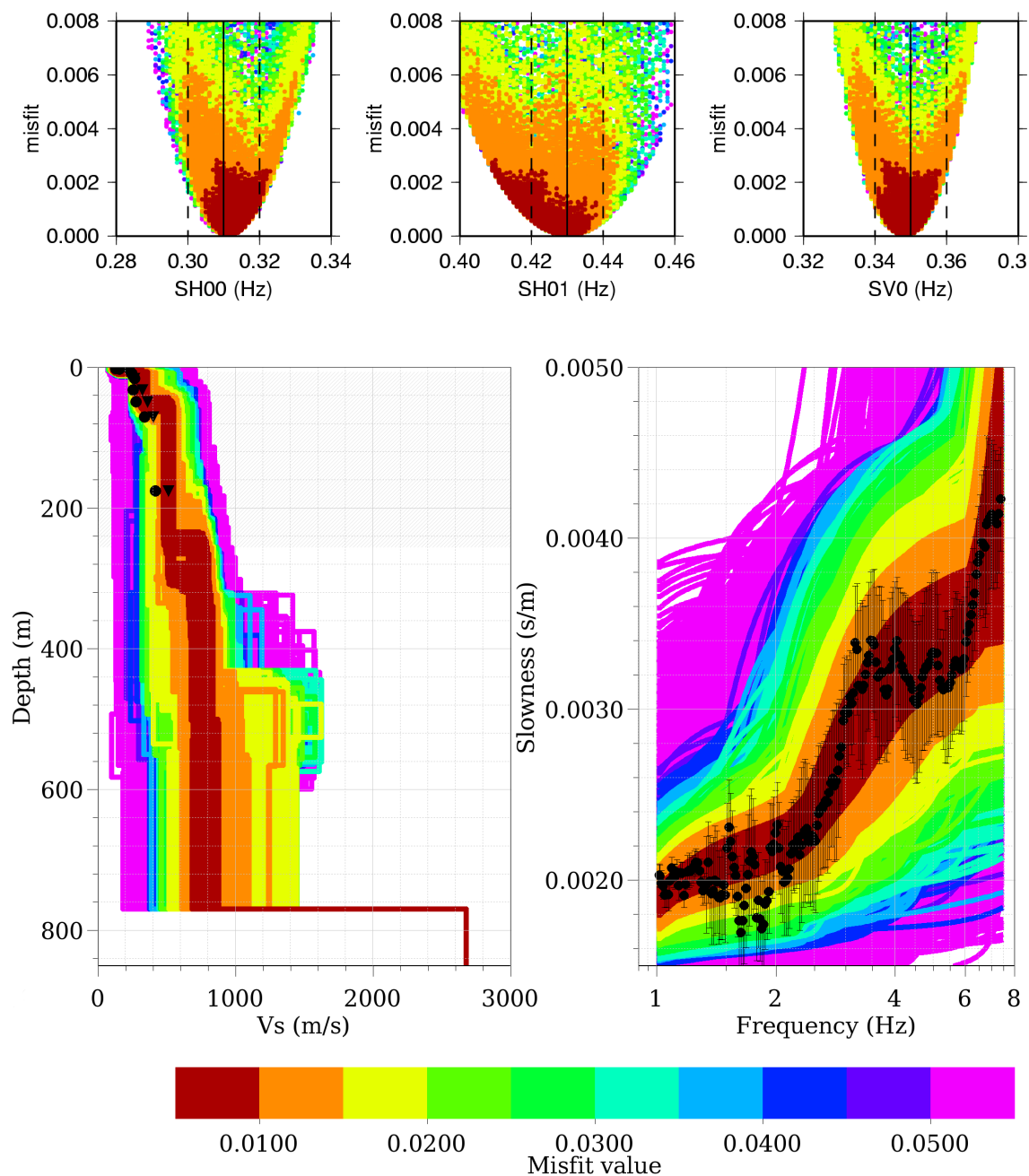


Figure 3.13: Results of the combined inversion for Vétroz obtained with a cosine-shaped parameterisation, $a=1500$ and $h=770$. *Top:* 2-D resonance frequencies of the different models as a function of misfit. *Bottom* V_s of models and dispersion curves. The black circles show results of shear-wave reflection/refraction measurements, the black triangles shear-wave velocities estimated from standard penetration tests (Frischknecht, 2000).

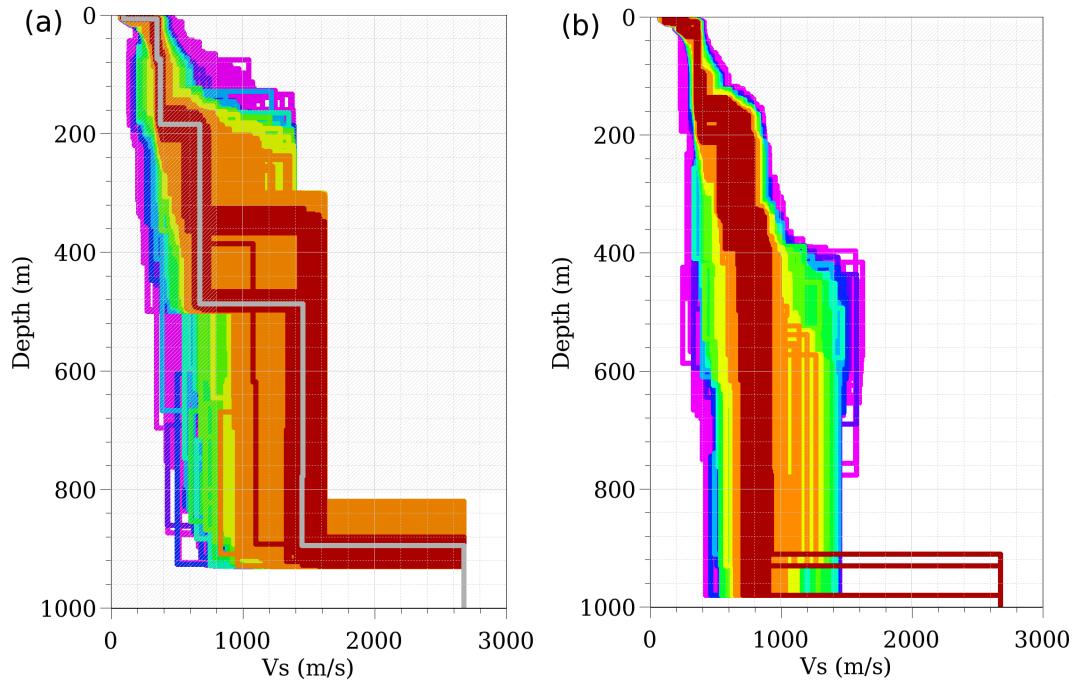


Figure 3.14: Comparison of simple inversion (a) and combined inversions with all three valley parameterisations (b) for Martigny. Models with an acceptable misfit level are plotted darkred.

3.6.4 Discussion

Figure 3.14 compares results of a simple inversion with results of the combined inversion obtained with all three valley parameterisations for Martigny. The simple inversion was done with the same parameter limits as the combined inversion, but without the additional constraint of fitting the observed 2-D resonance frequencies and with the whole dispersion curve down to 0.60 Hz. With the simple inversion (Fig. 3.14 a), velocities are well resolved until the interface at around 200 meters. Below that interface V_s ranges between 500 and 750 ms^{-1} , and for depths of more than 320 meters shear-velocities of up to 1600 ms^{-1} are obtained, which corresponds to the upper limit for this parameter allowed in the inversion.

If we calculate the 2-D resonance frequencies for the best-fitting model obtained by simple inversion for Martigny (grey line in Fig. 3.14 a), we find 0.41 Hz for SV_0 and 0.38 Hz for SH_{00} using the method of Paolucci (1999). These values are significantly higher than the resonance frequencies observed in spectral ratios calculated from ambient noise (Fig. 3.9).

Results from reflection seismics show that P-wave velocities in the sediment do not exceed 2400 ms^{-1} (Pfiffner *et al.*, 1997). A shear-wave velocity of 1600 ms^{-1} would therefore require a V_p/V_s ratio of around 1.5, which is unrealistically low for the unconsolidated sedimentary fill of the Rhône valley. Therefore we have to reject the solutions obtained from simple inversion of dispersion curves,

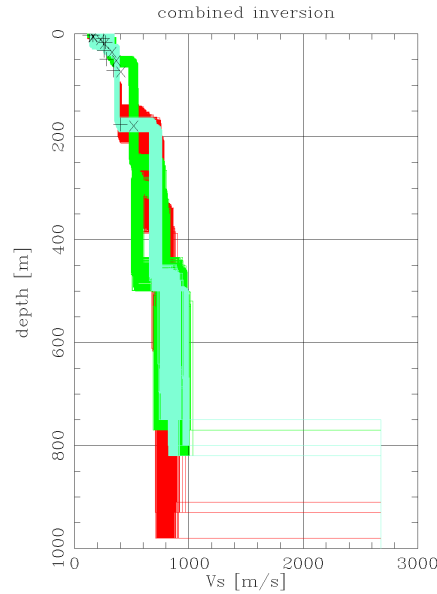


Figure 3.15: Velocity models with acceptable misfit found for Martigny (red), Saillon (cyan) and Vetroz (green) with all valley parameterisations. The black symbols show shear-wave velocities obtained with other methods.

because shear-wave velocities in the lower part of the sediment are definitely overestimated.

The acceptable velocity models obtained from the combined inversion (Fig. 3.14 b) scatter significantly less at depths below 320 meters, and similar velocities are obtained for all three valley parameterisations in the lower part of the sedimentary fill.

The depth of the interface at 200 meters can not be resolved very accurately and depends on the valley parameterisation. This impedance contrast is most likely representing the interface between lacustrine and glaciolacustrine deposits (Tab. 3.1), which appears as a strong reflector in seismic reflection profiles (Pfiffner *et al.*, 1997).

Figure 3.15 compares the acceptable velocity models obtained with all valley parameterisations at three sites. Shear-velocities for Saillon and Martigny are very similar in general, which is in agreement with the similar dispersion curves (Fig. 3.10). At Vétroz slightly higher velocities are encountered for the top 200 meters, and the depth of the next velocity contrast is sensitive to the chosen valley parameterisation. Our results suggest that shear-wave velocities inside the sedimentary fill are not exceeding 1000 ms^{-1} , but we can not exclude that they are as low as 700 ms^{-1} down to the sediment-bedrock interface.

In order to create a geophysical model of the Valais area, we tried to assign a shear-wave velocity to each layer identified from reflection seismics (Tab. 3.5). Our results show that the shear-wave velocities in the initial velocity model from

depth [m]	v_s [ms^{-1}]	geologic interpretation
0	100 – 200	uppermost layer
5 – 10	320 – 375	deltaic sediments
65 – 100	385 – 500	lacustrine deposits
175 – 210	500 – 800	glaciolacustrine deposits
350 – 500	700 – 1000	meltout and reworked till
550 – 800	700 – 1000	subglacial deposits

Table 3.5: Shear-wave velocities assigned to individual layers from results of the combined inversion (Fig. 3.15) at all sites. The uncertainties reflect the scatter within the acceptable velocity models and the variability of the velocity at the three sites.

Steimen *et al.* (2003, Tab.3.1) represent a good estimate.

3.7 Conclusion

In comparison with the simple inversion of dispersion curves, the additional constraint of the observed 2-D resonance frequencies significantly improves resolution at depth. Inversion of only dispersion curves would lead to poor resolution and overestimation of shear-wave velocities at depths below around 300 meters due to the 2-D structure of the site. Inversion of the 2-D resonance frequency helps to overcome this problem, and allows to estimate shear-wave velocities at depths not accessible by the inversion of only dispersion curves.

Acknowledgments

We thank the authors of the programs developed within the SESAME project that were used during this study, including Peter Moczo and Josef Kristek for their FD code (NOISE), and Matthias Ohrnberger (cap) and Fortunat Kind (capon routine) for the software employed to calculate f - k spectra. We thank Marc Wathelet for providing the code of the inversion program and for his support in implementing the combined inversion. The numerical code used for the calculation of 2-D resonance frequencies was kindly provided by Roberto Paolucci. Stefan Fritsche, Philipp Kästli-Krushelnytskyj and Marc Lambert helped in the field. The authors wish to thank two anonymous reviewers for many valuable remarks that helped to improve the paper. This research is part of the Interreg project SISMOVALP and the project SHAKE-VAL, funded by the Swiss National Science Foundation (No. 200021-101920 and 200020-109177).

Chapter 4

Site effects in the Rhône valley analysed from weak motion records and numerical simulations

D. Roten¹, D. Fäh¹, K. B. Olsen² and D. Giardini¹

¹ Institute of Geophysics, ETH Hönggerberg, 8093 Zürich, Switzerland.

² Department of Geological Sciences, San Diego State University, San Diego, California, USA

Submitted to *Geophys. J. Int.* on 2007 July 11

Summary

Site effects in the city of Sion in the Rhône valley are analysed from weak motion signals recorded on a dense temporary array. We simulate the recorded events with a 3-D finite difference method for frequencies up to 4 Hz using a recently developed velocity model of the Sion basin.

Site-to-reference Fourier spectral ratios are computed from 16 local and regional events. All sites exhibit amplification factors of up to 12 between 0.5 and 0.6 Hz, which can be reproduced by the numerical simulations. By rotating the weak motion to directions parallel and perpendicular to the valley axis we show that this low-frequency amplification is caused by the SH_{00} and SV_0 fundamental modes of 2-D resonance.

Additional peaks of amplification can be observed at higher frequencies, with amplification factors of up to 20 at some sites.

Application of the high-resolution frequency-wavenumber and the multiple signal characterisation method to the vertical component of recorded and simulated signals show that edge-generated surface waves arriving from almost all directions dominate the wavefield at 1.25 and 2.50 Hz.

Peak ground velocities computed from the simulated ground motion show interference patterns that depend strongly on the incidence direction, and the computed amplification of peak ground velocities are generally in agreement with the observations.

We conclude that the complex 3-D geometry of the basin needs to be considered to evaluate site effects up to at least 2.5 Hz.

Key words: Rhône valley, earthquake site effects, sedimentary basin, finite-difference methods, seismic array, spectral analysis

4.1 Introduction

The impact of local ground motion amplification on earthquake damage was demonstrated during many recent damaging earthquakes. In some cases, the trapping of waves in horizontally layered media has been able to explain the observed ground motion and increased damage (e.g. Hough *et al.*, 1990). If lateral heterogeneities are present, as in the case of 2-D or 3-D structures, this trapping will also affect surface waves. A common example of such 3-D structures are sedimentary basins filled with unconsolidated low-velocity deposits. Many numerical studies of seismic wave propagation in 2-D and 3-D basins have shown that basin edges play a major role in amplifying ground motion (e.g. Bard and Bouchon, 1980a,b, 1985; Frankel and Vidale, 1992; Olsen *et al.*, 2006). There is also good observational evidence for basin-edge-generated surface waves and for basin-focusing effects on ground motions. (Frankel *et al.*, 2001; Joyner, 2000). A well-known example includes the damage belts reported after the 1995 Kobe earthquake (Kawase, 1996).

In the framework of the SHAKE-VAL project, we are studying earthquake site effects in the Rhône valley, which is located in the area of the highest seismicity in Switzerland. The Valais region was struck by several large earthquakes in the last centuries, e.g. the 1946 M 6.1 earthquake of Sierre and the 1855 M 6.5 and 1755 M 6.1 earthquakes of Visp and Brig. Since the last large earthquake of 1946 the area has undergone extensive development, especially on the soft unconsolidated Rhône sediments, raising concern about the impact of site effects during future earthquakes.

Only a few studies on earthquake site effects in the Rhône valley have been published. Frischknecht *et al.* (2005) performed 2-D numerical simulations with the indirect boundary element method for a set of profiles below the city of Sion. They found that the largest amplification will occur at frequencies between 0.5 and 0.8 Hz due to the 2-D resonance of the deep basin; for the central valley they predicted amplification factors of up to 12. However, these findings have not yet been verified by earthquake observations, because only a few high-quality earthquake records have been acquired on the unconsolidated deposits of the Rhône valley.

In this study we analyse the site response of the Rhône valley from earthquake signals recorded on a dense temporary array of weak motion seismometers. We will quantify the average amplification by computing site-to-reference spectral ratios from a number of local and regional events.

To aid interpretation of our results we simulated 3-D wave propagation in the Sion basin with the 3-D finite difference method. These simulations were conducted with a recent velocity model that has been developed for the central Valais area. Shear-wave velocities in this model are based on results from ambient noise array measurements. We model four of the recorded events and compare synthetic site-to-reference spectral ratios with the observations to assess the reliability of the newly developed velocity model. We apply a frequency-wave number method to the synthetic and observed earthquake signals to estimate the direction of origin of seismic waves at the peak frequencies of amplification.

Additionally we perform a simulation of the 1946 M 6.1 Sierre main shock to estimate the importance of site effects during this historical earthquake. Finally we compute peak ground velocities from all simulations to analyse the interference patterns and identify the effects generating the peak amplifications.

4.2 Geophysical setting

The Rhône valley is a deeply eroded glacial valley filled with unconsolidated Quaternary deposits (Fig. 4.1). The structure of the sediment-bedrock interface is constrained from seismic reflection profiles (Pfiffner *et al.*, 1997; Besson *et al.*, 1993) and from gravimetric studies (e.g. Rosselli, 2001). The thickness of the sedimentary fill reaches up to 1000 meters at some places; below the city of Sion the basin is about 500 meters deep and less than 2000 meters wide.

In order to assess site effects in the Rhône valley with numerical simulations, an accurate geophysical model of the site is required. Because a leading cause of amplification is the trapping of S- and surface waves in the sediments, the shear-wave velocity is the most important parameter in the geophysical model. To improve the estimates of shear-wave velocities in the unconsolidated deposits a series of ambient noise array measurements was carried out at different sites in the Rhône valley. Figure 4.2 shows examples of shear-wave velocities obtained from ambient noise recorded at four representative sites.

Circular array layouts with apertures of up to 800 meters were used to estimate apparent Rayleigh wave phase velocities with the high-resolution frequency-wavenumber method (Capon, 1969; Kind *et al.*, 2005). However, dispersion curves alone can not be used to estimate shear-wave velocities in the deeper part of the basin, because standing waves evoked by 2-D resonance dominate at low frequencies (Roten *et al.*, 2006). This violates a basic supposition of the method, which requires that horizontally propagating surface waves dominate the noise wavefield.

Analysis of noise recorded on linear arrays running perpendicular to the valley axis allows definition of the different 2-D resonance frequencies. Together

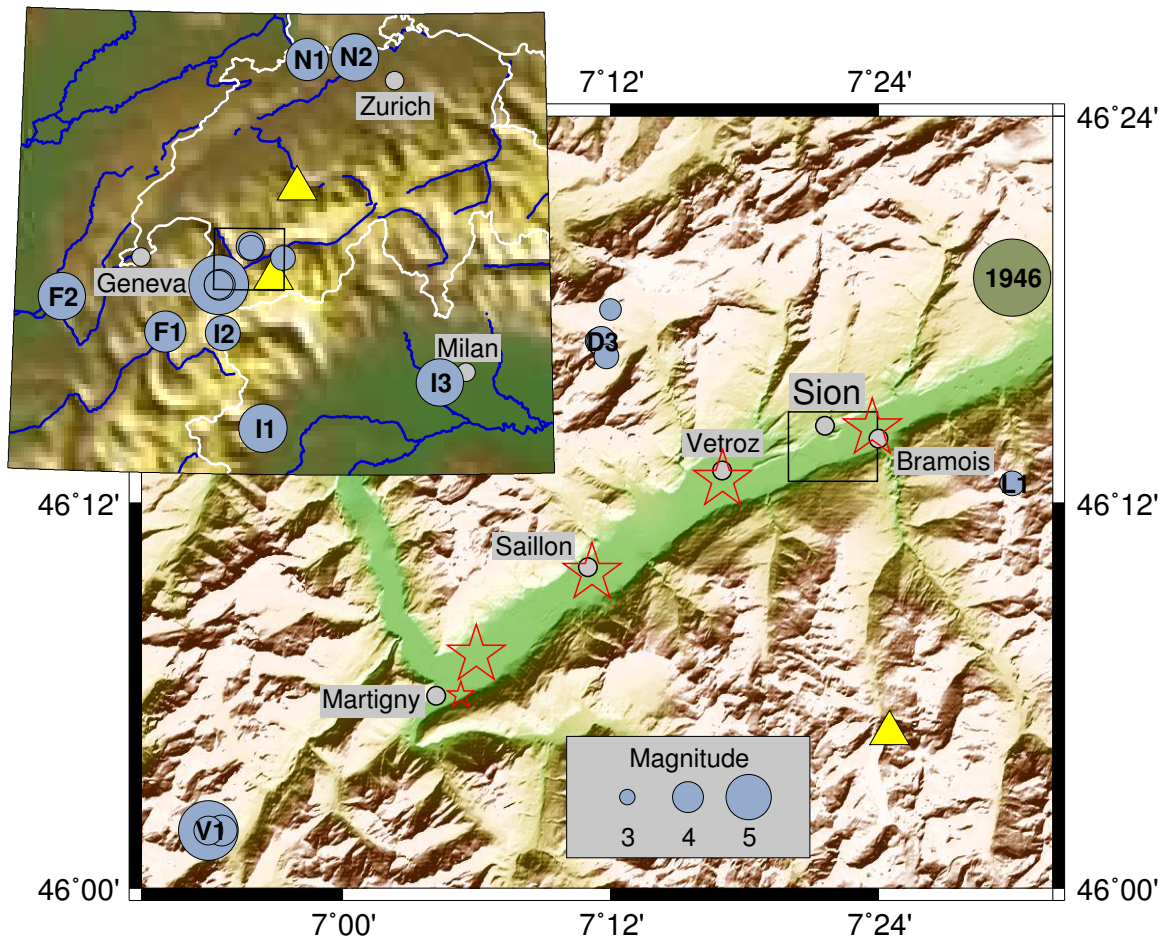


Figure 4.1: Map of the Rhône valley. Red stars show locations of ambient noise array measurements, yellow triangles the position of the broadband stations WIMIS and DIX. Epicentres of recorded earthquakes are plotted with blue circles; the green circle shows the epicentre of the 1946 Sierre earthquake.

with the dispersion curves obtained from circular arrays, these 2-D resonance frequencies are inverted for the shear-wave velocities of the unconsolidated deposits (Roten and Fäh, 2007). For this method, the forward problem of computing the 2-D resonance frequencies is solved by Rayleigh's principle with a method proposed by Paolucci (1999). The combined inversion improves the resolution in the lower part of the sedimentary fill, and it has successfully been tested on a synthetic ambient noise dataset (Roten and Fäh, 2007). Such combined inversions were performed at three sites west of Sion, near the towns of Vétroz, Saillon and Martigny (Fig. 4.1). Additionally, circular arrays were recorded on the Bramois alluvial fan, in the old town of Sion and in the vicinity of the three permanent

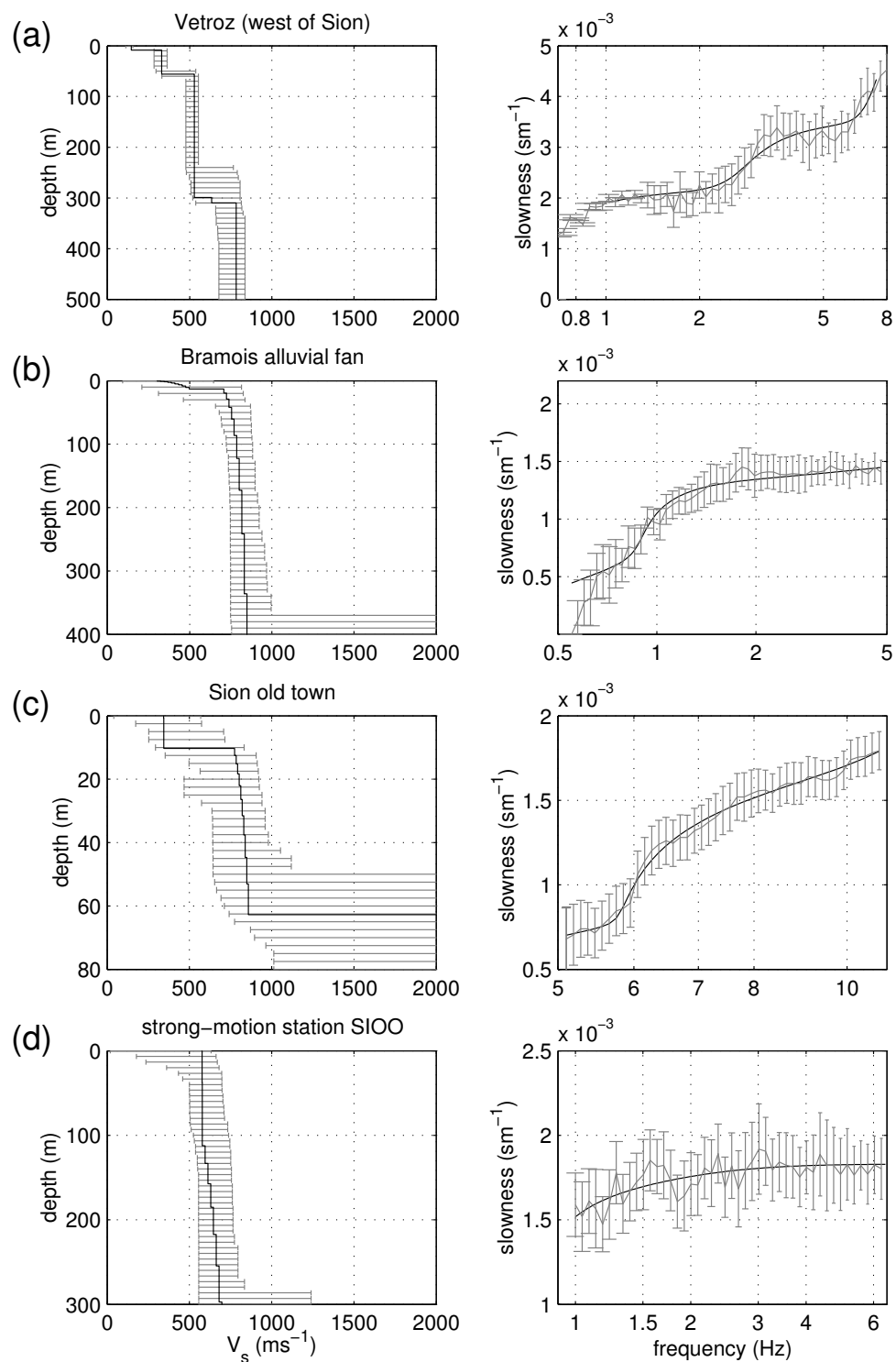


Figure 4.2: Inversion results obtained from array measurements of ambient noise in the Sion region. *Right:* measured dispersion curves with standard deviations (grey) and dispersion curves for the best-fitting velocity model (black). *Left:* Shear-wave velocities obtained from inversion. Errorbars are showing the velocity range contained in models with acceptable misfit.

strong-motion stations SIOV, SIOO and SIOM (Fig.4.3). We used the *geopsy*¹ program package (Wathelet *et al.*, 2004) for frequency-wavenumber analysis and for inversion of dispersion curves.

On the basis of array measurements performed at different parts of the Rhône sediments, the analysed sites can roughly be subdivided into two categories:

- (i) *fine lacustrine and deltaic deposits* (Martigny, Saillon and Vétroz, Fig. 4.2 a): At these sites a very shallow low-velocity layer (less than 15 meters deep) with shear-wave velocities as low as 100 ms^{-1} was resolved. Below this layer, V_s ranges between 320 and 500 ms^{-1} until about 250 meters depth, where a strong velocity contrast occurs, and V_s increases to 650 to 800 ms^{-1} . Shear-wave velocities in the lowest part of the sediment are in the range between 700 and 1000 ms^{-1} (refer to Roten and Fäh, 2007, for detailed results).
- (ii) *alluvial fans* (old town of Sion, Bramois, Figure 4.2 b, c): Apart from a shallow low-velocity layer, shear-wave velocities are much higher at these sites, with values of more than 600 ms^{-1} measured close to the surface.

It is therefore important to include the type of the sedimentary deposit in the velocity model. We extracted the outline of the alluvial fans from geologic maps of the central Valais area to define regions of higher shear-wave velocities inside the sedimentary fill (Figure 4.3).

Results from additional arrays recorded in the Sion area suggest that there is no sharp transition between fine lacustrine and coarse alluvial deposits. Shear-wave velocities measured near the strong-motion station SIOO (Fig. 4.2 d) and the temporary station SIOVE are not as large as those recorded on the top of the nearby alluvial fans, but clearly higher than in the fine deposits encountered in Martigny and Vétroz (west of Sion). Borehole data available for the Sion area reveal alternating layers of coarse alluvial gravel and fine sands. This implies that the velocity decreases gradually with increasing distance from the alluvial fans. In order to obtain a smooth decrease between these two deposit types, a transition zone was introduced within a predefined distance of the fan boundaries (Fig. 4.3). Within this transition zone the velocity decreases linearly with the shortest distance to the fan outline.

The depth of the sediment-bedrock interface was extracted from analog maps published by Frischknecht and Wagner (2004) and Rosselli (2001). Figure 4.3 shows contour lines of topography, bedrock depth and the positions of the permanent and temporary stations. The geophysical parameters of the different materials that compose our velocity model are listed in Table 4.1. Shear-wave velocities of the sedimentary fill in our model are significantly lower than the constant 800 ms^{-1} used by Frischknecht *et al.* (2005), especially for the fine lacustrine and deltaic deposits. P-wave velocities in table 4.1 are derived from seismic reflection results (Pfiffner *et al.*, 1997), and densities are provided from gravimetric studies (Rosselli, 2001). Quality factors are based on a velocity model developed by

¹available at <http://www.geopsy.org>

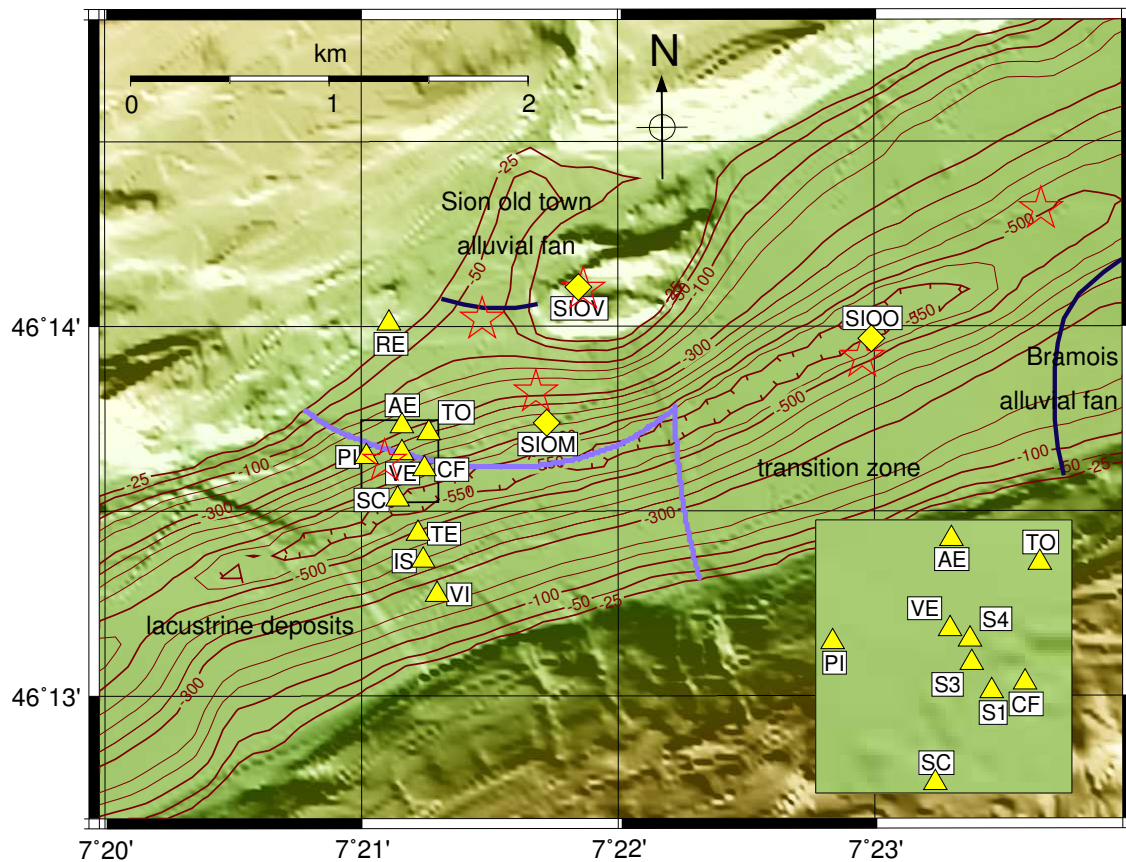


Figure 4.3: Bedrock depth (brown contours) and topography (colour shades) of the Sion area. Diamonds indicate the positions of the permanent strong-motion stations, triangles show receiver positions of the temporary array (station names are provided without the prefix 'SIO'). Darkblue and lightblue thick lines show the outline of alluvial fans and the transition zone, respectively. Stars are showing the central position of ambient noise array measurement performed in the area.

(Steimen *et al.*, 2003). The P- and S-wave velocity of the bedrock was taken from the literature (e.g. Maurer, 1993; Baumann, 1994).

4.3 Method

4.3.1 Weak motion records

A temporary network of up to 13 weak motion seismometers was installed in the town of Sion to quantify the level of amplification. The temporary network was operative during two recording periods: The first installation was maintained from April 2004 to October 2004, the second deployment lasted from June 2005 until April 2006. The first deployment consisted of 13 stations, while only 9 seis-

z	V_p	V_s	ρ	Q_p	Q_s	geological interpretation
0 – 225	1700	700	1700	25	25	alluvial fans
0 – 75	1600	320	1600	25	25	deltaic sediments
75 – 225	1900	480	1900	25	25	lacustrine deposits
225 – 400	1900	750	1900	25	25	glaciolacustrine deposits
400 – 500	1900	800	1900	25	25	meltout and reworked till
500 – 560	2000	900	2000	25	25	subglacial deposits
0 – 750	4000	2325	2500	100	100	bedrock

Table 4.1: Geophysical parameters of the different materials in the velocity model. Depth ranges z are in m, velocities V in ms^{-1} and densities ρ in kgm^{-3} . Geological characterisations correspond to the interpretation by Pfiffner *et al.* (1997).

Station	Longitude (°E)	Latitude (°N)	Elevation (m)	Sensor	Network
SIOV	7.364098	46.235095	558	ES-T	2
SIOO	7.383156	46.232776	495	ES-T	2
SIOR	7.351785	46.233476	514	3D/5s	1
SIOAE	7.352648	46.228850	488	3D/5s	1,2
SIOVE	7.352625	46.227627	487	3D/5s	1,2
SIOTO	7.354382	46.228524	488	3D/5s	1,2
SIOPI	7.350330	46.227448	486	3D/5s	1,2
SIOCF	7.354086	46.226901	489	3D/5s	1,2
SIOS1	7.353442	46.226784	488	3D/5s	1
SIOS3	7.353045	46.227164	488	3D/5s	1
SIOS4	7.353013	46.227484	488	3D/5s	1
SIOSC	7.352339	46.225536	486	3D/5s	1,2
SIOTE	7.353680	46.223987	485	3D/5s	1,2
SIOIS	7.354006	46.222773	486	3D/5s	1,2
SIOVI	7.354915	46.221244	485	3D/5s	1,2

Table 4.2: Positions of permanent strong-motion accelerometers and temporary weak-motion seismometers. The last column shows the deployment period of the stations (1: first recording period from April 2004 to October 2004, 2: second period from May 2005 to April 2006).

ometers were available for the second installation (Tab. 4.2). Additionally the two permanent strong-motion stations SIOV and SIOO were upgraded with continuous 24-bit digitisers to complement the second temporary network.

All temporary stations were equipped with Lennartz 3D/5s seismometers with a natural period of 5 seconds; the strong-motion stations SIOO and SIOV use an Episensor ES-T force-balance accelerometer, which has a flat response between DC and 50 Hz. This configuration allows us to analyse the deep resonance

ID	Origin time	Lon. (°E)	Lat. (°N)	Mag. (M_L)	Location	AZ (°)	Δ (km)
D1	2004.05.03 23:14	7.2	46.3	2.4	Derborance, VS	305	14
I1	2004.05.14 00:30	7.33	45.10	4.2	Condove, I	181	125
D2	2004.05.30 07:20	7.191	46.284	2.7	Derborance, VS	297	14
D3	2004.05.30 09:46	7.193	46.284	2.9	Derborance, VS	297	14
I2	2004.06.12 04:44	6.947	45.717	3.3	Pré St. Didier, I	209	66
D4	2004.06.12 16:47	7.197	46.276	2.6	Derborance, VS	294	14
N1	2004.06.21 23:10	7.713	47.505	3.8	Liestal, BL	11	143
N2	2004.06.28 23:42	8.169	47.525	4.0	Brugg, AG	23	155
V1	2005.09.08 11:27	6.897	46.032	4.9	Vallorcine, F	238	43
V2	2005.09.08 11:53	6.905	46.031	3.0	Vallorcine, F	237	43
V3	2005.09.08 14:10	6.897	46.033	2.9	Vallorcine, F	238	43
F1	2005.10.31 03:40	6.41	45.72	3.7	Albertville, F	233	91
N3	2005.11.12 19:31	8.166	47.523	4.1	Brugg, AG	23	155
I3	2005.11.20 10:48	8.96	45.40	4.1	Milan, I	126	155
F2	2006.01.11 10:32	5.44	45.93	4.1	Blanaz, F	258	147
L1	2006.03.18 22:49	7.50	46.21	2.6	Vissoie, VS	99	12

Table 4.3: Characteristics of the events recorded on the temporary network.

of the basin, which is expected at periods longer than 1 second (Frischknecht *et al.*, 2005). The sampling rate was set to at least 100 samples per second. GPS signals were used for time synchronisation.

The temporary station SIORE was deployed on a well-defined bedrock site on the northern margin of the basin and will be used as a reference station for the first deployment period; for the second installation the strong-motion station SIOV will serve as reference site.

Six of the temporary receivers (SIOAE, SIOVE, SIOSC, SIOTE, SIOIS and SIOVI) were arranged along a profile running perpendicular to the valley axis (Fig. 4.3) to study the variability of the amplification with distance from the valley edges. Three more stations (SIOTO, SIOCF and SIOPI) were installed on the north side of the profile to form a roughly circular array. For the first installation, the network was complemented with an inner array (SIOS1, SIOS3, SIOS4) to improve the resolution of frequency-wavenumber methods at higher frequencies (enlarged section in Figure 4.3).

Since the seismicity in the region is quite moderate and the noise level in the city was rather high, only few earthquakes provided an useful signal-to-noise ratio in the frequency range of interest (0.2 to 10 Hz). Table 4.3 lists the source parameters of the events discussed in this text.

During the first recording period in 2004 a sequence of more than 170 detected events occurred near Derborance, at 14 km epicentral distance from Sion (Baer *et al.*, 2005). For this study we will use the four strongest events of the se-

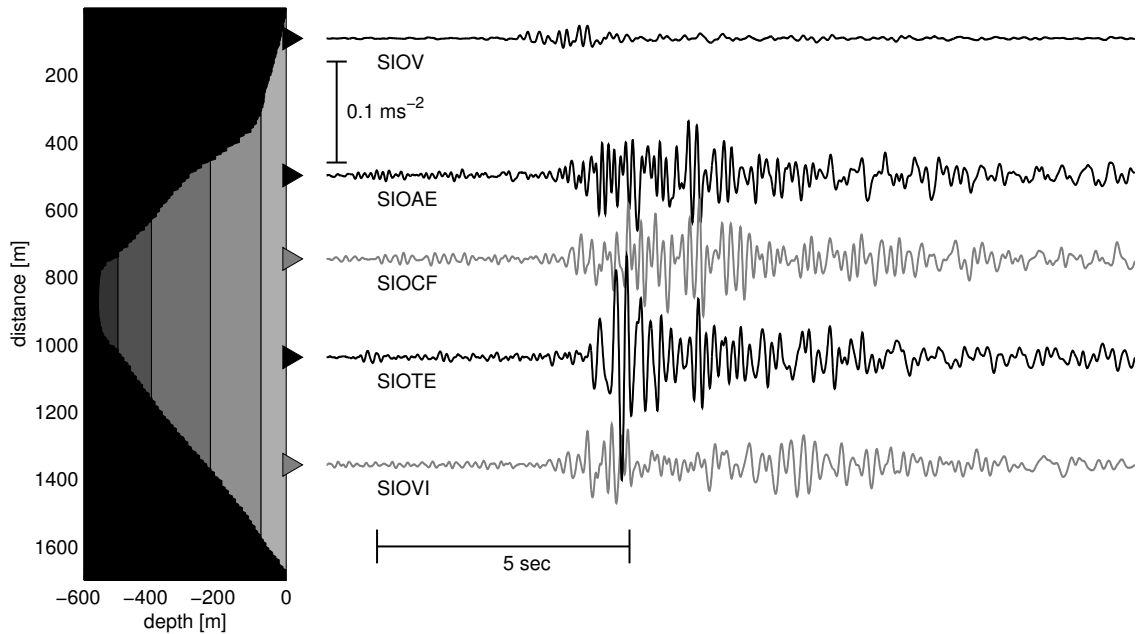


Figure 4.4: Accelerograms on reference site (top) and on the Rhône sediments recorded after the M_L 4.9 Vallorcine main shock. Seismograms were rotated to the direction perpendicular to the valley axis and low-pass filtered below 5 Hz.

quence, which reached magnitudes between 2.4 and 2.9 (Tab. 4.3). Additionally two events with local magnitudes of 3.8 and 4.0 occurred in northern Switzerland, within 155 km epicentral distance of the network, which provided useful signals. We will also analyse two events with magnitudes of 4.2 and 3.3 located in northern Italy at 125 and 66 km epicentral distance, respectively.

During the second deployment period, on September 8th 2005, a M_L 4.9 event occurred near Vallorcine (France), at an epicentral distance of 43 km from the array (Deichmann *et al.*, 2007). Figure 4.4 compares seismograms from stations located on the unconsolidated sediments, including the reference station. Two aftershocks which reached a magnitude of ~ 3.0 will also be included in the analysis. Unfortunately the station SIOSC in the valley center was not operative during this series. Four more events with local magnitudes between 3.7 and 4.1 were recorded within a radius of 155 km of the network (Tab. 4.3); additionally a local M_L 2.6 event was detected 12 km SE of Sion. All available signals from the events given in Table 4.3 will be used to estimate amplification levels.

4.3.2 3-D finite difference simulations

The seismic response of the Sion basin was simulated with the 3-D finite difference method using a code developed by Olsen (1994). The 3-D viscoelastic equations of motions are solved with the staggered-grid velocity-stress finite-difference scheme; the accuracy is 4th order in space and 2nd order in time. Vis-

coelasticity is modeled with a coarse-grained implementation of the memory variables for a constant Q solid.

The geophysical model (Tab. 4.1) was discretized with a grid spacing of 12.5 meters, which allows us to propagate frequencies up to 4 Hz using 6.4 grid points for the shortest shear-wavelength. At the sides of the computational domain, we applied absorbing boundaries of 20 grid points width which were padded with an attenuative material (Cerjan *et al.*, 1985).

The full model consists of $450 \times 360 \times 80$ nodes and covers a volume of $5625 \times 4500 \times 1000$ meters. The section shown in Figure 4.3 corresponds to the surface of the computational area without the absorbing boundaries. The simulations were run on a 128-processor 2.4 GHz Linux cluster at San Diego State University. We simulated 20 seconds of wave propagation using a timestep of 0.0015 seconds. With this configuration, one computation requires about 8 hours wallclock time using 20 CPU's.

In this study we will focus on modelling the response of the basin to four observed earthquakes. Since the hypocenters of those sources are far away from the computational area, we specified the sources by imposing seismograms along the bottom plane of the grid. The input signal on each grid point was delayed by the shear-wave traveltime of the bedrock and the corresponding direction of incidence to generate a plane wave. We used seismograms of the selected events recorded on permanent broadband stations (of the Swiss Digital SDSNET) as input velocity. The seismograms were low-pass filtered with a corner frequency of 3.5 Hz with a 3rd order two-pass butterworth filter.

We simulated four of the observed earthquakes to analyse the valley response to waves arriving from different directions. The main shock of the Vallorcine sequence (V1 in Tab. 4.3) was modelled with the signal from the permanent broadband station DIX, which is located south of Sion (Fig. 4.1). Figure 4.5 shows snapshots of simulated ground velocities which are discussed below. We also modelled the strongest M_L 2.9 event (D3) of the Derborance series. For this simulation seismograms acquired on the temporary station SIORE were used as input signal. The M_L 4.0 event of Brugg (N2) was simulated to represent the three events located in northern Switzerland, using a record from the broadband station WIMIS north of Sion. For the simulation of event I3 the seismogram recorded on the broadband station DIX served as input signal.

Additionally we simulated the historical M6.1 Sierre earthquake of January 25 1946. Wanner (1955) determined the location of the main shock from the few stations that were operating at that time. The epicentre was determined at $46^\circ 19' N$ and $7^\circ 30' E$, approximately 15 km ENE of Sion (Fig. 4.1). The source mechanism is not known. Because no records are available we queried the European strong-motion database (Ambraseys *et al.*, 2001) for a signal with a comparable frequency content. We chose a seismogram of the 1976 M_s 6.5 Friuli earthquake recorded at the station Tolmezzo-Diga Ambiesta, a rock site located 23 km from the rupture. As with the other simulations the source was implemented with a plane wave arriving from the hypocentral direction. In order to match the lower magnitude

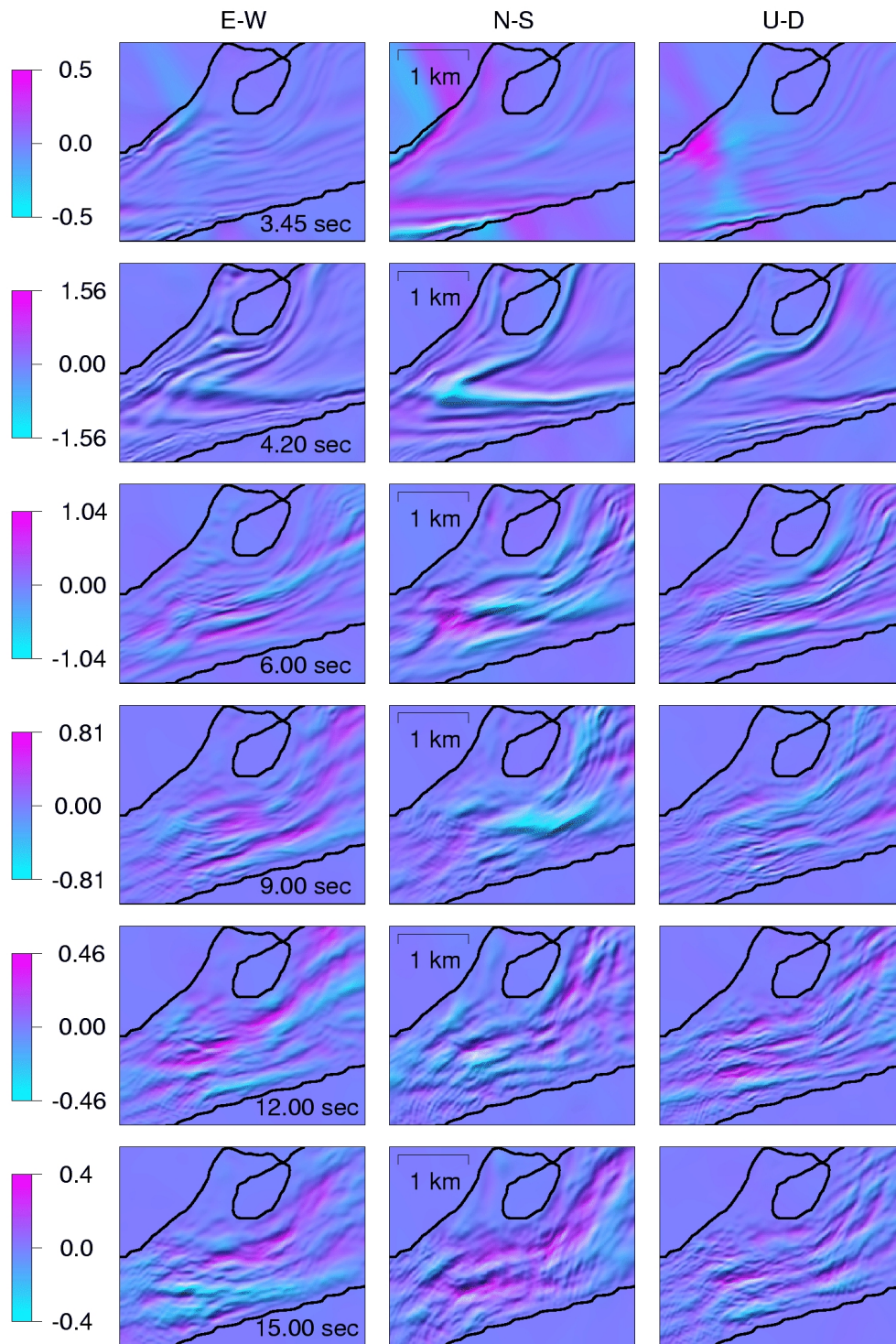


Figure 4.5: Snapshots of simulated wave propagation in the Sion basin after excitation with a plane wave corresponding to the Vallorcine main shock. Velocities are in 10^{-2} ms^{-1} ; the scale is time-dependent.

of the 1946 earthquake the input signal would need to be reduced first. However, since we will focus on amplification of Fourier spectra and peak velocities caused by the basin, the amplitudes are instead normalised by the reference station.

4.3.3 Analysis of signal-to-noise ratio

Since the noise level in the city is significantly higher than on the two reference sites, the signal-to-noise ratio at each station needs to be considered to prevent local noise sources from polluting spectral ratios. We computed the ratio of pre-event to event spectral amplitudes on both horizontal components for each station and each event. Only events with a signal-to-noise ratio above 2 (i.e. a pre-event to event ratio of at least 3) in the frequency range between 1 and 10 Hz were considered in our analysis (Tab. 4.3).

4.3.4 Estimation of Fourier amplification

We investigate site amplification in the Fourier spectral domain on both horizontal components using the same procedure for synthetic and simulated ground motion. Seismograms were converted to acceleration in ms^{-2} to allow comparison with the two strong-motion receivers. We removed the mean, applied a trapezoidal taper and selected a window containing the intense S-wave part of the seismograms. To increase resolution of the discrete Fourier transform at lower frequencies the extracted signals were zero-padded to 2^{14} samples. The amplitude spectra of the Fourier transform were smoothed using the window proposed by Konno and Ohmachi (1998) with a bandwidth of 20 samples. Finally the total spectral amplitude in the horizontal direction was computed and divided by the Fourier amplitude of the reference station. For computation of average Fourier amplifications of all events we discarded frequencies with signal-to-noise ratios below the threshold.

4.3.5 Frequency-wavenumber analysis

We apply frequency-wavenumber methods on recorded and simulated ground motion to estimate the direction of arrival and velocity of wave trains propagating through the basin. Results shown in this text were acquired with the high-resolution frequency-wavenumber technique (Capon, 1969) and the Multiple Signal Characterisation (MUSIC) method developed by Schmidt (1986a,b). A description of these methods can be found in e.g. Zerva and Zhang (1996) or Hartzell *et al.* (2003). We used the routines provided by the geopsy software package (Ohrnberger *et al.*, 2004) and adapted them for processing of interactively selected time windows.

From the f - k spectra computed with the high-resolution method, only the slowness and direction of the maximum array output was picked. The MUSIC

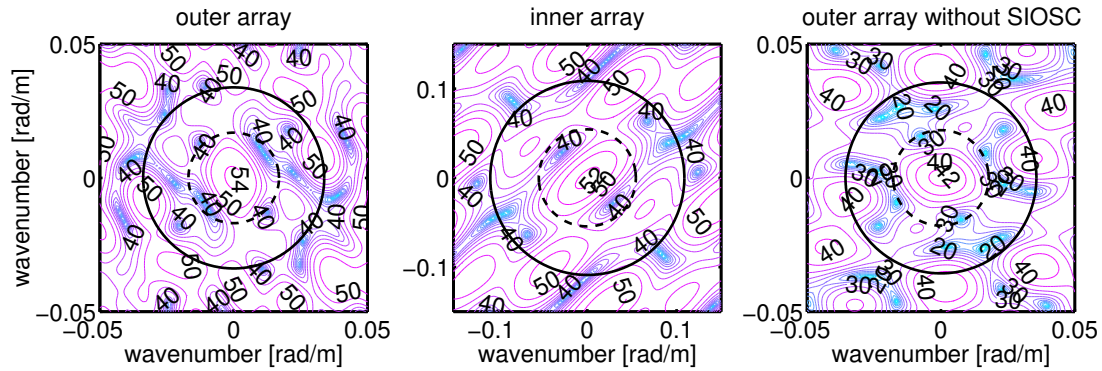


Figure 4.6: Array response beampatterns for the outer and inner temporary arrays and for the outer array without the station SIOSC. The solid rings reflect the location of the first aliasing peaks, and the wavenumber domain which can be analysed is within the dashed rings. Contours show the array output in dB.

algorithm is able to resolve multiple sources, but one difficulty is that the number of sources present in the signal must be known or estimated. We followed the Minimum Descriptive Length (MDL) criterion (Wax and Kailath, 1985), which is implemented in the geopsy routine, to determine the maximum number of sources. However, it has been shown that this method may induce an overestimation of the number of sources if the time windows are short (Marcos, 1998). Therefore, we only considered multiple sources determined by the MUSIC algorithm if the f - k map produced by the high-resolution method indicated more than one direction of origin.

Figure 4.6 shows the resolution beampatterns for the large outer array and the small inner array that was recording during the first installation period. The position of the receivers was predetermined by the distribution of buildings and the availability of power supplies, and it was not possible to achieve an ideal array configuration for the inner ring. The failure of the station SIOSC during the Vallorcine series has little impact on the array resolution capabilities (Fig. 4.6 right). Figure 4.7 compares the array resolution limits with Rayleigh wave phase velocities measured near the array center. The lower resolution limit was computed using a maximum wavelength of twice the array aperture. Only a narrow frequency band can be analysed with each array. We chose to perform the f - k processing at about 1.25 Hz with the outer array and at 2.5 Hz with the inner array; the observed phase velocities are well below the aliasing limits at these frequencies.

For f - k analysis of the simulated ground motion, we extracted synthetic seismograms on gridpoints belonging to circular arrays. The array geometry was chosen to match the analysed frequency band; we used a radius of 150 meters (12 gridpoints) and 50 meters (4 gridpoints) for processing at 1.25 Hz and 2.5 Hz, respectively.

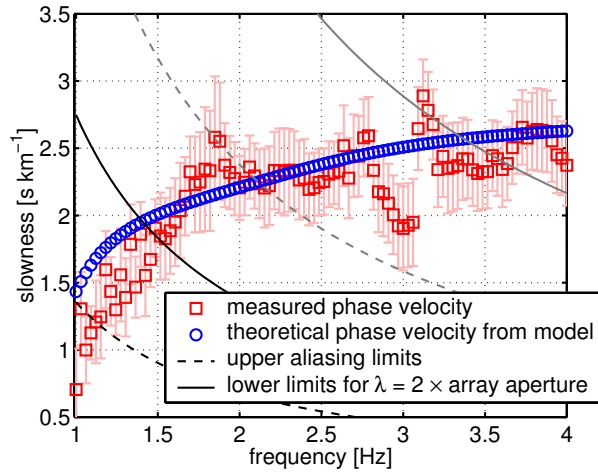


Figure 4.7: Array resolution limits for the outer (black) and inner (grey) arrays. The measured phase velocities (errorbars) were derived from ambient noise recorded in the vicinity of the station SIOVE. The theoretical phase velocity was computed from a 1-D column through the velocity model at the array center.

4.4 Observed and simulated Fourier amplifications

In this section, we will show Fourier amplifications of the events from Table 4.3. The events from the Derborance and Vallorcine series are analysed together, because similar results are expected from the almost identical location and source mechanism.

4.4.1 Vallorcine series

The M_L 4.9 mainshock (V1 in Tab. 4.3) and two aftershocks (V2 and V3) were recorded on eight receivers of the temporary network.

Figure 4.8 shows observed site-to-reference spectral ratios from the main event and the two aftershocks. Despite the different signal-to-noise ratios, all three events yield very similar amplifications for frequencies below 10 Hz. At all stations but SIOAE and SIOTO a first peak can be identified between 0.4 and 0.7 Hz, with the largest amplification of approximately 10 obtained at the station SIOIS. At most sites the highest amplitude is reached between 2 and 10 Hz. The most prominent peak can be seen at the station SIOTE for a frequency of 3.5 Hz, where the amplitude reaches a factor of 19. All sites exhibit significant amplifications near this frequency. At the site SIOAE another significant amplification peak appears at about 9 Hz.

In Figure 4.8, the observed Fourier spectral ratios are compared to spectral ratios computed from synthetic signals. At all stations, the synthetic spectral ratios show a first peak at about 0.5 Hz and increase again above 2 Hz. The simulated site response is very close to the observations for the stations SIOO, SIOTE and

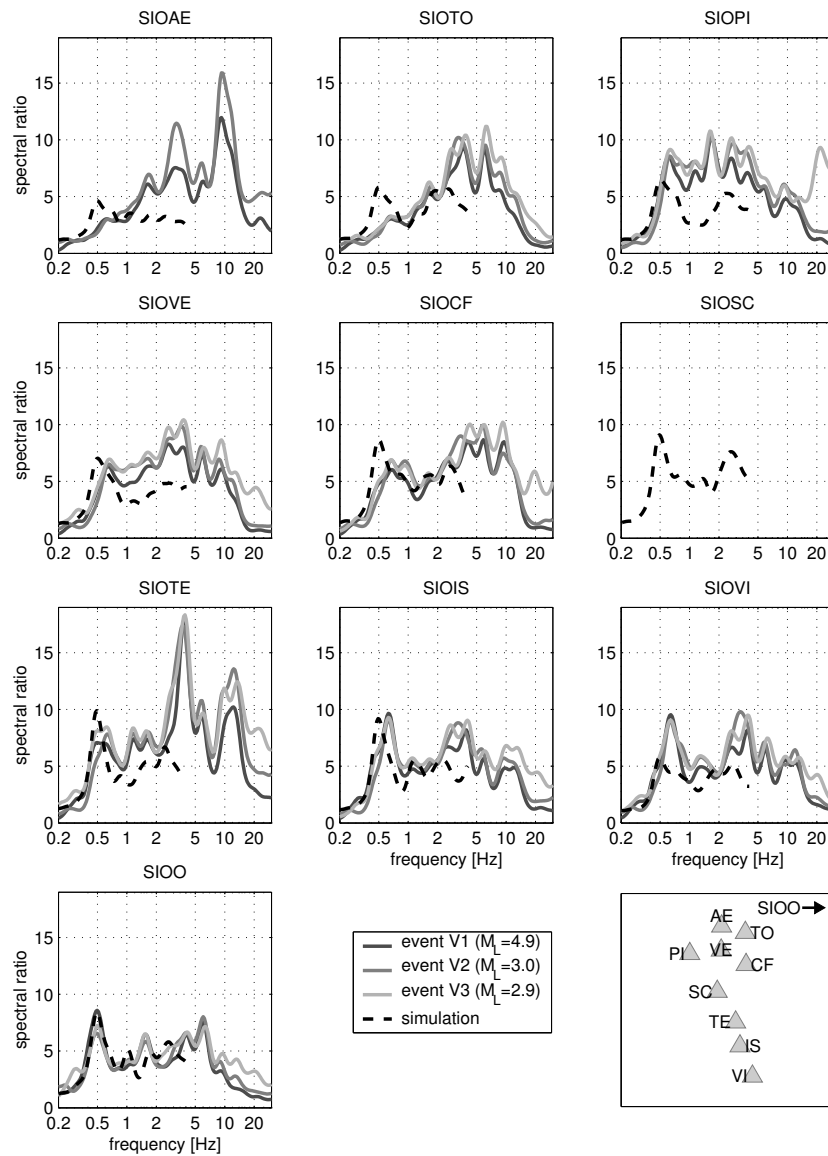


Figure 4.8: Observed (solid) Fourier spectral ratios computed from seismograms of the Vallorcine series (Tab. 4.3). The black dashed line shows Fourier spectral ratios computed from synthetics of the Vallorcine simulation. The relative station positions are indicated on the lower right plot, with the prefix 'SIO' stripped from station names.

SIOIS. At the site SIOCF the fundamental frequency is slightly underpredicted by the simulation. The simulated transfer function for the station SIOTO yields twice the value of the observations at 0.6 Hz. This could imply that this station is located outside the deeper part of the basin, or that shear-velocities are higher than in our structure model.

4.4.2 Derborance series

During the Derborance series the first temporary network with 13 weak motion instruments was recording. At the station SIOTE no signals were recorded for events D2-D4. We will not show spectral ratios acquired on the inner array stations SIOS1-SIOS4, because they are very similar to those acquired at the site SIOCF. Spectral ratios computed from signals of the Derborance sequence (D1-D4) are given in Figure 4.9. The four events are yielding similar Fourier amplifications at frequencies above 2 Hz for a given site, and all stations show a peak at about 2.8 Hz. Amplifications at the fundamental frequency of 0.6 Hz are showing a greater variability due to the lower signal-to-noise ratio, especially for the stations SIOPI and SIOVI. Synthetic spectral ratios are also exhibiting a fundamental peak, though at a lower frequency of 0.45 Hz and with generally higher amplitudes.

4.4.3 Northern Switzerland events

Three of the recorded events (N1-N3 in Tab. 4.3) occurred in northern Switzerland at comparable epicentral distance and azimuth. During the last event the strong-motion station SIOV did not provide useful signals; we will therefore use the permanent broadband station SENIN as reference site. The observed spectral ratios from the three events (Fig. 4.10) show larger variability at a given site than those of the Derborance and Vallorcine sequences (Figs. 4.9 and 4.8), though most spectral ratios show a fundamental frequency of 0.6 Hz and a second amplification at about 2.5 Hz. Simulated spectral ratios are exhibiting a first peak at about 0.5 Hz and secondary peaks at frequencies above 1 Hz.

4.4.4 Site characterisation

We computed average Fourier amplifications from the observed and simulated events to characterise the station sites of the temporary network. The signal-to-noise ratio was computed for each station, and only frequencies with a ratio above the threshold were considered to compute the average amplification. In general more events were available at frequencies above 1 Hz due to the better signal-to-noise ratio.

At most sites, average Fourier spectral ratios reach a level of at least 5 in the frequency range between 1 and 10 Hz. The deep resonance of the basin at 0.6 - 0.7 Hz is clearly visible at the stations SIOCF to SIOVI and SIOO.

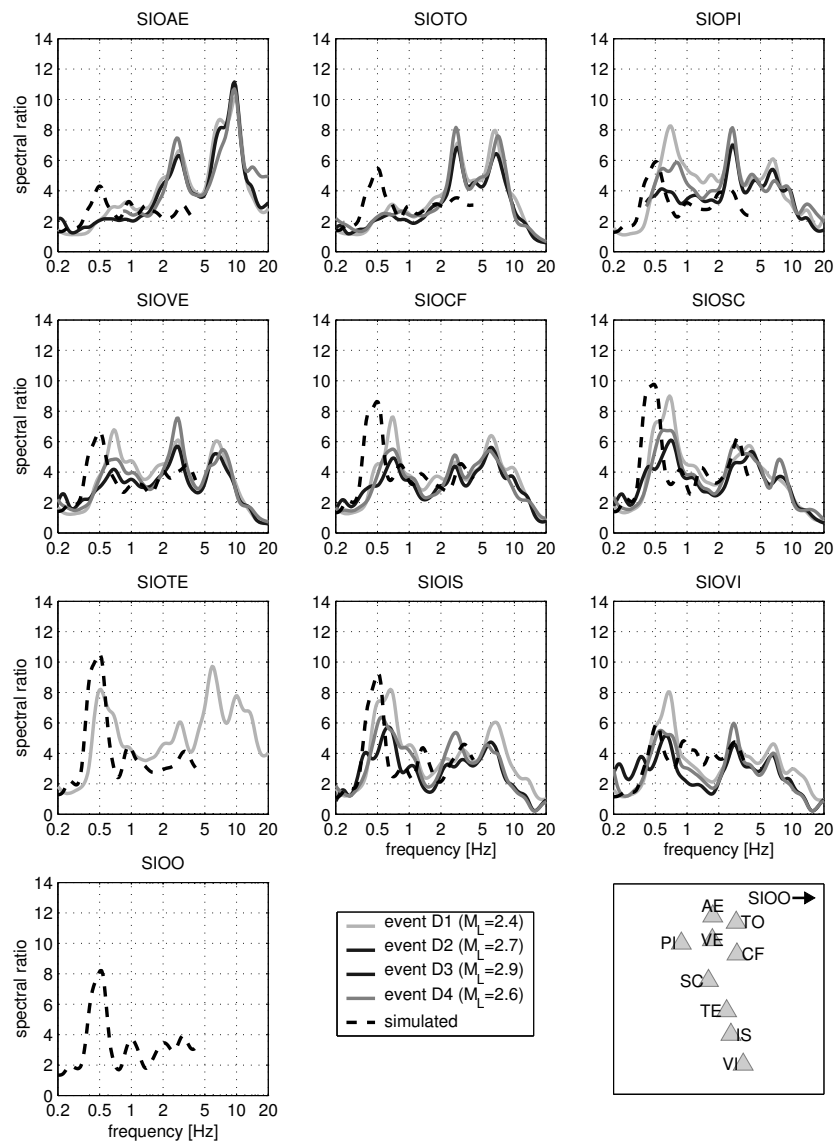


Figure 4.9: Observed (solid) and simulated (dashed) Fourier spectral ratios for Derborance series (D1-D4).

Simulated average spectral ratios are able to reproduce the fundamental deep valley response, though the fundamental frequency is underestimated at the stations SIOVE, SIOCF and SIOSC. At most sites simulated average amplifications are within the standard deviation of the observations. The discrepancies between the observations and simulations at stations SIOTO and SIOAE show that the velocity model needs to be improved in that region.

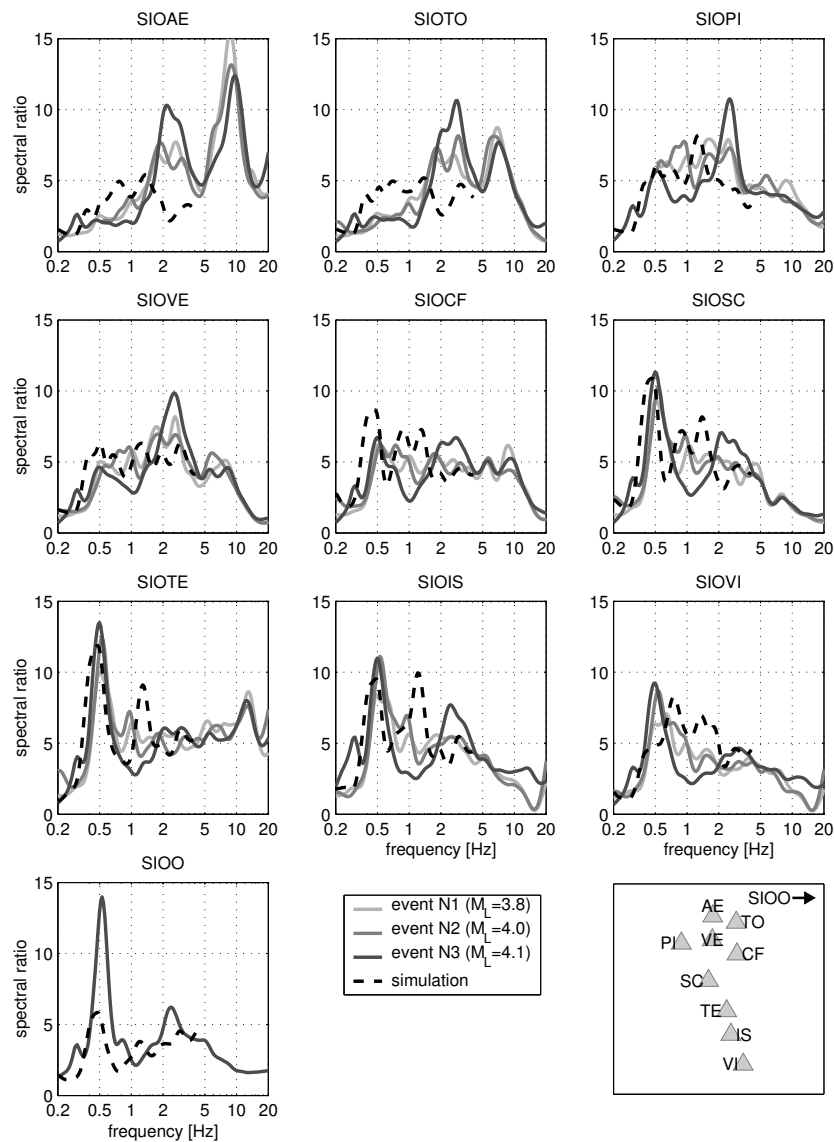


Figure 4.10: Observed (solid) and simulated (dashed) Fourier spectral ratios for northern Switzerland events (N1-N3).

4.5 Deep valley response

Site-to-reference spectral ratios computed from observed events exhibit a fundamental frequency at about 0.6 Hz (Fig. 4.8, 4.9 and 4.10), regardless of the position on the basin and the local sedimentary thickness. This is characteristic for the case of two-dimensional resonance, which has been predicted for deep embanked valleys with a high velocity contrast. Two-dimensional resonance is quite different from the one-dimensional response expected in rather shallow valleys, where the observed fundamental frequency reflects the local sedimentary thickness.

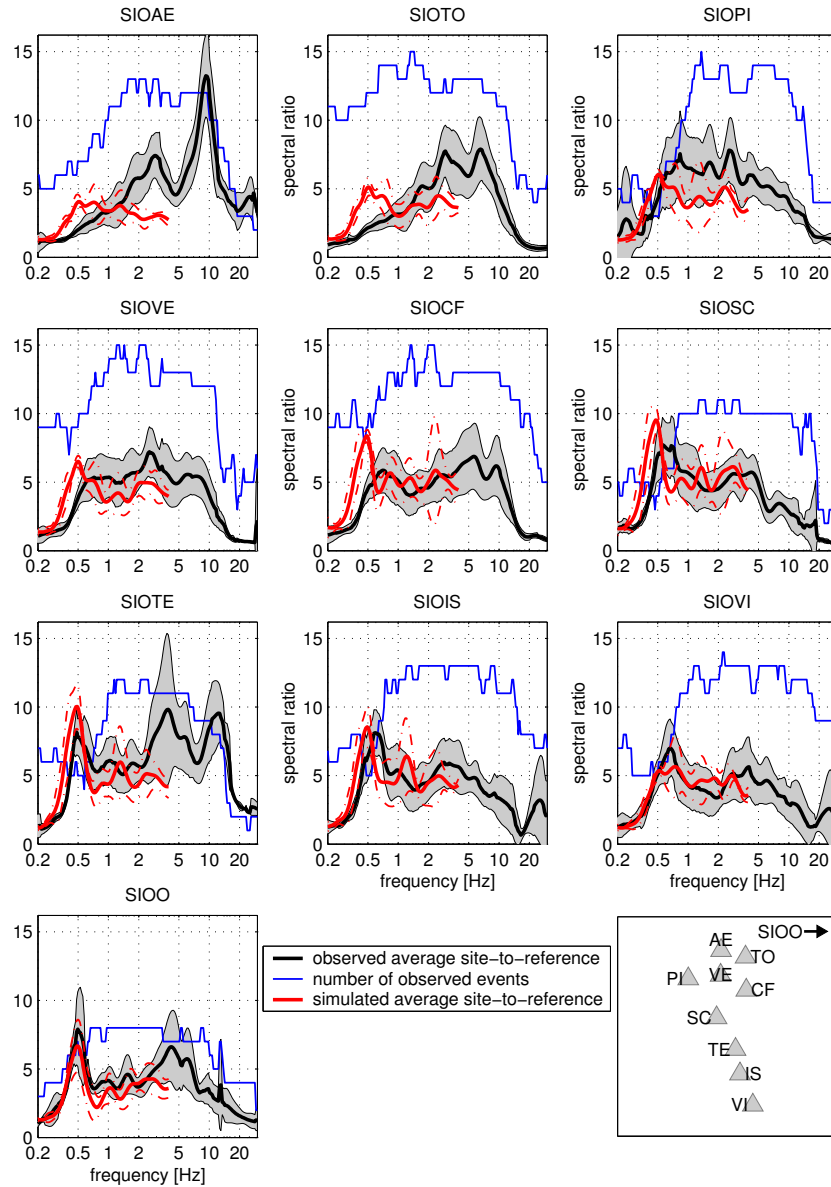


Figure 4.11: Comparison between average observed (bold black lines) and average simulated (bold red lines) Fourier amplification at the temporary stations. Standard deviations are indicated by the grey patch (observed) and dash-dotted red lines (simulated). Blue lines depict the number of recorded earthquakes used to compute the average amplification at each frequency.

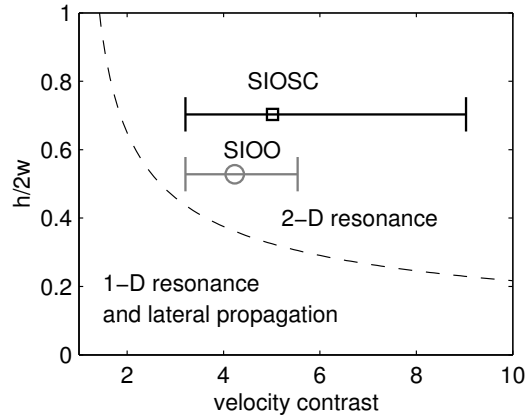


Figure 4.12: Critical shape ratio (dashed) as a function of the velocity contrast for the SH case. The shape ratios for the Rhône basin near the stations SIOSC (black) and SIOO (grey) are plotted for the corresponding velocity contrast, which was computed from a 1-D soil column below the respective station. Errorbars are indicating the velocity contrast for the minimum and maximum shear-velocities inside the sediment fill. (Modified from Bard and Bouchon, 1985).

Bard and Bouchon (1985) introduced the equivalent shape ratio as a simple criterion to distinguish between shallow valleys, dominated by 1-D resonance and lateral propagation, and deep valleys, dominated by 2-D resonance. The equivalent shape ratio corresponds to the maximum valley depth divided by the width over which the sediment thickness is more than half its maximum value. The critical shape ratio decreases with increasing velocity contrast between sediment and bedrock (Fig. 4.12).

We calculated the equivalent shape ratios from the sediment-bedrock interface in the velocity model for cross-sections at the temporary network and at the station SIOO. The shear-velocity contrast was computed with the traveltime-based average from soil columns taken through the velocity model (Tab. 4.1) at the stations SIOSC and SIOO. For the temporary network, a shape ratio of 0.7 and a velocity contrast of 5.0 is obtained, which places the site well inside the domain of 2-D resonance (Fig. 4.12). Even if the shear-velocities were as high as 900 ms^{-1} for the whole sediment fill (errorbars in Fig. 4.12), the equivalent shape ratio would still be above the critical value. For the cross-section at the station SIOO, the shape-ratio and velocity contrast are slightly lower, yet the site is still clearly located in the area where the development of 2-D resonance must be expected. In a previous study we have analysed ambient noise recorded at similar sites in the Rhône valley (Roten *et al.*, 2006; Roten and Fäh, 2007), and we suggested that observations in site-to-reference spectral ratios can be explained in terms of two-dimensional resonance.

2-D resonance involves three different modes, the SV, SH and P mode. The SH mode involves particle motion parallel to the valley axis (axial direction), the

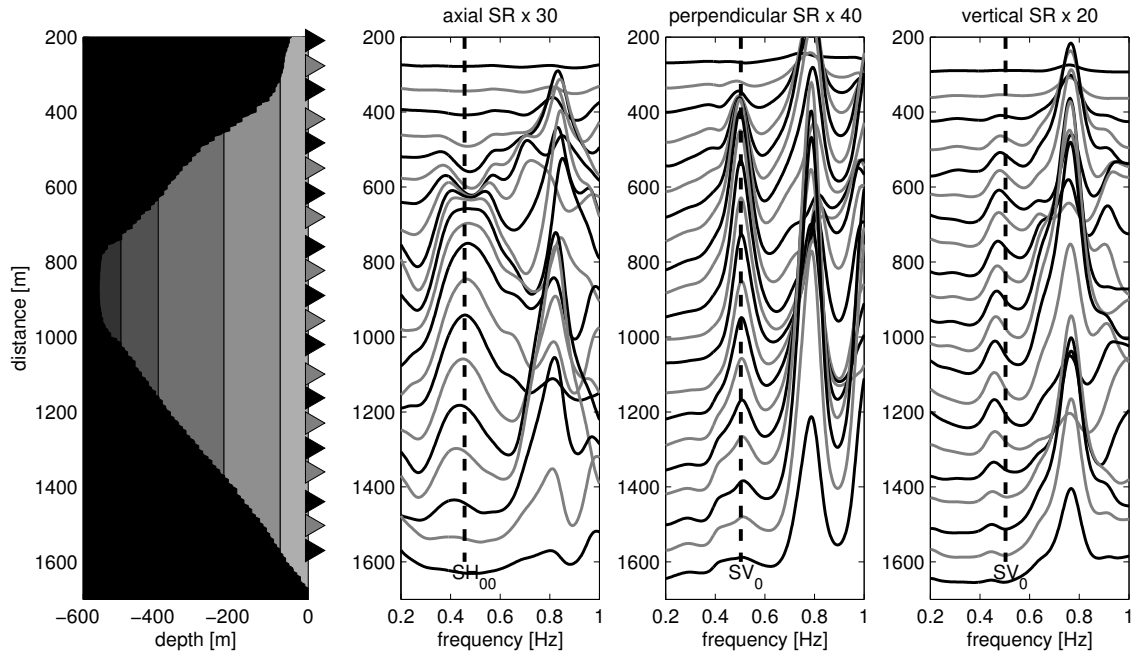


Figure 4.13: Spectral ratios computed from synthetics of event N3 for all components as a function of distance across the basin. Scale factors of 30, 40 and 20, respectively, were applied on spectral ratios. The cross-section through the velocity model is displayed for orientation.

SV mode produces particle motion in the direction perpendicular to the valley axis and on the vertical component. Both SH and SV mode show a maximum amplification in the valley center on the horizontal components.

These different modes can be distinguished if the horizontal components are rotated to the axial and perpendicular direction of the valley. Figure 4.13 shows spectral ratios computed from synthetics of event N3 as a function of distance on a profile across the basin. On the axial component, a first peak appears at about 0.42 Hz at all receivers, regardless of the position along the profile axis. The amplification at this frequency reaches a maximum near the valley center. These observations are in agreement with the behaviour expected for the SH_{00} fundamental mode of 2-D resonance. On the direction perpendicular to the valley axis, the SV_0 fundamental mode can be identified at about 0.50 Hz.

In Figure 4.14, the same analysis is done for observed seismograms from event N3. The main characteristics of recorded spectral ratios match the pattern inferred from the simulations, though the observed resonance frequencies are a bit higher. On the axial component the SH_{00} fundamental mode is visible at 0.55 Hz for most stations, and the fundamental mode SV_0 can be observed at 0.59 Hz on the perpendicular and vertical axis.

We carried out the above analysis for all recorded and simulated events and defined the frequencies of modes SH_{00} and SV_0 (Tab. 4.4). The frequencies of

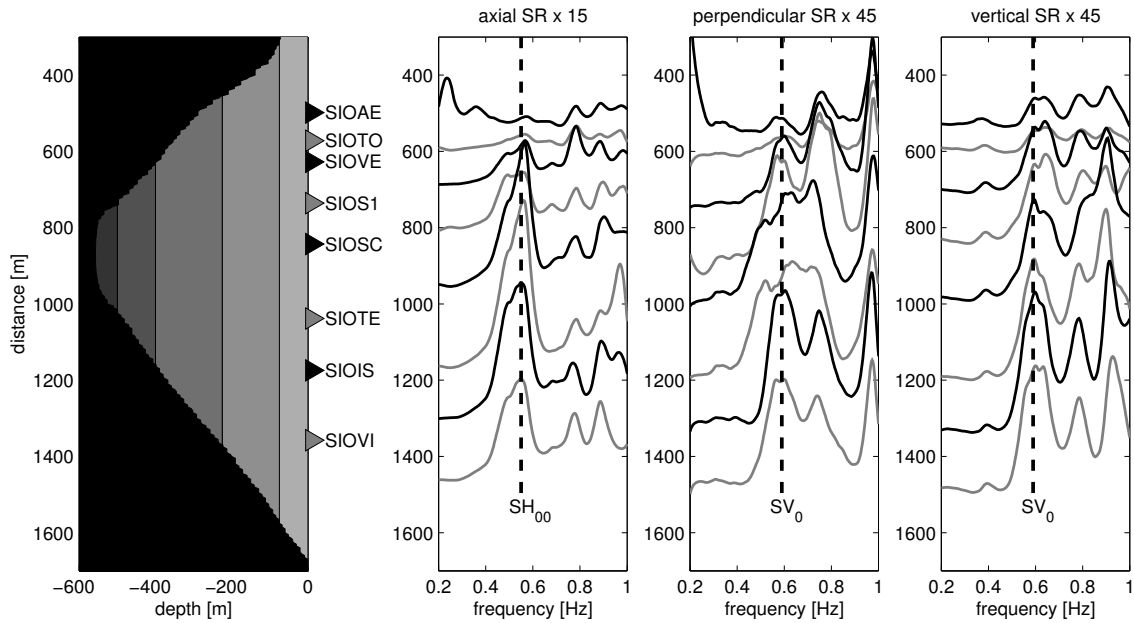


Figure 4.14: Like Figure 4.13, but for recorded seismograms of event N3.

these modes appear to be sensitive to the analysed event. Observed values range between 0.45 and 0.55 Hz for SH_{00} and between 0.59 and 0.70 Hz for SV_0 . These differences are probably caused by 3-D effects of the complex basin structure. However, for each individual event the frequencies are constant along the profile and do not depend on the local sedimentary thickness, as expected in the case of 2-D resonance. Earthquakes with similar source location and mechanism yield similar resonance frequencies, as can be seen from observations of the Vallorcine (V1-V3) and Derborance (D1-D4) series.

Additionally we determined the 2-D resonance frequencies from ambient noise using a one hour window of undisturbed nighttime records (entry termed NS in Table 4.4). The identified fundamental frequencies compare well with those found from the weak motion signals, which confirms that ambient vibrations may be used to identify 2-D resonances (Roten *et al.*, 2006).

Resonance frequencies determined from the simulated ground motion are also showing some variability with respect to the simulated incoming wavefield (Tab. 4.5), though not to the extent observed in the recorded earthquakes. This might be explained with the very simple source configuration used for our simulations, which is not able to reproduce the incoming wavefield at its full complexity, or with the limited accuracy of the velocity model.

The 2-D resonance frequencies defined from the simulations are always lower than the observed values, with 0.42 - 0.47 Hz for SH_{00} and 0.50 to 0.53 Hz for SV_0 . This implies that shear-wave velocities in the sedimentary fill could be higher than in our velocity model, or that the 3-D structure within the basin fill is more complicated. Another source of uncertainty is the geometry of the sediment-

Ev.	SH ₀₀	SV ₀
D1	0.52	0.70
D2	0.55	0.63
D3	0.53	~0.68
D4	0.53	~0.68
V1	0.45	0.62
V2	0.48	0.67
V3	0.48	0.63
N1	0.50	0.64
N2	0.55	0.59
N3	0.45	0.62
I1	0.48	0.61
I2	0.48	0.65
I3	0.50	0.61
F1	0.48	~0.67
F2	0.46	0.61
L1	0.47	~0.51
NS	0.52	0.60

Table 4.4: Fundamental mode 2-D resonance frequencies identified from all observed events. The last entry (NS) shows the resonance frequencies determined from ambient noise.

Sim.	SH ₀₀	SV ₀
D3	0.44	0.50
V1	0.42	0.52
N2	0.45	0.50
I3	0.47	0.53

Table 4.5: Fundamental mode 2-D resonance frequencies identified from the simulated ground motion.

bedrock interface below the temporary network, since it was mainly interpolated from nearby gravimetric and seismic surveys.

4.6 Frequency-wavenumber analysis

To determine the direction of arrival of waves propagating through the array, we applied the f - k techniques described above to the vertical component of recorded and simulated seismograms. We will show results of the M_L 4.9 Vallorcine mainshock (V1) and the M_L 4.0 Brugg event (N2).

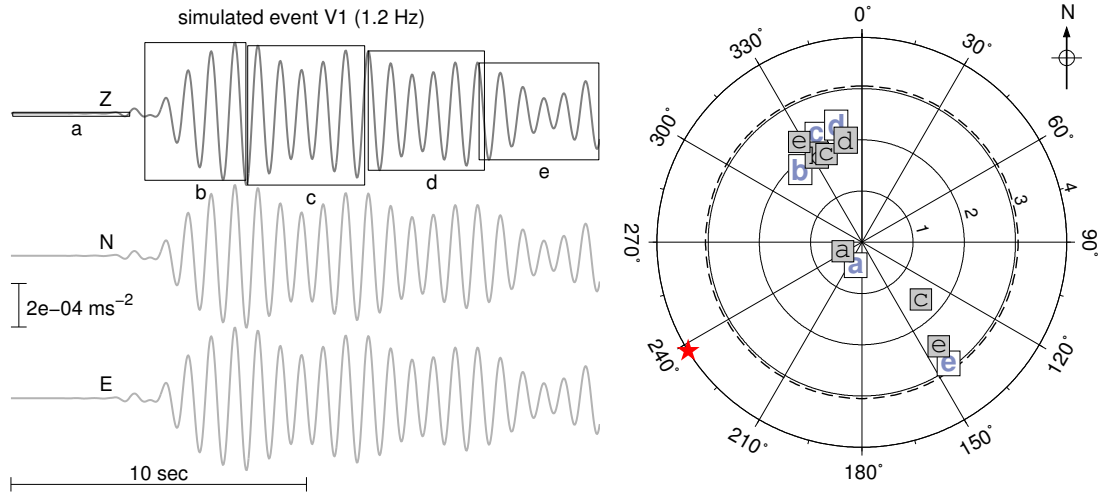


Figure 4.15: *Left*: Time windows for f - k analysis selected from a simulated seismogram at the array center. The synthetics have been bandpass filtered around the frequency of f - k analysis (1.25 Hz). *Right*: Estimated slowness and direction of origin of signals for the different time windows. Slowness is in seconds per km. Results obtained from the high-resolution method are plotted with bold lightblue letters, results from the MUSIC algorithm are indicated by the black characters in typewriter font. The thick dashed line at $\sim 3 \text{ skm}^{-1}$ corresponds to the aliasing limit. The azimuth of the simulated event is shown by the red star.

4.6.1 Vallorcine main event

Because no inner array was available during this event, we will limit the analysis to the frequency 1.10 – 1.25 Hz. For analysis of synthetic ground motion we used a circular array consisting of two rings with 150 and 75 meters radii centred at the same location as the real network. We selected five time windows of approximately 4 seconds length from the synthetic seismograms (Fig. 4.15 left).

The first time window (a) contains only the first arrival; both the high-resolution and MUSIC technique resolve an azimuth of about 240° and a slowness of approx. 0.4 skm^{-1} (2500 ms^{-1}). This is consistent with a body wave originating from the azimuth of the simulated event.

The next time window (b) yields an azimuth of 330° and a slowness of about 2 skm^{-1} (500 ms^{-1}), which is close to the theoretical Rayleigh wave phase velocity at 1.25 Hz computed from the geophysical model (Fig. 4.7). This identifies the phase as a Rayleigh wave generated at the basin edge northwest of the array center. The next two time windows (c,d) show a very similar pattern; the last window (e) shows surface waves originating south-east of the site. Additionally MUSIC identifies a signal propagating from the Northwest. Therefore, edge-generated surface waves originating from both sites are dominating the simulated wavefield (Fig. 4.5). This can also be seen very clearly in animations of the simulated earthquake scenario (online material).

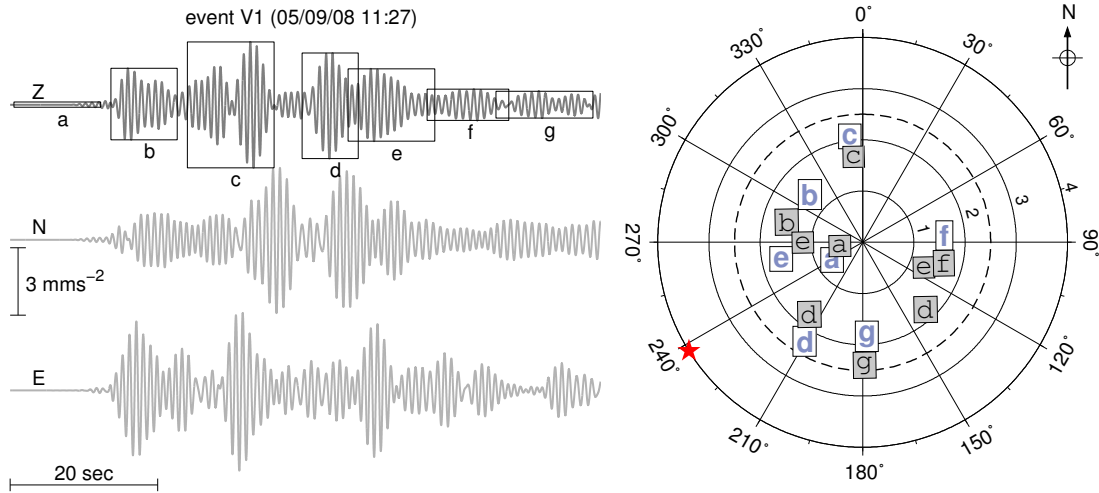


Figure 4.16: Results of f - k analysis at 1.1 Hz applied on recorded signals of the Vallorcine main shock (V1). See Figure 4.15 for more explanation.

Figure 4.16 shows results of the f - k processing applied on the recorded ground motion. The record length of the observed time series are longer than the simulations, which allows us to use more and longer time windows. Again, the first arrival (time window a) corresponds to a body wave arriving from the direction of the epicentre (Fig. 4.16). The time windows b and c show edge-generated surface waves originating in the northwest, similar to the simulations. Analysis of the remaining time windows reveals surface waves arriving from almost all directions.

The phase slowness of these surface waves is generally 20-25% lower than in the simulation. As we observed earlier, this suggests that shear-wave velocities near the array center are higher than the values used in the velocity model.

4.6.2 Northern Switzerland event N2

The M_L 4.0 event of Brugg was recorded during the first deployment period, for which the inner array is available. Therefore the analysis can be performed at both 1.25 and 2.5 Hz. This is especially interesting because site-to-reference spectral ratios determined from the northern Switzerland events (N1-N3) show significant peaks of amplification at about 2.5 Hz for most stations.

Figure 4.17 shows the selected windows and directions of origin derived from the simulation of event N2. At both frequencies, the first arrivals are arriving from the north, deviated by about 30 degrees from the direction to the epicentre. Arrivals from this direction can also be seen on later time windows, since the basin was excited during the whole simulation length. Additionally, surface waves arriving mainly from the NNW and SE are resolved. More different phases can be identified at 2.5 Hz because the shorter period allows to use a larger num-

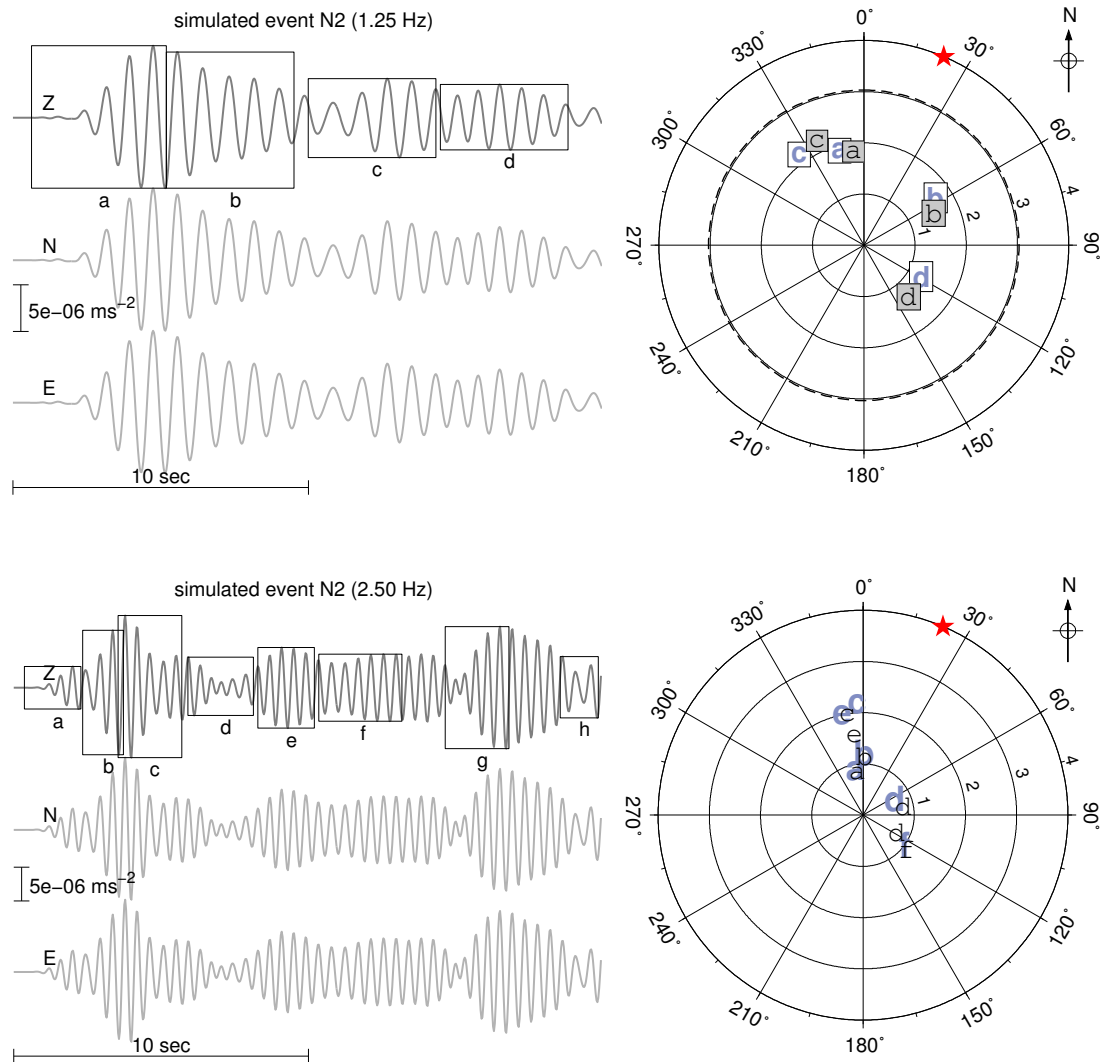


Figure 4.17: Results of f - k analysis at 1.25 (top) and 2.5 (bottom) Hz applied on synthetics of event N2. The aliasing limit for 2.5 Hz is outside the plotted range at 6 skm^{-1} .

ber of time windows.

Snapshots of the simulated surface velocity show that the first arrivals consist of surface waves generated on the northern margins of the basin (Fig. 4.18 top). Edge-generated surface waves from the NE appear on later snapshots.

We applied the same processing to recorded signals of event N2 (Fig. 4.19). Both frequencies reveal arrivals from the epicentre direction for the first time window. Later time windows reveal surface waves arriving from all directions between the NNW to SSW.

In summary, both simulated and recorded signals reveal Rayleigh surface waves originating at angles completely different from the epicentral direction. Such edge-generated surface waves have been reported from many numerical

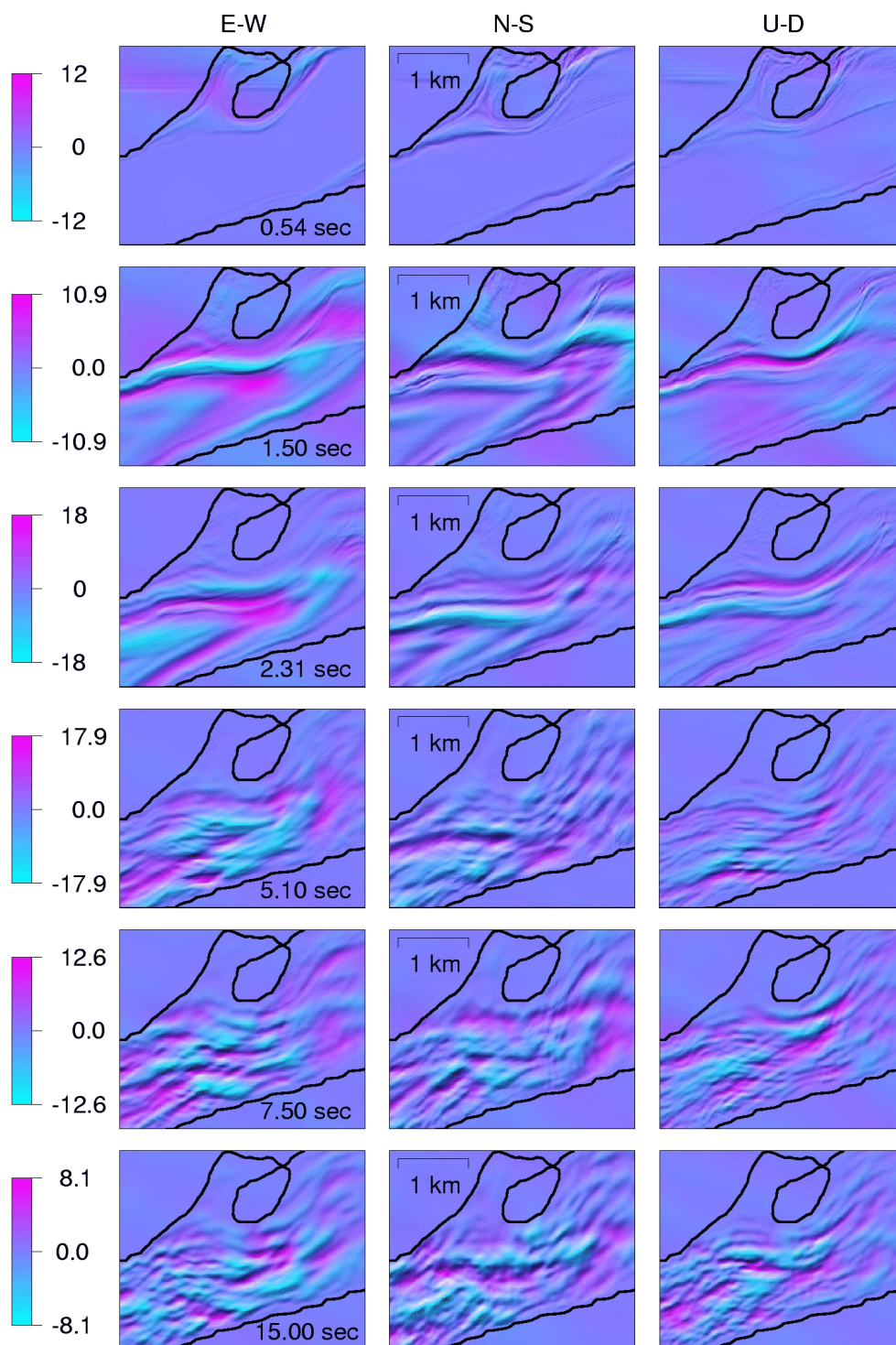


Figure 4.18: Snapshots of simulated wave propagation in the Sion basin after excitation with a plane wave arriving from the NNE, with input velocity from the Brugg event. Velocities are in 10^{-5} m s^{-1} .

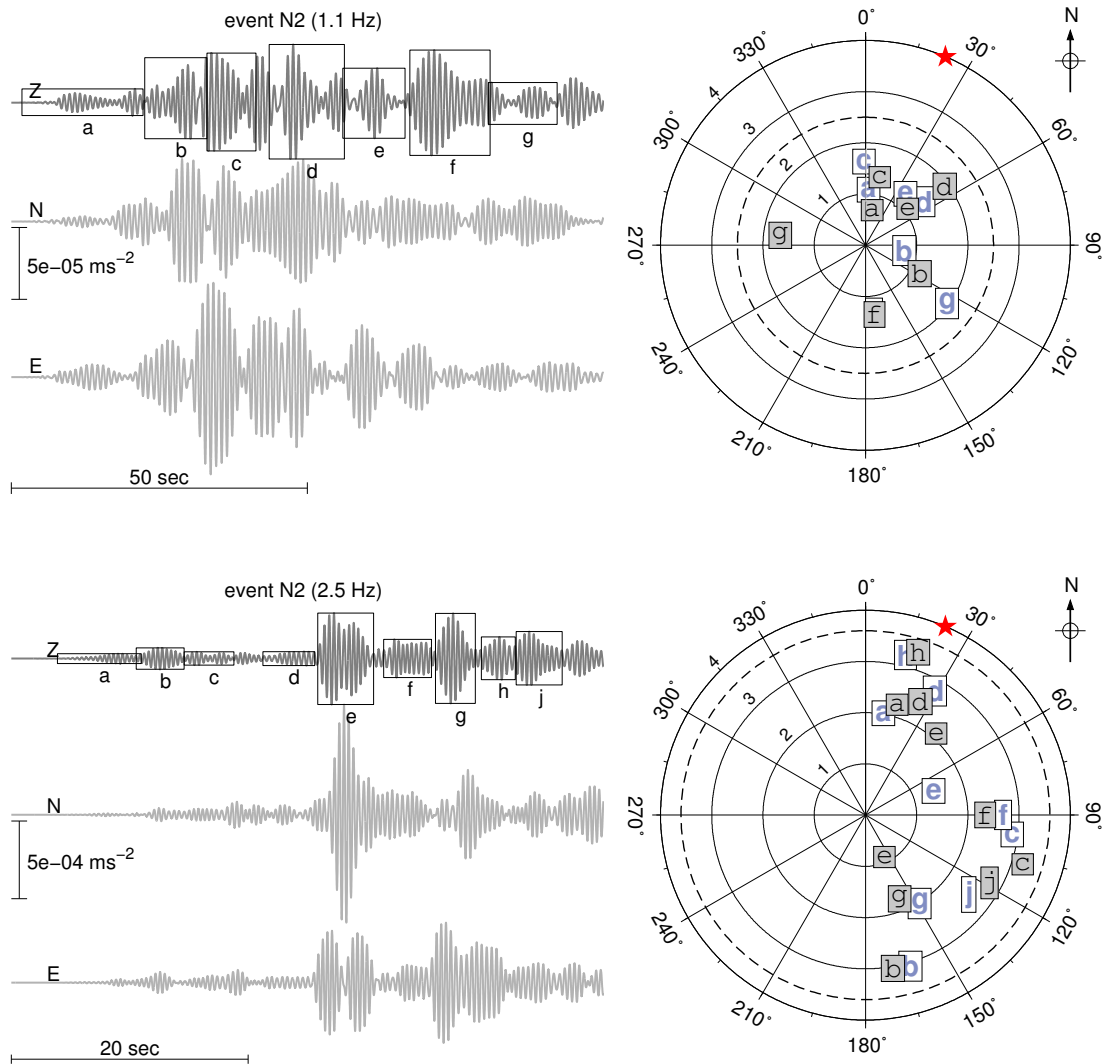


Figure 4.19: Results of $f-k$ analysis at 1.10 (top) and 2.5 (bottom) Hz applied on records of event N2.

simulations (e.g. Bard and Bouchon, 1980a; Kawase, 1996; Olsen, 2000), and there are a number of observations from recorded earthquakes (e.g. Cornou *et al.*, 2003; Frankel *et al.*, 2001; Hartzell *et al.*, 2003; Joyner, 2000; Field, 1996). These edge-generated surface waves are likely the cause for amplification at frequencies above 1 Hz. The fact that arrivals from both basin sides can be observed (Figs. 4.16 and 4.19) shows that these waves are not attenuating quickly enough within the embanked basin, at least not for weak ground motion at frequencies up to 2.5 Hz.

$f-k$ spectra from observed ground motion are generally more complicated than those determined from synthetics and yield arrivals from more different directions. Once more, this difference can be traced back to the simple source description used in our simulations, where the incident wave field was approximated by a plane S-wave. The lack of surface waves in the simulated incident

wavefield may account for the reduced complexity of simulated f - k spectra compared to the observations.

The above analysis was done using Rayleigh waves only, hence we have not yet been able to identify edge-generated Love waves, which may also contribute significantly to the observed amplification on the horizontal components.

4.7 Peak ground velocities

We computed peak ground velocities for all four simulated earthquakes and from all observations for the frequency range between 0 and 4 Hz. Peak velocities were normalised with the peak velocity at the reference station to estimate the amplification of the basin.

Figure 4.20 (top) shows simulated site-to-reference peak velocities for the Val-lorcine simulation. The highest values are encountered in a narrow band at the valley center, where peak velocities are 4 to 6 times higher than at the reference site. This belt of high amplification is caused by edge-generated surface waves arriving from both sides, which create positive interference near the valley center. As can be seen in the snapshot at 4.20 seconds (Fig. 4.5), the two interfering surface waves combine to a V-shaped wavefront with a central peak.

Outside the central band the amplification ranges between 1 and 4. Amplification levels are highest in the central part of the model and vanish towards the boundaries. This distribution can be explained with the curvature of the valley boundary in the north, which focuses edge-generated and reflected surface waves towards the model center, and with the narrowing valley with at longitude $7^{\circ}22'$. The vanishing peak velocities near the model border are probably just reflecting the vicinity to the absorbing boundaries.

Boxed numbers in Figure 4.5 show the observed relative peak velocities. To allow comparison with the simulated values, observed signals were first low-pass filtered above 4 Hz. Observed normalised peak velocities are generally similar to the values derived from the simulation. Since the exact geometry of the basement is not known, one might speculate that the band of interference is actually located more to the south. This would explain the high observed peak velocity at station SIOTE and the extreme amplification observed at 3.5 Hz in spectral ratios (Fig. 4.8). Acceleration perpendicular to the valley axis (Fig. 4.4) shows a large-amplitude phase at the station SIOTE, just after the S-wave onset. We can not verify this since no data is available for the station SIOSC, which is located right in the center of the simulated interference zone. However, f - k analysis performed on recorded ground motion shows a first arrival similar to the simulation, which supports the interpretation of interfering edge-generated surface waves.

Peak velocities for the simulated Derborance main event D3 (Fig. 4.20 bottom) show a similar pattern, though the amplification is generally lower. Outside the central interference zone high values are encountered on the south side of the basin. Observed amplifications agree well with the simulation for the southern part of the basin; on the north side the observed amplifications are larger than the

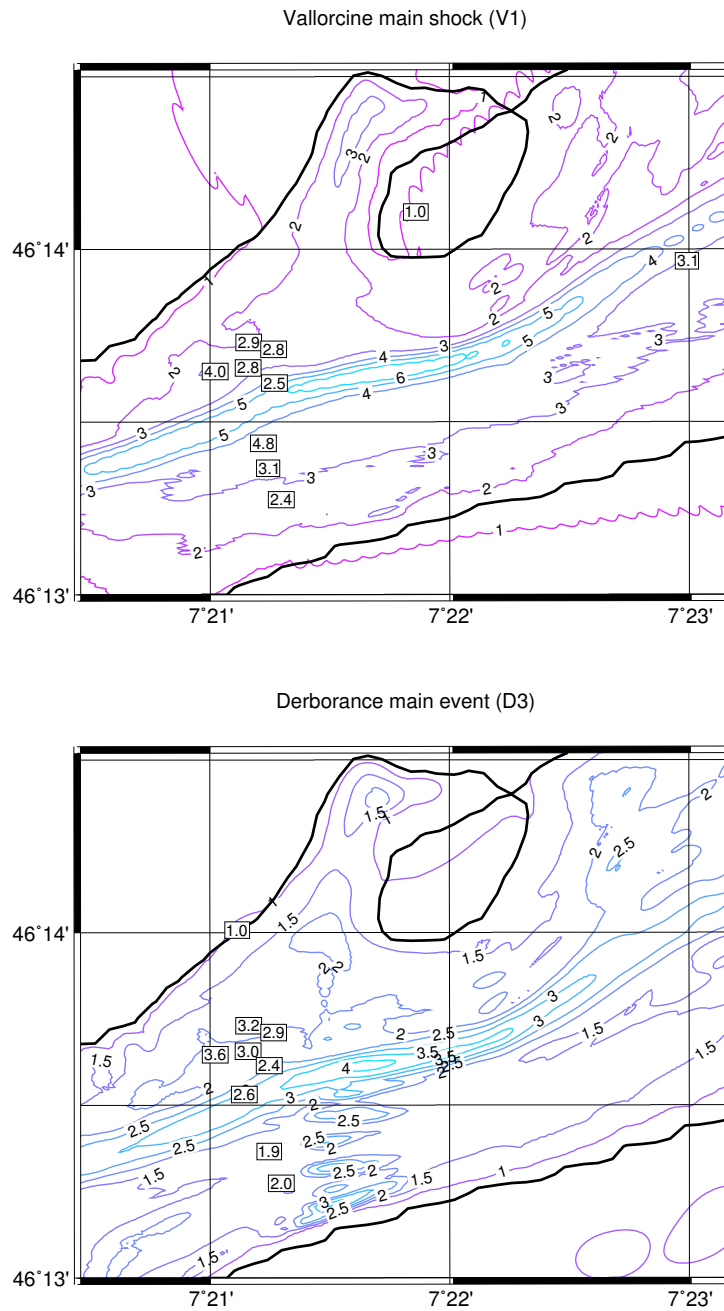


Figure 4.20: Simulated peak ground velocities for the central part of the computational domain normalised by the peak ground velocity at the reference site. Numbers enclosed by rectangles show the normalized peak ground velocities observed at the available stations. The station on the north was used as a reference for both simulated and recorded peak ground velocities (PGA = 1.0)

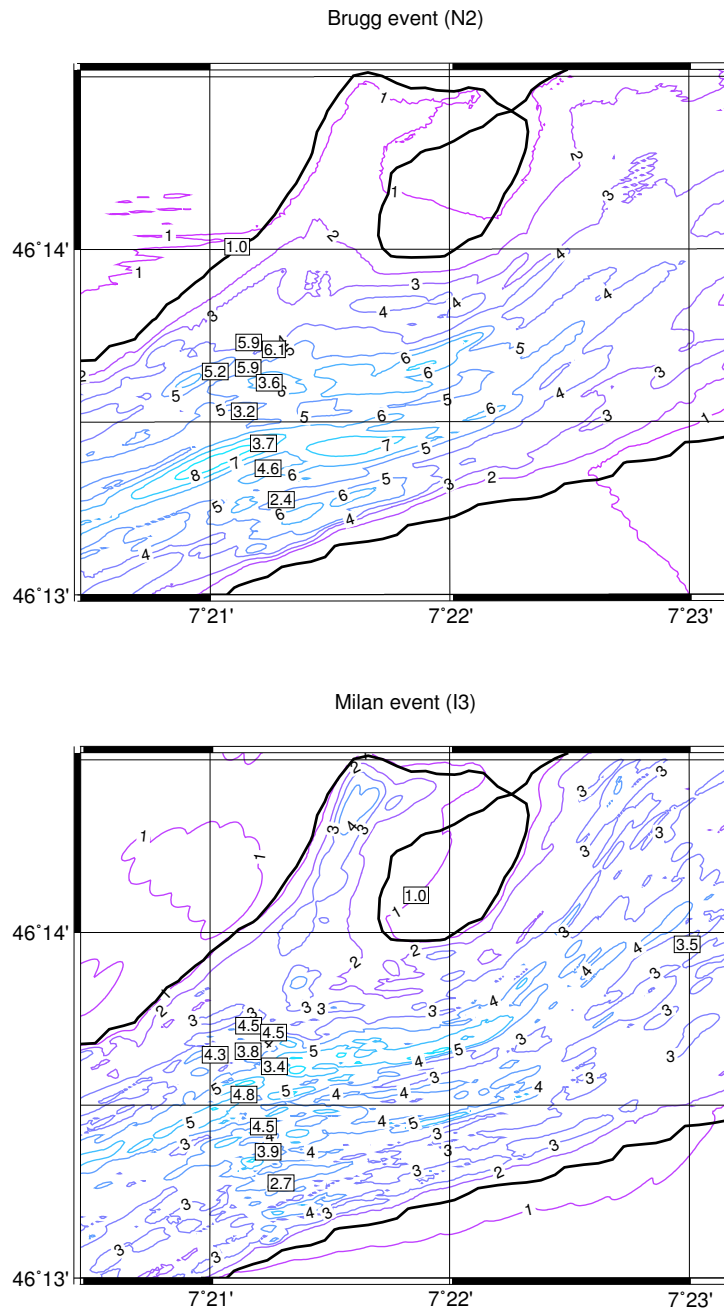


Figure 4.21: Like Figure 4.20, but for events D3 and I3

simulated values by up 50%.

Peak velocities show a more complicated distribution for events N2 and I3 (Fig. 4.21). The highest peak velocities are not concentrated in a central band, but distributed on spots located near the area of lowest shear-wave velocities

(Fig. 4.3). We presume that surface waves generated on the irregular northern margin of the basin (Fig. 4.18) exhibit a more complicated shape than the simpler wavetrains observed from the Vallorcine simulation (Fig. 4.5). Therefore, the interference pattern is also getting more complex, which can be seen on the distribution of peak ground velocities (Fig. 4.21 top). Recorded peak velocities for the Vallorcine event are also exhibiting a stronger amplification and greater variability than from the other events.

Simulated peak velocities for the northern Italian event I3 yield a lower amplification of up to 5. The plane wave used to simulate event I3 is arriving from the South-East, but due to the steep angle of incidence, surface waves are generated both on the southern and the northern margin of the basin. Spots of intense shaking are more numerous on the South side, which reflects the lower shear-wave velocities in that part of the velocity model.

Significant amplifications of up to 4 also occurs in the old town of Sion, which is located in the tributary valley on the North. This amplification may be explained with surface waves generated on the east and west side of the trench, and to a lesser extent it can also be observed for the simulation of the Derborance and Vallorcine main events (Fig. 4.20), but not for the Brugg event (Fig. 4.21 top). We can not confirm this dependence on the direction of incidence from observations, since no stations are available in this area. These effects are interesting because most buildings were located in this area during the M_L 6.1 event of 1946.

Figure 4.22 shows peak ground velocities obtained from the simulation of the 1946 earthquake. For this source configuration, no significant amplification can be observed in the old town of Sion. There are two effects that may explain this distribution: First, the incoming waves are propagating SW along the tributary valley towards the main basin, therefore no interference between reflected surface waves occurs in the northern part of the basin. Second, surface waves arriving from the direction of the epicentre have to pass the larger and deeper basin on the East on their way to the tributary basin. Due to the large impedance contrast between the unconsolidated sedimentary fill and the bedrock, these surface waves are diffracted towards the South, which can be seen in animations of the 1946 simulation (supplementary material). These results suggest that site effects have not contributed significantly to earthquake damage during the 1946 earthquake, at least not in the frequency range up to 4 Hz.

Certainly the validity of these results is limited due to the plane wave approximation and the uncertainties in the chosen source parameters. However, the orientation of the aftershock zone as well as macroseismical observations suggest that the 1946 earthquake ruptured from East to West on the northern side of the Rhône valley (Wanner, 1955). This implies that the Sion basin was excited by waves arriving mainly from the North to North-East, and the simulations of the Brugg event (Fig. 4.21 top) and the 1946 earthquake (Fig. 4.22) have shown that no amplification in the old town of Sion is expected for this direction of propagation.

These findings are supported by a reconstruction of the damage reported in the town of Sion after the 1946 earthquake (Stefan Fritsche pers. comm.). The

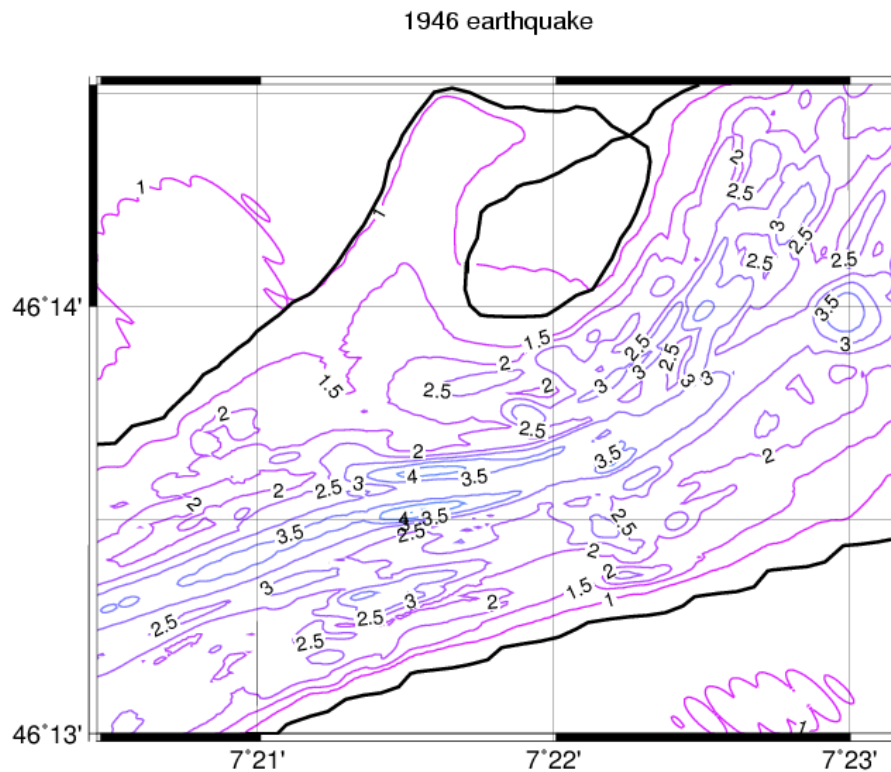


Figure 4.22: Normalized peak ground velocities obtained from the simulation of the 1946 Sierre earthquake.

affected buildings are evenly distributed over the old town, with no significant concentration on the Sionne alluvial fan.

4.8 Summary and Conclusions

We have analysed the seismic response of the Rhône valley at Sion from recorded weak motion signals and modelled the observations by numerical simulations of four selected events.

Site-to-reference Fourier spectral ratios of both horizontal components show a first peak at about 0.5-0.6 Hz, with an amplification level of up to 12 for some events. By analysing the motion perpendicular and parallel to the valley axis we show that this peak is caused by the SH_{00} and SV_0 fundamental modes of 2-D resonance. The frequency of these modes remains constant regardless of the position along the basin, though we observe some variability with respect to the analysed event. This confirms results from previous numerical studies performed for the Rhône valley (Frischknecht and Wagner, 2004; Frischknecht *et al.*, 2005).

Fourier spectral ratios are also exhibiting significant amplification at frequencies above 1 Hz, especially at about 3 Hz at most sites and at 10 Hz for the site SIOAE. Amplification levels of up to 18 can be observed at these frequencies. We applied the high-resolution frequency wavenumber technique and the multiple signal characterisation method to both recorded and synthetic seismograms. Results from these spatial array techniques show that the wavefield is dominated by edge-generated surface waves arriving from directions specific to the analysed events.

For three simulated events, we observed constructive interference between surface waves generated at adjacent valley borders, which is reflected by a narrow band of high peak ground velocities in the valley center. This effect is considered as a possible explanation for the unusually high amplification observed at the station SIOTE in the valley center, though our station spacing is not sufficient to confirm this assumption. Such central interference is only pronounced for plane waves arriving from the SW and NW; the interference pattern is getting more complicated for plane waves exciting the basin from the NNE and SE. Peak ground velocities obtained from the simulation of the 1946 Sierre main shock yield no amplification in the old town of Sion, which suggests that site effects were of little importance for the damage reported after this historical earthquake.

The 3-D numerical simulations are able to explain the main characteristics of the observations, especially the SH_{00} and SV_0 fundamental mode 2-D resonance frequencies and the edge-generated surface waves. We conclude that shear-wave velocities near the array center are probably higher than the values used in our velocity model. This could mean that the higher-velocity, coarse material from the Sionne alluvial fan extends further to the South than we assumed. Higher shear-wave velocities near the stations SIOAE and SIOTO would most likely improve the fit between observations and simulations at these sites (Fig. 4.11). For the stations SIOTE to SIOIS on the southern part of the basin, as well as for the site SIOO, the match between observations and simulations is generally quite good. While our simulations have yielded amplification at frequencies above 1 Hz, they have not been able to match the frequencies of these peaks for the simulated events (Fig. 4.8 to 4.10). This shows that more attention should be directed to the details of the shallow structure, especially the depth and velocity contrast of the two uppermost layers down to depths of about 200 meters.

Our results demonstrate that of 2-D and 3-D effects are important for the seismic response of the Sion basin, at least at frequencies up to 2.5 Hz. Peaks in observed Fourier spectral ratios suggest that edge-generated surface waves are also contributing to amplification at higher frequencies. Boreholes and ambient noise array measurements have revealed a shallow low-velocity layer of up to 10 meters depth. We have not included this layer in our numerical simulations, since our grid does not allow propagation of frequencies higher than 4 Hz. The amplification at ~ 10 Hz observed at the stations SIOAE and SIOTO (Fig. 4.11) could be attributed to such a shallow layer. While the frequency of the peak may

be reproduced by 1-D analysis using

$$f = \frac{V_s}{4h}$$

(e.g. $V_s = 200 \text{ ms}^{-1}$ and $h = 5 \text{ m}$), 1-D response alone is not able to cause an amplification level of up to 15 given the impedance contrast between the shallow layer and the deposits below. A combination of the basin edge effect with a shallow low-velocity layer or excitation of local surface waves inside the basin due to lateral heterogeneities could be possible explanations, but this should be verified by more detailed site investigations and higher-frequency numerical simulations.

We should keep in mind that the whole analysis presented in this text was focusing on weak ground motion, and the studied sites may respond to a future $M 6$ event in a different way. Some indications of non-linear soil behaviour were observed in the Rhône valley after the 1946 earthquake. While non-linear effects are unlikely to affect the deep resonance of the basin, the response of the shallow sandy layer may be modified significantly. This issue is currently being addressed with a fully non-linear 1-D model of wave propagation (Bonilla *et al.*, 2005).

Acknowledgments

We wish to thank the town of Sion and various individuals who supported us by operating seismic stations on their property. Thomas Stalder, Beat Rinderknecht, Peter Zweifel and other people from the electronics laboratory helped to implement the temporary array. Cécile Cornou assisted in site selection. Valentin Gischig was in charge of station maintenance. The routines for computation of Capon and MUSIC spectra were implemented by Matthias Ohrnberger. The 3-D FD simulations were run on the Babiaca cluster at San Diego State University, with support from Yifeng Cui and James Otto.

This research is part of the Interreg project SISMOVALP and the project SHAKEVAL, funded by the Swiss National Science Foundation (No. 200021-101920 and 200020-109177).

Chapter 5

Estimation of nonlinear site response in a deep Alpine valley

D. Roten¹, D. Fäh¹, F. Bonilla², S. Alvarez-Rubio¹, T. Weber³ and J. Laue³

¹ ETH Zurich, Institute of Geophysics, 8093 Zürich, Switzerland.

² Institut de Radioprotection et de Surete Nucléaire, BP 17, Fontenay-aux-Roses, Cedex, France

³ ETH Zurich, Institute for Geotechnical Engineering, 8093 Zurich, Switzerland

Article in preparation.

5.1 Introduction

It is generally accepted that soft, unconsolidated deposits tend to amplify earthquake ground motion, and increased damage associated with such soft soils has been observed during many devastating earthquakes.

A common seismological approach to quantify soft soil amplification consists in recording weak ground motion from local earthquakes on both rock and soft soil sites. These records are used to compute site-to-reference spectral ratios, on the basis of which frequencies of amplification are estimated and the amount of amplification is quantified. However, the validity of weak motion records to predict the site response during strong ground motion is questionable, because soft soils may exhibit nonlinear behaviour during strong earthquakes.

In the last decades the seismological community has become increasingly aware of the importance of nonlinear site response (e.g. Beresnev and Wen, 1996; Hartzell *et al.*, 2004; Bonilla *et al.*, 2005). Basically nonlinear soil behaviour marks the breakdown of the linear relationship between stress and strain. The shear modulus is reduced and damping increased at high strain levels. This increased damping may reduce the amplification of strong ground motion on soft soil, and even lead to a deamplification compared to a bedrock site. Additionally the reduced shear-wave velocity reduces the resonant frequency of the soft layer. Observational evidence for this type of soil response was, among others, found

in records of the 1989 Loma Prieta earthquake (Darragh and Shakal, 1991), the 1994 Northridge earthquake (Field *et al.*, 1997) and records from vertical arrays in Taiwan (Wen *et al.*, 1994). A comprehensive review of observed nonlinear soil behaviour can be found in Beresnev and Wen (1996).

However, nonlinearity does not necessarily involve reduced amplification or deamplification. Recent laboratory and field data suggest that cohesionless soils may partially recover their shear strength during cyclic loading due to their dilatant nature (Bonilla *et al.*, 2005). This effect produces large deformations and spiky shear stresses, and the resulting high-amplitude spikes in surface ground motion present significant accelerations.

Records of such spiky accelerograms at the Kushiro port (Iai *et al.*, 1995) and Wildlife refugee (Holzer *et al.*, 1989) vertical arrays demonstrate that these spikes are related to the soft unconsolidated soil. Bonilla *et al.* (2005) simulated the soil response of Kushiro port and Wildlife refugee using a fully nonlinear 1-D propagator, and obtained waveforms with high-frequency peaks riding on a low frequency carrier, similar to the observations. These findings demonstrate the complexity of soft soil response at high strain levels.

In this text we analyse the importance of nonlinear site effects for the Rhône valley in Southern Switzerland. In a previous study we estimated the seismic response of the Rhône basin using weak ground motion recorded on a temporary array in the city of Sion (Roten *et al.*, n.d.). Site-to-reference spectral ratios revealed an amplification level of up to 12 at the fundamental frequency of the basin between 0.5 and 0.6 Hz, which can be reproduced by 3-D numerical simulations using a detailed velocity model of the Sion basin. At some stations, amplifications of up to 20 were observed at higher frequencies of 8 to 10 Hz.

The Rhône valley is located in the area of highest seismicity in Switzerland, and the region was struck by several large earthquakes with magnitudes above 6 in the last decades, e.g. the 1946 M 6.1 earthquake of Sierre and the 1855 M 6.5 earthquake of Visp. Since the last large earthquake, extensive development has taken place especially on the soft unconsolidated Rhône deposits. The levels of amplification observed from weak ground motion would lead to unacceptably strong accelerations and significant damage during future M 6 events.

In order to prepare for future earthquakes engineers and seismologists need to know how nonlinear soil-behaviour will influence strong ground motion in the Rhône valley. Evidence of nonlinear soil response, such as cracks in the ground and lateral spreading, were observed at several sites after the 1946 and 1855 earthquakes (Fritsche *et al.*, 2006).

In this study we will assess the importance of nonlinear soil behaviour for the area using laboratory data of soil samples and numerical simulations with a fully nonlinear 1-D propagator (Bonilla *et al.*, 2005).

We will estimate at what level of rock acceleration reduced amplification, or even deamplification, may be expected. We will also assess how nonlinear soil response may affect signals recorded on the surface, especially considering the spiky waveforms discussed above.

5.2 Geophysical setting

The Rhône valley is a deeply eroded basin in the canton Valais in Southern Switzerland (Fig. 5.1). A few high-resolution seismic profiles (Pfiffner *et al.*, 1997;

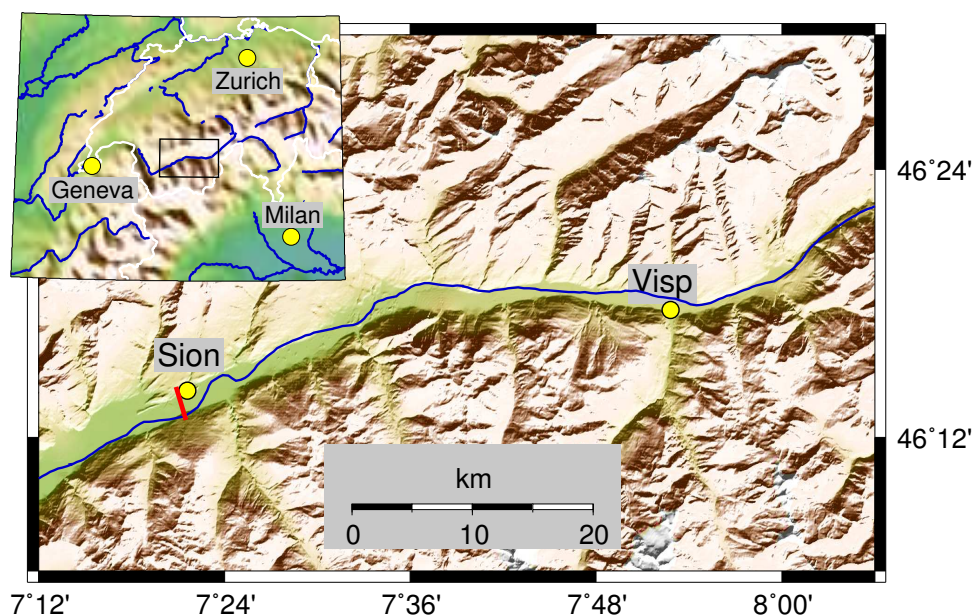


Figure 5.1: Map of the Rhône valley. Soil samples were taken in Visp. The red bar near Sion shows the location of the cross-section shown in Figure 5.3a.

Besson *et al.*, 1993) and gravimetric surveys (Rosselli, 2001) have been performed across the basin to examine the structure of the unconsolidated sedimentary fill. Below the city of Sion, the basin is about 500 meters deep. Array measurements of ambient noise were conducted at several places in the Rhône valley to constrain the shear-wave velocity of the sedimentary fill, especially in the Sion area (Roten and Fäh, 2007).

These ambient noise array measurements revealed a shallow superficial layer with shear-wave velocities between 150 and 250 ms^{-1} at most sites. Below this layer shear-wave velocities range between 320 and 500 ms^{-1} , and velocities of up to 1000 ms^{-1} were reported for the lowermost layer. At most recorded sites, including Martigny, Sion and Visp, a shallow layer with shear-wave velocities between 150 and 250 ms^{-1} was resolved. Figure 5.2 shows an example of inversion results obtained from an array measurement of ambient noise near Visp. The *geopsy*¹ program package (Wathelet *et al.*, 2004) was used for the frequency-wavenumber processing and the inversion of the dispersion curve. The uppermost low-velocity layer is about 30 meters thick at this site, with velocities between 200 and 250 ms^{-1} . Below this layer, the shear-velocity increases to more

¹available at <http://www.geopsy.org>

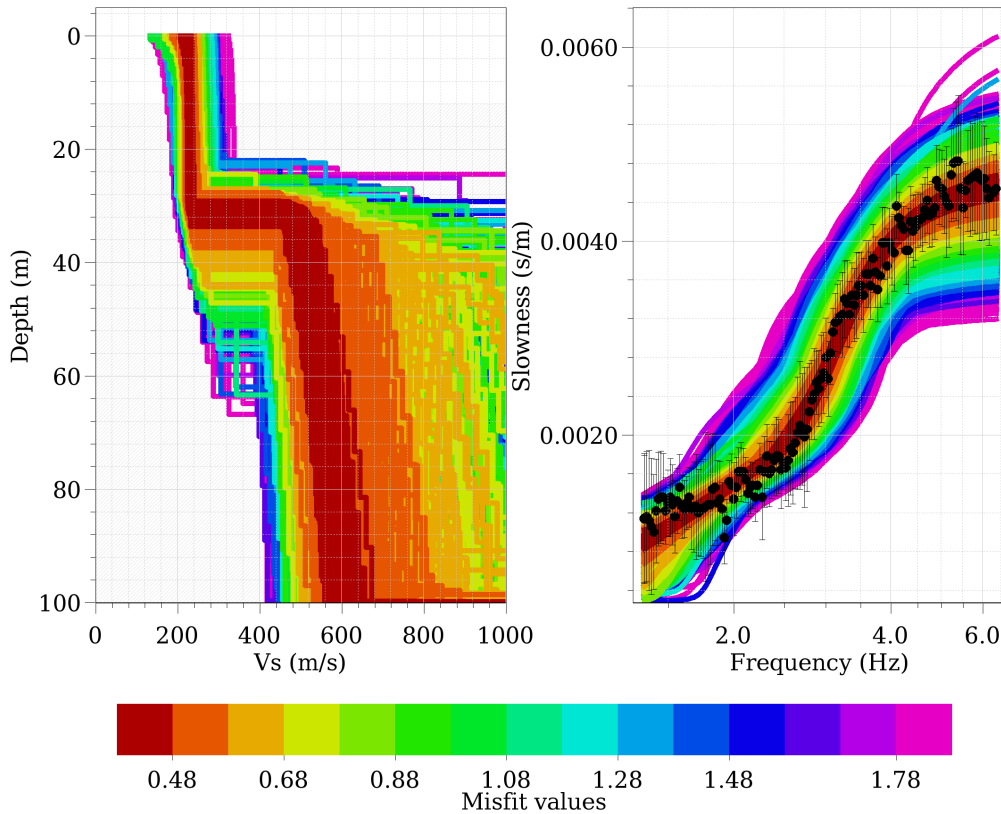


Figure 5.2: Inversion results from array measurement of ambient noise near Visp. *Right:* Recorded and modelled dispersion curves. *Left:* Shear-wave velocities of obtained models. Results with lowest misfit are plotted darkred.

than 500 ms^{-1} , which is similar to the values recorded at other sites. This low velocity layer is also encountered in borehole logs from various places in the valley. It consists of saturated sands and gravels from the Rhône, as most of the valley was a floodplain before the river was channelled in the 19th century.

To characterise the geotechnical properties of this low-velocity layer, a set of samples was taken from an excavation pit in Visp at a depth of 6 meters. We conducted a series of laboratory tests on these samples to estimate the parameters for the nonlinear analysis.

5.3 Method

We assume that only the uppermost low-velocity layer exhibits nonlinear behaviour, and use linear analysis for the remaining sedimentary fill down to the bedrock. We will use the *NOAH* program (Bonilla *et al.*, 2005), a nonlinear one-dimensional finite difference code which incorporates the strain-space multishear mechanism model (Towhata and Ishihara, 1985). However, we chose not to use 1-

D analysis for the whole sedimentary fill from previous experience. Both results from ambient noise (Roten *et al.*, 2006) and weak motion records (Roten *et al.*, n.d.) show that the deep response of the Rhône basin is caused by 2-D resonance, which causes higher amplification than 1-D response. In order to analyse both the 2-D response of the deep basin and the nonlinear response of the soft superficial layer, we combine results of 2-D numerical simulations for a cross-section through the valley with the 1-D nonlinear FD code.

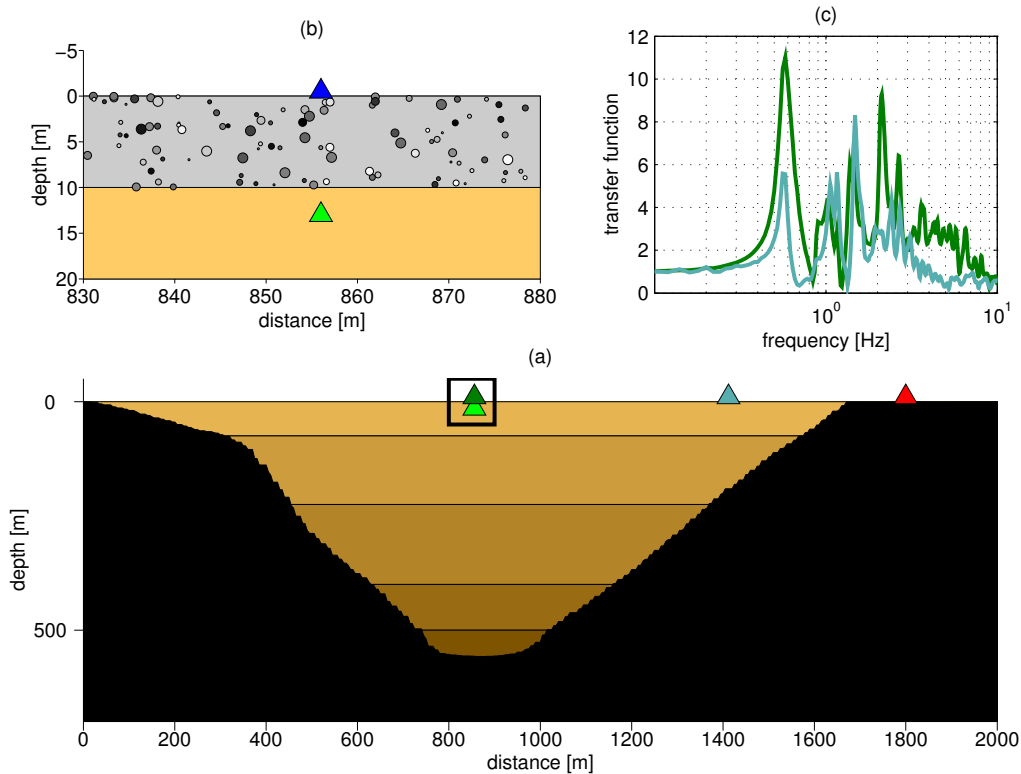


Figure 5.3: Overview of the different steps used to estimate the nonlinear response of the Sion basin. **(a)** 2-D cross-section for computation of transfer function between valley surface and bedrock. **(b)** The response of the superficial cohesionless layer is calculated using a fully nonlinear 1-D finite difference method. **(c)** Transfer function between a receiver near the valley centre (darkgreen) or near the basin edge (cyan) and outcropping bedrock.

5.3.1 Combined 2-D linear and 1-D nonlinear simulations

Figure 5.3a shows the cross-section that was used for the 2-D simulations. Although the soil samples were taken in Visp, we will model the response of the Sion basin, because our previous study of weak ground motion focused on the Sion area and no detailed velocity model has yet been developed for Visp. The cross-section was extracted from a 3-D velocity model created for the central

Valais region (Roten *et al.*, n.d.) and does not contain the low-velocity layer. Table 5.1 shows the physical properties of the individual layers in the velocity model. We will assume that the nonlinear properties of the soil are the same in Sion and

z	V_p	V_s	ρ	Q_p	Q_s	geological interpretation
0 – 10	800	200	1470	25	25	nonlinear sandlayer
10 – 75	1500	320	1600	25	25	deltaic sediments
75 – 225	1900	480	1900	25	25	lacustrine deposits
225 – 400	1900	750	1900	25	25	glaciolacustrine deposits
400 – 500	1900	800	1900	25	25	meltout and reworked till
500 – 560	2000	900	2000	25	25	subglacial deposits
0 – 750	4000	2325	2500	100	100	bedrock

Table 5.1: Geophysical parameters of the individual layers in the cross-section (Fig. 5.3). Depth ranges z are in m, velocities V in ms^{-1} and densities ρ in kgm^{-3} . Geological characterisations correspond to the interpretation by Pfiffner *et al.* (1997). The uppermost nonlinear layer was not used for the DBEM computations.

Visp, since no samples for Sion are available. The depth of the nonlinear layer was set to 10 meters to match observations made in the Sion area (Roten and Fäh, 2007).

Using the 2-D profile in Figure 5.3a, we simulated a vertically incident SV wave with the Direct Boundary Element Method (DBEM, Álvarez-Rubio *et al.*, 2004, 2005). Then we computed the transfer function between a station on bedrock and on the soil surface in the valley centre (Fig. 5.3a). Figure 5.3c shows the absolute value of the obtained transfer function. The 2-D resonance creates a dominant peak at about 0.5 Hz, and a further peak appears at 2 Hz.

The greatest uncertainty in our analysis comes from the input ground motion at the bottom of the velocity model. For the historical earthquakes reported in the Valais, the originating fault and source mechanisms are not known, and we have no indication about where a future earthquake will happen. We can, therefore, not simulate the input ground motion but have to use a stochastic method. We used the empirical method proposed by Pousse *et al.* (2006) to generate a set of non-stationary synthetic seismograms. To sample different levels of rock ground motion we used magnitudes of 4.0, 4.5, 5.0, 5.5, 6.0 and 6.5 and hypocentral distances of 5, 10 20 and 40 kilometers. We generated 60 synthetic seismograms for each magnitude-distance combination.

For each of the 1440 generated seismograms, the following steps were performed to compute the nonlinear ground motion on the valley surface:

1. The synthetic seismograms obtained with the method of Pousse *et al.* (2006) were computed for a velocity model with $V_{s30} = 900 \text{ ms}^{-1}$ (Cotton *et al.*, 2006). Therefore, the empirical seismograms are first deconvolved down to 511 meters, where the shear-velocity is 2325 ms^{-1} in the velocity model.

The resulting ground motion represents the signal recorded on outcropping rock next to the basin (red triangle in Figure 5.3a).

2. We compute the transfer function between a receiver near the valley centre and the outcropping rock from the results of the 2-D DBEM simulations. The ground motion on bedrock is convolved with this complex transfer function (darkgreen line in Fig. 5.3c) to obtain the signal on the surface at the basin centre (darkgreen triangle in Fig. 5.3a). The same procedure is followed for a receiver near the basin edge (cyan transfer function and triangle in Fig. 5.3).
3. Because the empirical input signal contains a random phase, convolution with the deterministic phase from the DBEM creates in some cases unrealistic seismograms, which exhibit an increasing envelope towards the end of the signal. From visual inspection of the 1440 synthetic seismograms, we rejected signals with unrealistic shapes. 928 signals were left for the remaining processing.
4. The signal on the basin surface is deconvolved to obtain the signal in a borehole at 12 meters depth (lightgreen triangle in Fig. 5.3a).
5. Finally the ground motion at the bottom of the soft layer is used as input for the NOAH finite difference code (Fig. 5.3b) using borehole boundary conditions. The results represents the acceleration on the surface of the nonlinear layer (red triangle in Fig. 5.3a).
6. Response spectra are computed for each signal on the soil surface and the corresponding rock ground motion. The ratio between the spectral acceleration on soil and rock is calculated for different frequencies.

This approach allows us to analyse the combined effects of the deep 2-D basin structure and the shallow nonlinear layer.

5.3.2 The Strain Space Multishear Mechanism Model

The *NOAH* simulation program (Bonilla *et al.*, 2005) is based on the Multishear Mechanism Model introduced by Towhata and Ishihara (1985), which describes the hysteretic behaviour of the stress-strain relationship and the generation of pore pressure. Iai *et al.* (1990a) expanded the model to account for the dilatant nature and cyclic mobility of sands.

In this model the behaviour of sand under the plane strain condition is represented as a relation between effective stress and strain vectors:

$$\vec{\sigma}' = \begin{pmatrix} \sigma'_x \\ \sigma'_y \\ \tau_{xy} \end{pmatrix} \quad \text{and} \quad \vec{\epsilon} = \begin{pmatrix} \epsilon_x \\ \epsilon_y \\ \gamma_{xy} \end{pmatrix} \quad (5.1)$$

where σ_x and σ_y represent normal stress, τ_{xy} represents shear stress and the strain components are given from displacements in u and v directions by

$$\epsilon_x = \frac{\partial u}{\partial x}, \quad \epsilon_y = \frac{\partial v}{\partial y}, \quad \gamma_{xy} = \frac{\partial u}{\partial y} + \frac{\partial v}{\partial x}. \quad (5.2)$$

The Multiple Shear Mechanism Model relates stress and strain through the following incremental equation (Iai *et al.*, 1990b):

$$d\vec{\sigma}' = K_a \vec{n}^{(0)} \vec{n}^{(0)T} (d\vec{\epsilon} - d\vec{\epsilon}_p) + \sum_{i=1}^I R_{L/U}^{(i)} \vec{n}^{(i)} \vec{n}^{(i)T} d\vec{\epsilon} \quad (5.3)$$

The first term ($i=0$) represents a volumetric mechanism specified with rebound modulus K_a , volumetric strain increment due to dilatancy $d\vec{\epsilon}_p$ and direction vector $\vec{n}^{(0)}$:

$$d\vec{\epsilon}_p = \begin{pmatrix} \frac{\epsilon_p}{2} \\ \frac{\epsilon_p}{2} \\ 0 \end{pmatrix}, \quad \vec{n}^{(0)} = \begin{pmatrix} 1 \\ 1 \\ 0 \end{pmatrix} \quad (5.4)$$

The second term in equation 5.3 represents the shear mechanism with the tangent shear modulus $R_{L/U}^{(i)}$. The subindices L and U indicate the loading and unloading processes, respectively, which are defined by the generalised Masing rules. Each mechanism i represents a one-dimensional shear-stress and shear-strain relation mobilised at angle θ_i given by:

$$\theta_i = (i - 1) \Delta\theta \quad (\text{for } i = 1, \dots, I) \quad \text{and} \quad \Delta\theta = \frac{\pi}{I} \quad (5.5)$$

The direction vectors $\vec{n}^{(i)}$ in Equation 5.3 are defined by

$$\vec{n}^{(i)} = \begin{pmatrix} \cos \theta_i \\ -\cos \theta_i \\ \sin \theta_i \end{pmatrix} \quad (5.6)$$

A detailed explanation of the method can be found in Iai *et al.* (1990a,b).

5.3.3 Dilatant behaviour soils

By examination of laboratory data, Towhata and Ishihara (1985) found that the pore pressure excess correlates with the cumulative shear work produced during cyclic loading. The model developed by Iai *et al.* (1990b,a) describes this correlation with five *dilatancy parameters*: The parameter w_1 controls overall dilatancy, p_1 the initial and p_2 the final phase of dilatancy. S_1 represents the ultimate limit of dilatancy and c_1 the threshold limit. These parameters are determined by fitting laboratory data from stress-controlled cyclic mobility tests. Details of this constitutive model can be found in Iai *et al.* (1990b,a).

To understand the behaviour of sand during cyclic loading, two different movements of the sand grains must be considered. Weak shearing causes a *slip-down* movement of sand grains in loose material, which results in a contractive

Description	Symbol	Value	Unit
in-situ dry density	ρ_d	1.41	kg/m ³
in-situ porosity	n	49.6	%
shear resistance angle	ϕ	39.7	°
phase transformation angle	ϕ_f	27.4	°
maximum hysteretic damping	ξ_{\max}	0.25	
maximum shear-velocity	V_s	210	ms ⁻¹

Table 5.2: Key soil parameters determined from laboratory testing

behaviour of the layer. Strong shearing, however, will cause a *roll-over* movement of sand grains, resulting in a dilatant behaviour of already compressed material. The *phase transition angle* ϕ_p marks the transition from contractive to dilatant behaviour in a plot of shear-stress vs. effective normal stress (Bonilla *et al.*, 2005).

5.3.4 Laboratory tests on soil samples

Several disturbed and undisturbed soil samples were extracted from an excavation pit at a construction site in Visp at 6.3 meters depth. The water table has been lowered artificially during construction below the site. For our computations we assume that the soil is fully saturated below the water table at 1.5 meters.

From these samples the porosity and density ρ were determined (Tab. 5.2). The angle of internal friction ϕ_f was determined to be 39.7° from standard triaxial tests. The phase transformation angle ϕ_p was estimated using

$$\tan(\phi_p) = \frac{5}{8} \tan(\phi) \quad (5.7)$$

(Ishihara and Towhata, 1982). A resonant column test was performed to determine the maximum shear modulus G_{\max} and maximum hysteretic damping ξ_{\max} . The largest measured shear-wave velocity was 210 ms⁻¹ at 200 kPa, which compares well with our results from the ambient noise array measurements (Fig. 5.2).

Six undrained cyclic triaxial tests with different shear stress were performed up to 5% peak-to-peak shear strain on the same samples to determine the parameters for the cyclic mobility model. A detailed description of all laboratory tests and results can be found in Weber *et al.* (2007).

5.3.5 Identification of dilatancy parameters

We followed the procedure described in Iai *et al.* (1990a) to identify the dilatancy parameters p_1 , p_2 , w_1 , S_1 and c_1 from the undrained cyclic triaxial tests. First we plotted the liquefaction resistance curve (Fig. 5.4), which shows the cyclic shear stress ratio vs. the number of cycles required to cause a shear strain of 5% double amplitude, The cyclic shear stress ratio is defined as the applied shear strain τ_{xy}

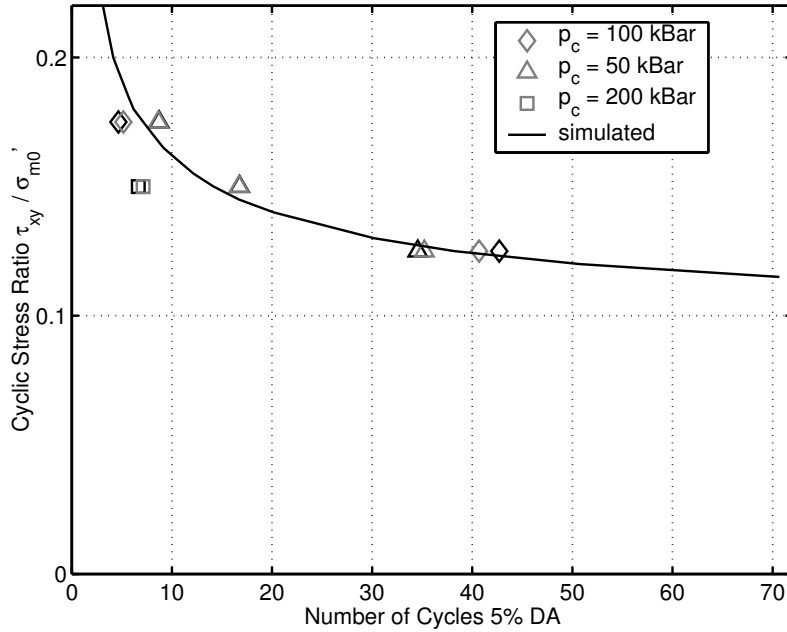


Figure 5.4: Liquefaction resistance curve. The cyclic shear stress ratio τ_{xy} / σ'_{m0} is plotted as a function of the number of cycles required to cause a shear strain of 5% double amplitude. Grey symbols denote results from the laboratory tests, black symbols results from the simulations. The solid black line shows the synthetic liquefaction resistance curve obtained from the determined dilatancy parameters (Tab. 5.3).

normalised by the initial effective confining pressure σ'_{m0} . For each cyclic test, we plotted the shear stress τ_{xy} , the shear strain γ_{xy} and the pore water pressure U as a function of the number of cycles. We determined the dilatancy parameters by fitting the simulated pore water pressure and strain amplitude to the observed values.

Figure 5.5 gives an example of observed and simulated cyclic tests. It also shows the stress-strain relationship (τ_{xy} vs. γ_{xy}) and the stress path (shear stress τ_{xy} vs. effective confining stress σ_m) as well as the effective confining stress σ_m as a function of the cycle number.

The parameter S_1 was set to 0.005 and c_1 to 1.0 as a first guess. Then we estimated p_1 and w_1 from the first part of the pore water generation curves by trial and error. Next the value for p_2 was determined by fitting the amplitude of the shear strain. We performed the analysis for all measured test data and found quite different values for p_1 , w_1 and p_2 depending on the analysed dataset.

As described in Iai *et al.* (1990a) we increased the value of c_1 by small steps and repeated the analysis for all our test data. Finally, using $c_1 = 1.5$ we found consistent values for p_1 , p_2 and w_1 (Tab. 5.3).

By computing the mean of these test results we obtained $p_1=0.42$, $w_1=1.80$ and $p_2=0.98$; these values will be used to characterise the nonlinear layer in our sim-

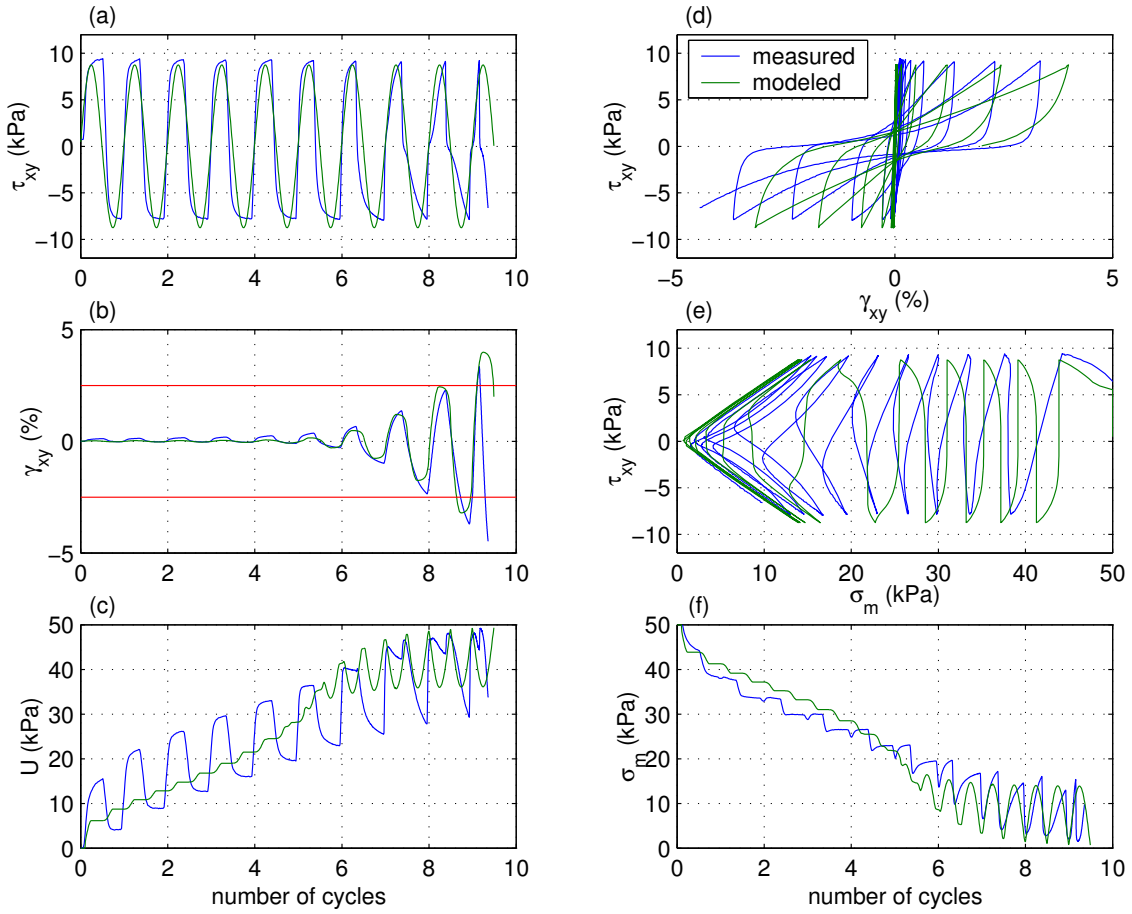


Figure 5.5: Results of undrained cyclic triaxial test number 8 (blue) on soil samples from Visp. The simulated curves (green) were obtained using $p_1=0.42$, $w_1=1.80$, $p_2=0.98$, $S_1=0.005$ and $c_1=1.5$ (Tab. 5.3). **(a)** shear stress τ_{xy} , **(b)** shear strain γ_{xy} , **(c)** pore water pressure U versus the number of cycles. **(d)** Shear-stress τ_{xy} vs. shear strain γ_{xy} . **(e)** Stress-path showing shear-stress τ_{xy} vs. effective mean stress σ_m . **(f)** Effective mean stress as a function of the number of cycles.

	p_1	p_2	w_1	S_1	c_1
Test 4	0.35	0.95	2.00	0.005	1.5
Test 5	0.40	1.05	1.50	0.005	1.5
Test 6	0.39	0.99	1.90	0.005	1.5
Test 7	0.38	0.95	1.55	0.005	1.5
Test 8	0.42	0.98	1.80	0.005	1.5
Test 9	0.40	1.00	1.10	0.005	1.5
mean	0.39	0.99	1.64	0.005	1.5
std.	0.02	0.03	0.30		

Table 5.3: Dilatancy parameters identified from the six laboratory tests

#	z	σ'_{ma}	V_s	ρ	ϕ	ϕ_p	K_0	ξ_{max}
1	1.5	7.2	200	1470	39.7	–	0.5	0.25
2	10	27.5	200	1470	39.7	27.4	0.5	0.25
3	12	44.5	320	1600	39.7	–	0.5	0.25

Table 5.4: Material properties for the nonlinear 1-D simulations. Depths z are in m, velocities V_s in ms^{-1} and densities ρ in kgm^{-3} . σ'_{ma} is the effective mean stress in kPa computed at the middle of each layer. K_0 is the coefficient of earth at rest.

ulations. Figure 5.4 shows the synthetic liquefaction resistance curve obtained with the identified dilatancy parameters.

5.3.6 1-D nonlinear simulations

The 1-D nonlinear simulation with the *NOAH* code were run for a 3-layer model (Tab.5.4). The top layer represents the unsaturated soil above the water table, the second layer the saturated nonlinear layer and the third layer corresponds to the deltaic sediments in Table 5.1. The coefficient of earth at rest K_0 represents the horizontal to vertical ratio of the initial effective normal stress. Given the young age of the deposit we assumed that the soil has not yet suffered strong perturbation due to seismic activity. Therefore we used $K_0 = 0.5$, which corresponds to normal consolidation.

We used a timestep dt of 10^{-4} seconds and a spatial step dx of 0.5 meters. The simulations were run up to 10 Hz, which corresponds to 40 grid points per wavelength. Since the deconvolved signal that served as input represents a simulated borehole record, it served as a dynamic boundary condition in the FD code.

5.4 Simulation results

We will first analyse the response of the nonlinear layer at the valley centre for a few selected events and then analyse the total site response for the complete set of synthetic earthquakes.

5.4.1 Example of linear soil response

Figure 5.6 shows the simulation results for a synthetic M 4.5 event at 40 km epicentral distance. Although the peak ground acceleration (PGA) on the outcropping rock (red) is less than 0.07 ms^{-2} , the response of the basin amplifies it to more than 0.20 ms^{-2} below the nonlinear layer (green). On the surface of the nonlinear layer the signal (blue) is further amplified, reaching a peak ground velocity of 0.31 ms^{-2} . We computed response spectra for the signals on the outcropping rock (red), below the nonlinear layer (green) and on the surface (blue). Amplification

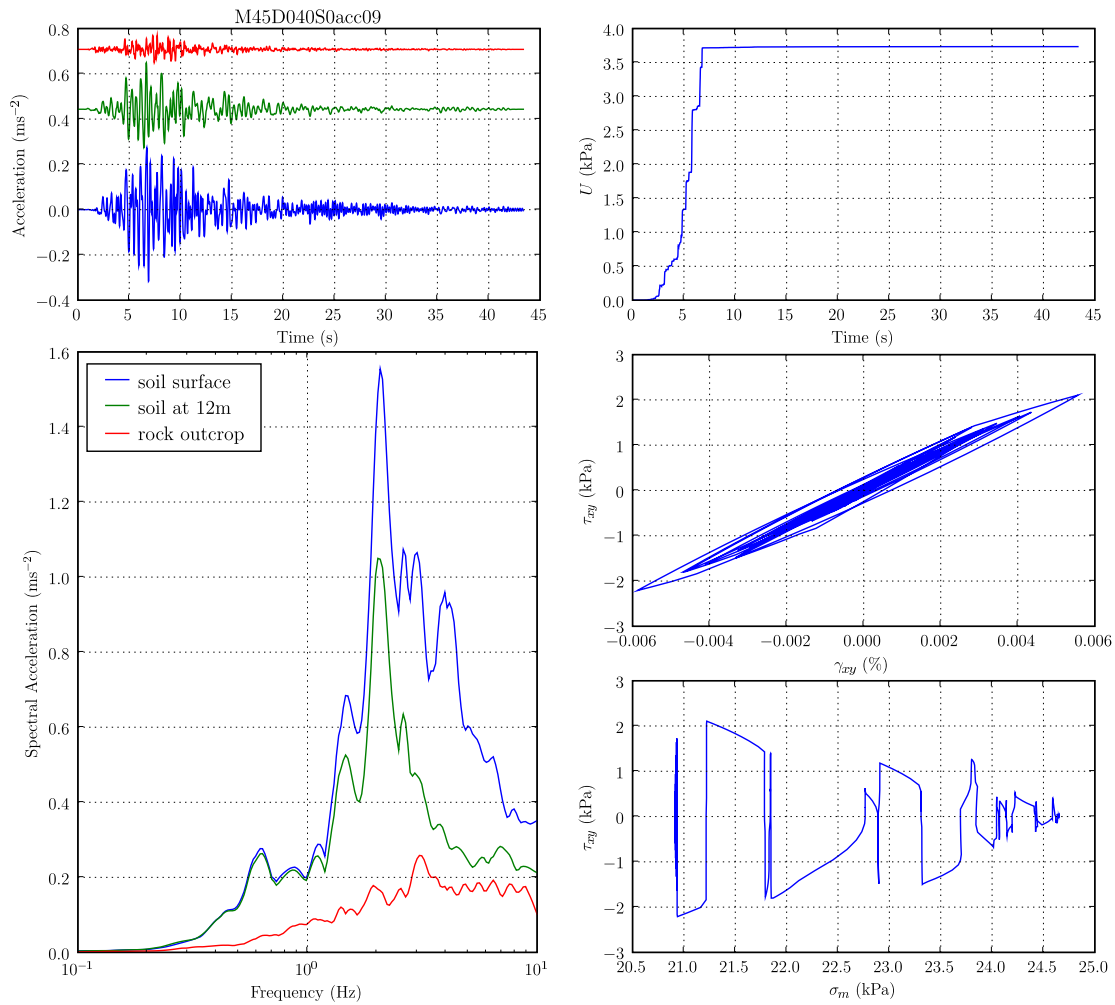


Figure 5.6: Results of combined 2-D linear and 1-D nonlinear simulations for a M 4.5 event at 40 km hypocentral distance. *Left*: Acceleration (*top*) and response spectra for 5% damping (*bottom*) representing ground motion on outcropping rock (red), below the nonlinear layer (green) and on the soil surface (blue). *Right*: Pore water pressure development (*top*), stress-strain relationship (*centre*) and stress path (effective confining pressure vs. stress, *bottom*) in the middle of the layer.

by the deep basin structure creates a significant peak at 2 Hz below the uppermost layer, which is even more dominant on the surface of the low-velocity layer (Fig. 5.6). Additionally a peak appears at approximately 5 Hz on the soil surface; this peak represents the resonance frequency of the shallow deposit. The fundamental frequency of the basin at 0.6 Hz is not affected by the uppermost layer. The right column in Figure 5.6 shows the development of excess pore water pressure, the stress-strain relation and the stress path. The excess pore water pressure increases quickly after the arrival of the first energetic S-wave phases, but it re-

mains well below the confining pressure. The stress-strain relation shows that the soil behaviour is approximately linear for this level of input ground motion.

5.4.2 Example of cyclic mobility

Figure 5.7 shows an example simulating an M 5 event at 40 km hypocentral distance. The first 10 seconds show a similar amplification as the linear example 5.6. The excess pore water pressure, however, increases very quickly, and almost

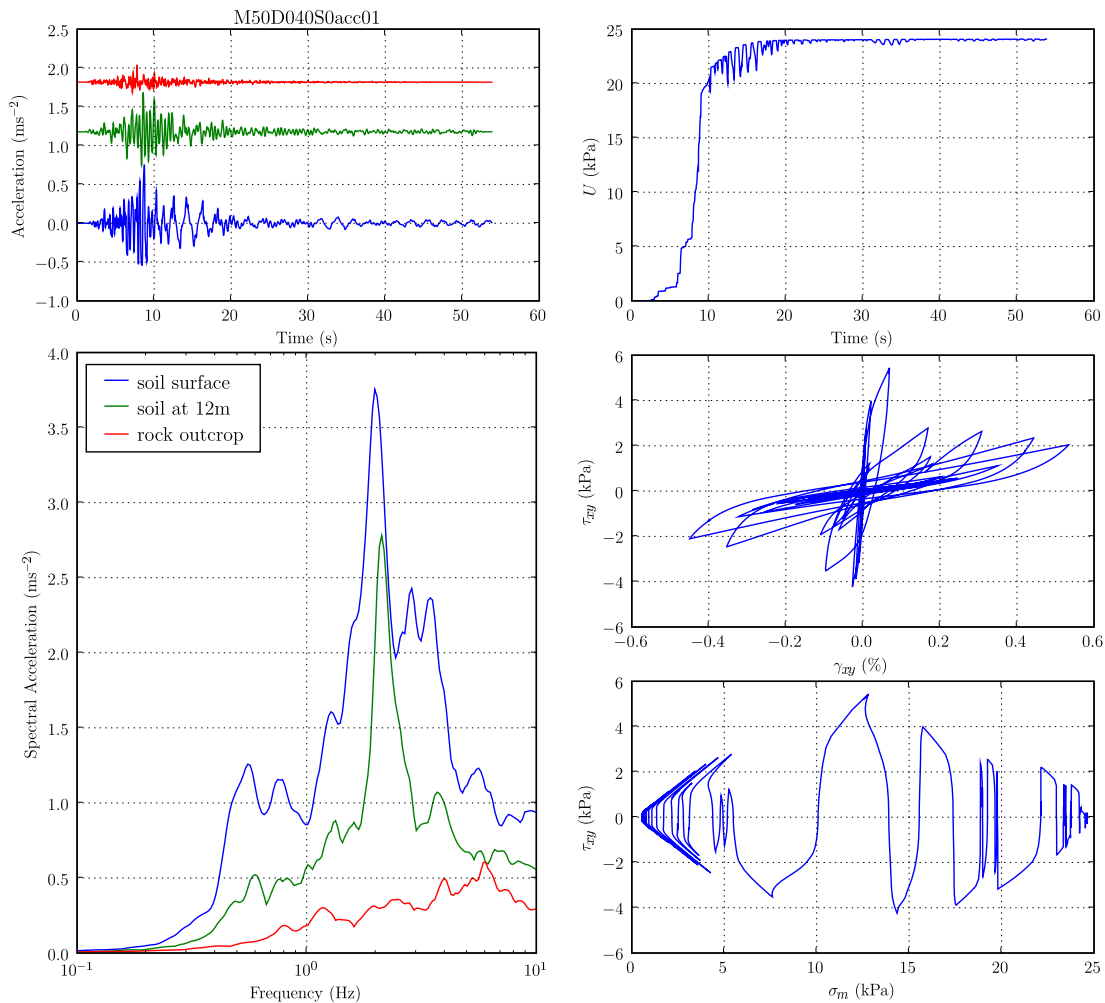


Figure 5.7: Like Figure 5.6, but for an M 5.0 event at 40 km hypocentral distance

equals the confining pressure after 10 seconds. Both the stress-strain relation and the stress-path show that the soil enters dilatant behaviour for this weak input ground motion. After approximately 10 seconds, spiky waveforms appear on the surface accelerogram.

Even though the soil exhibits cyclic mobility, it causes an overall amplification of response spectra at 2 and 5 Hz. Unlike in the linear case, the low-frequency

peak caused by the deep basin at 0.6 Hz shows a higher amplitude on the surface than at 12 meters depth. This is probably directly related to the triangle-shaped long-period phases in the surface accelerogram (Fig. 5.7).

5.4.3 Example of reduced amplification

In Figure 5.8, the simulation results for an M 5.5 event at 20 km hypocentral distance are shown. In this example the peak ground motion is 0.5 ms^{-1} on rock and 1.5 ms^{-1} below the nonlinear layer. The signal on the surface of the cohesionless soil reaches only 1.1 ms^{-1} PGA and shows the characteristic high-frequency spikes riding on a low-frequency carrier. A comparison of response spectra shows that the nonlinear layer causes a reduction of overall amplification, especially at high frequencies. Additionally the resonance frequencies are shifted to lower values. The pore water pressure increases very quickly and almost equals the confining pressure after three seconds.

5.4.4 Example of liquefaction

Figure 5.9 shows the same analysis for an M 6.5 earthquake located 20 km from the site. For this event the peak ground acceleration reaches 3 ms^{-2} below the nonlinear layer, though the spikes on the surface reach only 2.1 ms^{-2} . A comparison of response spectra shows that the nonlinearity results in an overall deamplification between rock and soil in the frequency range from 5 to 7 Hz. The deep basin response is shifted towards lower frequencies and reduced in amplitude. The shear strain is reaching 9% at 5 meters depth. Liquefaction is not directly implemented in the *NOAH* program; though if we follow the convention that 5% deformation means failure, liquefaction occurs for this event.

5.4.5 Dependency of spectral amplification on input ground motion

We computed spectral ratios from the synthetic ground motion on rock and on the surface of the nonlinear layer for all synthetic events. Then we calculated the ratio between spectral acceleration on the soil surface and on rock for different frequencies. Figure 5.10 shows the ratio of spectral acceleration (SA) at the valley centre as a function of rock spectral acceleration for 0.5, 1, 1.5, 2, 3, 5, 7.5 and 10 Hz as well as PGA (98 Hz). The SA ratios show a great variability at all levels of rock SA, which is a consequence of the complicated response of nonlinear soils. To outline the general trend a 3rd order polynomial was fitted through the data after computing the natural logarithm of the SA on rock and the amplification ratio. At most frequencies, the SA ratio is independent of the rock SA for input SA below 0.10 ms^{-2} , which corresponds to linear soil behaviour. For higher levels of input SA the ratio decreases and eventually drops below unity for rock SA above 2 – 3 ms^{-2} . This reflects the decreased amplification and deamplification occurring

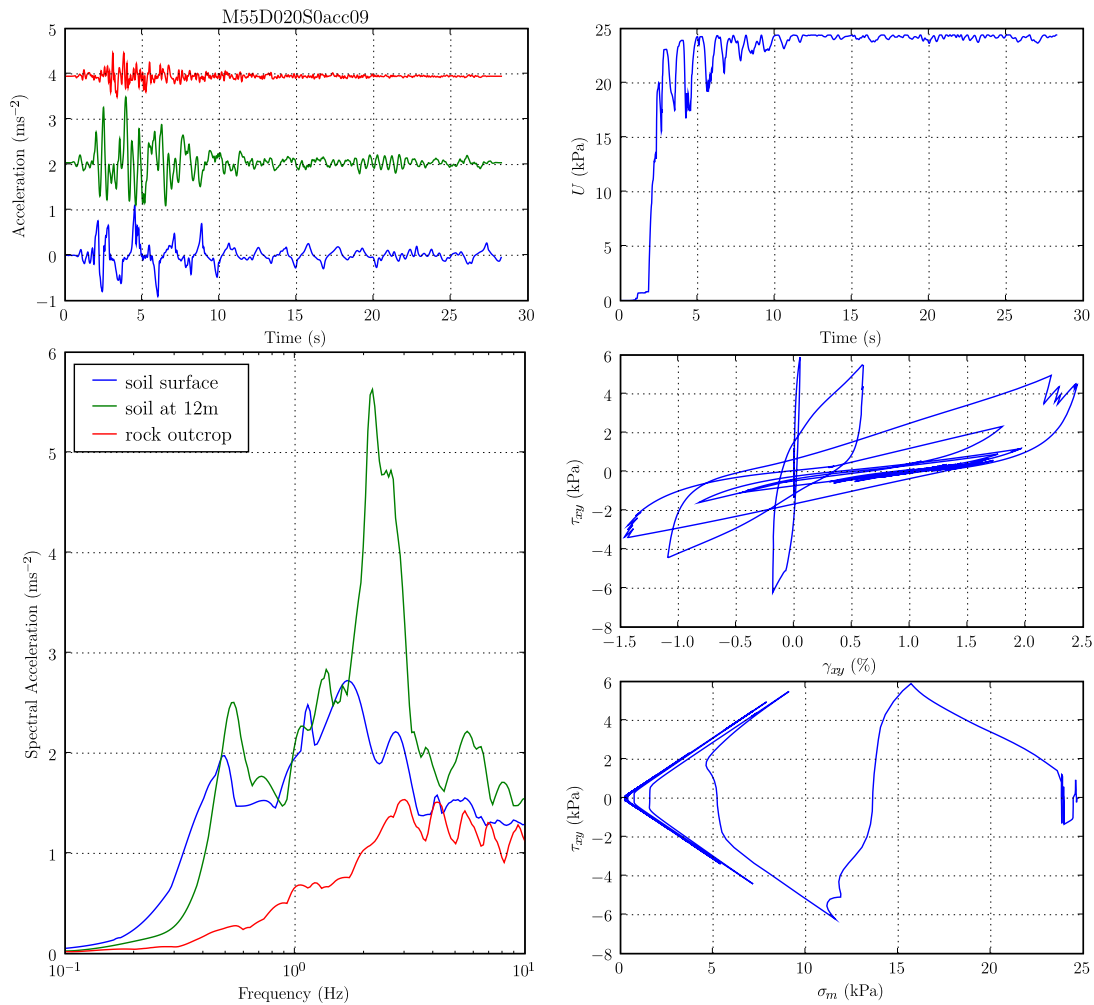


Figure 5.8: Like Figure 5.7, but for an M 5.5 event at 20 km hypocentral distance

for high levels of input ground motion. These results suggest that soil nonlinearity becomes important for very low levels of input ground motion compared to world-wide observations of nonlinearity. Beresnev and Wen (1996) stated that the onset of nonlinearity can be appreciated for rock accelerations above 1 to 2 ms^{-2} based on field seismological observations, which is clearly higher than the level of 0.5 ms^{-2} above which decreased amplification becomes notable in our results (Fig. 5.10).

At low frequencies ($0.5 - 2 \text{ Hz}$), the SA ratio is often higher for rock SA of about 0.10 ms^{-2} than for 0.01 ms^{-2} , which is the opposite of the expected behaviour. This suggests that increased amplification may occur at the onset of cyclic mobility before reduced amplification becomes notable. This confirms the earlier observations from the examples shown in Figures 5.6 and 5.7, where the low-frequency resonance of the basin was amplified by the uppermost nonlinear layer.

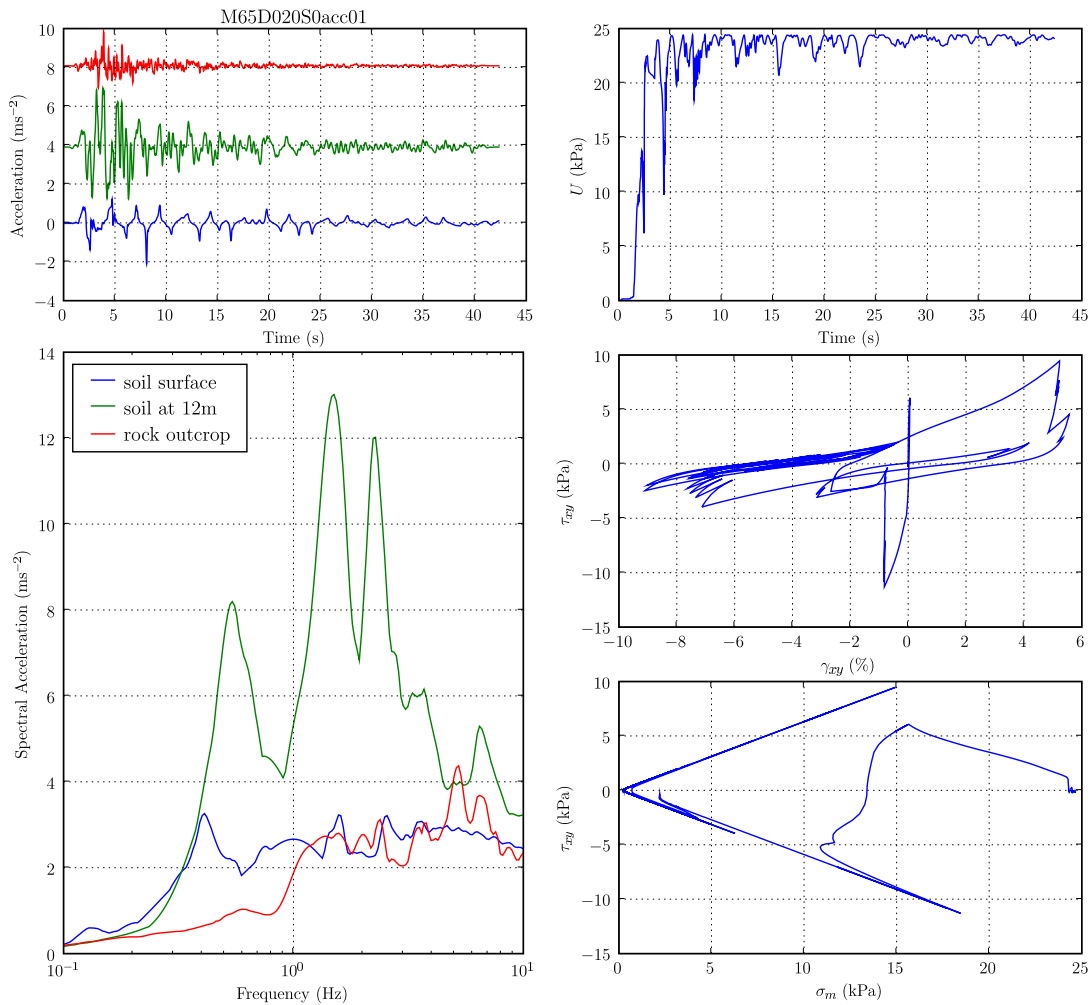


Figure 5.9: Like Figure 5.7, but for an M 6.5 event at 20 km hypocentral distance

Figure 5.11 shows the spectral ratios for a receiver near the basin edge as a function of spectral acceleration on rock. Compared to the valley centre the spectral ratios are generally lower, especially at 0.5 Hz and between 5.0 and 10 Hz. This reflects the differences in the transfer functions of the two receiver positions (Fig. 5.3c). The differences are more pronounced for low levels of rock spectral acceleration than for high levels. Nonlinearity therefore tends to reduce the differences in site response between the two receiver positions. Near the basin edge reduced amplification becomes appreciable for spectral acceleration exceeding about 0.5 ms^{-1} on rock.

5.4.6 Absolute spectral accelerations

In Figure 5.12 we have plotted the response spectra for 5% damping of the simulated events with magnitudes between 6.0 and 6.5 and with hypocentral distances

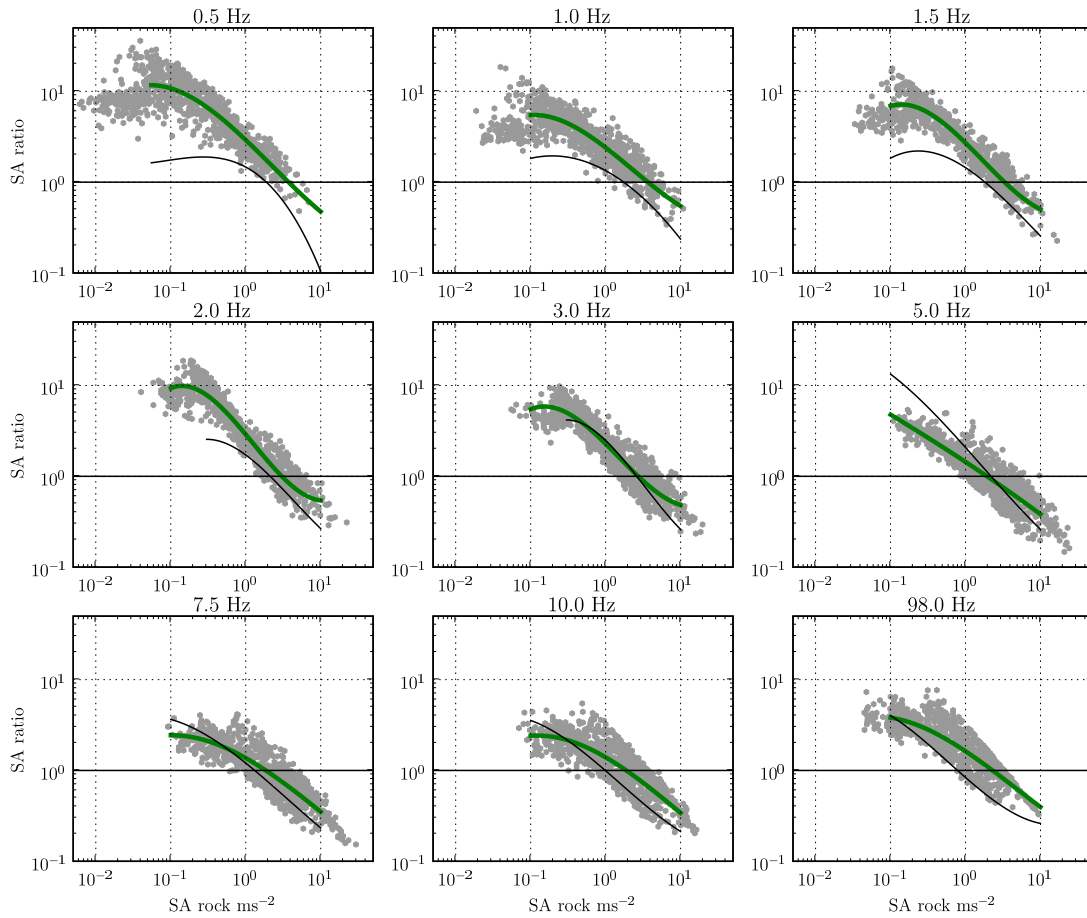


Figure 5.10: Ratio between spectral acceleration on the surface at the valley centre and rock as a function of spectral acceleration on rock for different frequencies and peak ground acceleration (98 Hz). The green lines show 3rd order polynomials fitted through the logarithm of the ratios. The thin black lines shows the fit obtained from 1-D nonlinear simulations neglecting the 2-D basin.

between 10 and 40 km. Both results for the basin edge and for the valley centre are shown.

For comparison the applicable design spectra SIA261 is shown Schweizerischer Ingenieur-und Architektenverein (2003). The design spectra was computed for soil type "D", which is defined as a deposit of unconsolidated fine sands, silts and clays with a thickness of more than 30 meters and shear-wave velocities between 150 and 300 ms^{-1} .

At the valley centre the design spectra is exceeded during most simulated events at a frequency of approximately 0.5 Hz. This frequency corresponds to the 2-D resonance frequency of the basin, which is shifted towards lower values by the nonlinear behaviour of the uppermost soil. Exceedance of the design spectra by a factor of up to 2 occurs for many simulated events at this frequency. Spec-

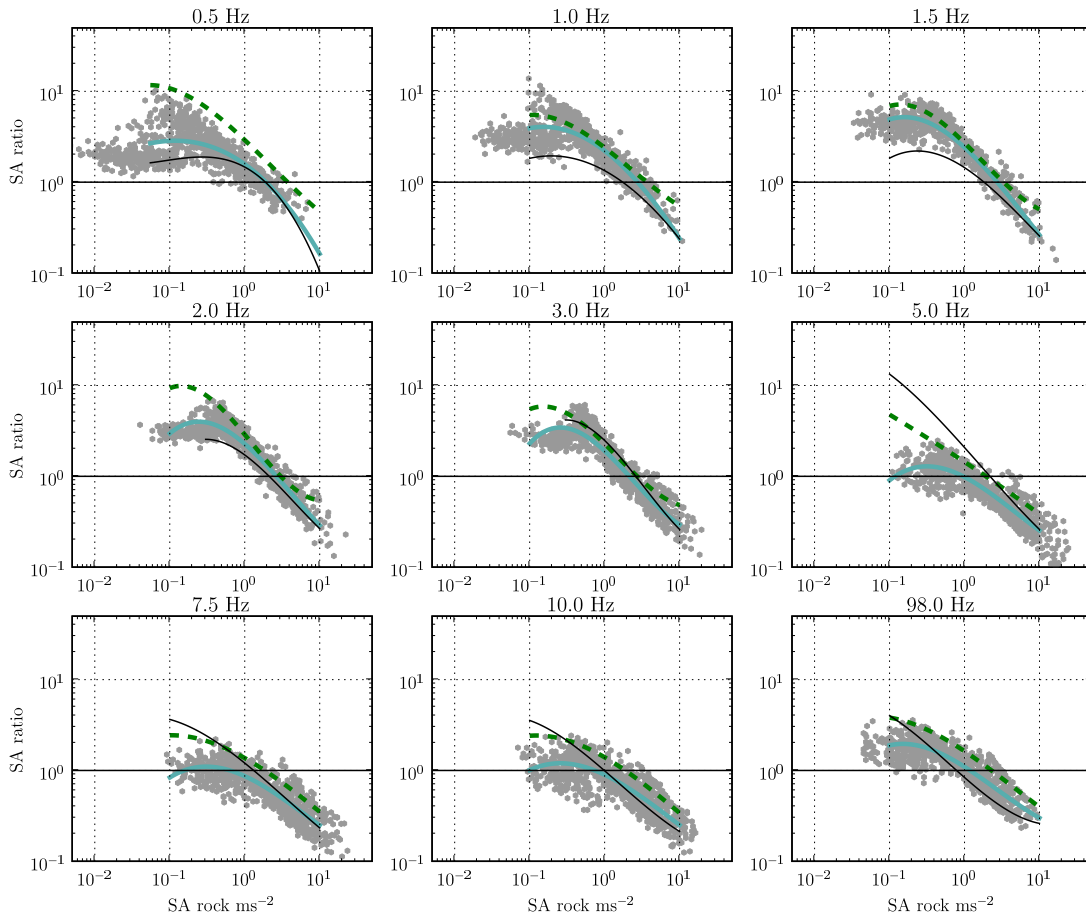


Figure 5.11: Like Figure 5.10, but for a receiver near the basin edge. Cyan lines show the 3rd order polynomials fitted through the ratios; the polynomials for the valley centre are given by dashed green lines.

tral accelerations exceeding the design spectra can also be observed for a number of events at about 0.70 Hz. At higher frequencies above 1 Hz the spectral acceleration of most events remains below the design spectra, and the exceedance amounts to less 30% for the vast majority of the simulated events.

Near the basin edge no significant exceedance of the design spectra occurs at 0.50 Hz, and the spectral acceleration remains below the norm for the prevailing number of events at higher frequencies.

5.4.7 Influence of deep basin on nonlinear soil behaviour

In order to estimate the influence of the deep basin on the overall analysis of non-linearity we repeated the above calculation without using the transfer function of the 2-D simulation. Instead, the synthetic seismograms obtained by the method of Pousse *et al.* (2006) were deconvolved down to a depth of 12 meters and fed di-

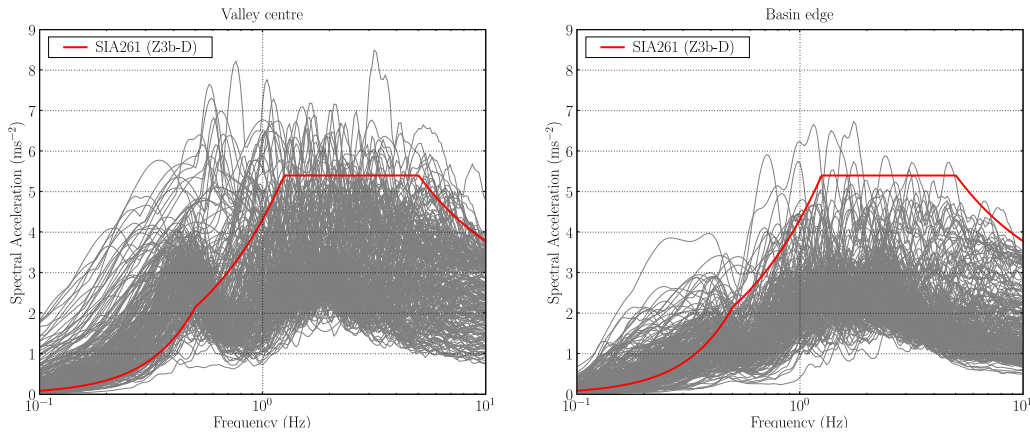


Figure 5.12: Absolute response spectra of all simulated events with magnitudes between 6.0 and 6.5 and hypocentral distances between 10 and 40 km. The red line shows the design spectra of the norm SIA261 for soil type "D" (Schweizerischer Ingenieur-und Architektenverein, 2003).

rectly into the *NOAH* program as input ground motion. The result represents the ground motion on the surface of a shallow nonlinear low-velocity layer overlying a horizontally layered structure.

The black lines in Figure 5.10 and 5.11 show the polynomials obtained from these purely 1-D nonlinear simulations. As we observed earlier the differences are most pronounced for low levels of input ground motion, and the polynomials obtained from the three different methods tend to coincide for high acceleration levels on rock (Fig. 5.11).

For frequencies between 0.5 and 2.0 Hz the spectral ratios obtained for the basin edge and the basin centre are generally larger than those obtained for a horizontal structure. At higher frequencies (5.0 - 10 Hz) the spectral ratios obtained from the 1-D simulations are similar to those obtained for the basin centre, while the amplifications near the basin edge are lower than those of the 1-D simulations for low acceleration levels on rock.

The onset of nonlinearity occurs at comparable levels of rock SA for the purely 1-D simulations and the simulations including the basin structure. This implies that the main reason for the early onset of nonlinearity is the soil, rather than the influence of the basin. The dilatancy parameters obtained from the cyclic tests show that the soil is very weak, which is reflected by the strong impact of cyclic mobility in our simulations.

5.4.8 Evaluation of liquefaction potential

To estimate the importance of soil liquefaction we evaluated the maximum strain encountered in the simulated scenarios. For each magnitude-distance combination, we determined the number of events for which liquefaction would be trig-

gered according to the 5% strain convention, and divided it by the total number of events simulated for the same magnitude-distance combination. Figure 5.13a shows a contour plot with the occurrence of 5% strain or more as a function of magnitude and distance for the basin centre and the basin edge. For the basin centre (Fig. 5.13 left) our simulations indicate that liquefaction may occur at rather large hypocentral distances for a given magnitude, e.g. in 10% of the cases at 20 kilometers hypocentral distance for an M 5.5 event.

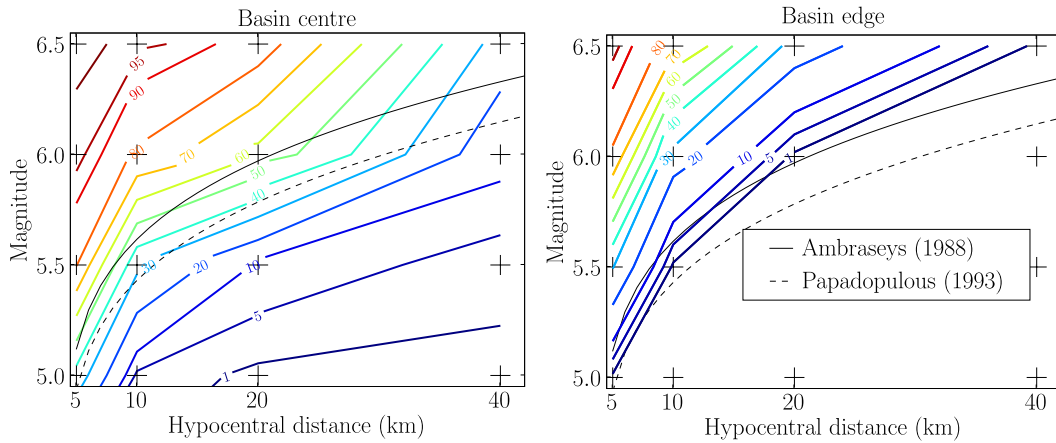


Figure 5.13: Occurrence of liquefaction (%) as a function of hypocentral distance and magnitude for the valley centre (*left*) and the basin edge (*right*). For comparison two empirical relations are shown.

For comparison we are considering two empirical relations that estimate the limiting epicentral distance of sites at which liquefaction has been observed as a function of moment magnitude for shallow earthquakes. Since the synthetic earthquakes generated for this study are based on the hypocentral distance we used the Joyner-Boore distance (Joyner and Boore, 1981) assuming a depth of 5km to evaluate the empirical relations.

Figure 5.13 (left) compares the liquefaction occurrence obtained from our analysis with empirical relations from Ambraseys (1988) and Papadopoulos and Lefkopoulos (1993). The results for the valley centre are yielding soil liquefaction at distances well above those provided by the empirical relations. Given an M 5.5 earthquake, for example, our simulations generated soil liquefaction in 10% of the cases at a hypocentral distance of 20 km. The empirical relations by Ambraseys (1988) and Papadopoulos and Lefkopoulos (1993) yield a limiting distance of 8 and 12 km, respectively, for an M 5.5 event.

The results for the basin edge (Fig. 5.13 right), however, are in agreement with the distance limits computed from the empirical relations, and liquefaction is only triggered at distances below the empirical threshold. This suggests that the strong amplification of the incident wavefield at the basin centre extends the radius within which liquefaction must be expected.

5.5 Discussion

5.5.1 Historical reports of liquefaction

After the 1855 M 6.4 earthquake of Visp, a number of surface changes on soft soil were observed that may be related to liquefaction (Fritsche *et al.*, 2006). Sources reported subsidence of farmland below the Rhône level, wavelike structures on previously even soil and wide cracks in the ground. The exact position of these observations is not known, though they were made in the vicinity of our sampling location in Visp.

The epicentre of the 1855 mainshock was located approximately 7 km from Visp. Using the macroscopically determined depth of 12 km, this places the sites at about 14 km hypocentral distance. Considering the liquefaction occurrence in Figure 5.13 (left) for this magnitude and distance, it is very realistic that liquefaction did occur during this event, because it happened in 90% of the simulated scenarios at the valley center. Even for the simulations near the basin edge (Fig. 5.13 right) liquefaction occurred in 40% of the cases for a magnitude of 6.4 at 14 km hypocentral distance. However, we must keep in mind that these liquefaction occurrences may not be accurate for Visp, because they were computed with the transfer function of the Sion basin.

5.5.2 Influence of deep valley resonance

It is likely that long-period excitation of the nonlinear layer is important for liquefaction, since the differences between the basin centre and the basin edge are most pronounced at low frequencies (Fig. 5.11). Figure 5.14 compares simulated accelerations at the valley centre with accelerations for the basin edge for an M 6.5 event at 40 km hypocentral distance (Example discussed in section 5.4.4).

The acceleration time series below the interface seem quite similar for the basin centre and the basin edge (Fig. 5.14 top). However, the input ground motion at the basin centre carries four times more energy at 0.6 Hz than the input ground motion near the basin edge. This is related to the deep two-dimensional resonance of the basin, which produces the highest amplification in the central part of the valley.

On the surface of the soft soil sharp spikes appear in the accelerogram at the valley centre, which are not present near the basin edge (Fig. 5.14 bottom). These peaks represent the highest acceleration and are related to the maximum strain. Similar to observations made for Kushiro port (Iai *et al.*, 1995; Bonilla *et al.*, 2005), the high-frequency spikes are riding on a low-frequency carrier. In our case, the low-frequency carrier corresponds to the deep basin response at 0.6 Hz, which is still very dominant on the surface of the nonlinear layer, and shifted slightly towards lower frequencies (Fig. 5.14 bottom). In the example in Figure 5.14 the maximum strain reaches 9% at the valley centre, but only 4% near the basin edge. This shows that the frequent occurrence of liquefaction near the valley centre (Fig. 5.13) can be attributed to the strong long-period amplification.

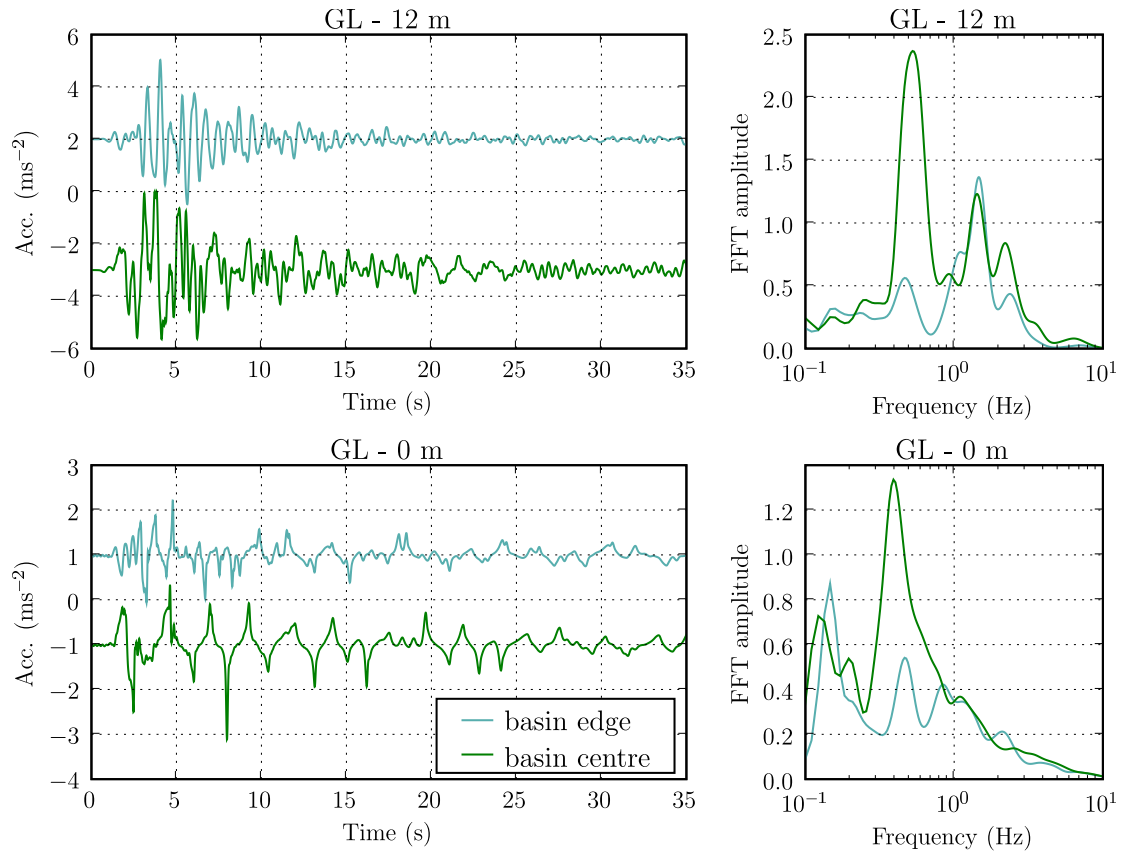


Figure 5.14: Comparison between simulated ground motion near the basin edge (cyan) and near the basin surface (darkgreen). Acceleration time series (*left*) and FFT amplitudes (*right*) are shown at 12 meters depth (*top*) and on the surface (*bottom*).

5.5.3 Limitations

Certainly this study is based on a number of assumptions and there are some limitations. We assumed that only the uppermost layer will exhibit nonlinear response, and that the whole remainder of the sedimentary fill can be described as linear. No soil samples of the lower sedimentary layers are available which would be required to determine the dilatancy parameters. Since both shear-wave velocities obtained from ambient noise and boreholes show that the uppermost layer differs from the deeper deposit, extrapolation of the available dilatancy parameters to greater depth would not represent a reasonable option.

The empirical relation used for the synthetic input seismograms is based on observations including sites that exhibit strong 2-D and 3-D effects, similar to the Rhône basin. Since these signals were deconvolved using 1-D response only and then the 2-D response was added, it is possible that this approach overestimates the input ground motion at the bottom of the nonlinear layer. More accurate results could be obtained with a deterministic approach, though this would require

knowledge of location, magnitude and rupture details of possible future earthquakes.

Finally the soil samples extracted from one location site may not be representative for the whole Rhône valley. To fully assess the impact of nonlinearity more laboratory tests with samples from different locations would be needed.

The parameter of earth at rest K_0 is not well constrained. We assumed normal consolidation because the soil is rather young, though we don't know to what extent it has already been perturbed by seismic activity. A higher value of K_0 would increase the strength of the material and reduce the nonlinear effects.

5.6 Summary and Conclusions

We have analysed nonlinear soil response in the Rhône valley by convolving empirical input ground motion with the 2-D linear valley response and propagating it through a nonlinear layer using the 1-D FD program *NOAH*. The dilatancy parameters that are required for the nonlinear simulations were obtained from fitting of laboratory data and show that the soil is rather weak.

The simulation results suggest that soil nonlinearity becomes appreciable at spectral acceleration levels as low as 0.5 ms^{-2} on rock (Fig. 5.10). At low frequencies ($< 2 \text{ Hz}$), the onset of cyclic mobility may cause an increase in overall amplification compared to the linear case. With increasing intensity of input ground motion the amplification between rock and soil surface decreases, and deamplification occurs at rock spectral accelerations exceeding approximately 2 ms^{-2} . For most simulated events the absolute spectral acceleration remains below the design spectra for frequencies above 1 Hz. Only near the valley centre the norm is generally exceeded at frequencies of about 0.50 Hz.

However, it is important to note that strong nonlinear effects are very likely to occur at high levels of input ground motion. Figure 5.15 shows the strain level at 4.5 meters depth near the valley centre as a function of peak ground acceleration on rock. Although the relation exhibits a strong variability, the liquefaction criterion of 5% strain is exceeded by a prevailing number of events for rock PGA above 2 ms^{-2} .

Evaluation of the liquefaction occurrence for specific magnitudes implies that soil failure may occur at distances exceeding those predicted by empirical relations at the valley centre. Near the basin edge, however, the simulated liquefaction occurrence agrees with the empirical relation. We suggested that amplification of long-period ground motion by the deep basin response may provide the low-frequency carrier for the high-frequency spikes, which create the largest acceleration and, therefore, provide the necessary strain to trigger liquefaction. This shows that the response of the whole structure needs to be simulated in order to estimate the importance of non-linear soil behaviour.

To isolate the impact of the 2-D basin structure we repeated all the simulations using only the 1-D nonlinear method. Results of these 1-D nonlinear simulations differ from the combined simulations especially at low frequencies, though

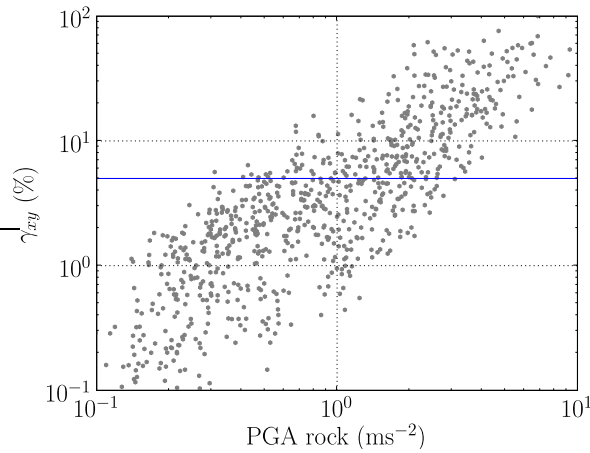


Figure 5.15: Strain γ_{xy} (%) at 4.5 meters depth as a function of PGA on rock for the valley centre.

they are producing cyclic mobility at similarly low levels of input ground motion. This suggests that the strong dilatant nature of the sampled soil, rather than the 2-D basin effect, is responsible for the early onset of nonlinearity. We observed that nonlinearity reduces the differences in spectral ratios between the basin centre, the basin edge and the horizontally layered velocity model at high levels of ground motion on bedrock.

In this study we used a very simple approach and we treated wave propagation in nonlinear media only in one dimension. The disadvantage of this method is that effects of nonlinearity on 2-D and 3-D phenomena such as edge-generated surface waves are neglected.

The results of this study suggest that nonlinear soil behaviour is an important factor in the analysis of site effects in the Rhône valley. Results of the simulations confirm that nonlinearity is not just reducing the amplification between soil and bedrock in all cases, but more complicated phenomena may develop which impose additional hazard. Spiky waveforms due to partial strength recovery (Bonilla *et al.*, 2005) evolved in many simulated scenarios, and it seems that this effect increases the amplification for low levels of input ground motion (Fig. 5.7). Soil liquefaction poses a significant threat to structures, and our simulation suggest that liquefaction may occur before deamplification.

However, more soil samples and simulations are needed to analyse the importance of nonlinear site response for the whole Rhône basin. Since our results suggest that cyclic mobility will occur for rather low levels of input ground motion, records of moderate local earthquakes on a vertical array, with accelerometers and piezometers at different depths and on the surface, would allow to reject or confirm these findings.

Chapter 6

Discussion and Conclusions

In this work we analysed site effects in the Rhône valley with different approaches, including ambient noise, records of weak ground motion and 3-D numerical simulations of wave propagation. Furthermore we estimated the impact of nonlinear soil properties during strong ground motion.

In this section we will recapitulate the main conclusions drawn from the previous chapters, and discuss their implications for site effects assessment in the Rhône valley.

6.1 Two-dimensional resonance of the basin

Both measurements of ambient noise and weak motion records have provided clear evidence that the observed fundamental frequency of the basin is caused by two-dimensional resonance. This interpretation is based on the observation that the fundamental frequency of the basin is independent of the position along the profile (e.g. Fig. 4.11). Additionally, we have demonstrated that the SH_{00} and SV_0 fundamental modes can be isolated by rotation of the horizontal components (e.g. Fig. 2.21, Fig. 4.13).

Since two-dimensional resonance produces higher amplification than one-dimensional response, we must be prepared that the basin will exhibit strong amplifications at the identified 2-D resonance frequencies during future large earthquakes. The simulations shown in the last chapter are implying that this low-frequency amplification will be reduced by nonlinear soil response, but the resulting spectral accelerations at about 0.5 Hz are still exceeding the design spectra during most simulated events with magnitudes of 6.0 to 6.5. A crude rule of thumb to estimate the resonance frequency f of a building is

$$f = \frac{10}{N} \quad (6.1)$$

where N is the number of storeys. Most buildings in the Sion area are less than 10 storeys tall, and have resonance frequencies well above the 2-D resonance frequency of the basin (~ 0.6 Hz) according to this rule.

However, reduced stiffness decreases the fundamental frequency of a building after it has suffered damage. During the 1985 Michoacán earthquake, the greatest damage occurred in those portions of the lake zone underlain by 38 to 50 m of soft soil (Stone *et al.*, 1993), where the characteristic amplification frequency was between 0.35 and 0.52 Hz (Kramer, 1996). In this zone, most badly damaged or collapsed buildings had between 5 and 20 storeys. In view of these reports it can not be excluded that 2-D resonance in the Sion basin could be hazardous to taller buildings during strong ground motion, and the low-frequency amplification should be taken into account for structure design or retrofitting of existing buildings. Additionally, it must be kept in mind that non-building structures like long-span bridges or oil tanks (Koketsu *et al.*, 2005) may be affected by the long-period amplification.

In this study we focused on test sites in the middle and lower Valais, but similar resonance effects must be expected for sites upstream of Sion or for tributary valleys which are shallower and less wide. Such sites would develop 2-D resonance at higher frequencies, possibly coinciding with the fundamental frequency of residential buildings which have only a few storeys. It is therefore crucial to identify the 2-D resonance frequencies of embanked Alpine valleys. In chapter 2 we have shown that measurements of ambient noise on linear arrays may be used to define the 2-D resonance frequency of the basin (Fig. 2.31).

Figure 6.1 compares the average Fourier amplification in Sion derived from our weak motion records and numerical simulations with H/V spectral ratios. H/V ratios were calculated from one hour of ambient noise acquired at the temporary stations. While the fundamental frequency in the H/V spectral ratio agrees well with the 2-D resonance frequency of the basin at some sites (e.g. SIOSC or SIOTE), H/V spectral ratios are not always able to identify the low-frequency amplification (e.g. SIOO, SIOVI). The 3-D numerical simulations, however, are generally able to reproduce the measured amplification below 1 Hz, except at the sites SIOAE and SIOTO, where the velocity model is not accurate.

6.2 Edge-generated surface waves

The average weak motion spectral ratios of all observed events are showing significant amplification at higher frequencies; at many stations the average is at least above 5 in the frequency range between 1 and 10 Hz (e.g. SIOPI, SIOVE and SIOTE in Figure 6.1). We suggested that these higher-frequency amplification is caused by edge-generated surface waves which we identified by their apparent slowness and direction of origin in $f-k$ spectra (Chapter 4).

Comparison of H/V spectral ratios with average weak motion site-to-reference spectral ratios (Fig. 6.1) shows that this higher-frequency amplification can not reliably be predicted from H/V ratios only. At a few stations, secondary peaks in H/V ratios can be associated with peak frequencies of amplification in weak motion spectral ratios (e.g. SIOAE or SIOTE).

But H/V spectral ratios are often close to unity despite high average amplifi-

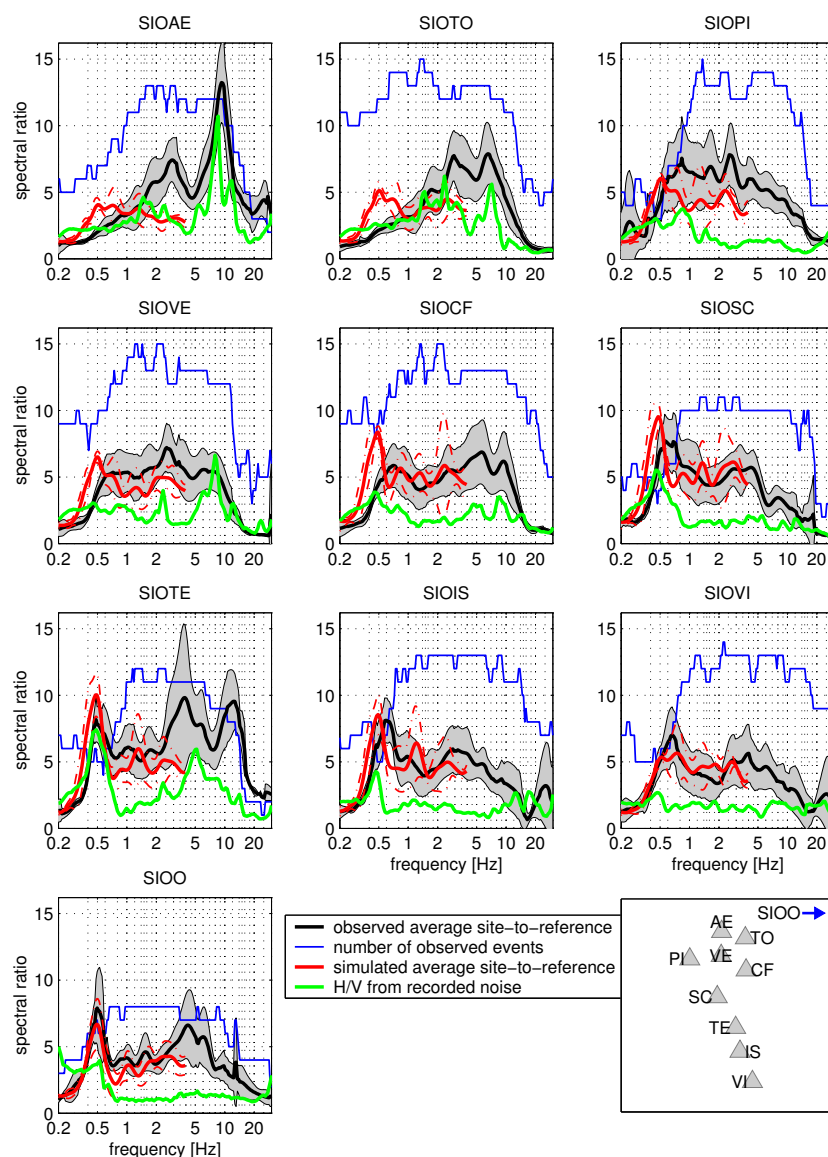


Figure 6.1: H/V spectral ratios obtained from ambient noise compared with average Fourier amplification from observed weak motion and numerical simulations. See Figure 4.11 for more explanations

cation was observed at the same frequency; e.g. between 1 and 10 Hz at the site SIOO, SIOSC and SIOVI. The simulated site-to-reference spectral ratios, however, are generally in agreement with the observed values between 1 and 4 Hz. This shows that the 3-D numerical simulations are able to predict wave propagation effects, such as edge-generated surface waves, which are not visible in the ambient vibration wavefield. A requirement is a reliable velocity model for the area of interest.

The results of the nonlinear simulations have shown that this higher-frequency

amplification may also be reduced substantially during strong ground motion. As a consequence, the simulated spectral accelerations are not exceeding the design spectra dramatically at frequencies above 1 Hz (Fig. 5.12). However, we must consider that 2-D nonlinear simulations would be required to model the propagation of edge-generated surface waves in nonlinear media. Additionally, we must recall that the soft soil deposit that was sampled in this study may not be present at all sites in the Rhône plain.

6.3 Methods for site effect evaluation

Numerical simulations are only meaningful if a reliable velocity model is available for the region of interest. In this work a substantial amount of research was directed towards the development and application of ambient noise array measurements, and we relied on a large amount of information from previous studies to develop the 3-D velocity model.

Additionally the recordings of local earthquakes gathered on the two temporary networks proved to be essential for the verification and improvement of the velocity model, as well as for the general understanding of wave propagation effects in the Sion basin.

Results from the nonlinear analysis are indicating that cyclic mobility of soils should also be taken into account, and the impact of strong nonlinear effects (e.g. liquefaction) must be considered.

The broad methodology chosen for this work is far more extensive than the approaches that are employed in the standard microzonation practise. But the complexity of the observed wave propagation effects and the achieved match between observations and simulations shows that these efforts are justified in the case of irregularly shaped 3-D structures like the Rhône basin. We conclude that site effect evaluation in deep Alpine valleys should be based on observations of local earthquakes, development of velocity models, 3-D numerical simulations and analysis of nonlinear soil behaviour. Results from such extensive studies should be considered for seismic hazard evaluation, and they may eventually lead to site-specific building codes which take 3-D effects into account.

6.4 Outlook

Array measurements of ambient noise have been performed at many locations in the Valais, on the basis of which more detailed velocity models will be developed. Definitely more earthquake records should be collected to analyse the amplification on the Rhône sediments. A permanent strong motion network with 24-bit receivers and broadband accelerometers, comparable to the installations at the sites SIOO and SIOV, would allow evaluation of both weak and strong ground motion. Eventually such a network could provide field observations of nonlinear soil behaviour, i.e. reduced amplification in site-to-reference spectral ratios and

lowered resonance frequencies. Nonlinear soil behaviour in the Rhône valley will also be further explored using vertical arrays with seismometers at different depths, as has been proposed for the upcoming project COGEAR.

Appendix A

Additional array measurements

A.1 Strong-motion station VMAR

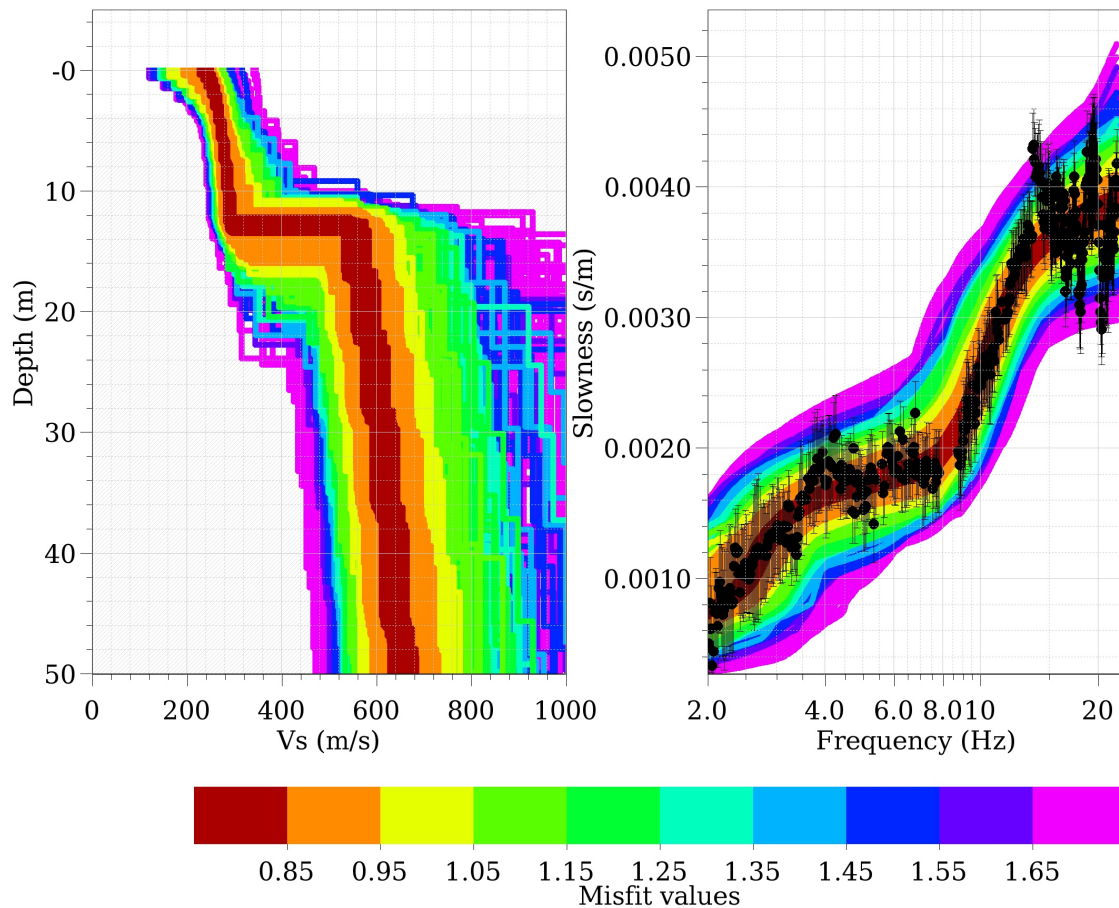


Figure A.1: Results of ambient noise measurements with circular array configurations near the permanent strong-motion station VMAR in Martigny.

A.2 Strong-motion station SVIP

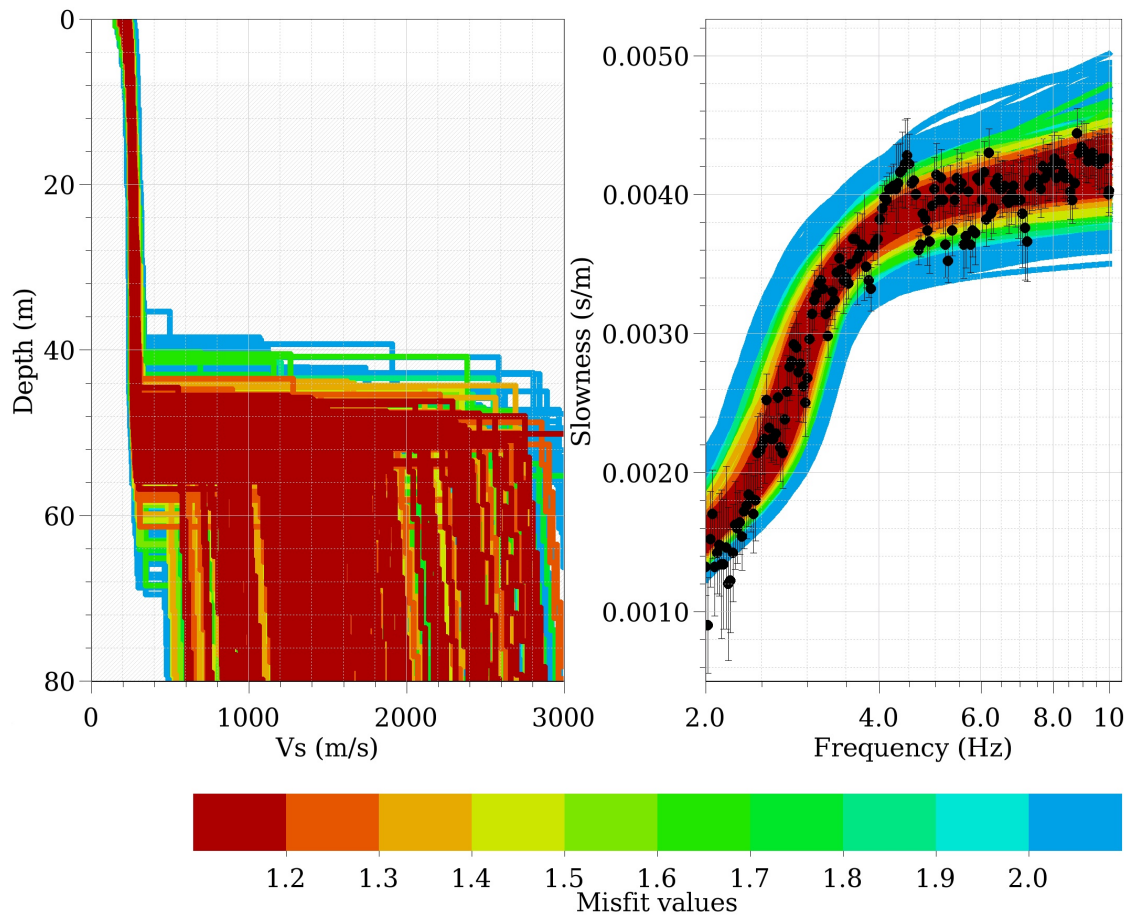


Figure A.2: Results of ambient noise measurements with circular array configurations near the permanent strong-motion station SVIP west of Visp.

A.3 Linear array Saillon

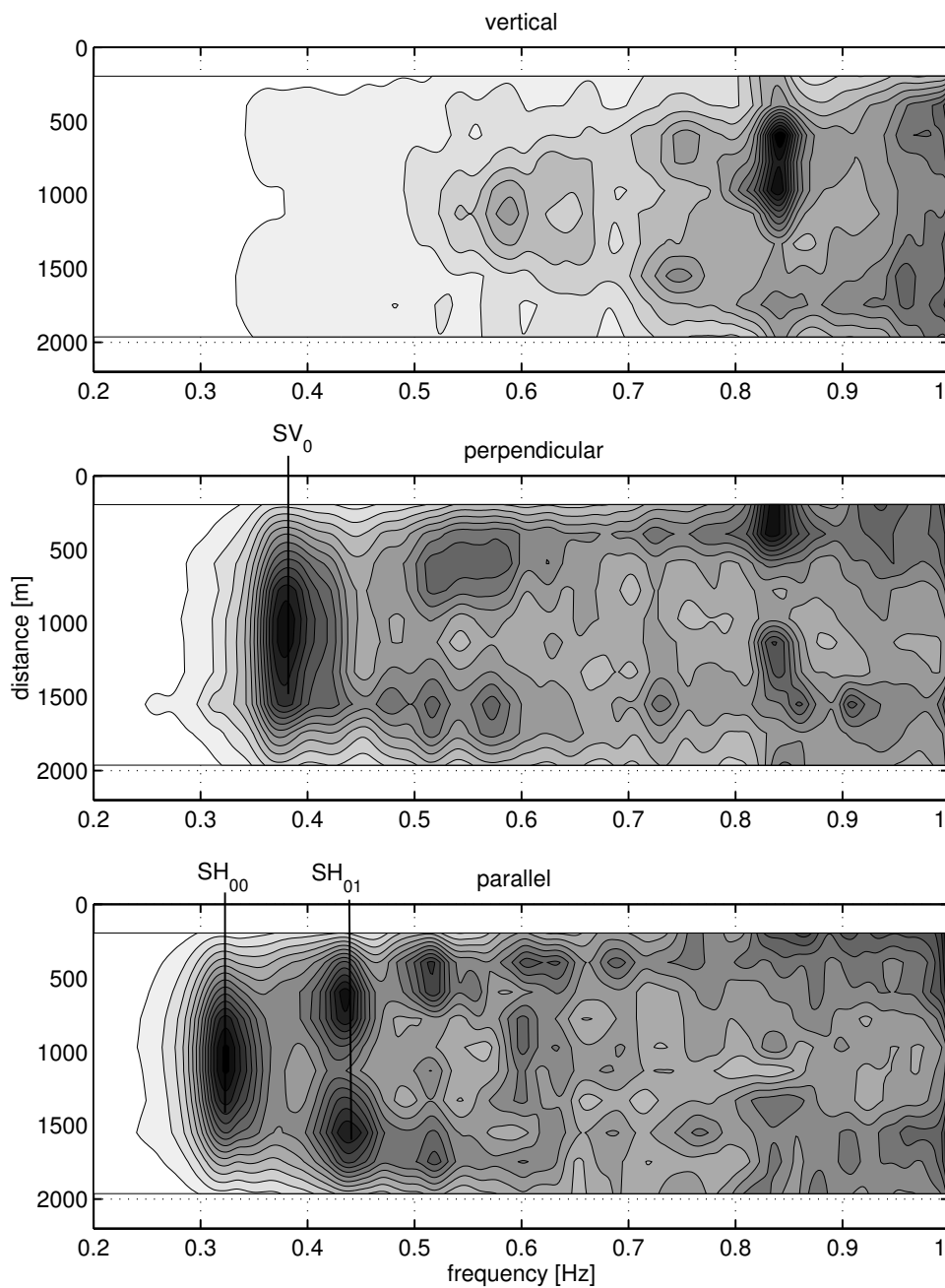


Figure A.3: Spectral ratios obtained from the linear array near Saillon as a function of frequency and distance along the profile axis for vertical (*top*), perpendicular (*centre*) and axial (*bottom*) component.

Appendix B

Ratio of response spectra

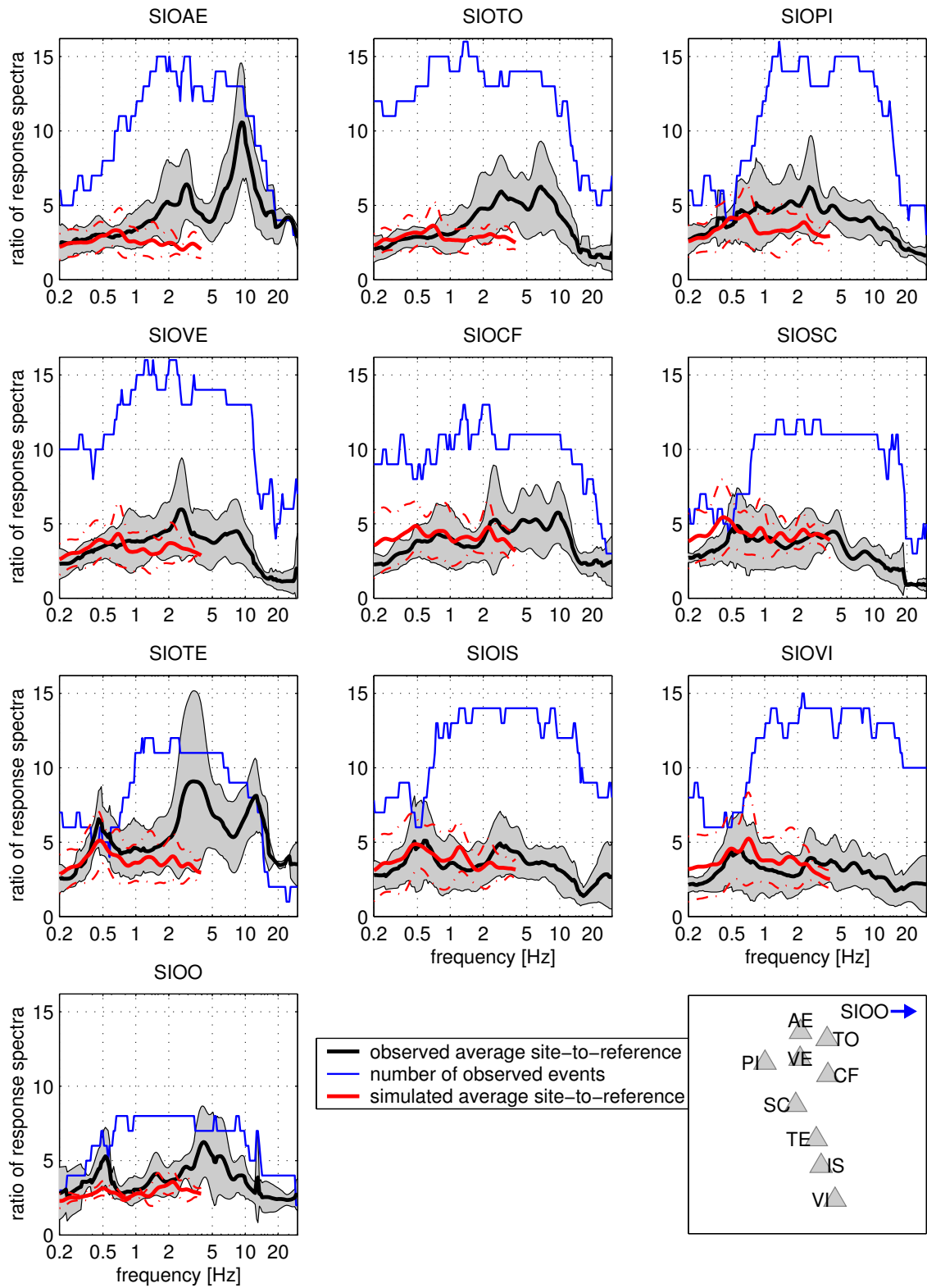


Figure B.1: Comparison between observed and simulated average amplification like in Figure 4.11, but using acceleration response spectra instead of Fourier spectra.

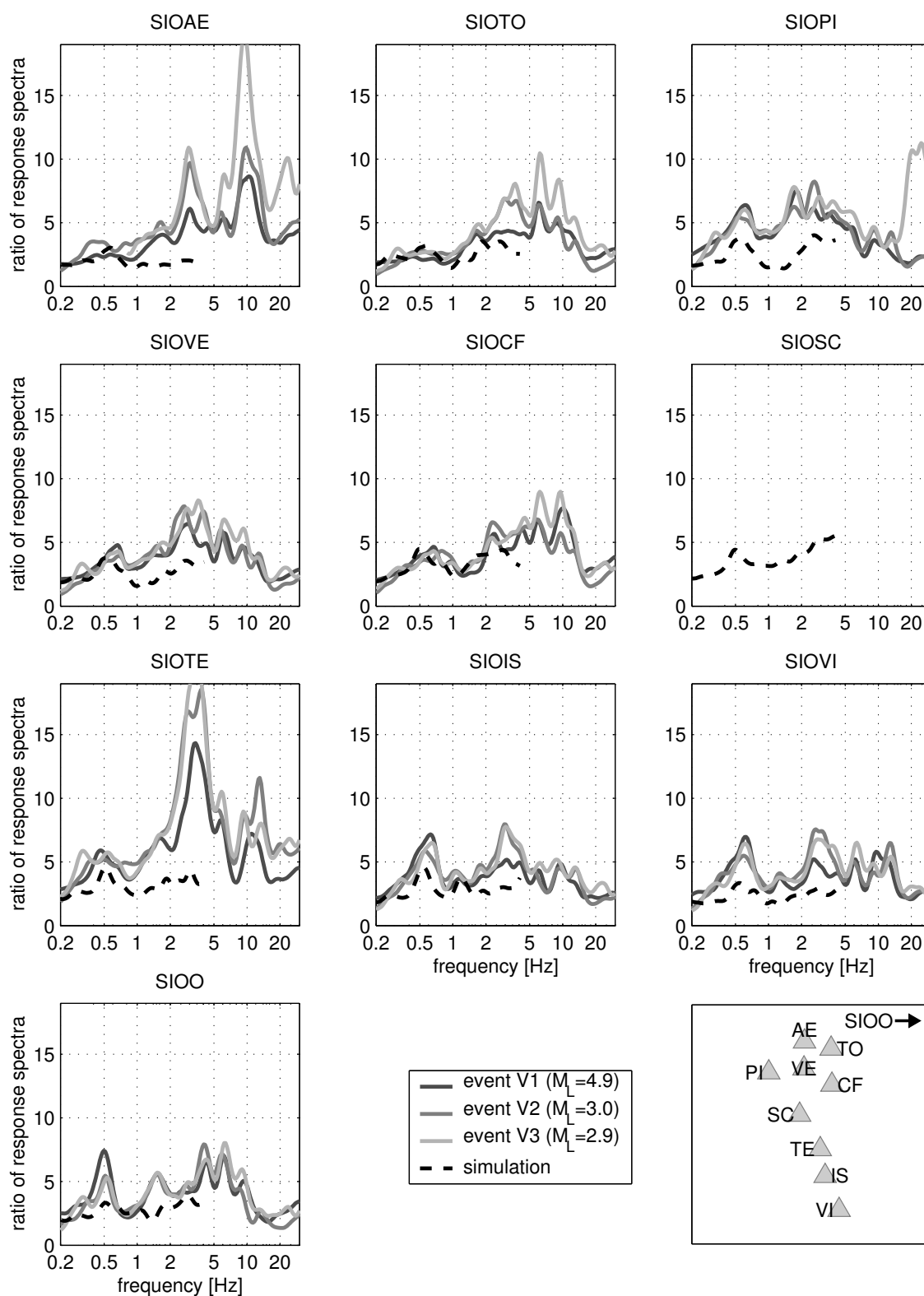


Figure B.2: Ratio of acceleration response spectra computed from Vallorcine series (solid) and simulation of event V1 (dashed). See Figure 4.8 for more explanations.

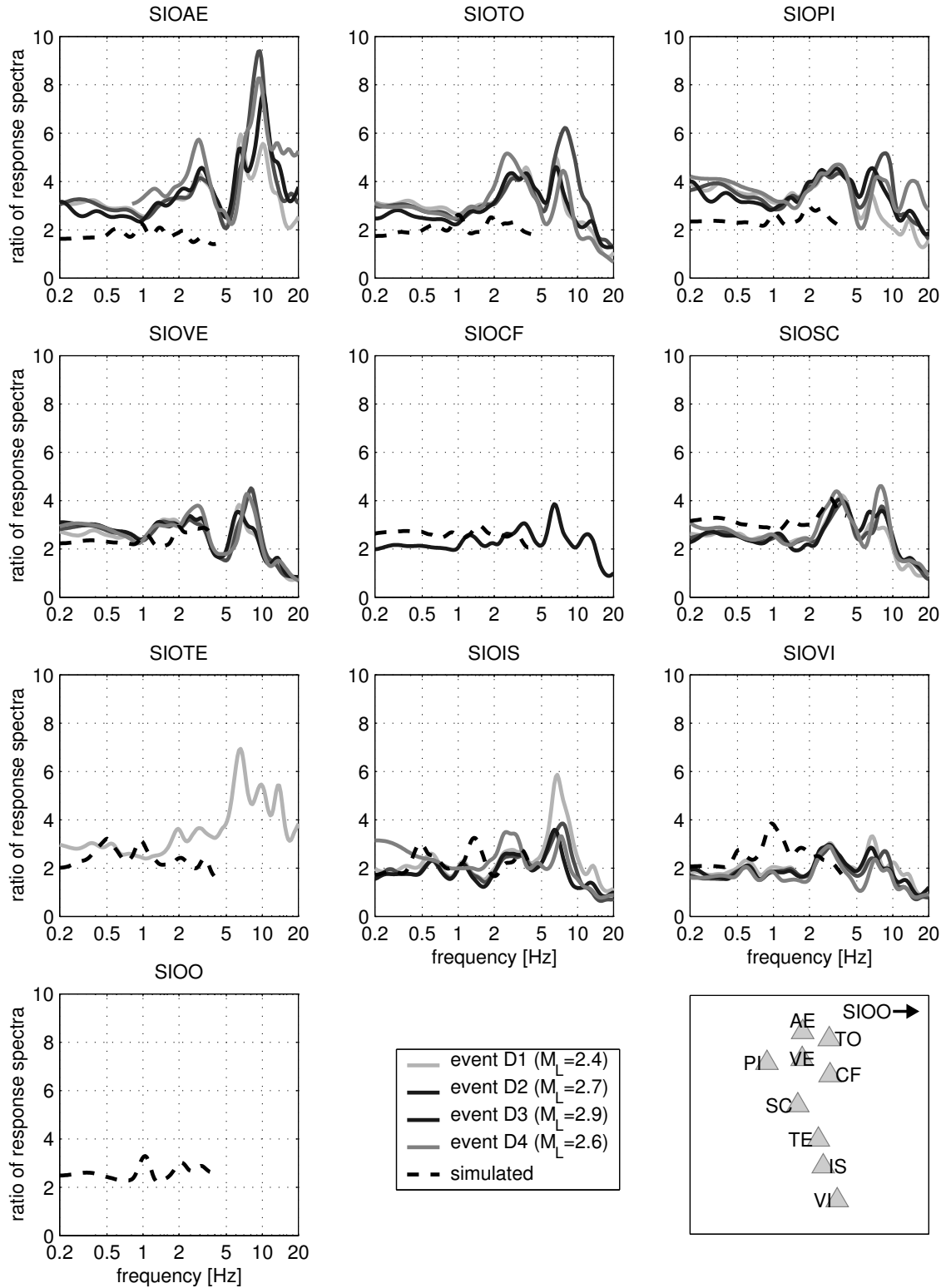


Figure B.3: Ratio of acceleration response spectra computed from Derborance series (solid) and simulation of event D3 (dashed).

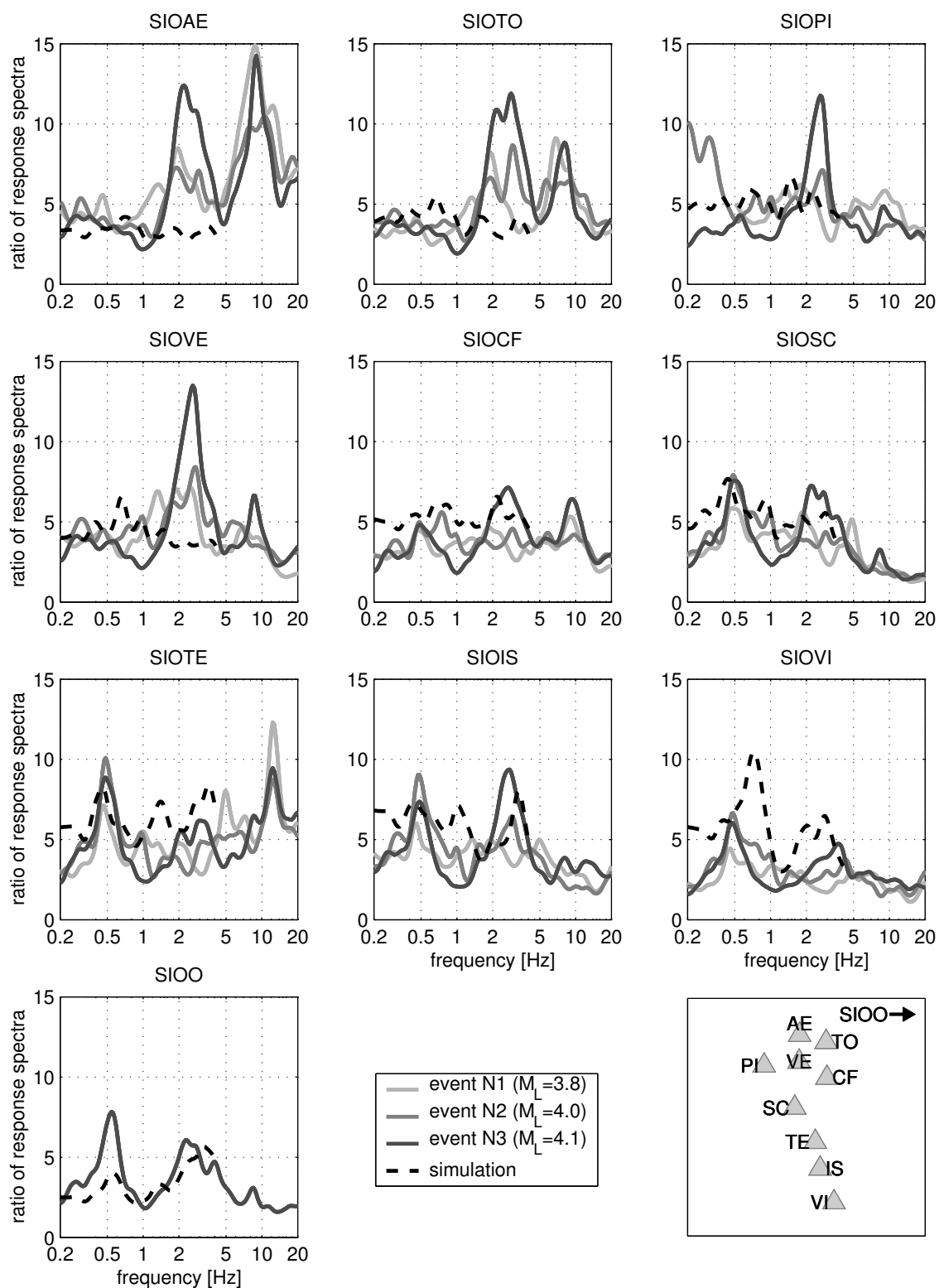


Figure B.4: Ratio of acceleration response spectra computed from northern Switzerland events (solid) and simulation of event N2 (dashed).

Appendix C

Simulated normalised response spectra

C.1 Vallorcine main shock V1

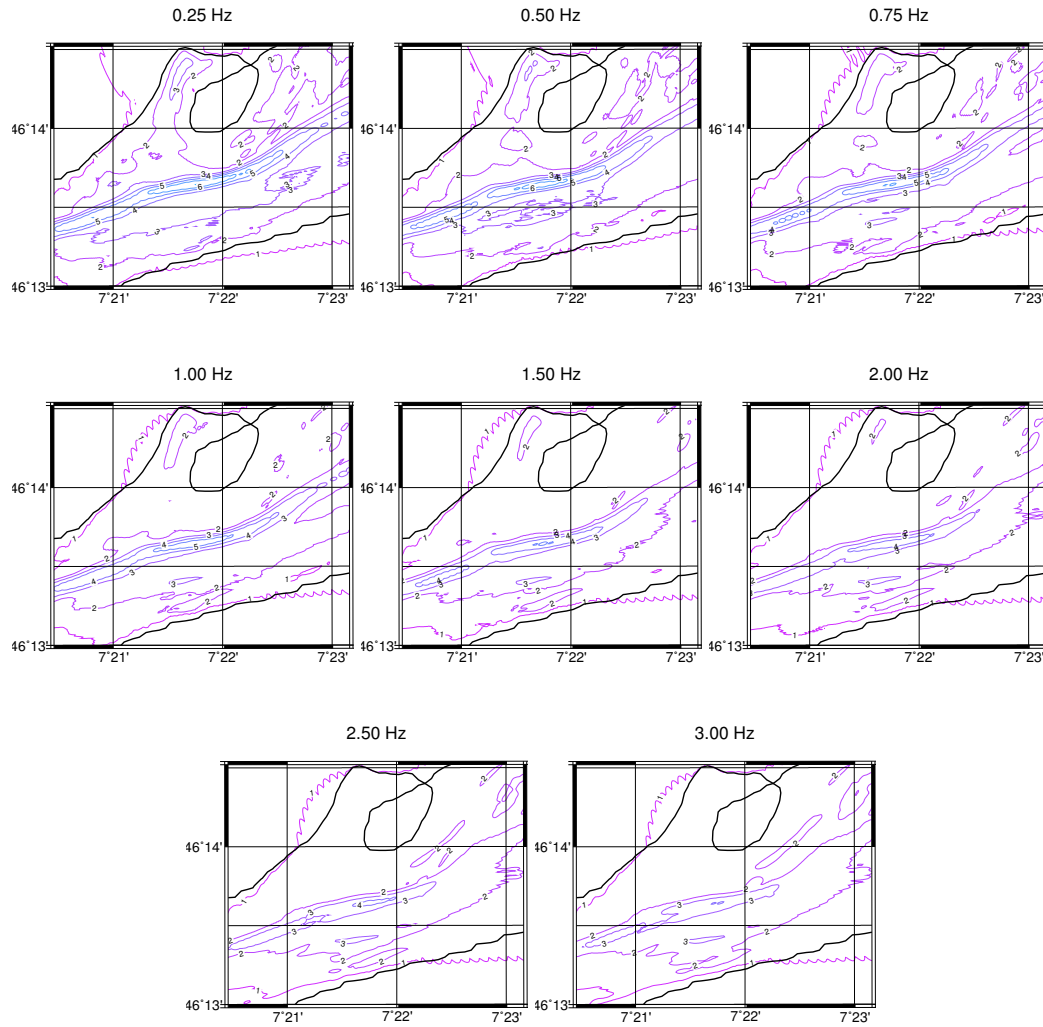


Figure C.1: Acceleration response spectra normalised by the spectral acceleration at the reference site for the simulation of event V1 at different frequencies.

C.2 Northern Switzerland event N2

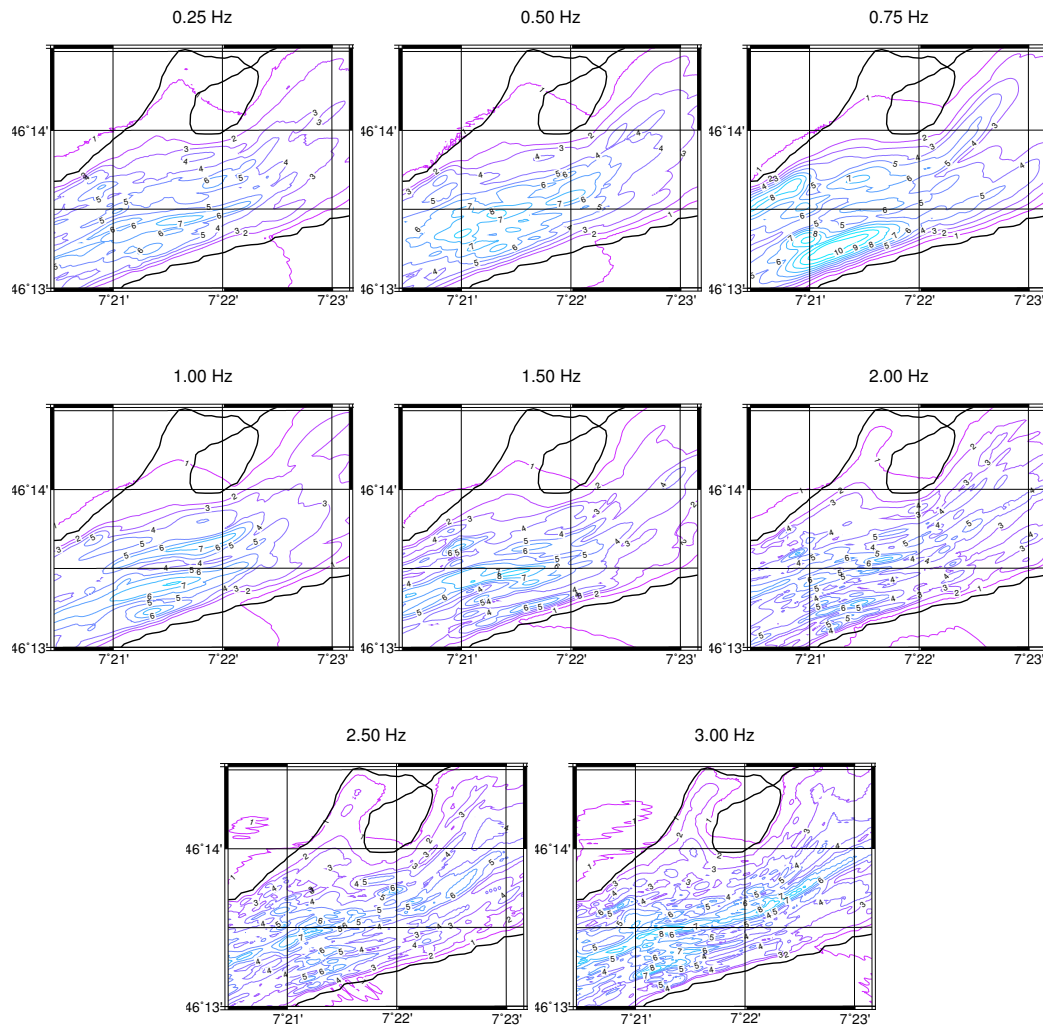


Figure C.2: Acceleration response spectra normalised by the spectral acceleration at the reference site for the simulation of event N2 at different frequencies.

C.3 Derborance main shock D3

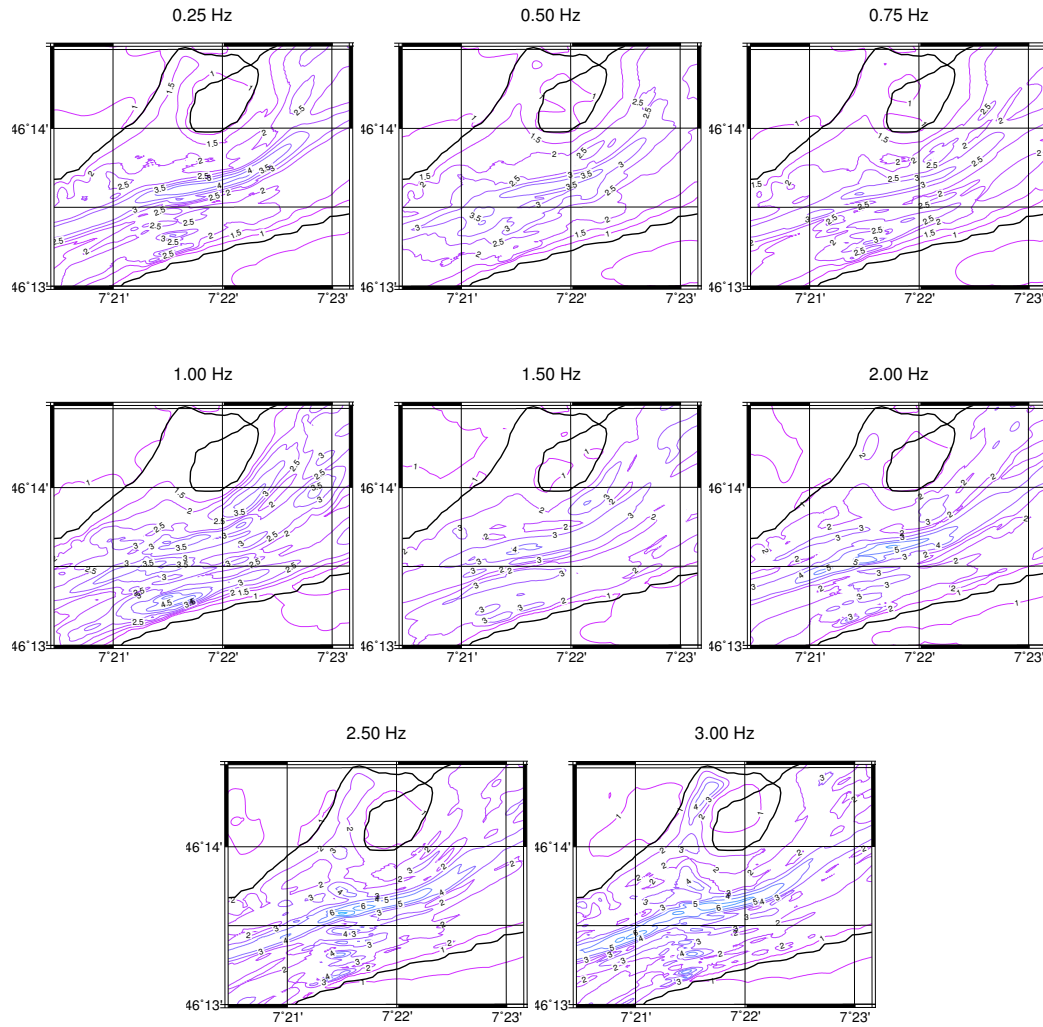


Figure C.3: Acceleration response spectra normalised by the spectral acceleration at the reference site for the simulation of event D3 at different frequencies.

C.4 Northern Italy event I2

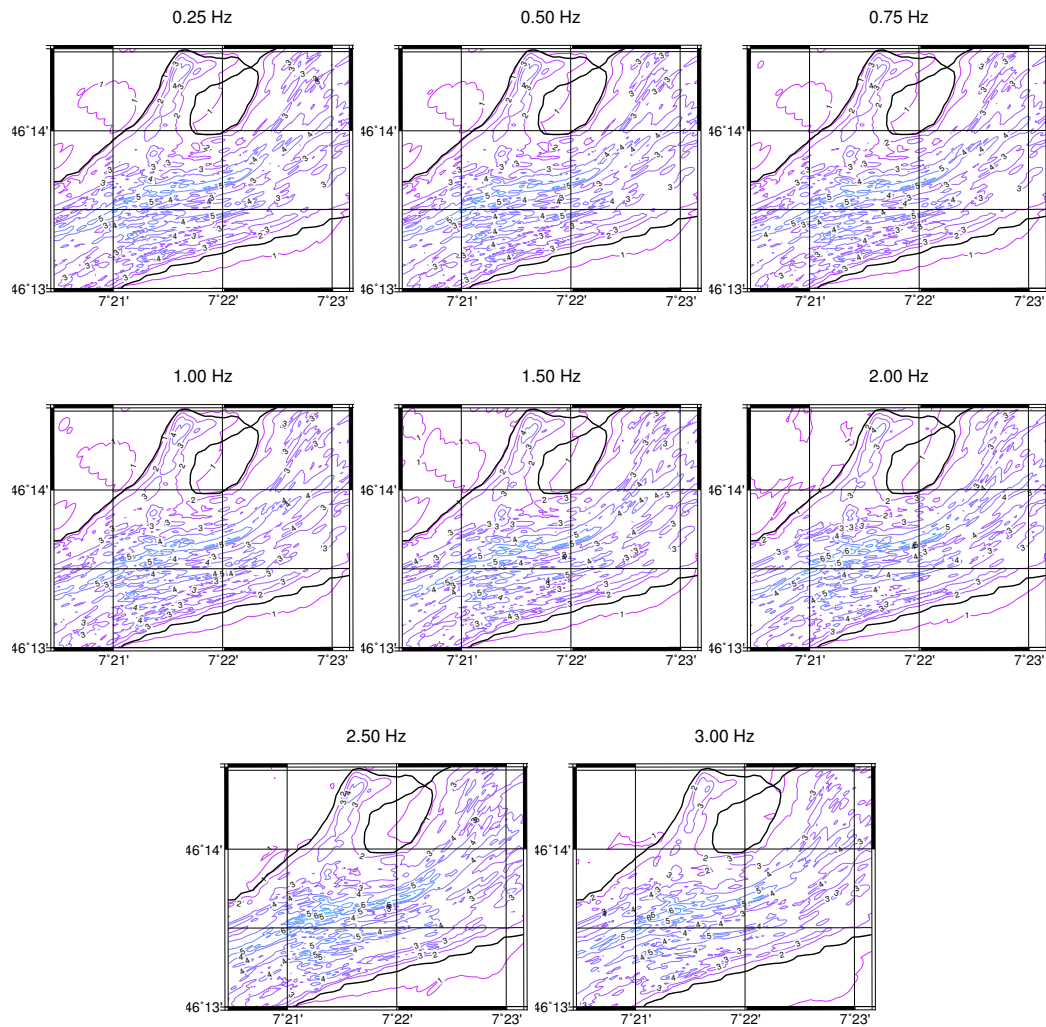


Figure C.4: Acceleration response spectra normalised by the spectral acceleration at the reference site for the simulation of event I2 at different frequencies.

Acknowledgements

Many people have contributed essentially to the completion of this thesis. First of all I'd like to thank my supervisor Dr. Donat Fäh for his patient support and competent supervision in the course of the project, and for providing this challenging research opportunity at the Swiss Seismological Service and the institutions abroad. I want to thank Prof. Domenico Giardini for referring this thesis and for his supportive recommendations. I'd like to thank Prof. Pierre-Yves Bard for agreeing to co-examine the defence.

Many thanks to Prof. Kim Bak Olsen for providing the 3-D finite difference code and for his helpful support during my visit at SDSU. Dr. Louis Fabián Bonilla made his fully nonlinear program *NOAH* available for this research, and he contributed greatly to the implementation of the nonlinear analysis. I'd like to thank Thomas Weber for performing the laboratory tests on the soil samples and his help in the field. Thanks to Dr. Jan Laue and Prof. Sarah Springman for the successful collaboration with the Geotechnical Institute.

Many people in the hazard and risk group contributed to this work through valuable discussions and by helping in the field, including Sibylle Steimen, Cécile Cornou, Ivo Opršal, Hans-Balder Havenith, Gabriela Stamm, Marc Lambert, Valerio Poggi and Philipp Kästli. Thanks to Stefan Fritsche for providing the reconstruction of the damage field.

This research is part of the Interreg project SISMOVALP and the projects SHAKE-VAL I and SHAKE-VAL II, funded by the Swiss National Science Foundation (No. 200021-101920 and 200020-109177).

Curriculum Vitae

Personal Details

Name: Daniel Roten
Address: St. Jodernstr. 22, 3930 Visp, Switzerland
Date and place of birth: February 25th 1976, Visp
Email: daniel.roten@alumni.ethz.ch

Education

Diploma, Earth Sciences, ETH Zurich, April 2002

- Thesis title: "Moment tensor inversion of local earthquakes in Switzerland"
- *Subjects:* Seismology, Applied Geophysics, Geodynamics, Hydrology

Matura, Kollegium Brig, 1996

Research experience

November 2003 till present

Ph.D. student, Hazard and risk group, **Swiss Seismological Service** (ETH Zurich), Switzerland, working on earthquake site effects in Alpine valleys

May 1st to October 30th 2003

Research assistant, Hazard and risk group, **Swiss Seismological Service** (ETH Zurich), Switzerland, working on ambient vibration methods for site response analysis

November 2002 to February 2003

Work experience, Earthquake and tsunami hazard group, **Geoscience Australia**, Canberra, Australia. Topic: "Moment tensor inversion of Australian Earthquakes "

April to October 2002

Research assistant, Seismic verification group, **Swiss Seismological Service** (ETH Zurich), Switzerland, working on moment tensor inversion of local earthquakes

September 2001 to March 2002

Graduate student, **ETH Zürich**, Switzerland, working on diploma thesis

2001

Part-time research assistant, Hazard and Risk group, **Swiss Seismological Service**, (ETH Zurich), Switzerland, working on implementation of ground motion attenuation relations

Awards and Grants

"Outstanding student presentation award", 6th PhD student's and advisor's meeting in the field of natural hazards, Cardada (Locarno), Switzerland, 18th to 20th September 2005

"Award for excellent contributions to young scientists in the session site response and site effects", First European Conference on Earthquake Engineering and Seismology, Geneva, Switzerland, 3rd to 8th September 2006

Fellowship for prospective researchers, Swiss National Science Foundation. Research project: "Earthquake scenarios for Salt-Lake valley and Southern California", April 5 2007

Qualifications

Computer skills

- Operating systems: UNIX (Linux, SunOS, FreeBSD), MacOS
- languages: C/C++, Python, Fortran basics, MPI basics, shell scripting, visualization toolkit (vtk), Matlab
- Signal processing of seismic noise and earthquakes using Matlab, SAC and sesarray. Spectral analysis, frequency-wavenumber methods
- 3-D finite difference simulation of wave propagation, high performance computing
- Visualization of time-dependent 2-D and 3-D data

Fieldwork experience

- Data acquisition with Lennartz LE3D/5s sensors, Mars-88 and Quanterra Q330 acquisition systems
- multi-station array measurements, single-station noise recording, acquisition of earthquake records

List of Publications

- Roten, D. and Fäh, D., 2006. "A combined inversion of Rayleigh wave dispersion and 2-D resonance frequencies". *Geophys. J. Int.*, doi: 10.1111/j.1365-246X.2006.03260.x
- Roten, D., Fäh, D., Oprsal, I., Olsen, K. and Giardini, D., 2006. "Analysis of deep valley response by ambient noise, earthquake records and numerical simulations", *First European Conference on Earthquake Engineering and Seismology*. Geneva, Switzerland, 3-8 September 2006, paper number 1108.
- Roten, D., Fäh, D. and Giardini, D., 2006. "Site effects in the Rhône valley analysed from ambient noise, local earthquakes and numerical simulations", *Third International Symposium on the Effects of Surface Geology on Seismic Motion*, Grenoble, August 30 - September 1, 2006, paper number 92.
- Roten, D., Fäh, D., Cornou, C. and Giardini, D., 2006. "Two-dimensional resonances in Alpine valleys identified from ambient vibration wavefields". *Geophys. J. Int.*, **165**, 889-905
- Roten, D., Fäh, D. and Giardini, D., "Earthquake Shaking in Alpine Valleys." *Proceedings of the 6th PhD Students' and Advisors' Meeting*, 18th - 20th September 2005 in Cardada, Locarno.
- Roten, D., Álvarez-Rubio, S., Fäh, D. and Giardini, D., "Revealing the two-dimensional response of a sediment-filled valley from ambient vibration records". *European Geosciences Union (EGU), General Assembly*. Vienna, 24-29 April 2005.
- Roten D., Cornou C., Steimen S., Fäh D. and Giardini D., "2D Resonances in Alpine Valleys Identified from Ambient Vibration Wavefields", *Proceedings of the 13th WCEE*, 1 - 6 Aug. 2004, Vancouver, Canada, paper No 845
- Roten D., 2003. "Tutorial for moment tensor inversion in Australia", Internal report, *Geoscience Australia*, 22 pages
- Roten D. and Braunmiller, J., 2002. "Local moment tensor inversion of weak earthquakes in Switzerland", *European Seismological Commission XXVIII General Assembly*, Genoa, 1 - 6 September 2002
- Roten D., 2002. "Momententensorinversion lokaler Erdbeben in der Schweiz", Diploma thesis, ETH Zurich, 131 pages

Bibliography

- Aki, K. 1957. Space and time spectra of stationary stochastic waves, with special reference to microtremors. *Bull. Earthq. Res. Inst. Tokyo*, **35**, 415–457.
- Aki, K., and Larner, K.L. 1970. Surface motion of a layered medium having an irregular interface due to incident plane SH waves. *J. Geophys. Res.*, **75**, 933–954.
- Álvarez-Rubio, S., Benito, J.J., Sánchez-Sesma, F.J., and Alarcón, E. 2004. The direct boundary element method: 2D site effects assessment on laterally varying layered media (methodology). *Soil Dyn. Earthq. Eng.*, **24**, 167–180.
- Álvarez-Rubio, S., Sánchez-Sesma, F.J., Benito, J.J., and Alarcón, E. 2005. The Use of Direct Boundary Element Method for gaining insight into complex seismic Response. *Computer and Structures*, **83**, 821–835.
- Ambraseys, N., Smit, P., Sigbjörnsson, R., Suhadolc, P., and Margaris, B. 2001. *Internet-Site for European Strong-Motion Data*. <<http://www.isesd.cv.ic.ac.uk>>, EVR1-CT-1999-40008. European Commission, Directorate-General XII, Environmental and Climate Programme, Bruxelles, Belgium.
- Ambraseys, N.N. 1988. Engineering seismology. *Earthquake Engineering and Structural Dynamics*, **17**, 1–105.
- Anderson, J.G., Bodin, P., Brune, J.N., Prince, J., Singh, S.K., Quaas, R., and Onate, M. 1986. Strong ground motion from the Michoacan, Mexico, Earthquake. *Science*, **233**, 1043–1049.
- Asten, M.W. 1978. Geological control of the three-component spectra of Rayleigh-wave microseisms. *Bull. seism. Soc. Am.*, **68**(6), 1623–1636.
- Asten, M.W. 2004. Comment on "Microtremor observations of deep sediment resonance in metropolitan Memphis, Tennessee" by Paul Bodin, Kevin Smith, Steve Horton and Howard Hwang. *Engineering Geology*, **72**(3/4), 343–349.
- Asten, M.W., and Henstridge, J.D. 1984. Array estimators and the use of microseisms for reconnaissance of sedimentary basins. *Geophysics*, **49**(11), 1828–1837.

- Asten, M.W., Stephenson, W.R., and Davenport, N. 2005. Shear-wave velocity profile for holocene sediments measured from microtremor array studies, SCPT, and seismic refraction. *Journal of Engineering and Environmental Geophysics*, **10**(September), 235–242.
- Baer, M., Deichmann, N., Braunmiller, J., Husen, S., Fäh, D., Giardini, D., Kästli, D., Kradošfer, U., and Wiemer, S. 2005. Earthquakes in Switzerland and surrounding regions during 2004. *Eclogae geol. Helv.*, **98**, 407–418.
- Bakır, B. S., Sucuoğlu, H., and Yılmaz, T. 2002. An overview of local site effects and the associated building damage in Adapazarı during the 17 August 1999 İzmit earthquake. *Bull. seism. Soc. Am.*, **92**(1), 509–526.
- Bard, P.-Y., and Bouchon, M. 1980a. The seismic response of sediment-filled valleys. Part 1. The case of incident SH waves. *Bull. seism. Soc. Am.*, **70**(4), 1263–1286.
- Bard, P.-Y., and Bouchon, M. 1980b. The seismic response of sediment-filled valleys. Part 2. The case of incident P and SV waves. *Bull. seism. Soc. Am.*, **70**(5), 1921–1941.
- Bard, P.-Y., and Bouchon, M. 1985. The two-dimensional resonance of sediment-filled valleys. *Bull. seism. Soc. Am.*, **75**(2), 519–541.
- Bard, P.-Y., Jongmans, D., Ohrnberger, M., and Wathelet, M. 2005. *Recommendations for quality array measurements and processing*. SESAME deliverable D24.13. SESAME EVG1-CT-2000-00026 project (<http://sesame-fp5.obs.ujf-grenoble.fr>).
- Baumann, M. 1994. *Three-dimensional seismic image of the Alpine crustal structure*. Ph.D. thesis, ETH Zürich.
- Beresnev, I. A., and Wen, K.-L. 1996. Nonlinear Soil Response - A Reality? *Bull. Seism. Soc. Am.*, **86**(6), 1964–1978.
- Besson, O., Marchant, R., Pugin, A., and Rouiller, J.-D. 1993. Campagne de sismique-réflexion dans la vallée du Rhône entre Sion et St. Maurice: perspectives d'exploitation géothermique des dépôts torrentiels sous-glaciaires. *Bull. du Centre d'hydrogéologie de l'Université de Neuchâtel*, **12**, 39–58.
- Bonilla, L.F., Archuleta, R.J., and Lavalée, D. 2005. Hysteretic and Dilatant Behavior of Cohesionless Soils and Their Effects on Nonlinear Site Response: Field Data Observations and Modeling. *Bull. Seism. Soc. Am.*, **95**(6), 2373–2395.
- Bonnefoy-Claudet, S., Bard, P.-Y., and Cotton, F. 2004. *Nature of noise wavefield*. SESAME Deliverable D13.8. SESAME EVG1-CT-2000-00026 project (<http://sesame-fp5.obs.ujf-grenoble.fr>).

- Bonnefoy-Claudet, S., Cornou, C., Bard, P.-Y., Cotton, F., Moco, P., Kristek, J., and Fäh, D. 2006. H/V ratio: a tool for site effects evaluation. Results from 1-D noise simulations. *Geophys. J. Int.*, **167**, 827–837.
- Borcherdt, R.D. 1970. Effects of local geology on ground motion near San Francisco Bay. *Bull. seism. Soc. Am.*, **60**, 29–61.
- Bundesamt für Bevölkerungsschutz, Bern. 2003. *Katstrophen und Notlagen in der Schweiz - Eine Risikobeurteilung aus der Sicht des Bevölkerungsschutzes*.
- Capon, J. 1969. High-resolution frequency-wavenumber spectrum analysis. *Proceedings of the IEEE*, **57**(8), 1408–1419.
- Cerjan, C., Kosloff, D., and Reshef, M. 1985. A nonreflecting boundary condition for discrete acoustic and elastic wave equations. *Geophysics*, **50**, 705–708.
- Chávez-García, F. J., Castillo, J., and Stephenson, W. R. 2003. 3D Site Effects; A Thorough Analysis of a High-Quality Dataset. *Bull. seism. Soc. Am.*, **92**(5), 1941–1951.
- Chávez-García, J., and Stephenson, W. R. 2003. Reply to "Comment on '3D Site Effects: A thorough analysis of a high-quality dataset' by F. J. Chávez-García, J. Castillo, and W. R. Stephenson," by R. Paolucci and E. Faccioli. *Bull. seism. Soc. Am.*, **93**(5), 2306–2316.
- Cornou, C., Bard, P.-Y., and Dietrich, M. 2003. Contribution of Dense Array Analysis to the Identification and Quantification of Basin-Edge-Induced Waves, Part II: Application to Grenoble basin (French Alps). *Bull. seism. Soc. Am.*, **93**, 2624–2648.
- Cotton, Fabrice, Scherbaum, F., Bommer, J., and Bungum, H. 2006. Criteria for selecting and adjusting ground-motion models for specific target regions: Application to Central Europe and rock sites. *Journal of Seismology*, **10**, 137–156.
- Darragh, R. B., and Shakal, A. F. 1991. The site response of two rock and soil station pairs to strong and weak ground motion. *Bull. seism. Soc. Am.*, **81**, 1885–1899.
- Deichmann, N., Baer, M., Braunmiller, J., Husen, S., Fäh, D., Giardini, D., Kästli, D., Kradošfer, U., and Wiemer, S. 2007. Earthquakes in Switzerland and surrounding regions during 2005. *Eclogae geol. Helv.*, **99**, 443–452.
- Dunkin, J. W. 1965. Computation of model solutions in layered, elastic media at high frequencies. *Bull. Seism. Soc. Am.*, **55**, 335–358.
- Fäh, D., Suhadolc, P., and Panza, G. F. 1993. Variability of seismic ground motion in complex media: the case of a sedimentary basin in the Friuli (Italy) area. *Journal of Applied Geophysics*, **30**, 131–148.

- Fäh, D., Kind, F., and Giardini, D. 2001. A theoretical investigation of average H/V ratios. *Geophys. J. Int.*, **145**, 535–549.
- Field, E. H. 1996. Spectral amplification in a sediment-filled valley exhibiting clear basin-edge-induced waves. *Bull. seism. Soc. Am.*, **86**, 991–1005.
- Field, E. H., and Klaus, J. 1995. A Comparison and Test of Various Site-Response Estimation Techniques, Including Three That Are Not Reference-Site Dependent. *Bull. seism. Soc. Am.*, **85**(4), 1127–1143.
- Field, E. H., Johnson, P. A., Beresnev, I. A., and Zeng, Yu. 1997. Nonlinear ground-motion amplification by sediments during the 1994 Northridge earthquake. *Nature*, **390**, 599–602.
- Frankel, A., and Vidale, J. 1992. A three-dimensional simulation of seismic waves in the Santa Clara Valley, California, from a Loma Prieta aftershock. *Bull. seism. Soc. Am.*, **82**, 2045–2074.
- Frankel, A., Carver, D., Cranswick, E., Bice, T., Sell, R., and Hanson, S. 2001. Observations of basin ground motion from a dense seismic array in San Jose, California. *Bull. seism. Soc. Am.*, **91**, 1–12.
- Frischknecht, C. 2000. *Seismic Soil Amplification in Alpine Valleys. A Case Study: The Rhône Valley, Valais, Switzerland*. Ph.D. thesis, Sections des Sciences de la terre, Université de Genève.
- Frischknecht, C., and Wagner, J.-J. 2004. Seismic Soil Effect in an Embanked Deep Alpine Valley; A Numerical Investigation of Two-Dimensional Resonance. *Bull. seism. Soc. Am.*, **94**, 171–186.
- Frischknecht, C., Rosset, P., and Wagner, J.-J. 2005. Toward Seismic Microzonation – 2-D Modeling and Ambient Seismic Noise Measurements: The Case of an Embanked, Deep Alpine Valley. *Earthquake Spectra*, **21**(3), 635–651.
- Fritsche, S., Fäh, D., Gisler, M., and Giardini, D. 2006. Reconstructing the damage field of the 1855 earthquake in Switzerland: historical investigations on a well-documented event. *Geophys. J. Int.*, **166**(2), 719–731.
- Gaffet, S., Larroque, C., Deschamps, A., and Tressols, F. 1998. Dense array experiment for observation of waveform perturbations. *Soil. Dyn. and Earth. Eng.*, **17**, 475–484.
- Giardini, D., Wiemer, S., Fäh, D., and Deichmann, N. 2004. *Seismic hazard assessment of Switzerland, 2004*. Report. Swiss Seismological Service.
- Gisler, M., Fäh, D., and Deichmann, N. 2004. The Valais earthquake of December 9, 1755. *Eclogae geol. Helv.*, **97**(3), 411–422.
- Gutenberg, B. 1958. Microseisms. *Advan. Geophys.*, **5**, 53–92.

- Hartzell, S., Carver, D., Williams, R. A., Harmsen, S., and Zerva, A. 2003. Site Response, Shallow Shear-Wave Velocity, and Wave Propagation at the San Jose, California, Dense Seismic Array. *Bull. seism. Soc. Am.*, **93**(1), 443–464.
- Hartzell, S., Bonilla, L. F., and Williams, R.A. 2004. Prediction of Nonlinear Soil Effects. *Bull. Seism. Soc. Am.*, **94**(5), 1609–1629.
- Hermann, R. B. 2002. *Computer Programs in Seismology – An Overview of Synthetic Seismogram Computation Version 3.30*. Department of Earth and Planetary Sciences. St. Louis University.
- Holzer, T.L., Youd, T. L., and Hanks, T.C. 1989. Dynamics of Liquefaction during the 1987 Superstation Hills, California, Earthquake. *Science*, **244**(4900), 56–59.
- Hough, S.E., Friberg, P.A., Busby, R., Field, E.F., Jacob, K.H., and Borchardt, R.D. 1990. Sediment-induced amplification and the collapse of the Nimitz Freeway. *Nature*, **344**, 853–855.
- Iai, S., Matsunaga, Y., and Kameoka, T. 1990a. Parameter identification for a cyclic mobility model. *Report of the Port and Harbour Research Institute*, **29**, 57–83.
- Iai, S., Matsunaga, Y., and Kameoka, T. 1990b. Strain space plasticity model for cyclic mobility. *Report of the Port and Harbour Research Institute*, **29**, 27–56.
- Iai, S., Morita, T., Kameoka, T., Matsunaga, Y., and Abiko, K. 1995. Response of a dense sand deposit during 1993 Kushiro-Oki Earthquake. *Soils Found.*, **35**, 115–131.
- Ishihara, K., and Towhata, I. 1982. Dynamic response analysis of level ground based on the effective stress method. *In: Soil Mechanics - Transient and Cyclic Loads*, Pande G.N. and Zienkiewicz, O.C. Chichester a.o.: Wiley. (A Wiley-Interscience publication).
- Jafari, M. K., Ghayamghamian, M. R., Davoodi, M., Kamalian, M., and Sohrabi-Bidar, A. 2005. Site effects of the 2003 Bam, Iran, earthquake. *Earthquake Spectra*, **21**(S1), S125–S135.
- Joyner, W. B. 2000. Strong Motion from Surface Waves in Deep Sedimentary Basins. *Bull. seism. Soc. Am.*, **90**(6B), S95–112.
- Joyner, W.B., and Boore, D.M. 1981. Peak horizontal acceleration and velocity from strong-motion records including records from the 1979 Imperial Valley, California, earthquake. *Bull. seism. Soc. Am.*, **71**(6), 2011–2038.
- Kagami, H. Duke, M.C., Liang, G.C., and Ohta, Y. 1982. Observation of 1 to 5 second microtremors and their application to earthquake engineering. Part 2. Evaluation of site effect upon seismic wave amplification due to extremely deep soil deposits. *Bull. seism. Soc. Am.*, **72**, 987–998.

- Kawase, H. 1996. The Cause of the Damage Belt in Kobe: "The Basin-Edge Effect, "Constructive Interference of the Direct S-Wave with the Basin-Induced Diffracted/Rayleigh Waves. *Seism. Res. Lett.*, **67**(5), 25–34.
- Kind, F., Fäh, D., and Giardini, D. 2005. Array Measurements of S-Wave Velocities from Ambient Vibrations. *Geophys. J. Int.*, **160**, 114–126.
- King, J.L., and Tucker, B.E. 1984. Observed variations of earthquake motion over a sediment-filled valley. *Bull. seism. Soc. Am.*, **74**, 173–152.
- Koketsu, K., Hatayama, K., Furumura, T., Ikegami, Y., and Akiyama, S. 2005. Damaging long-period ground motions from the 2003 Mw 8.3 Tokachioki, Japan, earthquake. *Seism. Res. Lett.*, **76**, 67–73.
- Konno, K., and Ohmachi, T. 1998. Ground-Motion Characteristics Estimated from Spectral Ratio between Horizontal and Vertical Components of Microtremor. *Bull. seism. Soc. Am.*, **88**(1), 228–241.
- Kramer, S. L. 1996. *Geotechnical earthquake engineering*. Prentice Hall, New Jersey.
- Kristek, J., and Moczo, P. 2003. Seismic-Wave Propagation in Viscoelastic Media with Material Discontinuities: A 3D Fourth-Order Staggered-Grid Finite-Difference Modeling. *Bull. seism. Soc. Am.*, **93**(5), 2273–2280.
- Kristek, J., Moczo, P., and Archuleta, R. J. 2002. Efficient methods to simulate planar free surfaces in the 3D 4th-order staggered-grid finite-difference schemes. *Studia Geophys. Geod.*, **46**, 355–381.
- Lermo, J., and Chávez-García, F. J. 1994. Are Microtremors Useful in Site Response Evaluation? *Bull. seism. Soc. Am.*, **85**(5), 1350–1364.
- Marcos, S. 1998. *Les méthodes à haute résolution: traitement d'antenne et analyse spectrale*. Edition Hermès, Paris.
- Maurer, H. 1993. *Seismotectonics and upper crustal structure in the western Swiss Alps*. Ph.D. thesis, ETH Zürich.
- Mayer-Rosa, D. 1993. *Erdbeben in der Schweiz*. Schweizerischer Erdbebendienst, ETH Zürich.
- Moczo, P., and Kristek, J. 2002. *FD code to generage noise synthetics*. SESAME deliverable D09.02. SESAME EVG1-CT-2000-00026 project (<http://sesame-fp5.obs.ujf-grenoble.fr>).
- Moczo, P., Kristek, J., and Bystrický, E. 2001. Efficiency and optimization of the 3D finite-difference modeling of seismic ground motion. *J. Comp. Acoustic*, **9**(2), 593–609.

- Moczo, P., Kristek, J., Vavrycuk, V., Archuleta, R. J., and Halada, L. 2002. 3D Heterogeneous Staggered-Grid Finite-Difference Modeling of Seismic Motion with Volume Harmonic and Arithmetic Averaging of Elastic Moduli and Densities. *Bull. seism. Soc. Am.*, **92**(8), 3042 – 3066.
- Nakamura, Y. 1989. A method for dynamic characteristics estimation of subsurface using microtremor on the ground subsurface. *Quarterly Report of the Railway Technical Research Institute, Tokyo*, **30**(1), 25–33.
- Ohori, M., Mobata, A., and Wakamatsu, K. 2002. A comparison of ESAC and FK methods of estimating phase velocity using arbitrarily shaped microtremor arrays. *Bull. seism. Soc. Am.*, **92**(6), 2323–2332.
- Ohrnberger, M., Bonnefoy-Claudet, S., Cornou, C., Guillier, B., Kind, F., Koehler, A., Schissele-Rebel, E., Savvaidiss, A., and Wathelet, M. 2004. *User manual for software package CAP - a continuous array processing toolkit for ambient vibration array analysis*. SESAME deliverable D18.06. SESAME EVG1-CT-2000-00026 project (<http://sesame-fp5.obs.ujf-grenoble.fr>).
- Olsen, K. B. 1994. *Simulation of three-dimensional wave propagation in the Salt Lake Basin*. Ph.D. thesis, University of Utah, Salt Lake City, Utah.
- Olsen, K. B. 2000. Site Amplification in the Los Angeles Basin from 3D Modeling of Ground Motion. *Bull. seism. Soc. Am.*, **90**, S77–S94.
- Olsen, K. B., Day, S. M., Minster, J. B., Cui, Y., Chourasia, A., Faerman, M., Moore, R., Maechling, P., and Jordan, T. 2006. TeraShake: Strong shaking in Los Angeles expected from southern San Andreas earthquake. *Seism. Res. Lett.*, **77**, 281–282.
- Paolucci, R. 1999. Shear Resonance Frequencies of Alluvial Valleys by Rayleigh's Method. *Earthquake Spectra*, **15**(3).
- Paolucci, R., and Faccioli, E. 2003. Comment on "3D Site Effects: A thorough analysis of a high-quality dataset" by F. J. Chávez-García, J. Castillo, and W. R. Stephenson. *Bull. seism. Soc. Am.*, **93**(5), 2301–2305.
- Papadopoulos, G. A., and Lefkopoulos, G. 1993. Magnitude-distance relations for liquefaction in soil from earthquakes. *Bull. seism. Soc. Am.*, **83**(3), 925–938.
- Pfiffner, O. A., Heitzmann, S., Mueller, S., and Steck, A. 1997. Incision and back-filling of Alpine valleys: Pliocene, Pleistocene and Holocene processes. *Pages 265–276 of: Deep Structure of the Swiss Alps - Results of NRP 20*. Birkhäuser, Basel.
- Pousse, G., Bonilla, L.F., Cotton, F., and Margerin, L. 2006. Nonstationary Stochastic Simulation of Strong Ground Motion Time Histories Including Natural Variability: Application to the K-Net Japanese Database. *Bull. Seism. Soc. Am.*, **96**(6), 2103–2117.

- Rosselli, A. 2001. *Modélisation gravimétrique bi- et tridimensionnelle du substratum rocheux des vallées alpines*. Ph.D. thesis, Université de Lausanne.
- Roten, D., and Fäh, D. 2007. A combined inversion of Rayleigh wave dispersion and 2-D resonance frequencies. *Geophys. J. Int.*, **168**, 1261–1275.
- Roten, D., Fäh, D., Olsen, K.B., and Giardini, D. A comparison of observed and simulated site response in the Rhône valley. *submitted to Geophys. J. Int.*
- Roten, D., Cornou, C., Fäh, D., and Giardini, D. 2006. Two-dimensional resonances in Alpine valleys identified from ambient vibration wavefields. *Geophys. J. Int.*, **165**, 889–905.
- Sambridge, M. 1999a. Geophysical inversion with a neighbourhood algorithm: I. Searching a parameter space. *Geophys. J. Int.*, **138**, 479–494.
- Sambridge, M. 1999b. Geophysical inversion with a neighbourhood algorithm: II. Appraising the ensemble. *Geophys. J. Int.*, **138**, 727–746.
- Satoh, T., Kawase, H., and Matsushima, S. 2001. Estimation of S-wave velocity structures in and around the Sendai Basin, Japan, using array records of microtremors. *Bull. seism. Soc. Am.*, **91**(2), 206–218.
- Schisselé, E., Guilbert, J., Gaffet, S., and Cansi, Y. 2004. Accurate time-frequency-wavenumber analysis to study coda waves. *Geophys. J. Int.*, **158**, 577–591.
- Schmid, C. 2000. *Eigenfrequenzen von Flusstälern*. Semesterarbeit. ETH Zürich.
- Schmidt, R. 1986a. Multiple emitter location and signal parameter estimation. *IEEE Trans. Ant. Prop.*, **34**(3), 276–280.
- Schmidt, R. 1986b. Multiple source df signal processing: an experimental system. *IEEE Trans. Ant. Prop.*, **34**(3), 281–290.
- Schnabel, P., Seed, H. Bolton, and Lysmer, J. 1972. Modification of seismograph records for effects of local soil conditions. *Bull. Seism. Soc. Am.*, **62**(6), 1649–1664.
- Schweizerischer Ingenieur-und Architektenverein, Zurich. 2003. *Einwirkungen auf Tragwerke*. Schweizer Norm - SN; 505 261, Bauwesen.
- Seo, K. 1997. Comparison of measured microtremor with damage distribution. *In: JICA research and development program on earthquake disaster prevention*.
- Steimen, S., Fäh, D., Kind, F., Schmid, C., and Giardini, D. 2003. Identifying 2D Resonance in Microtremor Wave Fields. *Bull. seism. Soc. Am.*, **93**(2), 583–599.
- Stone, W. C., Yokel, F. Y., Celebi, M., Hanks, T., and Leyendecker, E. V. 1993. *Engineering aspects of the September 19, 1985 Mexico earthquake*. NBS building Science Series, 160. National Bureau of Standards, Washington, D.C.

- Towhata, I., and Ishihara, K. 1985. Modeling soil behavior under principal axes rotation. *Pages 523–530 of: Fifth International Conference on Numerical Methods in Geomechanics, Nagoya, Japan.*
- Tucker, B.E., and King, J.L. 1984. Dependence of sediment-filled valley response on input amplitude and valey properties. *Bull. seism. Soc. Am.*, **74**, 153–166.
- Wanner, E. 1955. Die Lage der Erdbebenherde im Mittelwallis. *Eclogae geol. Helv.*, **48**(2), 245–255.
- Wathelet, M. 2005. *Array recordings of ambient vibrations: surface-wave inversion.* Ph.D. thesis, University of Liège, Belgium.
- Wathelet, M., D., Jongmans, and Ohrnberger, M. 2004. Surface wave inversion using a direct search algorithm and its application to ambient vibration measurements. *Near Surface Geophysics*, **2**, 211–221.
- Wathelet, M., D., Jongmans, and Ohrnberger, M. 2005. Direct Inversion of Spatial Autocorrelation Curves with the Neighborhood Algorithm. *Bull. seism. Soc. Am.*, **5**(5), 1787–1800.
- Wax, M., and Kailath, T. 1985. Detection of signals by information theoretic criteria. *IEEE Transactions on ASSP*, **33**(2), 387–392.
- Weber, T., Laue, J., and Springmann, S. M. 2007. *Geotechnical laboratory tests for identification of soil parameters for the cyclic mobility model of sandy soil from Visp (VS).* Project report - SHAKE-VAL 2. ETH Zürich, Institute for Geotechnical Engineering.
- Wen, K.-L., Beresnev, I. A., and Yeh, Y. T. 1994. Nonlinear soil amplification inferred from downhole strong seismic motion data. *Geophysical Research Letters*, **21**(24), 2626–2628.
- Zerva, A., and Zhang, O. 1996. Estimation of signal characteristics in seismic ground motion. *Prob. Eng. Mech.*, **11**, 229–242.